

UNIVERSITY OF BIRMINGHAM

STUDY ON AMMONIA/HYDROGEN COMBUSTION FOR DISRUPTIVE HEAT ENGINE DEVELOPMENT

by

FANGYU ZHANG

A thesis submitted to the University of Birmingham for the degree of

DOCTOR OF PHILOSOPHY

Department of Mechanical Engineering
School of Engineering
College of Engineering and Physical Sciences
University of Birmingham
June 2023

UNIVERSITY OF
BIRMINGHAM

University of Birmingham Research Archive

e-theses repository

This unpublished thesis/dissertation is copyright of the author and/or third parties. The intellectual property rights of the author or third parties in respect of this work are as defined by The Copyright Designs and Patents Act 1988 or as modified by any successor legislation.

Any use made of information contained in this thesis/dissertation must be in accordance with that legislation and must be properly acknowledged. Further distribution or reproduction in any format is prohibited without the permission of the copyright holder.

[THIS PAGE INTENTIONALLY LEFT BLANK]

Abstract

Ammonia and hydrogen portrays a favourable potential to act as alternative fuels due to no carbon-related emissions. This thesis aims to investigate the characteristics of ammonia and hydrogen combustion, providing guidance for the development of a disruptive heat engine using ammonia and hydrogen.

Nakamura's mechanism is found to best predict the fundamentals of ammonia and hydrogen combustion and employed in the numerical study. The premixed laminar flame speed, ignition delay and flame structure of ammonia and hydrogen combustion are explored with various parameters. It shows an equivalence ratio of 1.1 is advantageous for both combustion stability and emission control. Hydrogen enrichment and oxygen enrichment effectively promote the laminar flame speed and reduce the ignition delay time. However, they comes at the cost of higher NO emission. Elevated pressure tends to reduce NO emission.

A lab-scaled swirl-enhanced combustor rig is established to analyse the characteristics of non-premixed ammonia and hydrogen flame. The results indicate increasing hydrogen blending ratios, initial gas temperature and decreasing the swirl numbers are effective ways to broaden the flame stability range. The optimal emission control occurs at stoichiometric condition. More hydrogen involvement leads to the increase of NO and NO_2 emissions and the decrease in ammonia slip. However, the effect is weakened under fuel-rich conditions.

The numerical and experimental emission results are compared with those from various ammonia-based heat engines. Most results exceeds EURO 7 regulation standards. The two-zone rich-lean neat ammonia fuelled micro gas turbine shows the best control of emission with thermal efficiency of $\sim 22\%$.

"As I get older, I realise being wrong isn't a bad thing like they teach you in school. It is an opportunity to learn something."

Richard Feynman

Acknowledgements

I would like to first express my sincere gratitude to my supervisors, Dr Dawei Wu and Dr Mehdi Jangi, who have continued to support me and provided me with professional guidance and encouragement throughout these years of study. If it was not for them, I would not have studied here and have had such a wonderful academic experience.

Thanks are also due to Newcastle University for offering me the scholarship in my first-year of study.

I would like to also thank two research fellows, Dr Gen Chen and Dr Gengxin Zhang. They have provided me with their insights into how to approach this research area and have shown excellent examples of how to be an independent scientific researcher.

It has been my pleasure working with the technician team, namely, Mr Sonny Duc Mao, Mr Jack Garrod and Mr Kevan Charlesworth. Without their ceaseless help and contribution on the experimental setup, I would not have been able to complete the experimental work on time.

I would also like to thank my colleagues and friends who shared my hardships, especially those who helped me during my experiments, namely, Dr Meixi Liu, Mr Yi Li, Mr Mingqiang Li, Miss Yuqi Zhang, Mr Peihao Chen, Mr Zeyu Sun, Mr Fanggang Zhang, Mr Chengqing Wen, Mr Xu He and Mr Jinhai Wang from University of Birmingham, and additionally Dr Gulcan Ozel-Erol and Dr Samuel Wood from Newcastle University.

The list could not have been complete without my beloved boyfriend, Mr Ilias Konstantinou, who has gone through all my sorrows and pains over the years

and always help me in my academic research and personal life in general.

Last but not least, my deepest gratitude goes to my family members, Mr Jianrong Wang, Mrs Ling Zhang, Mr Yuanhong Zhang and Mrs Qixin He. It is hard to imagine how difficult it would have been to pursue my goal of studying abroad and pursuing a PhD while experiencing a pandemic without the love and care they have always given me.

Miss Fangyu Zhang

[THIS PAGE INTENTIONALLY LEFT BLANK]

Contents

Abstract iv

Acknowledgements vii

Nomenclature xix

List of Figures xxvi

List of Tables xxviii

List of Publications xxix

1 Introduction **1**

1.1 Decarbonisation challenges in transportation 1

1.2 Heat engines 5

1.3 Future fuels – Ammonia and Hydrogen 7

1.4 Aims and Objectives 15

1.5 Layout of Thesis 16

2 Literature Review **18**

2.1 Ammonia chemical kinetic reaction mechanisms 18

2.2 Fundamentals of ammonia combustion 25

2.3 Ammonia-based combustion emissions 35

2.4 Heat engines powered by ammonia 43

2.5 Summary 49

3 Methodologies **52**

3.1 Introduction . . . 52

3.2 Numerical methodology . . . 53

3.2.1 Premixed Laminar Flame Speed Modelling . . . 53

3.2.2 Ignition Delay Time Modelling . . . 59

3.2.3 Burner-Stabilised Flame Structure Modelling . . . 64

3.2.4 Continuous combustion model . . . 66

3.3 Experimental setup . . . 72

3.3.1 Combustor . . . 73

3.3.2 Swirl-enhanced ammonia combustor rig . . . 75

3.3.3 Ignition system . . . 82

3.3.4 Exhaust emissions measurement instruments . . . 83

3.3.5 Optical setup for OH^* chemiluminescence imaging . . . 91

3.4 Summary . . . 92

4 Kinetic study of premixed ammonia/hydrogen combustion characteristics **93**

4.1 Introduction . . . 93

4.2 Ammonia chemical kinetic reaction mechanism selection . . . 94

4.3 Parametric study . . . 99

4.3.1 Laminar flame speed . . . 99

4.3.2 Ignition delay time . . . 104

4.3.3 Flame structure 109
4.3.4 Selected parameters for the external combustor of the free piston engine 119
4.4 Modelling of premixed ammonia and hydrogen combustion in generic gas turbine 123
4.5 Summary 129

5 Experimental analysis of non-premixed ammonia flame with hydrogen in a swirl-enhanced combustor 133

5.1 Introduction 133
5.2 Blowoff limit 134
5.2.1 Blowoff limit measurement procedure 134
5.2.2 Results and Discussion 135
5.3 Exhaust emissions analysis 140
5.3.1 Exhaust emissions measurement procedure 140
5.3.2 Results and Discussion 143
5.3.2.1 Emission performance of different hydrogen blending ratios at different equivalence ratios 143
5.3.2.2 Emission performance at different initial temperatures 146
5.3.2.3 Emission comparison under the wall insulated and non-insulated conditions 148

5.3.2.4 Emission performance at different swirl numbers . 148
5.4 OH* chemiluminescence 151
5.4.1 Image processing technique 151
5.4.2 Results and Discussion 155
5.5 Summary 162

6 Comparison of emission characteristics of different ammonia fuelled heat engines 164

6.1 Introduction 164
6.2 Development of ammonia fuelled heat engines 164
6.2.1 Spark-ignition engines 164
6.2.2 Compression-ignition engines 168
6.2.3 Gas turbines 172
6.2.4 Free piston engines 174
6.3 Calculation methodology for emission comparison 176
6.4 Comparison results 178
6.5 Summary 188

7 Conclusions and future work 190

7.1 Conclusions 190
7.2 Future work 194

Appendices 196

Bibliography 228

Nomenclature

Abbreviations

0D	**Z**ero-**D**imensional
1D	**O**ne-**D**imensional
AIST	**A**dvanced **I**ndustrial **S**cience and **T**echnology
ANR	**AN**alyser **R**ack unit
ATDC	**A**fter **T**op **D**ead **C**entre
CDI	**C**apacitor **D**ischarge **I**gnition
CFD	**C**omputational **F**luid **D**ynamics
CFR	**C**ooperative **F**uel **R**esearch
CI	**C**ompression-**I**gnition
CLD	**C**hemi**L**uminescence **D**etector
CRN	**C**hemical **R**eactor **N**etwork
DME	**D**i**M**ethyl **E**ther
DRGEP	**D**irected **R**elation **G**raph with **E**rror **P**ropagation
FPE	**F**ree **P**iston **E**ngine
FTIR	**F**ourier **T**ransform **I**nf**R**ared
GHG	**G**reen**H**ouse **G**as
GT	**G**as **T**urbine

GTRC	**G**as **T**urbine **R**esearch **C**entre
HGV	**H**eavy **G**oods **V**ehicle
HITE	**H**ighest **I**ndicated **T**hermal **E**fficiency
HP	**H**ighest **P**ower output
HTE	**H**ighest **T**hermal **E**fficiency
ICE	**I**nternal **C**ombustion **E**ngine
IMO	**I**nternational **M**aritime **O**rganisation
KAUST	**K**ing **A**bdullah **U**niversity of **S**cience and **T**echnology
KIER	**K**orea **I**nstitute of **E**nergy **R**esearch
LAE	**L**owest **A**mmonia **E**mission
LGHG	**L**owest **G**reen**H**ouse **G**as **E**missions
LHV	**L**ower **H**eating **V**alue
LNE	**L**owest **N**Ox **E**missions
MBMS	**M**olecular **B**eam **M**ass **S**pectrometry
MCU	**M**ain **C**ontrol **U**nit
MFC	**M**ass **F**lowrate **C**ontroller
MPA	**M**agneto-**P**neum**A**tic
NA	**N**ot **A**pplicable
NSRL	**N**ational **S**ynchrotron **R**adiation **L**aboratory
NTP	**N**ormal **T**emperature and **P**ressure
OVN	**O**ven **UN**it

PDD	**P**ulse **D**ischarge helium ionisation **D**etector
PFR	**P**lug **F**low **R**eactor
PIV	**P**article **I**mage **V**elocimetry
PLIF	**P**laner **L**aser and **I**nduced **F**luorescence
PSR	**P**erfectly **S**tirred **R**eactor
RCM	**R**apid **C**ompression **M**achine
ROP	**R**ate **O**f **P**roduction
RSD	**R**elative **S**tandard **D**eviation
SCR	**S**elective **C**atalytic **R**eduction
SI	**S**park-**I**gnition
SODI	**S**tart **O**f **D**iesel **I**njection
SOFC	**S**olid **O**xide **F**uel **C**ells
STP	**S**tandard **T**emperature and **P**ressure
TCD	**T**hermal **C**onductivity **D**etector
THC	**T**otal **H**ydro**C**arbon
VUV	**V**acuum **U**ltra**V**iolet

Greek Symbols

Symbol	Unit	Name
α	$^\circ$	the vane angle of the swirler
κ	–	magnetic susceptibility of oxygen

λ	$-$	air-fuel equivalence ratio
τ	ms	ignition delay time
ϕ	$-$	fuel-air equivalence ratio
ϕ_{global}	$-$	global fuel-air equivalence ratio
$\phi_{overall}$	$-$	overall fuel-air equivalence ratio
Ω	$-$	oxygen contents in the oxidant
Ω_{comp}	$-$	piston motion pattern during compression process in FPEs
Ω_{exp}	$-$	piston motion pattern during expansion process in FPEs

Latin Symbols

Symbol	**Unit**	**Name**
D_i	mm	inner diameter of the swirler
D_o	mm	outer diameter of the swirler
F_m	$-$	moisture correction factor
H	A/m	magnetic field strength
$I_{OH^*_{ij}}$	$-$	intensity of excited hydroxyl the i^{th} column and the j^{th} row
II^*_{OH}	$-$	intensity of excited hydroxyl
m	g	mass
M	g/mol	molar mass of the species
N	$-$	times of the measurement
$O_{2_{mea}}$	$-$	measured oxygen concentration in the exhaust gases

P	bar	initial pressure
ppm_{dry}	–	dry emission concentration
ppm_{mea}	–	measured emission concentration
ppm_{norm}	–	normalised emission concentration
ppm_{wet}	–	wet emission concentration
S	–	swirl number
S_L	cm/s	laminar flame speed
T	K	initial temperature
$\bar{x}$	–	average value of the five times measurements
x_i	–	the average value for each measurement
$x[NH_3]_{start}$	–	molar fraction of imported NH_3
$x[NO_x]_{end}$	–	molar fraction of NO_x emission
$x[NO_x]'_{end}$	–	molar fraction of normalised NO_x emission

Notation

$E\%...$	energy fraction of ... in the fuel blends
$\dot{m}(...)$	mass flow rate of ... (g/s)
$x[...]$	mole fraction of ...
$x\%...$	mole fraction of ... in the fuel blends

Subscripts

$(...)_{air,sec}$	secondary air property
$(...)_{exh}$	exhaust gas property
$(...)_{fuel}$	fuel property
$(...)_{fuel,stoich}$	fuel property at stoichiometric condition
$(...)_{in}$	inlet property
$(...)_{out}$	outlet property
$(...)_{oxidant}$	oxidant property
$(...)_{oxidant,stoich}$	oxidant property at stoichiometric condition

Superscripts

$(...)^{*}$	excited radical

Uncommon units

sl/min	a unit of gas flow rate at standard temperature and pressure

List of Figures

1.1 GHG emissions from different sectors in the UK in 2019 2

1.2 Transport decarbonisation roadmap 3

1.3 The working principles of ICEs 5

1.4 The working principle of a GT 6

1.5 The configuration of different types of FPEs 7

1.6 Energy use and projected fuel mix 2018-2050 for the simulated IMO ambitions pathway with main focus on design requirements 11

1.7 Ammonia economic cycle with production, storage, distribution and utilisation 12

1.8 Hydrogen density in hydrogen carriers 12

2.1 Stable premixed ammonia/air flame 27

2.2 Ammonia fuelled micro gas turbine combustor in Tohoku University 36

2.3 Premixed swirl burner in GTRC 40

2.4 Swirl burner in KAUST 40

2.5 The swirl combustor with four different sample points for local NO measurements in KAUST 42

2.6 Gazamo system and ammonia fuelled motor bus 45

2.7 Modified SI engine with ammonia and hydrogen injectors 47

2.8 Photo of ammonia powered micro gas turbine power plant 47

2.9 Schematic diagram of ammonia powered micro gas turbine 48

3.1 Simulation diagram of premixed laminar flame speed 54

3.2 Ansys Chemkin-Pro simulation process 55

3.3 Diagram of Closed-Homogeneous Batch Reactor 60

3.4 Typical definition of ignition delay time in a shock tube 61

3.5 Diagram of flame structure simulation 66

3.6 Diagram of the continuous combustion model 68

3.7 Schematic of the continuous combustion model 69

3.8 (a) Combustor geometry and (b) Half section view of the combustor 74

3.9 3D CAD model of the combustor head 74

3.10 3D CAD model of the fuel nozzle 75

3.11 3D CAD model of the swirler 76

3.12 Schematic diagram of experiment test rig 78

3.13 Photo of the test room 79

3.14 Photo of the control room 80

3.15 Photo of the Phantom® v710 CMOS camera 81

3.16 Photo of the UV-Nikkor 105mm f/4.5 lens 81

3.17 Schematic diagram of the ignition system 83

3.18 (a) front angle of the ignitor location (b) 45° angle of the ignitor location 84

3.19 Photo of the HORIBA MEXA-7100DEGR multi-gas analyser . . . 85

3.20 Photo of Thermo Fisher Trace 1300 gas chromatography 89

3.21 Chemiluminescence visualisation setup 91

4.1 Comparison of experimental and computational premixed laminar flame speed of ammonia/hydrogen as a function of equivalence ratios at different ammonia fractions by energy 95

4.2 Comparison of experimental and computational ignition delay time of $0.01143NH_3/0.00857O_2/0.98Ar$ ($\phi = 1.0$) under different pressure . 96

4.3 Comparison of experimental and computational concentration profiles of (a) NH_3, H_2, N_2 and (b) NO, NH_2, N_2O 98

4.4 The function of laminar flame speed of premixed ammonia/hydrogen flame with equivalence ratios at various hydrogen blending ratios 99

4.5 Radical profiles of O, H, OH at the equivalence ratio of 1.10 when $x\%H_2$ is (a) 0.0, (b) 0.2, (c) 0.4 and (d) 0.6 101

4.6 The function of laminar flame speed of premixed ammonia/hydrogen flame with oxygen contents in the oxidant 102

4.7 The function of laminar flame speed of premixed neat ammonia flame and ammonia/hydrogen flame with initial temperature at various pressure 103

4.8 Variation of ignition delay time of premixed ammonia/hydrogen with hydrogen blending ratios at different equivalence ratios 105

4.9 Normalised sensitivity analysis of OH with (a) $x\%H_2 = 0\%$ and (b) $x\%H_2 = 20\%$ . . . 105

4.10 Normalised sensitivity analysis of OH with (a) $\phi = 0.5$ and (b) $\phi = 1.5$ 107

4.11 Variation of ignition delay time of premixed ammonia/hydrogen with oxygen contents in oxidant . . . 108

4.12 Normalised sensitivity analysis of OH with (a) $\Omega = 0.21$ and (b) $\Omega = 1.00$ . . . 108

4.13 Ignition delay time of premixed ammonia/hydrogen with various initial temperature and pressure at (a) $x\%H_2 = 0\%$ and (b) $x\%H_2 = 30\%$ . . . 109

4.14 (a) $NH_3, H_2, NO, NO_2, N_2O$ emissions and (b) normalised NO_x emission as a function of equivalence ratios for a $70\%NH_3/30\%H_2$ flame 111

4.15 ROP analysis for NO at the equivalence ratio of (a) 0.9 and (b) 1.2 112

4.16 (a) $NH_3, H_2, NO, NO_2, N_2O$ emissions and (b) normalised NO_x emission as a function of hydrogen blending ratios . . . 114

4.17 ROP analysis of NO at the hydrogen blending ratios of (a) 0.0, (b) 0.2 and (c) 0.5 . . . 115

4.18 ROP analysis of H_2 at the hydrogen blending ratios of (a) 0%, (b) 20% and (c) 50% . . . 116

4.19 (a) $NH_3, H_2, NO, NO_2, N_2O$ emissions and (b) normalised NO_x emission as a function of oxygen contents in the oxidant for a $70\%NH_3/30\%H_2$ flame . . . 117

4.20 ROP analysis of NO with oxygen content in the oxidant at (a) 0.21 and (b) 1.00 118

4.21 $NH_3, H_2, NO, NO_2, N_2O$ emissions as a function of pressures for a $70\%NH_3/30\%H_2$ flame 119

4.22 Major species concentration under rated operation condition of free piston engines 122

4.23 ROP analysis of NO under rated operation condition of free piston engines 122

4.24 Variations of (a) peak heat production rate and (b) outlet temperature and emissions with different equivalence ratios 124

4.25 Variations of (a) peak heat production rate and (b) outlet temperature and emissions with different hydrogen blending ratios 126

4.26 Variations of (a) peak heat production rate and (b) outlet temperature and emissions with different oxygen contents in the oxidant . 126

4.27 Variations of (a) peak heat production rate and (b) outlet temperature and emissions with different pressures 127

4.28 Variations of (a) peak heat production rate and (b) outlet temperature and emissions with different initial temperature 128

4.29 Variations of (a) peak heat production rate and (b) outlet temperature and emissions with secondary air injection 129

5.1 Blowoff limits of non-premixed ammonia/hydrogen flames and ammonia/methane flames 137

5.2 Blowoff limits of non-premixed CH_4, $60\%NH_3/40\%H_2$ and $40\%NH_3/60\%CH_4$ flames under different initial gas temperature 139

5.3 Blowoff limits of non-premixed $70\%NH_3/30\%H_2$ flames with different swirl numbers 140

5.4 (a) NO, (b) NO_2, (c) H_2 and (d) NH_3 emissions of non-premixed ammonia/hydrogen flames versus various global equivalence ratios at different hydrogen blending ratios 144

5.5 (a) NO, (b) NO_2, (c) H_2 and (d) NH_3 emissions of non-premixed ammonia/hydrogen flames versus different initial temperature . . . 146

5.6 (a) NO, (b) NO_2, (c) H_2 and (d) NH_3 emissions of non-premixed ammonia/hydrogen flames versus various global equivalence ratios under insulated and non-insulated wall conditions 149

5.7 (a) NO, (b) NO_2, (c) H_2 and (d) NH_3 emissions of non-premixed ammonia/hydrogen flames versus various global equivalence ratios with different swirl numbers 150

5.8 The workflow of image processing 152

5.9 An example of image processing before using Abel inversion algorithm 153

5.10 Background-corrected, minimum-value-corrected, noise-removed image without false colormap 154

5.11 Time-averaged OH^* chemiluminescence distributions (a) before and (b) after Abel inversion algorithm in different regions 154

5.12 (a) OH^* chemiluminescence profiles (b) OH^* intensity for non-premixed $60\%NH_3/40\%H_2$ flames with various global equivalence ratios 157

5.13 (a) OH^* chemiluminescence profiles (b) OH^* intensity for non-premixed ammonia/hydrogen flames with various hydrogen blending ratios 158

5.14 (a) OH^* chemiluminescence profiles (b) OH^* intensity for non-premixed $60\%NH_3/40\%H_2$ flames at various initial temperature . . 160

5.15 (a) OH^* chemiluminescence profiles (b) OH^* intensity for non-premixed $70\%NH_3/30\%H_2$ flames with various swirl numbers . . . 161

6.1 (a) CO, (b) CO_2, (c) NO_x and (d) NH_3 emission from Ammonia/-natural gas SI engine 168

6.2 (a) Indicated specific CO_2, (b) indicated specific N_2O and (c) GHG emissions from ammonia/diesel dual fuelled CI engines 170

6.3 (a) NO, NO conversion ratio and (b) NH_3, N_2O, NO_2, O_2 emission from ammonia/kerosene GT 173

6.4 (a) NO_x emission and (b) NH_3 emission from ammonia/methane dual-fuelled FPE 175

6.5 Examples of (a) symmetric and (b) asymmetric piston motion patterns 175

1 NO analyser linearization report. 196

2 NO_x analyser linearization report. 197

List of Tables

1.1 Chemical and physical properties of hydrogen, ammonia, methane, propane and diesel 9

2.1 List of ammonia chemical kinetic reaction mechanisms. 23

3.1 Worksheet for premixed laminar flame speed modelling. 57

3.2 Simulation worksheet for ignition delay time modelling. 62

3.3 worksheet for burner-stabilised flame structure modelling. 67

3.4 Calculated initial component ratios for studying the impact of equivalence ratios 70

3.5 Calculated initial component ratios for studying the impact of hydrogen blending ratio 71

3.6 Calculated initial component ratios for studying the impact of oxygen contents in the oxidant 71

3.7 Operational conditions for the selected initial component ratio . . . 72

3.8 Initial conditions for studying the impact of secondary air injection under $T = 300$ K, $P = 1$ bar 72

3.9 Technical data of three radial swirlers. 76

3.10 Specifications of the Phantom® v710 CMOS camera 82

3.11 Technical data table of HORIBA MEXA-7100DEGR 87

3.12 Technical data table of Thermo Fisher Trace 1300 gas chromatography 90

4.1 Summary of candidate ammonia mechanisms validated with experimental data. 98

4.2 Inlet components with different equivalence ratios for a $70\%NH_3/30\%H_2$ flame. 111

4.3 Inlet components with hydrogen blending ratios when $\phi = 1.1$. . . . 114

4.4 Inlet components at different oxygen contents in the oxidant for a $70\%NH_3/30\%H_2$ flame. 118

5.1 The experimental conditions for blowoff limit test. 135

5.2 The experimental conditions for emission measurements and OH^* chemiluminescence imaging. 141

6.1 Summary of experimental emissions from ammonia fuelled SI engines. 180

6.2 Proposed EURO 7 regulation standards of NO_x and ammonia emissions for buses and commercial trucks with internal combustion engines [203]. 181

6.3 Summary of experimental emissions from ammonia fuelled CI engines. 184

6.4 Summary of emissions from ammonia fuelled GTs. 186

6.5 Summary of simulated emissions from ammonia fuelled FPEs. . . . 187

List of Publications

Journal Paper

1. **Characterising premixed ammonia and hydrogen combustion for a novel Linear Joule Engine Generator**

   Fangyu Zhang, Gen Chen, Dawei Wu, Tie Li, Zhifei Zhang, Ning Wang (International Journal of Hydrogen Energy: https://doi.org/10.1016/j.ijhydene.2021.04.110)

2. **Experimental Study on the Adhesive Fuel Features of Inclined Wall-Impinging Spray at Various Injection Pressure Levels in a Cross-Flow Field**

   Gengxin Zhang, Penghua Shi, Panpan Dong, Fangyu Zhang, Yifei Zhang and Hongliang Luo (Sustainability: https://doi.org/10.3390/su15076312)

3. **Experimental Investigation on Combustion and Emission Characteristics of Non-premixed Ammonia/Hydrogen Flame**

   Fangyu Zhang, Gengxin Zhang, Zhongcheng Wang, Mehdi Jangi, Dawei Wu, Hongming Xu (Submitted to the International Journal of Hydrogen Energy. Reference number: HE-D-23-09039R1)

Conference contribution

1. **Characteristics of Ammonia/Hydrogen Premixed Combustion in a Novel Linear Engine Generator**

   Fangyu Zhang, Gen Chen, Dawei Wu, Tie Li, Zhifei Zhang, Ning Wang (Presented at the First World Energies Forum, 14 Sep–05 Oct, 2020)

https://doi.org/10.3390/WEF-06925

Awarded the ***Best Oral Presentation Award***

2. **Combustion characteristics and emission characteristics of ammonia/hydrogen dual-fuelled gas turbine**

   Fangyu Zhang, Gen Chen, Dawei Wu (Presented at the European Combustion Meeting 2021, 14-15 April, 2021)

   https://research.birmingham.ac.uk/en/publications/combustion-and-emission-characteristics-of-ammoniahydrogen-dual-f

3. **Characterising Injection and Combustion of Ammonia as a Marine Fuel**

   Fangyu Zhang, Zhifei Zhang, Ning Wang, Tie Li, Dawei Wu (Presented at the 3^{rd} International Conference on Smart & Green Technology for shipping and Maritime Industries) https://www.bib.irb.hr/1170165/download/1170165.SMATECH_2021_Proceedings.pdf#page=100

4. **Investigation on flame stability limits of ammonia/hydrogen and ammonia/methane diffusion combustion**

   Fangyu Zhang, Dawei Wu, Mehdi Jangi, Tie Li, Zhifei Zhang, Ning Wang (Presented at the Hydrogen Fuelled Transportation, 20-22 September, 2022)

   https://www.youtube.com/watch?v=gGoHHmsWtk4

5. **The design and simulation of the linear engine generator used for electric propulsion system of the marine transportation and offshore gas/oil platforms**

   Mingqiang Li, Ugo Ngwaka, Dawei Wu, Fangyu Zhang, Gen Chen (Presented at the ICSOT Indonesia 2021, 19-20 November,2021) https://icsot.ppns.ac.id/for-authors/proceeding-icsot/

Chapter 1. Introduction

1.1 Decarbonisation challenges in transportation

Increasingly prominent environmental issues and energy crisis are topics of great concern to the transport industry nowadays. As a result of global warming, there is a growing commitment among countries to achieve Net Zero target, for example, the UK has pledged to achieve zero emission targets by 2050 according to a recent law [1]. According to the UK Transport and Environment Statics annual report published in 2021, transport accounted for nearly 27% of the UK's total emissions in 2019, totalling 122 $MtCO_2e$ [2]. Figure 1.1 shows greenhouse gas (GHG) emissions of different sectors in the UK in 2019 [3]. As coal-fired power generation has been replaced mainly by natural gas, the emissions from energy sector have been significantly reduced but the emissions from transport are about the same as in past years [2]. The transport sector has been the largest emitter since 2016 [2]. International Maritime Organisation (IMO) set goals to minimise the carbon intensity of international shipping by 70% and the total annual GHG emissions of international shipping by at least 50% compared to 2008 by 2050 as a response [4]. The decarbonisation of the transport sector is an indispensable component of the climate change mitigation. As a result, new stringent regulations will keep on being imposed on the transport industry.

On the other hand, gasoline-fuelled or diesel-fuelled conventional transport faces a greater challenge due to the global energy crisis. A growing demand for energy has been one of the most burdensome issues to be addressed in the 21^{st} century. Despite the development and improvement of the renewable en-

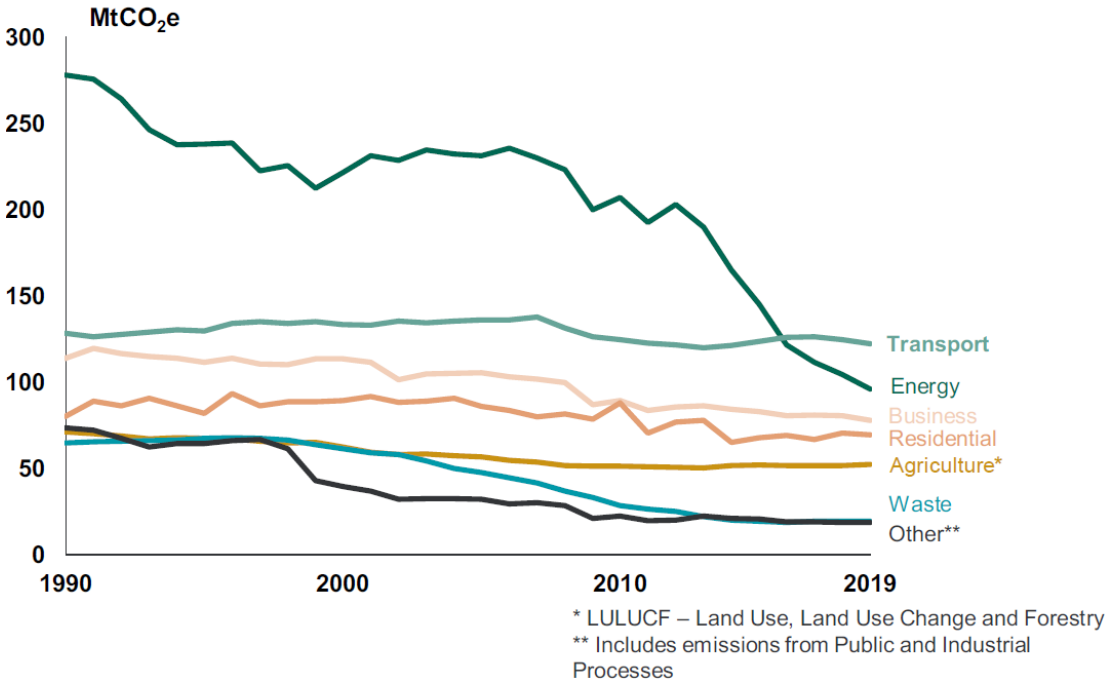


Figure 1.1: GHG emissions from different sectors in the UK in 2019 [3].

ergy utilisation, fossil fuels continue to be the primary source of energy. However, the declining global gasoline and diesel reserves in conjunction with the Russo-Ukrainian War have further exacerbated the global energy crisis. In order to reduce the transportation's reliance on fossil fuels, many European countries planned to cease selling new gasoline and diesel vehicles in the upcoming years. For example, the UK has promised to ban the sale of such vehicles by 2035 [5]. The shipping and rail freight industries are considering the use of an alternative fuel, in recognition of this being one of the viable ways to combat against the energy crisis while maintaining a competitive status.

Decarbonising the transport industry cannot rely on a single approach. A rough roadmap of decarbonising transport is illustrated in Figure 1.2. Battery electric vehicles are a new trend in the market to ease the stress of decarbonizing short-distance travel vehicles with a light-duty. A battery can be fast charged or

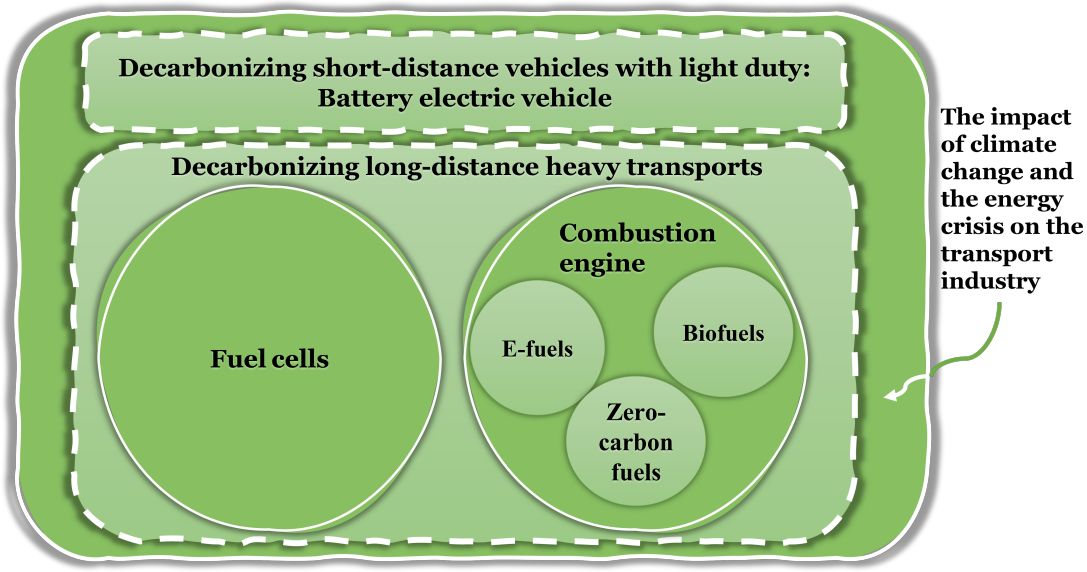


Figure 1.2: Transport decarbonisation roadmap.

replaced at a charging station and a more efficient electric motor and powertrain can offset part of the weight penalty to vehicles [6]. However, it is difficult to electrify large-scale transport, i.e. HGV, rail freight and maritime shipping, which is used to transport goods and products due to heavy loads and long distances. Given the best battery technology, the energy stored in one pound of gasoline is equivalent to the energy stored in 40 pounds of battery [6]. Although battery trucks are under operation for short-distance travel, heavy-duty trucks using current lithium-ion batteries and electric motors carry approximately 40% less goods than the conventional trucks for the same range [7]. Moreover, it is unlikely that maritime shipping can refuel frequently during journeys [6]. Hence, electrifying heavy transports with battery technology does not seem to be a feasible option. The decarbonisation of heavy transport is imminent.

The key to decarbonising heavy transport is finding a transportable, high-energy-density energy storage solution. One of the most reliable energy storage options is chemical energy storage. In recent years, fuel cells have received in-

creasing attention as they directly convert chemical energy into electricity with fewer emissions than hydrocarbon-fuelled engines and a much shorter refuelling time than batteries. There are, however, a number of issues that need to be addressed before fuel cells become commercially viable. For instance, hydrogen fuel cells face problems concerning hydrogen storage and the high cost of infrastructure investment and raw materials (platinum and iridium, which are commonly used as catalysts) [8, 9]. Solid oxide fuel cells (SOFCs) require a high operating temperature, resulting in a long start-up and cooling-down time [10]. It is also important to take into account the fuel properties, for example, ammonia SOFCs require catalysts in order to increase the rate of ammonia conversion [10].

Another effective method to extract chemical energy is combustion. When substances react through chemical reactions, they release energy and heat to the engine, converting chemical energy to mechanical energy. It is a very mature and robust technology that has been widely used in all means of transportation over decades. Finding an alternative carbon-neutral fuel, rather than giving up the engine, would be the most efficient solution to achieving decarbonisation, as well as reducing reinvestment costs. Some attractive candidates are e-fuels, biofuels and zero-carbon fuels. E-fuels are synthetic fuels that combine captured carbon with hydrogen produced by electrolyzing water using sustainable energy. Well-to-wake emissions from e-fuels, such as e-methanol, can reach 99% reduction in GHG emissions, provided the production is completely based on renewables [11]. Biofuels are produced from biomass through pyrolysis process. Bioethanol made from corn and biodiesel made from soybeans are the most common biofuels. Biofuels have proven to have considerably fewer GHG emissions than gasoline, but GHG emissions from the biofuel synthesis method are of great concern [12]. In addition, zero-carbon fuels, namely hydrogen (H_2) and ammonia (NH_3), benefit

from yielding no carbon emissions, which is the primary reason why they are receiving worldwide attention as potential future fuels.

1.2 Heat engines

One of the typical heat engines is the internal combustion engine (ICE), which is frequently used in automobiles, motorbikes, locomotives, and ships. As it has a long history of development and theoretical basis, ICE is very reliable and always considered for engine retrofits. In ICE, by burning fuel in the internal combustor, high-temperature high-pressure combustion gases as working fluid provide a force on the piston, transforming chemical energy into kinetic energy. Kinetic energy is then converted into mechanical energy by the cranktrain (reciprocating piston engines) or rotor (rotary piston engines). Figure 1.3 shows the working principle of ICEs. The ICE is also flexible for various gaseous fuels (e.g. nature gas, propane, biogas) and liquid fuels (e.g. gasoline, methanol, ethanol) [13], which inspires the research topic of hydrogen or ammonia fuelled ICEs [14, 15, 16, 17, 18].

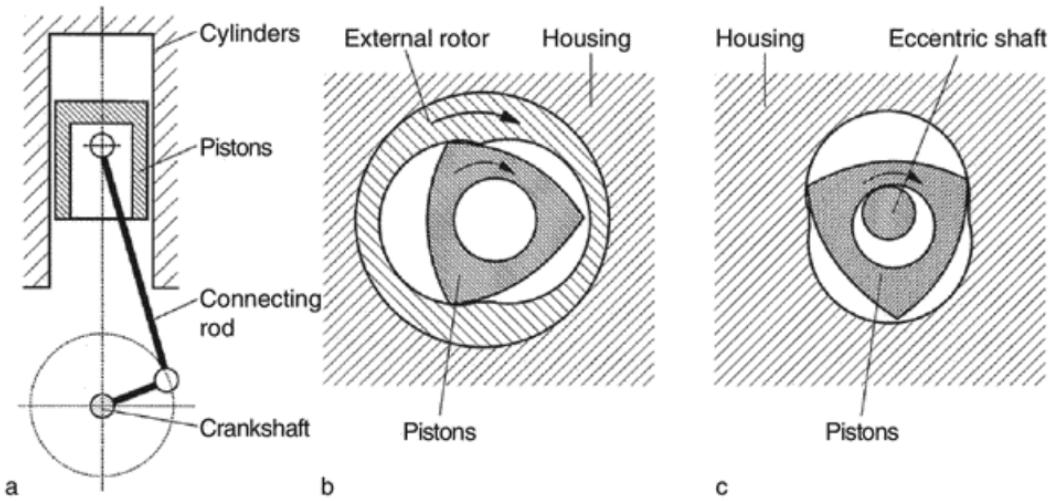


Figure 1.3: The working principles of ICEs, (a) reciprocating piston engines, (b) and (c) rotary piston engines [13].

Comparing with the reciprocating engines, the power-to-weight ratio of a gas turbine (GT) is relatively higher. Namely, in order to produce the same amount of power, GT is lighter than the reciprocating engines, resulting in GT's wider use as marine and aviation propulsion. A classic GT consists of three major components, a compressor, a combustor and a turbine. Figure 1.4 illustrates the working principle of a GT. The air pressure is increased by an air compressor and then enters the combustor where the fuel is injected. The combustion gas after the combustion chamber is therefore in a state of high temperature and high pressure, and generates shaft work through the turbine. GTs are usually powered by kerosene, natural gas, and diesel with recent developments attempting to use hydrogen blends and biomass as fuel [19].

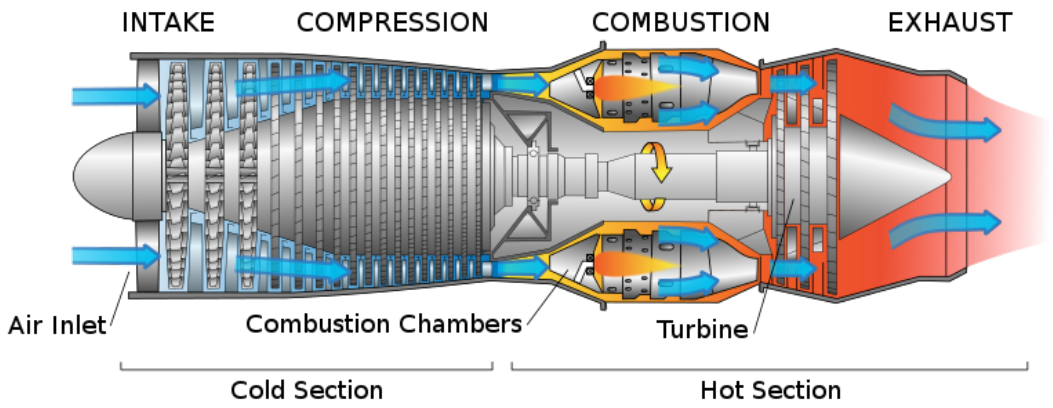


Figure 1.4: The working principle of a GT [20].

There is another promising heat engine to alleviate the stress of decarbonizing heavy transport which is Free Piston Engine (FPE). FPE is crankless and able to generate electricity directly through a linear engine generator. Compared with a conventional ICE, FPE has no crankshaft, gudgeon pins, connecting rods and flywheel [21]. The main components are combustor, load device and a rebound device [22]. Figure 1.5 presents several types of FPE including single-power piston,

dual-power piston, single double-acting power piston, split-cycle double-acting power piston expander and compressor and opposed dual-power piston [23]. Due to the compact and mechanically simple structure, FPEs have the benefit of lower friction and heat transfer losses than traditional ICEs. Since FPEs operate under different compression ratios, they are also suitable for a variety of fuels, enabling the use of alternative fuels and combustion technologies.

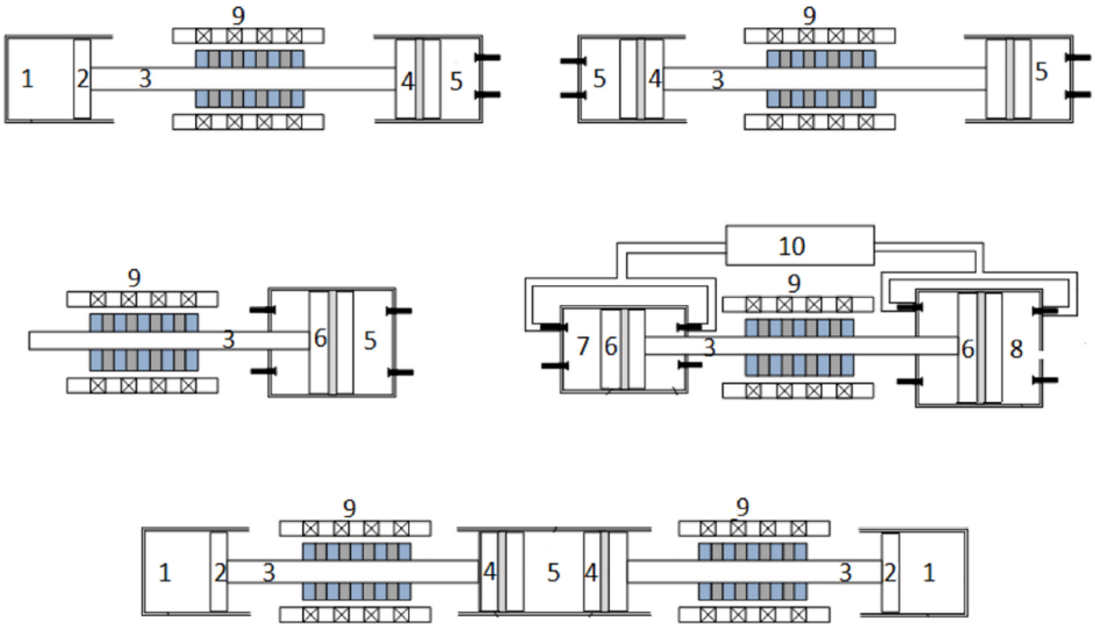


Figure 1.5: The configuration of different types of FPEs [23].

1.3 Future fuels – Ammonia and Hydrogen

As hydrogen is a carbon-free and nitrogen-free elementary substance, it has been considered as a potential future fuel. However, hydrogen cannot be easily stored due to its normal boiling point and vapour pressure, as shown in Table 1.1. Hy-

drogen can either be liquified under $-253°C$, 1 bar or compressed to supercritical state under 300 or 700 bar at the ambient temperature. The extreme cold temperature leads to a technical problem for storage while high pressure induces safety concerns. Transport and distribution of hydrogen are also significant costs associated with hydrogen delivery. These hurdles have made hydrogen difficult to commercialize widely.

Apart from hydrogen, ammonia is also regarded as a promising carbon-free future fuel. According to DNV's report titled Energy Transition Outlook - Maritime Forecast to 2050, the most promising carbon-neutral marine fuels towards 2050 in a decarbonization trajectory will be e-ammonia, blue ammonia, and biomethanol based on a 30-scenario model [40]. In Figure 1.6, it is projected in the model that ammonia will start to be used commercially as a maritime fuel from 2037, become the principal fuel choice for new ships by 2042, and occupy 25% of maritime fuel mix in shipping by 2050 [41, 42]. It is found in Table 1.1 that the physical properties of ammonia and propane are similar [43, 44, 45]. Ammonia can be readily liquified under approximately $-34°C$ at atmospheric pressure or compress in a ~ 10 bar tank at ambient temperature. Since ammonia has been extensively applied as fertilizer and cleaning chemicals in agriculture, the production, transportation and distribution of ammonia are deep-rooted. Although the traditional Haber-Bosch ammonia generation approach is still currently employed around the world, the motivation of using renewable energy to produce hydrogen for a new type of Haber-Bosch ammonia generation method is driving the production of green ammonia [46, 47, 48, 49]. In this way, any carbon footprints in the lifecycle of utilising ammonia as a fuel can be minimized to a great extent. It was announced by BP Australia that green ammonia and green hydrogen production is feasible using solar and wind energy in large scale (9 million tonnes of green

Table 1.1: Chemical and physical properties of hydrogen, ammonia, methane, propane and diesel [24, 25, 26, 27, 28, 29, 30, 31, 32, 33, 34, 35, 36, 37, 38, 39]

Properties	**Hydrogen (H_2)**	**Ammonia (NH_3)**	**Methane (CH_4)**	**Propane (C_3H_8)**	**Diesel ($C_{20}H_{42}$*)**
Molar mass (g/mol)	2.016	17.031	16.043	44.096	282.548
Density @ STP (standard temperature (0°C) and pressure (1 bar)) (kg/m^3)	0.089	0.761	0.708	1.984	846**
Normal boiling point (°C)	−252.781	−33.318	−161.483	−42.114	∼ 163–357
Vapour pressure @ 25°C (bar)	1653.200	9.999	621.282	9.533	6.159×10^{-9}
Lower heating value (LHV) (MJ/kg)	120.100	18.800	50.140	45.700	42.6

*Diesel is a complex mixture of hydrocarbons. On average, its properties resemble those of $C_{20}H_{42}$.

**Liquid diesel fuel density @ (15°C), 1 bar

(Continued at the next page)

Table 1.1 Chemical and physical properties of hydrogen, ammonia, methane, propane and diesel [24, 25, 26, 27, 28, 29, 30, 31, 32, 33, 34, 35, 36, 37, 38, 39]. (continued)

Properties	**Hydrogen (H_2)**	**Ammonia (NH_3)**	**Methane (CH_4)**	**Propane (C_3H_8)**	**Diesel ($C_{20}H_{42}$*)**
Autoignition temperature (°C)	560	630	537	450	210
Flammable range (equivalence ratio) (-)	0.100 – 7.100	0.630 – 1.400	0.500 – 1.700	0.700 – 2.200	0.130 – 1.628
Maximum laminar flame speed @NTP (normal temperature (27°C) and pressure (1 bar)) (m/s)	2.910	0.070	0.370	0.455	0.867***
Adiabatic flame temperature (°C)	2210	1800	1963	1977	2327
Stoichiometric air-fuel ratio (-)	34.5	6.0	17.2	15.5	14.3

*Diesel is a complex mixture of hydrocarbons. On average, its properties resemble those of $C_{20}H_{42}$.

***The maximum laminar flame speed of diesel was measured @196 K, 1 bar

(End of Table)

ammonia every year under full scale renewable power) and can be export globally to facilitate the decarbonisation [50, 51]. An ammonia cycle map containing ammonia production, storage, distribution and utilisation is presented in Figure 1.7. It is also noteworthy that ammonia has the highest volumetric hydrogen density of 10.7 kg H_2/100 L as well as a high gravimetric hydrogen density of 17.8 wt%H_2 compared to all other hydrogen carriers shown in Figure 1.8 [44, 52]. Since ammonia can be decomposed to generate hydrogen by an appropriate catalyst without producing other emission gases but only nitrogen, ammonia is considered as a competitive hydrogen carrier considering the convenience of ammonia storage.

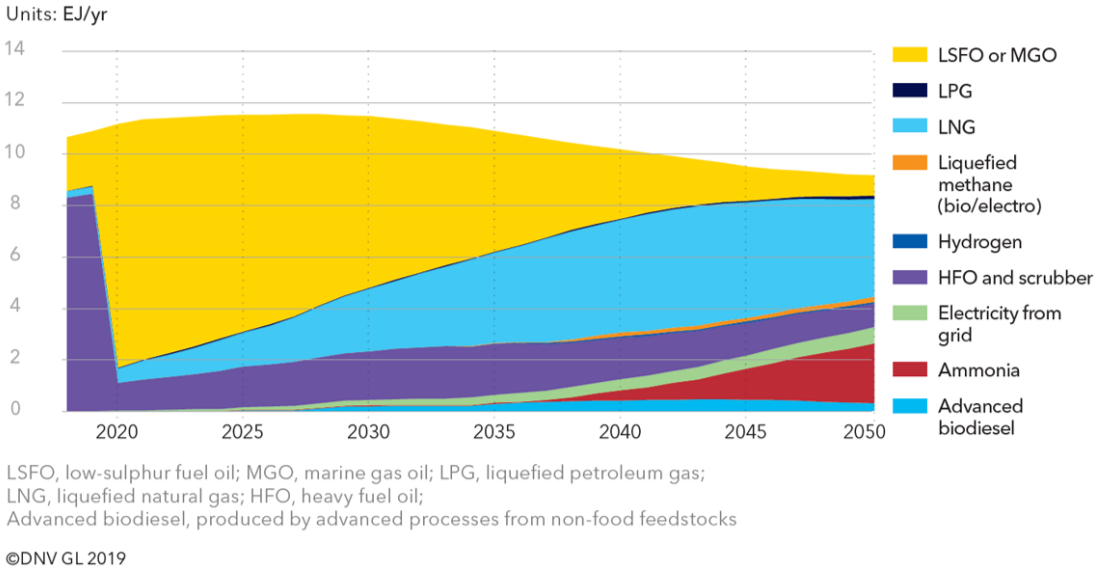


Figure 1.6: Energy use and projected fuel mix 2018-2050 for the simulated IMO ambitions pathway with main focus on design requirements [41, 42].

By combining ammonia which is a carbon-free alternative fuel with heat engines (ICEs, GTs and FPEs) to form ammonia fuelled disruptive heat engines, substantial carbon emissions in heavy transport can be reduced, further migrating the decarbonisation challenge of transports. In fact, the concept of ICE powered by ammonia was proposed and examined in the previous work [53, 54, 55]. Ow-

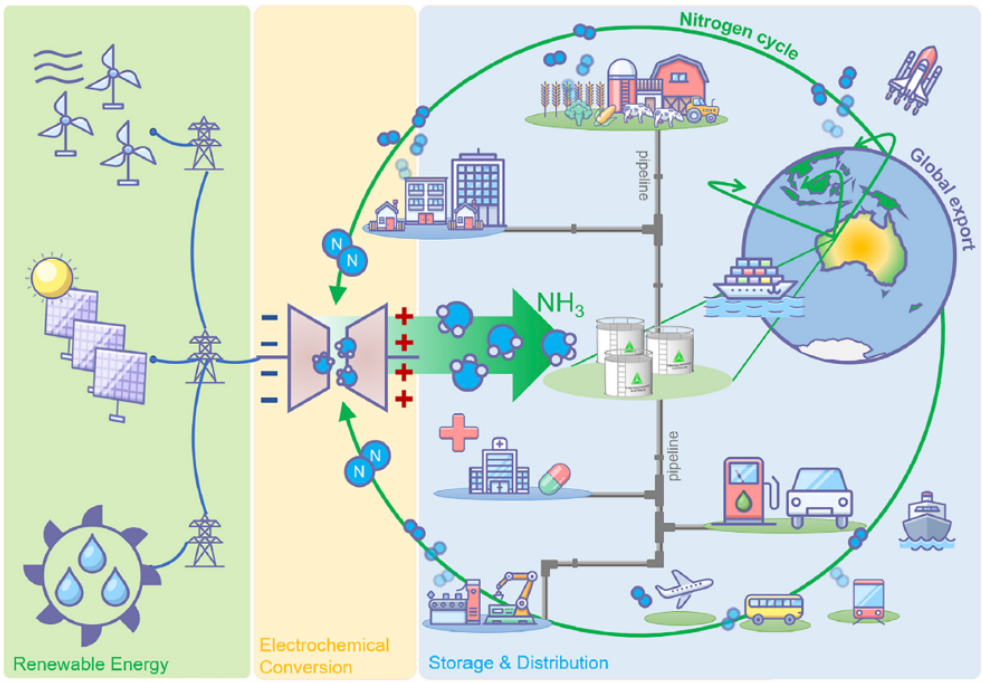


Figure 1.7: Ammonia economic cycle with production, storage, distribution and utilisation [48].

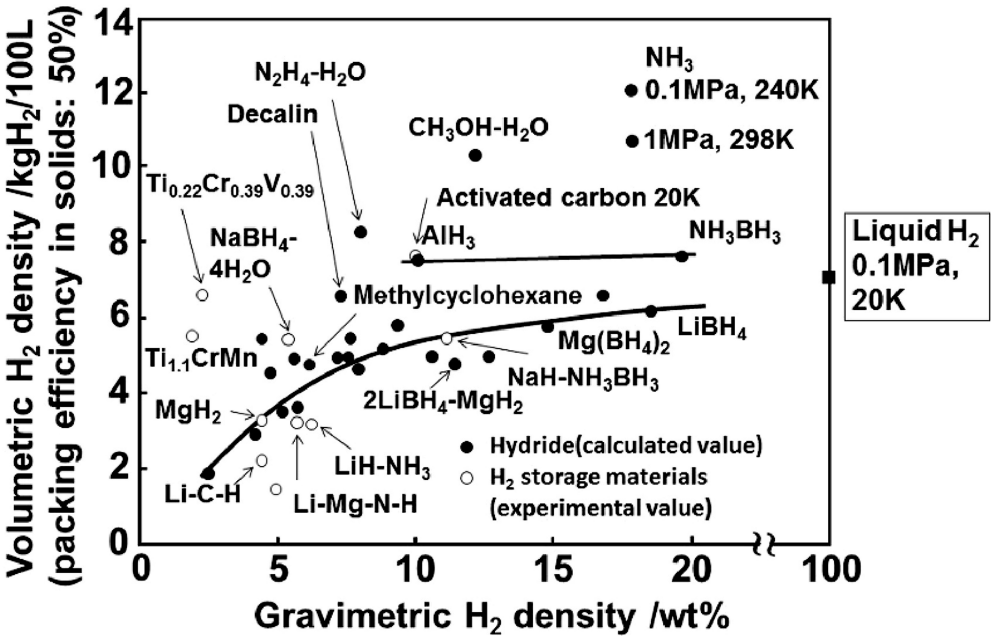


Figure 1.8: Hydrogen density in hydrogen carriers [44, 52].

ing to the ammonia properties and ammonia combustion characteristics, utilising ammonia as the sole fuel for combustion engines is faced with many obstacles. As presented in Table 1.1, ammonia requires a high temperature to ignite and the flammability range is narrow. At room temperature and atmospheric pressure, the maximum laminar flame speed of ammonia, i.e., the maximum propagation speed of a freely burning premixed laminar flat ammonia flame into the unburnt cold flow, is one-fifth that of a methane flame under the same condition. These lead to difficulty in ammonia flame stability. It was revealed by Grannell *et al.* that reasonable performance of a spark ignition engine is difficult to achieve by using a single fuel of ammonia and it was suggested to blend ammonia with a more reactive fuel such as gasoline [15]. Many studies have been conducted to introduce hydrocarbon fuel (e.g. methane, gasoline, dimethyl ether (DEM) and Kerosene) [15, 56, 57, 58, 59, 60] or hydrogen [61, 62, 63] as a promoter for ammonia combustion stabilisation. Considering increasingly stringent transportation regulations, the use of ammonia as a primary fuel with hydrogen serving as a promoter for heat engines is proposed in this research. It is because hydrogen does not emit carbon-related exhaust gases and it can be cracked from ammonia decomposition which avoids an additional on-board tank. To prevent flashback (the upstream propagation of the flame into combustor tubes) and blowoff (the extinguishing of the flame from a lifted condition), it is essential to conduct a flame stability analysis for ammonia blends.

Furthermore, although no carbon-related emissions could be yielded from ammonia and hydrogen combustion according to the chemical reactions 1.3.1 and 1.3.2, NO_x emissions are inevitable.

$$NH_3 + 0.75\ (O_2 + 3.76\ N_2) \rightarrow 1.5\ H_2O + 3.32\ N_2 \tag{1.3.1}$$

$$H_2 + 0.5\ (O_2 + 3.76\ N_2) \rightarrow H_2O \tag{1.3.2}$$

NO_x is formed mainly via three methods: thermal NO, prompt NO, and fuel-bound NO. Thermal NO is also called Zel'dovich mechanism. The elementary reactions are

$$O + N_2 \rightarrow NO + N \tag{1.3.3}$$

$$N + O_2 \rightarrow NO + O \tag{1.3.4}$$

$$N + OH \rightarrow NO + H \tag{1.3.5}$$

As a high activation energy is required to initiate the thermal NO mechanism, it is considered especially under a high temperature (above 1800 K). Prompt NO is formed via the reaction between nitrogen and CH or C in the fuel. Since carbon-free fuel blends are used in this research, NO emssions cannot be generated via prompt NO method. Fuel-bound NO is the crucial concern in ammonia combustion because of the nitrogen atom in ammonia (NH_3). Fuel containing nitrogen atoms first produces nitrogen intermediates. When ammonia is used as a fuel, the nitrogen intermediates include NH_2, NH,HNO, etc. The nitrogen intermediates oxidise to form NO. On the other hand, the nitrogen intermediates consume NO to produce N_2. Besides, ammonia/hydrogen combustion also leads to ammonia slip and hydrogen slip, which affects the combustion efficiency.

Therefore, achieving a robust ammonia/hydrogen flame and minimizing emissions including NO_x, unburnt ammonia and unburnt hydrogen are the most important goals for the development of ammonia/hydrogen fuelled disruptive heat engine. A number of physical and chemical factors are closely related, such as initial temperature, compression ratios, fuel-air mixing ratios (equivalence ratios), chemical kinetic reaction, flow field, etc. A comprehensive knowledge of the fac-

tor influence helps to develop heat engines powered by ammonia and hydrogen. For example, autoignition is important for compression ignition (CI) and homogeneous charge compression ignition (HCCI) engines and it changes under different working conditions. A lot of research is still required to analyse and understand the relationship between the factors involved in ammonia/hydrogen combustion for the aim of developing reliable, low-emission disruptive heat engines.

1.4 Aims and Objectives

The aim of this research is to investigate the characteristics of ammonia and hydrogen combustion, providing guidance for the decarbonisation of heavy transport with heat engines using carbon-free blends. In this research, ammonia is considered as a primary fuel and hydrogen is considered as an auxiliary fuel. To achieve this aim, the entire research consists of 0D and 1D kinetic modelling with Ansys Chemkin-Pro, experiments in a laboratory-scale combustor and an emission comparison across different ammonia fuelled heat engines. The study includes ammonia/hydrogen combustion fundamentals, blowoff limits, emission characteristics and OH^* chemiluminescence. The primary objectives of this research are as follows:

1. to identify suitable ammonia chemical kinetic reaction mechanisms for numerical simulations, taking into account all aspects of premixed laminar flame speed, ignition delay time and flame structure,

2. to understand the combustion fundamentals of premixed ammonia flames and ammonia/hydrogen flames comprehensively over a wide range of hydrogen blending ratios, equivalence ratios, oxygen contents in the oxidant, initial temperature and initial pressure,

3. to establish a swirl-enhanced ammonia/hydrogen combustor rig with optical chemiluminescence system and emission analysers,

4. to understand the blowoff limits, emissions, OH^* chemiluminescence of non-premixed ammonia/hydrogen combustion experimentally,

5. to compare the emissions results obtained with those published from heat engines using ammonia and identify the type of ammonia-powered heat engines with the best emission control.

1.5 Layout of Thesis

This Ph.D. thesis is comprised of seven chapters in the following manner:

- *Chapter 1 Introduction*, introduces the background, motivation, aims and objectives of this thesis.

- *Chapter 2 Literature Review*, reviews ammonia chemical kinetic reaction mechanisms, ammonia-based combustion fundamentals, ammonia combustion emissions and state-of-the-art heat engines powered by ammonia studied in the previous studies.

- *Chapter 3 Methodologies*, supplies 0D and 1D chemical kinetics modelling methodology for the analysis of premixed ammonia/hydrogen combustion, and experiment test rig setup for the investigation of non-premixed ammonia/hydrogen combustion.

- *Chapter 4 Kinetic study of premixed ammonia/hydrogen combustion characteristics*, presents the laminar flame speed, ignition delay time and flame structure over various hydrogen blending ratios, equivalence ratios, oxygen contents in the oxidant, initial temperature and initial pressure. A 1D gas

turbine model is also employed to investigate the peak heat release rate, outlet temperature and emissions.

- *Chapter 5 Experimental analysis of non-premixed ammonia flame with hydrogen in a swirl-enhanced combustor*, presents measurement results on ammonia/hydrogen flame blowoff limits, emission characteristics and OH^* chemiluminescence.

- *Chapter 6 Comparison of emission characteristics of different ammonia fuelled heat engines*, presents the current state of key emissions from different heat engines and identifies the best emission control heat engines using ammonia based on the comparison of normalised emission results.

- *Chapter 7 Conclusions and future work*, summarises the main findings of this thesis and recommendations are made for future research directions.

- *Appendix*, presents the calibration reports for NO_x analysers and MATLAB code for OH^* chemiluminescence image processing.

Chapter 2. Literature Review

2.1 Ammonia chemical kinetic reaction mechanisms

The oxidation chemistry of ammonia is indispensable to understand flame characteristics and the pathways of emissions such as nitrogen oxides. As listed in Table 2.1, several chemical kinetic reaction mechanisms of ammonia oxidation have been developed since 1983. The first detailed ammonia kinetic mechanism proposed by Miller *et al.* was based on the chemical process of thermal de-NOx, where ammonia is one of the main components of selective non-catalyst reduction for tailpipe aftertreatment [66]. The mechanism contains 22 species and 98 reactions and was validated against the measured NH_3/O_2 and $NH_3/H_2/O_2$ flame in terms of flame structure and flame speed. Miller's mechanism was found to predict ammonia oxidation well under fuel-lean conditions to moderately fuel-rich conditions and poorly under very rich flames due to the lack of some necessary pyrolysis steps [66]. An important pathway was identified in lean flames proposing that nitric oxide is mainly produced via HNO and consumed via NH and NH_2 [66].

In 1994, Lindstedt *et al.* [67] developed a detailed ammonia chemical mechanism to predict laminar premixed $NH_3/H_2/O_2, NH_3/NO/H_2/O_2$ and NH_3/O_2 flames over a variety of temperatures and stoichiometries. The predicted flame structure was compared with experimental results in literature. It showed a general satisfactory agreement between predictions and measurements although there was some differences found in nitric oxide profile when the equivalence ratio was equal to and above the unity [67]. Nitric oxide strongly depends on the reaction between NH and OH in all three types of flames [67]. Additionally, thermal NO

plays an important role in nitric oxide formation and destruction in ammonia/hydrogen flames [67].

An elaborate chemical mechanism developed by Konnov can be used to analyse ammonia blends with hydrogen and small hydrocarbons (methane, ethylene, ethane and propane) [68]. The detailed mechanism is comprised of more than 120 species and 1200 reactions [68]. There have been modifications made to the low-temperature methane oxidation pathway, the NNH route for NO formation, and the hydrogen sub-mechanism with the introduction of two new species $HNCN$ and NCN [68]. The prediction performance in NO formation and conversion has been significantly improved and Konnov's mechanism has been widely used in predicting ammonia flames [69, 70, 71, 72].

An assessment of prediction accuracy under 0.05–0.12 bar was made by Duynslaegher *et al.* [73, 74] using premixed $0.21NH_3/0.13H_2/0.21O_2/0.45Ar$ (concentration) flames. They validated mechanisms including GRI [75], San Diego [76], Lindstedt *et al.* [67], Bian [77] and Konnov [68, 78] against the measured flame structure and laminar flame speed. It was found that Konnov's mechanism showed the best agreement with the experimental results among the five mechanisms, despite disparities in the mole fracture of N_2O and NH_2 [74]. Therefore, Duynslaegher *et al.* updated the Konnov's mechanism with improvement in accuracy of N_2O and NH_2 and a reduced version with 19 species and 80 reactions was also presented [73].

Tian *et al.* analysed eleven premixed $NH_3/CH_4/O_2/Ar$ flame under 0.04 bar at stoichiometric condition with tunable synchrotron vacuum ultraviolet (VUV) photoionization and molecular beam mass spectrometry (MBMS) [79]. The measured species and intermediates were used as reference to validate for the proposed mechanism. The comparison of flame structure in experimental data and com-

putational results were in good performance for most species and intermediates [79]. Furthermore, it was noticed NO and N_2 conversions substantially rely on reactions $H + O_2 \rightarrow O + OH, NH_2 + O \rightarrow HNO + H, NH_2 + NO \rightarrow N_2 + H_2O$ and $NH + NO \rightarrow N_2O + H$ [79].

Mendiara *et al.* studied ammonia chemistry in methane oxidation over a variety of temperature ($973 - 1773$ K) and equivalence ratios ($0.13 - 1.55$) in a lab-scaled flow reactor [80]. The findings extended the Tian's mechanism by correcting the interaction of nitrogen containing radicals and CO_2 as well as hydrocarbons and amine species [80]. In general, the improved mechanism shows a similar pattern with all the measured flame structures, especially when the measured temperature profile is taken into account. The results also identified the importance of HNO, mainly generated from NH_2 and O, for NO formation [80].

The ignition delay time of $NH_3/NO_x/H_2$ flame was measured under high temperature in a shock tube by Mathieu *et al.* [81]. The ignition delay measurements were compared with computational results using various mechanisms, indicating the need to improve the ammonia mechanism with the new set of available ignition delay measurements. The sub-mechanisms of $H_2/CO, NH_3, HCN, N_2O$, NO_2, NNH are therefore adopted to the developed mechanism [81]. The calculated ignition delay time and some species (i.e. NH_3, NO_2, N_2O) generated from the developed mechanism aligned well with the measurements.

Ammonia oxidation under high pressure (30 and 100 bar) and intermediate temperature ($450 - 925$ K) were analysed experimentally by Song *et al.* [82]. N_2 and N_2O were detected in the products. Due to the limited detection range, the experimental results lacked NO and NO_2 concentration data [82]. The findings were interpreted as a detailed chemical kinetic mechanism involving 33 species and 204 reactions. The computational results showed a satisfactory performance

against the measurements. $NH_3 \xrightarrow{+\mathrm{OH}} NH_2 \xrightarrow{+HO_2,NO_2} H_2NO \xrightarrow{+O_2} HNO \xrightarrow{+O_2} NO \xrightarrow{+NH_2} N_2$ was found to be the main pathway of ammonia oxidation at high pressure [82].

A detailed ammonia chemical kinetic mechanism in a microflow reactor was developed using Miller's mechanism [83] by Nakamura *et al.* [84]. The modification consists of the $H_2/NH_x/N_2O/NNH$ chemistry, which was derived from the findings of Mathieu and Petersen [81], the chemistry of N_2H_x, with the exception of NNH, which was based on Konnov's work [68] and the updated thermochemical properties, which were determined by Bugler *et al.* [85]. Using the presented mechanism, the calculated flame structure agreed well with the experimental data while the predictions of the flame speed and ignition delay time were validated against the literature in reasonable agreement [84].

Otomo *et al.* [86] modified the elementary reactions containing NH_2, HNO and N_2H_2 based on Song's mechanism [82]. The effect of equivalence ratios and pressure on laminar flame speed, ignition delay time and ammonia slip and NO_x emission was investigated using the improved mechanism. According to Otomo's mechanism, hydrogen yielded in the products was partially generated from ammonia decomposition in rich ammonia/hydrogen flames [86].

Okafor *et al.* [56] developed a detailed chemical mechanism for ammonia/methane blends based on Tian's work [79] and GRI Mech 3.0 [75] which is famous for natural gas chemical mechanism involving NO_x conversion and reburn reactions. The laminar flame speed of premixed ammonia/methane was examined under different equivalence ratios and ammonia concentrations experimentally at room temperature and atmospheric pressure. The results were used to verify the developed mechanism, demonstrating a better predication than Tian's mechanism [79], Mendiara's mechanism [80] and San Diego mechanism [76]. In

addition, Okafor *et al.* [87] carried out the experiment on the laminar flame speed of ammonia/methane under high pressure up to 5 bar. After optimizing their previous work [56] for high-pressure conditions, their findings were interpreted as a reduced mechanism. The reduced mechanism has been extensively employed in Computational Fluid Dynamics (CFD) simulations [88, 89, 90, 91, 92].

Li *et al.* [93] developed two reduced chemical mechanism for ammonia and hydrogen for CFD studies. In the first part, a detailed mechanism consisting of 128 species and 957 reactions was obtained for $NH_3/H_2/CH_4$. Then it was reduced by using directed relation graph with error propagation (DRGEP) and DRGEP with sensitivity analysis method [93]. There were two versions of mechanisms for ammonia and hydrogen mixtures (34 species and 252 reactions, and 28 species and 213 reactions) when the carbon-related species and reactions were removed from the detailed and reduced mechanisms presented above [93]. The mechanisms can be adopted over a wide range of temperature ($1000-2000$ K), pressure ($1-50$ bar) and equivalence ratio ($0.5-2.0$) [93]. It must be noted, however, the ignition delay time was underestimated by both mechanisms under high-pressure conditions.

In brief, available mechanisms are capable of accurately predicting the combustion fundamentals of ammonia and ammonia blends over some certain range. There is no ammonia chemical mechanism that covers all operating conditions so far. In recent years, increasing studies have been devoted to optimizing ammonia mechanisms and ammonia blends mechanisms in order to understand the pathway of ammonia oxidation and NO_x formation pathway (in particular, fuel-bound NO_x pathway). More experimental data are crucial and beneficial for mechanism validation and improvement. For kinetic modelling simulations, an appropriate ammonia chemical mechanism needs to be selected based on similar operating conditions.

Table 2.1: List of ammonia chemical kinetic reaction mechanisms.

Author	**Year**	**Number of species**	**Number of reactions**	**Mixture**	**Parameters validated in their work**	**Ref**
Miller *et al.*	1983	22	98	NH_3/O_2 and $NH_3/H_2/O_2$	Flame structure, flame speed	[66]
Lindstedt *et al.*	1994	21	95	$NH_3/H_2/O_2$, $NH_3/NO/H_2/O_2$ and NH_3/O_2	Flame structure	[67]
Konnov	2009	127	1207	$CH_4/N_2/O_2$, $C_2H_4/N_2/O_2$, $C_2H_6/N_2/O_2$ and $C_3H_8/N_2/O_2$	Flame structure	[68]
Tian *et al.*	2009	84	703	$NH_3/CH_4/O_2/Ar$	Flame structure	[79]
Mendiara *et al.*	2009	97	779	$NH_3/CH_4/O_2$	Flame structure	[80]
Duynslaegher *et al.*	2012	19	80	$NH_3/H_2/O_2/Ar$	Flame structure, laminar flame speed	[73, 94]
Mathieu *et al.*	2015	55	278	$NH_3/NO_x/H_2$	Flame structure, ignition delay time	[81]
Song *et al.*	2016	33	204	$NH_3/O_2/N_2$	Flame structure	[82]

Table 2.1 List of ammonia chemical kinetic reaction mechanisms (Continued).

Author	**Year**	**Number of species**	**Number of reactions**	**Mixture**	**Parameters validated in their work**	**Ref**
Nakamura *et al.*	2017	33	232	NH_3/air	Flame structure, ignition delay time, laminar flame speed	[84]
Otomo *et al.*	2018	32	213	$NH_3/air, NH_3/H_2/air$	Ignition delay, species profiles, laminar flame speed	[86]
Okafor *et al.*	2018	59	356	$NH_3/CH_4/air$	Flame structure, laminar flame speed	[56]
Okafor *et al.*	2019	42	130	$NH_3/CH_4/air$	Flame structure, laminar flame speed	[87]
Li *et al.*	2019	128	957	$NH_3/H_2/CH_4/O_2/Ar$	Ignition delay, laminar flame speed	[93]

2.2 Fundamentals of ammonia combustion

In general, flames are categorised into three types: premixed flame, non-premixed flame (also called as diffusion flame) and partially premixed flame. In premixed combustion, mixing process of fuel and oxidizer and burning process are separated. Namely, fuel and oxidizer are mixed before entering the combustor. The premixed flame propagates from the flame front to the unburnt cold stream, which is characterized as flame speed. Some examples of premixed laminar flame are Bunsen flame and flat flame while premixed turbulent flame occurs in Spark Ignition (SI) gasoline engine and stationary gas turbine [64]. In non-premixed combustion, fuel and oxidizer start to mix and burn simultaneously in the combustor and actually mixing often takes longer than reaction times. Candle and woodfire are typical non-premixed laminar flame, while non-premixed turbulent flame can be found in diesel engines and pulverized coal combustion [64]. It is worth noting that non-premixed combustion exhibits higher operational stability than premixed combustion, but potentially lead to a higher NO_x emission [95]. Another type, partially premixed combustion, stands between premixed and non-premixed combustion. Fuel and oxidizer are premixed un-uniformly before they react. For instance, an additional oxidizer or fuel stream is introduced into a premixed combustion system, gas-fired domestic burners, industrial furnaces [96]. Partially premixed combustion has advantages over both premixed type and non-premixed combustion, i.e. less pollution and the combustion zone is easy to control. Studying the fundamentals of premixed ammonia combustion and non-premixed ammonia combustion is a great way to understand partially premixed ammonia combustion because direct combustion using ammonia as fuel is a relatively new research topic. Thus, this work mainly discusses fully premixed ammonia and non-premixed ammonia combustion.

One of the well-known impediments for ammonia combustion is to obtain a stable ammonia flame, which is normally characterised as blowoff limit and laminar flame speed. Hayakawa *et al.* carried out an experiment on the effect of combustor geometry and swirl number on the stabilization of premixed ammonia/air flame [97]. Despite its slow laminar flame speed, an ammonia/air flame was obtained as shown in Figure 2.1 [97]. The results illustrate ammonia/air flames were stabilized in a narrower range when employing a larger swirl number and the combustor length has minor effect on the flame stability [97]. The laminar flame speed of premixed ammonia/air was examined up to 5 bar by the same research group. Pressure has a negative effect on ammonia/air unstretched flame speed, which is the same trend as hydrocarbon flames [69]. The unstretched laminar flame speed was at about 7 cm/s which is much lower than the hydrocarbon flames, as shown in Table 1.1 [69].

Because of the low flame speed of neat ammonia, numerous researchers have also proposed the introduction of a high reactivity substance as a promoter into the fuel to achieve a steady ammonia flame, for example methane [56, 58, 87, 98, 99, 100, 101] and hydrogen [63, 72, 102, 103, 104, 105]. Premixed ammonia/methane flames were tested with the swirl number of 1.05 in Gas Turbine Research Centre (GTRC) in Cardiff University [100, 101]. It demonstrated $61\%NH_3/39\%CH_4$ (molar fraction) was the only tested successful blends. Neat ammonia and ammonia flames with methane blending ratio below 30% were either not able to be ignited or the flame was unstable. Zhang *et al.* [98] studied the blowoff behaviour of premixed ammonia/methane flames in a swirl combustor experimentally and computationally. The introduction of 50% (molar fraction) methane significantly widened the ammonia flame blowoff limits and it can be extended further with a higher swirl number [98]. Khateeb *et al.* [104] discovered

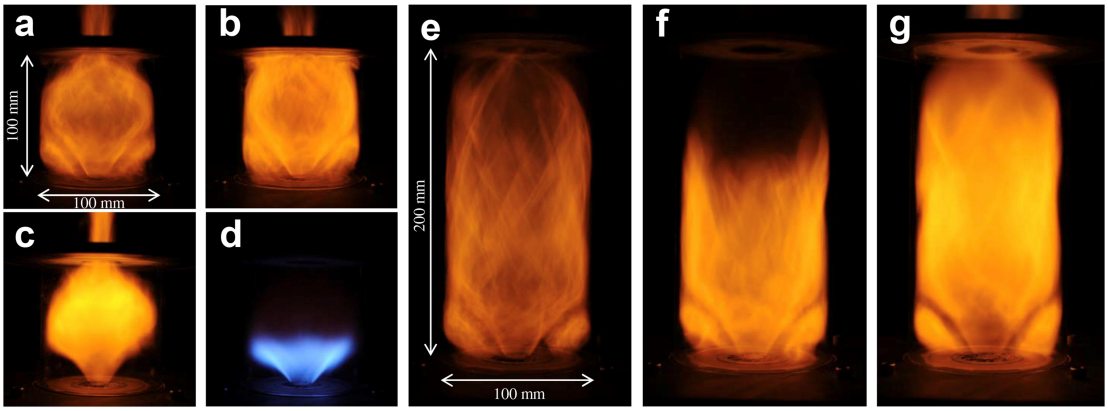


Figure 2.1: Stable premixed ammonia/air flame at (a) $\phi = 1.0$ with combustor height at 100 mm, mixture inlet velocity at 3.14 m/s; (b) $\phi = 1.2$ with combustor height at 100 mm, mixture inlet velocity at 3.14 m/s; (c) $\phi = 1.2$ with combustor height at 100 mm, mixture inlet velocity at 3.35 m/s; (e) $\phi = 0.8$ with combustor height at 200 mm, mixture inlet velocity at 3.14 m/s; (f) $\phi = 1.0$ with combustor height at 200 mm, mixture inlet velocity at 3.14 m/s; (g) $\phi = 1.2$ with combustor height at 200 mm, mixture inlet velocity at 3.14 m/s; and (d) stable premixed methane/air flame at $\phi = 1.0$ with combustor height at 100 mm, mixture inlet velocity at 3.14 m/s [97].

the equivalence ratios at lean blowoff limit and flashback of premixed ammonia/methane flame were increased when more ammonia was added in the fuel. Premixed ammonia/methane flames were examined in a constant volume chamber under high pressures $(1, 3, 5$ bar) and room temperature for the first time by Okafor *et al.* [87]. Adding methane into the fuel contributes to the ammonia flame stability under all pressure conditions. The unstretched laminar flame speed decreased with increasing pressure. Ichikawa *et al.* [58] also explored premixed ammonia/methane flames under a high pressure (5 bar) with OH planar laser-induced fluorescence (OH-PLIF). Under the constant ratio of the turbulence intensity and unstretched laminar flame speed, the ratios of the turbulent burning velocity and the unstretched laminar flame speed increased when ammonia concentration increased from 0.0 to 0.2 [58]. Flame stretch was investigated using

Markstein length and Lewis number, but neither parameter was found to correlate with the phenomena. The authors recommended considering the influence of the change in the flame surface density. The effects of equivalence ratios and ammonia concentrations on the laminar flame speed of premixed ammonia/methane flames were studied employing Schlieren technology at the ambient temperature and pressure [56]. The unstretched laminar flame speed rose non-linearly when ammonia concentration in the fuel was increased from 0% to 30% (on the basis of LHV values). There was an increasing trend in the laminar flame speed first, then a decreasing trend with the equivalence ratio increasing from 0.8 to 1.3.

Ammonia/hydrogen flames have been studied in attempts to use hydrogen as a fuel for heat engines. Utilising hydrogen as a fuel brings the safety concerns (potential explosion hazards) and knock-limited operation in ICEs. Therefore, it was proposed by Lee *et al.* [102] that hydrogen can be either blend with ammonia or hydrocarbon for a fuel mixture. When ammonia was added to the fuel, a significant decrease in laminar flame speed was observed in experiments, which is the same behaviour as blending methane and hydrogen. The results also showed, at fuel-rich condition, NO_x emission was increased when ammonia was involved but decreased when ammonia concentration further increased. When small amount of ammonia was introduced in the fuel blends, fuel-bound NO_x facilitated the NO_x formation and thermal NO_x method still dominated in the NO_x formation. This explains the increase in NO_x with a small amount of ammonia in the fuel blends. As more ammonia was involved in the fuel blends, the flame temperature decreased which inhibited thermal NO_x formation and consumption. At fuel-rich conditions, fuel-bound NO_x formation was also inhibited. Therefore, NO_x decreased with a further increase in ammonia concentration in the fuel blends. It was concluded that adopting ammonia/hydrogen as fuel could

be a safe means of utilizing hydrogen [102]. The effects of pressure (up to 5 bar) and hydrogen blending ratios $(0-1)$ on the laminar flame speed of ammonia/hydrogen were investigated through a constant volume vessel [72]. The schlieren images indicated the unstretched laminar flame speed increased non-linearly with more hydrogen addition while it decreased under a higher pressure [72]. Lhuillier *et al.* [103] analysed premixed ammonia/hydrogen flame in a 0.042 m^2 spherical vessel under atmospheric pressure. By increasing the initial temperature from room temperature to 473 K, the laminar flame speed increased and flame propagation became steadier in most cases [103]. The laminar flame speed of premixed $NH_3, NH_3/H_2, NH_3/CO, NH_3/CH_4$ flames were experimentally investigated with the heat flux method [105]. The results showed hydrogen addition has the greatest effect on enhancing ammonia flames. A generic swirl burner was used to test the stability limits of premixed ammonia/hydrogen flames up to 5 bar in KAUST (King Abdullah University of Science and Technology) [104]. It indicated that the stability range was widened by increasing the pressure, however, the influence is inapparent. Additionally, the finding illustrated $40\%NH_3/60\%H_2$ flame was surprisingly stabilized even at very lean conditions ($\phi \sim 0.3$).

From the oxidizer point of view, oxygen-enriched ammonia combustion [106, 107, 108, 109] or the use of stronger oxidants [110] instead of air have been proposed to enhance the flame stability of ammonia. Oxygen occupies $\sim 21\%$ in the air. If the oxygen concentration in the oxidants changes above 21% or even pure oxygen, it is called oxygen-enriched combustion or oxy-fuel combustion. The oxy-fuel technology has been commonly utilised in industrial furnaces, i.e. aluminium-remelting furnace, glass-melting furnaces and ladle furnaces, for the purpose of productivity improvement, energy consumption reduction and NO_x emission minimization [111, 112]. Theoretically NO_x emission yielded from oxy-fuel combustion

is much less than the combustion using air for the oxidant because there is less nitrogen in the oxidant. Oxygen-enriched conditions were considered in hydrocarbon combustion in previous studies [80, 111, 113, 114, 115]. There have been a handful of studies on oxygen-enriched ammonia combustion, but few studies on ammonia/hydrogen combustion under oxygen-enriched conditions so far. Liu *et al.* [109] studied the propagation process of premixed ammonia/oxygen flame by observing Schlieren images. The ammonia/oxygen flame reached a maximum of 109 cm/s at 0.5 bar [109]. The effect of oxygen content in the oxidant varying from 21% to 30% on ammonia combustion was studied numerically in Chemkin software with a freely propagating adiabatic, premixed, laminar flame speed calculation model [106]. The oxygen-enriched conditions significantly improved ammonia laminar flame speed and increased the adiabatic flame temperature. Laminar flame speed of ammonia is approximately 2.6 times greater with 30% oxygen in the oxidant than 21% oxygen in the oxidant. An experimental and numerical investigation of premixed laminar flame speeds of ammonia was conducted by Mei *et al.* with $25\% - 45\%$ oxygen in the oxidant [108]. The experimental findings align with the numerical results published in Li's work [106]. Moreover, the buoyancy effect was reduced under oxygen-enriched ammonia combustion. Xiao *et al.* [116] examined the effect of oxygen enrichment on premixed $61\%NH_3/39\%CH_4$ flames numerically. When the oxygen contents in the oxidant changed from 21% to 40%, there was a linear relationship between laminar flame speed and oxygen concentrations at the equivalence ratio of unity. Furthermore, when the oxygen content in the oxidant is 40%, the laminar flame speed is more than three times that of ammonia/methane/air combustion. In addition to oxygen enrichment approach, Wu *et al.* [110] attempted to employ hydrogen peroxide (H_2O_2) instead of pure air as the oxidant for extending ammonia flammability. Hydrogen peroxide

is a strong oxidizing agent which decomposes to only water and oxygen. The researchers found the ammonia flame propagation was boosted and the adiabatic temperature rose considerably as the hydrogen peroxide gradually replaced the air to 100% hydrogen peroxide.

Ignition is a time-varying process. During ignition, the reaction between radicals starts slowly and grows exponentially, but the temperature remains nearly the same until there are enough radicals to consume the fuel [64]. Knowing when the flame mixture ignites under specific operating conditions, i.e. the ignition delay time, is critical for engine design. A few studies on ignition delay in ammonia flames have been conducted. Mathieu *et al.* [81] carried out the measurement of the ignition delay times of $NH_3/O_2/Ar$ flames in a shock tube over an extensive range of temperature ($1560 - 2455$ K), pressure ($1.4, 11, 30$ atm) and equivalence ratio ($0.5, 1.0, 2.0$). Nine different ammonia chemical mechanisms were selected to compare the numerical results with the measured ignition delay times, but most of these provided an underestimated prediction of ignition delay times. The effects of temperature and pressure were extended to $1100 - 1600$ K and 20 and 40 bar in Shu's work [117]. The autoignition behaviour of ammonia was analysed experimentally at the equivalence ratio of $0.5, 1.0, 2.0$. Only pressure had the same impact as Mathieu's work [81]. It was implied that the difference is because the presented work was undiluted, whereas Mathieu's work was in highly diluted argon ($98 - 99\%$). As beforementioned ammonia is usually blended with hydrocarbon fuel, the ignition delay time of ammonia/dimethyl ether (DME) was studied under high pressure ($10 - 70$ bar) with a rapid compression machine (RCM) [118]. The experimental outcomes illustrate the concentration of DME had a great effect on enhancing the ignition under all three pressure conditions, but the relationship was not linear. The autoignition behaviour of ammonia/methane was calculated

in a closed homogeneous reactor model in Cantera software [57]. The ignition delay time was determined to be the time associated with the steepest rate of OH generation in their simulation [57]. It was reported that the ignition delay time prolonged monotonically when the ammonia concentration ($0\% - 100\%$) or when the equivalence ratio ($0.6, 1.0, 1.4$) rose. Shock-tube measurements were conducted for $60\%NH_3/40\%CH_4$ flames under various equivalence ratios ($0.5, 1.0, 2.0$), pressure ($2, 5$ bar) within $1369 - 1804$ K [119]. It was noted that the ignition delay time was shortened with the increase in inlet temperature and pressure. Regarding to ammonia/hydrogen blends, Li *et al.* [120] analysed the ignition delay time in a homogeneous charge compression-ignition model using Chemkin software. In their work, the time from null to maximum concentration of NH_2 and OH radicals was considered as the ignition delay time [120]. Simulation results show that the ignition of ammonia was significantly enhanced with the addition of hydrogen and increased pressure. The ignition process of ammonia/hydrogen blends at high pressure ($20 - 75$ bar) was reported based on experiments using RCM [121]. The hydrogen blending ratio varied from 0% to 10%, finding a significant effect on shortening ignition delay time.

Reducing NO_x emissions has always been one of the main goals of heat engines development, especially when using ammonia mixtures as fuel. Investigation on flame structure facilitates understanding of NO_x formation and consumption pathways. Otomo *et al.* [86] examined the species profiles of NH_3, NH_2, NO, N_2O, OH and H_2 under the equivalence ratios of $0.7, 1.1, 1.3, 1.5$. When the equivalence ratio was greater than 1.3, the concentration of NH_2 was high at the post flame zone. It was later concluded by the researchers that NH_2 radical is an important role in NO reduction. At the National Synchrotron Radiation Laboratory (NSRL) in China, the combustion intermediates and products of

premixed $NH_3/CH_4/O_2/Ar$ flames were identified by VUV photoionization and MBMS [79]. It revealed the species profiles of reactants (NH_3, CH_4, O_2, Ar) intermediates (HCN) and products ($H_2, CO, H_2O, CO_2, NO, N_2, NO_2$). At the constant flow rate velocity (41 cm/s), the effect of the mole ratio of ammonia and methane (R) on mole fraction profiles was studied. When the mole ratio of ammonia and methane rose, the concentration of NO and N_2 increased but NO_2 reduced because the CH_3 radical is known as an effective intermediate to convert NO_2 to NO [79, 122]. Flame structure of premixed ammonia/methane combustion was analysed using Tian's mechanism [79] over various ammonia concentration in the fuel $(0.2, 0.4, 0.6, 0.8)$ at stoichiometric conditions [57]. The profiles of $OH, H, O, NH_2, CO, NO, HCO, HNO$ were reported. Notably, the distance of CO and NO peaks and OH, H, O radical peaks were the same, indicating that the formation of CO, NO emissions primarily occur at the flame front [57]. HNO and HCO were also suggested as the primary intermediates in NO and CO generation. Duynslaegher *et al.* [74] experimentally explored the flame structure of premixed $NH_3/H_2/O_2/Ar$ flames using MBMS equipment. By adding $5-15\%$ hydrogen to the fuel, the flame front moved forward to the burner by 2.5 mm at the same inlet flow velocity and equivalence ratio (1.02) [74]. Equivalence ratio had a significant impact on NO production, particularly sensitive between 0.9 and 1.0. The mole fraction profile of NH_2 and N_2 remained constant when the equivalence ratio varied. The maximum concentration of N_2O under fuel-lean conditions was higher but similar when the equivalence ratio was greater and equal to unit. Premixed $70\%NH_3/30\%H_2$ flame structure at the equivalence ratio of 1.3 was numerically investigated using Otomo's mechanism [86]. It denoted ammonia decomposition was induced in the reaction zone because hydrogen concentration was decreased first then increased within 1 cm distance [86]. An analysis of a two-zone combus-

tor consisting of a rich-burn zone and a lean-burn zone fuelled by ammonia and hydrogen was carried out by Li *et al.* based on Tian's mechanism [123]. The major NO_x generation and consumption reactions were analysed deeply with ROP (rate of production) analysis. The flame zone and post flame zone were studied separately. It concluded that in order to control NO_x emission, the equivalence ratio of the rich-burn zone is more important and sensitive than the global equivalence ratio of the whole system. By doing so, the amount of secondary air may be expanded without causing penalties on NO_x emission.

Ammonia has only recently been reconsidered as a potential fuel. Neat ammonia or ammonia/hydrocarbon (especially methane) combustion fundamental has been explored under different operating conditions in some studies, but there is still a need to gain a deep insight into combustion fundamentals of ammonia/hydrogen blends comprehensively, particularly under conditions associated with disruptive heat engines. In this thesis, disruptive heat engine is considered as a heat engine (ICEs, GTs and FPEs) fuelled by ammonia/hydrogen blends. Few studies have been conducted on laminar flame speed of premixed ammonia/hydrogen under practical operating conditions of heat engines. The ignition delay time and flame structure of ammonia/hydrogen blends, in particular under oxygen-enriched conditions, have been seldom discussed.

The heat value of ammonia is lower than that of hydrogen. As hydrogen is substituted by ammonia in fuel blends, ammonia and hydrogen combustion produces less thermal NO_x than that from pure hydrogen combustion. Meanwhile, attention should be paid to fuel-bound NO_x in ammonia/hydrogen combustion. It is critical to understand how species and radicals interact and flame structure under various conditions and ammonia/hydrogen blends in order to minimize emissions.

2.3 Ammonia-based combustion emissions

Emissions are a common concern with ammonia direct combustion, namely, NO_x emission. If the combustion is incomplete, unburnt ammonia known as ammonia slip also remains in the exhaust and become part of the emissions. NO_x is an abbreviation for nitric oxide (NO), nitrogen dioxide (NO_2) and nitrous oxide (N_2O). Nitric oxide and nitrogen dioxide are major components of NO_x, and both are responsible for smog and acid rain formation and affect tropospheric ozone, which leads to changes in soil chemistry and biodiversity in certain habitats [124]. Despite being a minor part of NO_x, nitrous oxide is the one of most important long-lived greenhouse gases, which can contribute significantly to climate change [125]. Ammonia is a toxic chemical with a short lifespan at the atmosphere, but if it reacts with nitrogen oxide or sulphur dioxide, it is likely to generate particulate matter (PM) that contribute to air pollution [126, 127]. Since hydrogen residues are produced when ammonia/hydrogen is incompletely combusted, unburnt hydrogen is also emphasized in some studies to analyse the combustion efficiency.

Hayakawa *et al.* [128] explored NO_x emission characteristics of premixed ammonia/air flame in a nozzle-type burner under different equivalence ratios ($0.7 - 1.1$) and pressures (up to 3 bar). As a water bubbling equipment was employed for the sampling gas, ammonia and water were removed prior to the emission measurements. A NO emission trend was observed when the amount of ammonia and water were excluded in the emission results. NO emission peaked at the equivalence ratio of 0.8 at the atmospheric pressure and decreased as the pressure increased. Later, a two-zone ammonia fuelled micro gas turbine was designed by experimentally studying the impacts of fuel injection angles, inlet temperature, equivalence ratios and ambient pressures on flame stability and emissions in Tohoku University [129]. The experiment test rig is depicted in Figure 2.2. Both

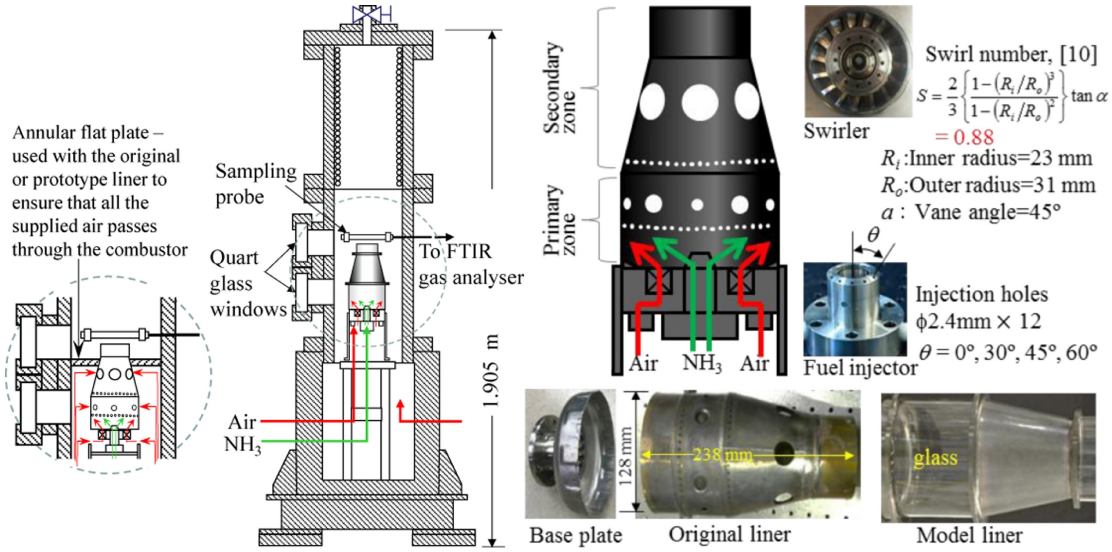


Figure 2.2: Ammonia fuelled micro gas turbine combustor in Tohoku University [129].

non-premixed and premixed ammonia/air combustion were analysed at the two-zone combustor, finding that the premixed combustion emitted less NO_x than the non-premixed combustion. With the primary equivalence ratio (for the first zone) at 1.1 and overall equivalence ratio at around 0.4, the NO_x emission in premixed type was minimized to 42 ppmv and the combustion efficiency was 99.5% at 3 bar [129]. Meanwhile, ammonia slip was found very low (close to zero).

Okafor *et al.* [89] examined ammonia/methane flames with the same combustor. The emissions, flow field and flame structure were analysed by employing Fourier Transform Infrared (FTIR) gas analyser, Particle Image Velocimetry (PIV) and Planar Laser Induced Fluorescence (PLIF) imaging [89]. For the single-zone combustor, NO_x emission was found to be twice than that of premixed ammonia/air combustion reported in the work [129] under the similar working conditions [89]. Comparing with premixed combustion, for single-zone combustor, NO at the exhaust of non-premixed ammonia/methane flame was less. Since

the unburnt fuel was found to be substantially higher in non-premixed combustion, it was concluded the reason for lower NO in non-premixed combustion was insufficient mixing. Furthermore, it was noted that when the equivalence ratio was greater than 1.2, NO emission is lower in single-zone combustor than that in two-zone rich-lean combustor. At the identical equivalence ratio, unburnt hydrogen showed similar emission level under various methane blending ratios. In two-zone rich-lean combustor, NO emission measured from ammonia/methane flame is lower than that from ammonia/air flame at the same primary equivalence ratio [89, 129]. The high pressure optical chamber setup with a generic premixed swirl burner was used to study premixed ammonia/methane combustion at GTRC in Cardiff University [101]. Figure 2.3 illustrates the premixed swirl burner. To measure the emissions under 2 bar, bypass air was introduced to a separate chamber to provide sufficient flow. The flame was ignited with pure methane first then ammonia flow rate was increased to the specific value for investigation. Emissions of $NO, NO_2, CO, CO_2, NH_3, O_2$ and THCs (Total Hydrocarbons) were measured, and a large amount of unburnt fuel was found at the exhaust. It was concluded that a fully premixed injection strategy is not the optimal injection strategy for ammonia/methane blends due to the low combustion efficiency [101]. Woo *et al.* [130] examined NO_x emission characteristics of non-premixed ammonia/methane flame under oxygen-enriched environment. The experiment was carried out in a coflow jet burner. The results of $10\%NH_3/90\%CH_4$ blends were compared with that of pure methane flame. It revealed that NO_x emission yielded from $10\%NH_3/90\%CH_4$ blends was higher than that produced from pure methane flames when the oxygen concentration in the oxidant was less than 0.4. NO_x emission rose when the oxygen content in the oxidant was increased to approximately 0.7. Then, as the oxygen content in the oxidant continued to increase,

NO_x emission began to decrease. NO_x emission was less in $10\%NH_3/90\%CH_4$ blends than that in pure methane flames when the oxygen concentration in the oxidant was between 0.4 and 0.9. In general, ammonia is stored in liquid state. If liquid ammonia can be directly used for fuel without converting gaseous state, energy and costs for vaporizers and accumulators could be saved. The emissions (NO, NO_2, N_2O, NH_3, CO, HCN, H_2) of liquid ammonia co-firing with methane was explored in a non-premixed swirl combustor at the inlet temperature of 500 K [99]. When liquid ammonia was injected to the chamber, flash boiling occurred. However, according to the observation at the bottom of the flame, there were still some liquid ammonia droplets, indicating ammonia vaporization was incomplete. The phenomenon resulted in the temperature drop of the flame and affected further the flame stability and emissions. The results showed emission behaviour of liquid ammonia and methane flames is similar to that of gaseous ammonia/methane flames. The heat loss due to the vaporization was increased with an increasing equivalence ratio. Consequently, the peak flame temperature was shifted to fuel-lean conditions. Hence, NO emission was high and unburnt ammonia and methane were low at fuel-lean conditions while high CO, H_2, HCN, NH_3 were observed under fuel-rich conditions. Considering both ammonia slip and NO emission, the optimal equivalence ratio was found to be 1.06 [99]. KAUST carried out an experiment in a premixed swirl combustor to analyse the effect of pressure (up to 5 bar) on NO emission when ammonia was blended with either methane or hydrogen [104]. As shown in Figure 2.4, the combustor was fitted in a high-pressure combustion duct supporting a maximum of 40 bar at 250°C [104]. Premixed ammonia/methane flames were attempted to measure under a very lean conditions ($\phi < 0.6$), but it was difficult to stabilize and obtain the emission results. At the equivalence ratio of 0.6, NO emission was still high. When

ammonia was blended with hydrogen, the robust flame was observed even at the equivalence ratio of 0.50 and 0.55. NO emission at all measurement under $2-4$ bar appeared less than 200 ppmv@6%O_2 [104]. Nevertheless, N_2O emission was found to be extremely high ($1000-1800$ ppmv@6%O_2) under the very lean conditions in the numerical results. Zhu *et al.* [131] analysed the premixed ammonia/methane flames using chemiluminescence imaging technology. Chemiluminescence intensities of $OH^*/CH^*, CN^*/OH^*, CN^*/NO^*, NH^*/CH^*, NH^*/OH^*$ and CN^*/NH^* were calculated to see if there was a relationship between any intensity ratios with the equivalence ratios. In hydrocarbon flames, OH^*/CH^* is usually regarded as a representative of equivalence ratio, but the measurement revealed that it is not true in ammonia/methane flames. As $CN^*/OH^*, CN^*/NO^*, NH^*/CH^*$ increases monotonically with the increase in the equivalence ratio and insensitive to ammonia concentration in the fuel blends, they are recognised as potential substitutes for equivalence ratios in certain range. It was also concluded that NH^*/OH^* and CN^*/NH^* may provide both information of equivalence ratio and ammonia concentration in the fuel blends simultaneously as they are both monotonically related to the equivalence ratio and ammonia concentration in the fuel blends.

NO_x emission of premixed ammonia/hydrogen flames was measured in a tube-type combustor under normal temperature and pressure (NTP) by Joo *et al.* [63]. When ammonia concentration in the fuel increased from 0.1 to 0.3, more NO_x emission were measured, but the ratio of the yielded NO_x mass to the supplied mass of ammonia and hydrogen remained almost identical. A $50\%NH_3/50\%H_2$ premixed flame was conducted under fuel-lean conditions ($\phi: 0.41-0.56$) in GTRC under room temperature and pressure [62]. NO_x emission was high in fuel-lean conditions and reached over 1000 ppmv when the equivalence ratio was 0.52 and 0.56. The test rig shown in Figure 2.3 was also employed to study premixed

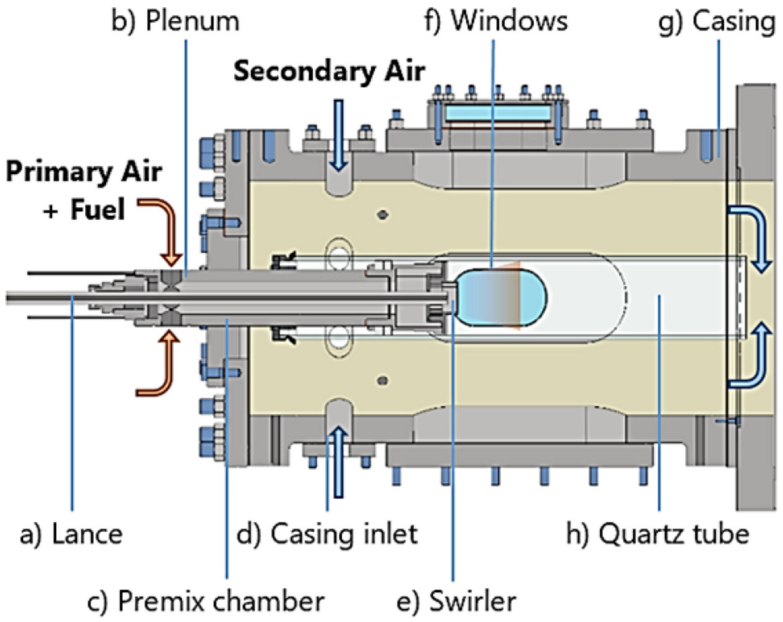


Figure 2.3: Premixed swirl burner in GTRC [132].

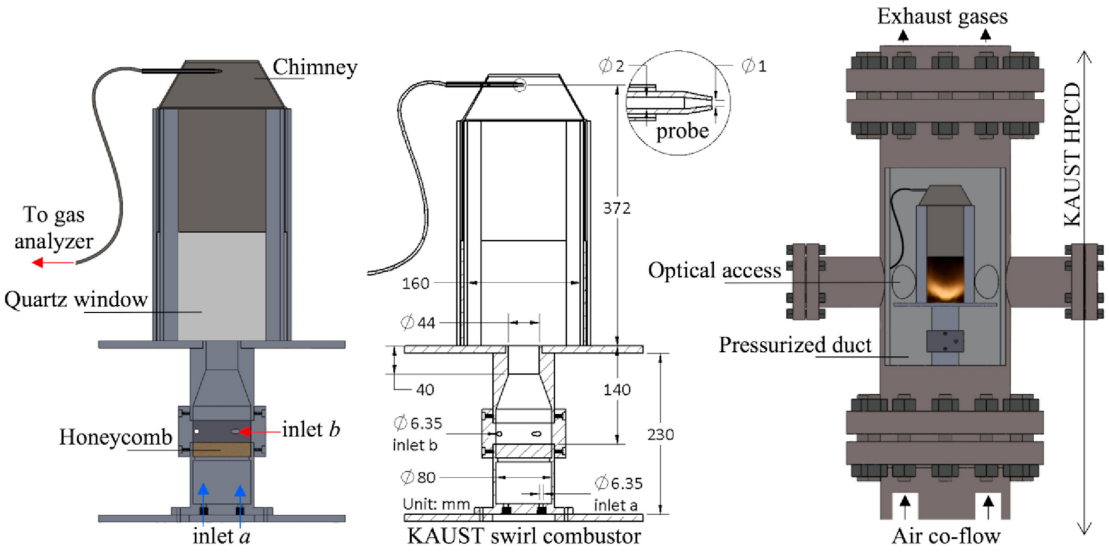


Figure 2.4: Swirl burner in KAUST [104].

70%NH_3/30%H_2 combustion under fuel-rich conditions, as 60%NH_3/40%H_2 flame tended to flashback [132]. It was observed that NO_x emission decreased when the equivalence ratio increased from 1.0 to 1.4. Experimental results of ammonia slip were not published in the work. A porous medium is often used in premixed

hydrocarbon flames to help improve the stability. Nozari *et al.* [133] carried out ammonia/hydrogen combustion test with an inert silicon-carbide porous block under standard temperature and pressure. NO_x concentrations were examined at the exhaust, illustrating a very low pollution ($\sim$ 35 ppmv) generated from $80\%NH3/20\%H_2$ when the equivalence ratio was at 1.5. The injection strategy was discussed by introducing some amount of ammonia/hydrogen to the downstream to control NO_x emissions in Hussein's work [134]. The effects of various ammonia/hydrogen ratios ($0-4\%$vol) in the second injection and residence time on NO emission were studied with Chemical Reactor Network (CRN) model in Chemkin software [134]. The modelling results illustrated that a larger ammonia/hydrogen ratio in the second injection reduced NO emission and the longer residence time facilitated the NO reduction further. According to the simulation results on NO emission, the proposed injection strategy seems to be promising for a premixed ammonia/hydrogen combustion. The relationship between NO concentration and OH^* in premixed ammonia/hydrogen flames was explored under fuel-lean conditions by Zhu *et al.* [135]. As shown in Figure 2.5, P_1, P_2, P_3 are three probe locations for measuring local NO concentration while P_0 is located at the exhaust for NO emission measurement [135]. The local NO concentration and NO emission were found to align well with the local OH^* chemiluminescence intensity in the combustor when the equivalence ratio was at $0.40-0.85$ and ammonia concentration in the fuel was greater than 0.25. It indicates OH^* chemiluminescence imaging technology can be employed to qualitatively visualise local NO concentration trends or NO emission trend in premixed ammonia/hydrogen flames which is a very cost-effective approach compared to local NO detection using OH-PLIF technology. Pugh *et al.* [136] investigated OH^*, NH_2^*, NH^* chemiluminescence in premixed ammonia flame, non-premixed ammonia flame and partially premixed

$70\%NH_3/30\%H_2$ flame with the same net thermal power at 25 kW. There were two types of configurations of partially premixed ammonia/hydrogen flame. One is premixed ammonia and air entering from outer swirling flow and hydrogen entering from the central flow, which was called H_{2Diff}. The other is premixed hydrogen and air entering from outer swirling flow and ammonia entering from the central flow, which is called NH_{3Diff}. By comparing the premixed ammonia flame, H_{2Diff} and NH_{3Diff}, it was noted that for the case of NH_{3Diff}, NH_2^* chemiluminescence intensity was the greatest and OH^* and NH^* chemiluminescence intensities were the lowest among three. Meanwhile, NO emission produced in NH_{3Diff} showed the lowest value. When both the temperature and pressure were lifted, a similar relational phenomenon was observed, i.e., NH_2^* intensity increased, OH^* intensity and NO emission decreased.

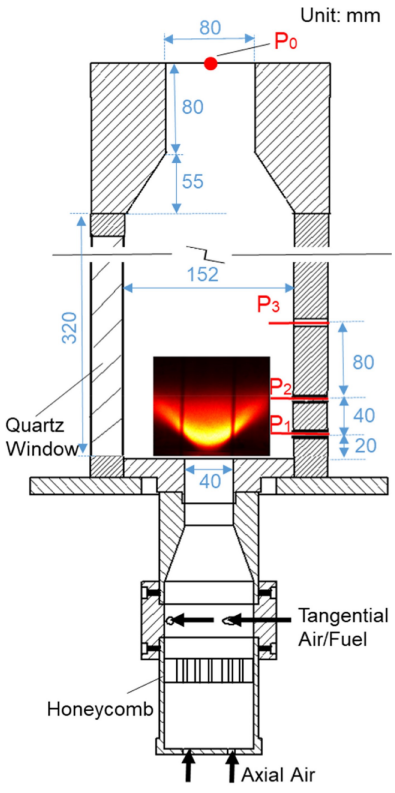


Figure 2.5: The swirl combustor with four different sample points for local NO measurements in KAUST [135].

Studies on ammonia-based combustion emissions have been carried out either experimentally or computationally in terms of single-zone combustion, two-zone rich-lean combustion, premixed combustion of liquid ammonia and methane, combustion with porous medium etc. In addition to gas analyser for pollution detection at the exhaust, chemiluminescence imaging technology has also been applied to explore local radicals and emission formation pathway. Nonetheless, it is still unclear about the emission characteristics of non-premixed ammonia/hydrogen, especially with different hydrogen blending ratios and swirlers. Experimental data on NO_x emission has been reported in many ammonia combustion studies but it is equally important to have unburnt ammonia and hydrogen to provide solid evidence for chemical mechanism development and model validation. In recent years, chemiluminescence imaging technology has been used to analyse ammonia-based combustion, and more information about ammonia flames can be obtained through this technique.

2.4 Heat engines powered by ammonia

It is imperative that combustion engines are adapted to the availability of ammonia as a fuel in order for widespread application to be possible. When considering ammonia-powered heat engines, retrofitting of the ammonia fuel container, fuel supply system, compression ratio, spark ignition system, and engine materials are required [14]. The fuel container and fuel supply system are usually heavier and take up more space than current heat engines powered by conventional fossil fuel. Ammonia requires a high ignition temperature compared to hydrocarbon fuels, so the ignition system in the heat engine needs modification. Reiter *et al.* [137] reported that operating the Compression-Ignition (CI) engine by neat ammonia is not feasible as it requires a very high compression ratio (35 : 1). Under high

temperature, hydrogen is generated from ammonia decomposition. Therefore, in order to prevent flashback, it is necessary to modify the spark plug material and spark plug system. In addition, due to the corrosiveness of ammonia, the selection of engine materials should exclude copper, nickel, plastics, etc.

An early record of studies on an ammonia fuelled combustion engine in a limited scale backdates to 1905 and a patent was issued to Ammonia Casale, Ltd in Italy in 1935-1936 [138, 139]. During the World War II, ammonia/coal fuelled internal combustion engines were a temporary solution in Belgium in 1942 to overcome the difficulty of diesel shortage [138, 139]. It was in a sizable scale using system named as Gazamo process with around 100 buses involving ammonia in the fuel mixture [138]. A Gazamo system is shown in Figure 2.6 with ammonia in the front cylinder and compressed coal gas in the back cylinder, and an ammonia-fuelled motor bus with gas cylinders at the top is illustrated on the right [138]. However, the project was halted once the diesel shortage eased [139]. In 1964, NASA tested a modified aircraft X-15A-2 with rocket engine fuelled by liquid ammonia and liquid oxygen [140]. The aircraft added external tanks for the fuel and oxidizer which helped to extend engine burning time by approximately 60 seconds and reached the normal speed of aircraft X-15 but the aircraft drag was considerably increased [140]. Meanwhile, U.S Army conducted a research on the performance of ammonia-powered gas turbine, and the results showed that the slow ammonia-air reaction leads to the low combustion efficiency [141, 142]. It was not until the 1990s, when the motivation to find alternative fuels emerged in response to global warming, that a small amount of additional research was conducted on ammonia combustion engines.

In 2010s, interest in making use of ammonia in heat engines such as internal combustion engines (ICE) for transportation and gas turbines (GT) for

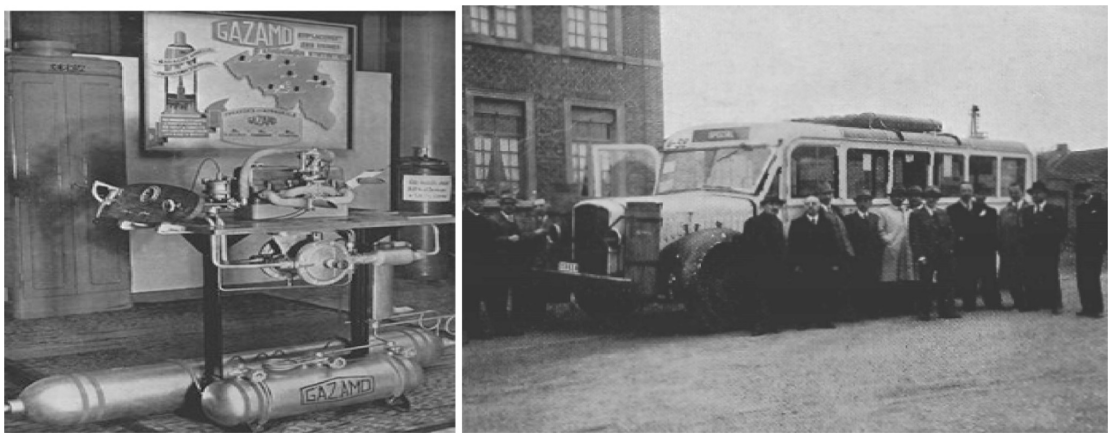


Figure 2.6: Gazamo system and ammonia fuelled motor bus [44, 138].

power generation has been revived. As it was difficult to reach a desirable and reasonable performance with neat ammonia fuelled Spark Ignition (SI) engines, Grannell *et al.* [15] studied the engine efficiency and power output of ammonia/gasoline dual fuelled SI engines with a cooperative fuel research (CFR) engine in 2008. The results suggested the compression ratio at $10:1$ was beneficial for ammonia/gasoline SI engines, because the returns on thermal efficiency and minimizing gasoline use at rough limits were reduced when the compression ratio was above $10:1$. In Gross's work, direct injection of liquid ammonia with DME was explored for the first time in a CI engine [55]. An altered injection system was employed to avoid fuel blends from vaporising. The outcome illustrated the engine load conditions were narrowed as ammonia was introduced to the fuel. CO and HC pollutions were high, because ammonia combustion pressure and temperature were relatively low. As ammonia introduces fuel-NO formation pathway to the chemical reaction, NO_x concentration at the exhaust was high. Ammonia slip was detected in the hundreds of ppm range under majority cases tested. Meanwhile, soot emissions was reported to be very low in all the cases explored. The effect of ammonia concentration in ammonia/DME blends on the performance of CI engine

was discussed with a Yanmar L70V single-cylinder, direct-injection diesel engine [143]. Three blends, 100%DME, 60%DME/40%NH_3 and 40%DME/60%NH_3 (by weight), were assessed in the experiment. It was discovered that comparing with 100%DME case, increased ammonia concentration in the fuel decreased the engine speed and engine power [143]. Regarding to the emissions, the trends of CO, HC, NO_x and soot matched with Gross's work [55]. Unburnt ammonia increased with more ammonia addition in the fuel blends from 40% to 60%. The configuration of ammonia/hydrogen fuelled range extender for electric vehicles with on-board catalytic ammonia cracking system was proposed by Frigo *et al.* [144]. The range extender used in the experiment was a 505 cm^3 Lombardini two-cylinder SI engine [144]. Because it was originally powered by gasoline, the intake manifold was added with six electro-injectors to inject gaseous fuel blends, when gasoline was replaced by ammonia and hydrogen (shown in Figure 2.7). The material of ammonia tank and piping was stainless steel. NO_x emission reached 1700 ppm at full load and a rotational speed at 3000 rpm [144]. A 100 ppm threshold sensor was used to track ammonia leaks, and no alarms went out throughout the experiment. It was clarified that the modified injection system demonstrated good mechanical performance but requires long-term validation to ensure its reliability.

The National Institute of Advanced Industrial Science and Technology (AIST) in Japan has succeeded in implementing the micro gas turbine power generation system for the first time powered by ammonia and kerosene [60], ammonia and air [145, 146, 147], as well as ammonia and methane [145] with selective catalytic reduction system (SCR) for NO_x aftertreatment [145]. Figure 2.8 and Figure 2.9 present the photo and schematic diagram of ammonia-based micro gas turbine power plant. The system was a 50 kW class micro gas turbine manufactured by Toyota Turbine and System Inc. [147]. Non-premixed combustion was applied

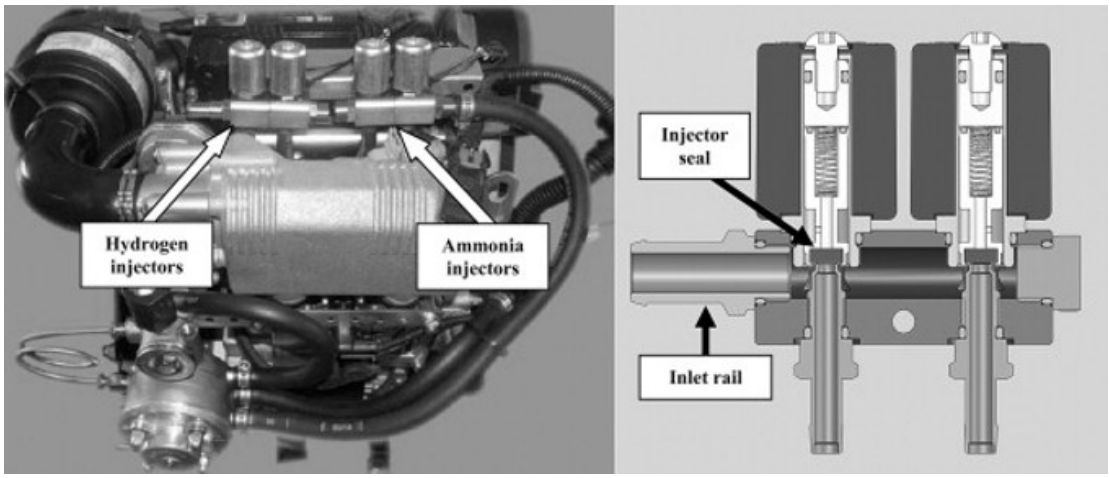


Figure 2.7: Modified SI engine with ammonia and hydrogen injectors [144].

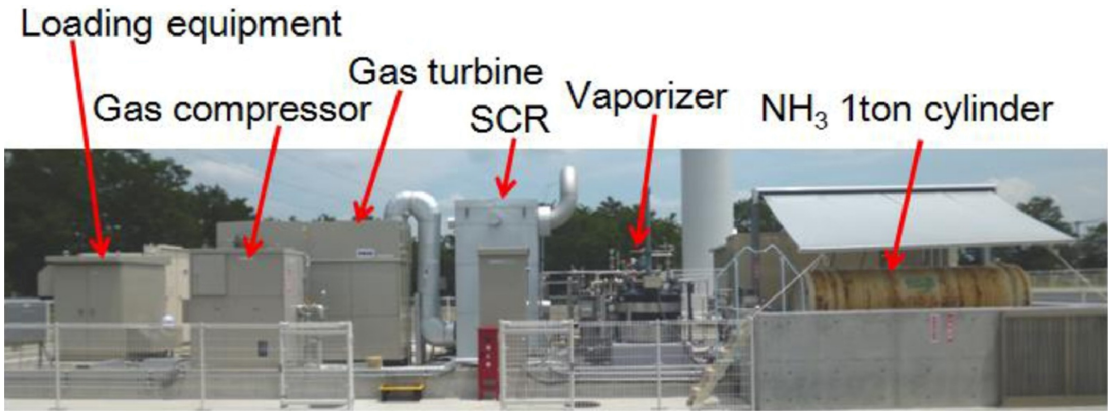


Figure 2.8: Photo of ammonia powered micro gas turbine power plant [145].

with a recuperator to improve the inlet temperature and optimize the combustion efficiency. Since neat ammonia failed to be ignited at atmospheric pressure, kerosene was first ignited as a combustion aid, and then ammonia concentration ratio was slowly enhanced with kerosene flow rate decreasing to zero [145]. 30%Ammonia/70%kerosene managed to generate 21 kW power in the demonstration test, but the substantial amount of NO_x emission was a great concern [60]. Neat ammonia fuelled power plant produced $18.4-44.4$ kW at $70,000-80,000$ rpm, and at the condition of $80,000$ rpm, the combustion efficiency changed between

89% and 96% [145]. The range was wider in ammonia/methane case, which was able to produce the power in the range of $15.8 - 41.8$ kW at $70,000 - 80,000$ rpm [145]. Later, a two-zone combustor for gas turbine was analysed with neat ammonia by the same research group, which achieved an even wider range of power ($10 - 40$ kW) at $75,000 - 80,000$ rpm [148]. These researches were in line with Japan's electricity industry plan, which is to import ammonia and directly burn ammonia to support at least 1% of power supply by 2030 [149].

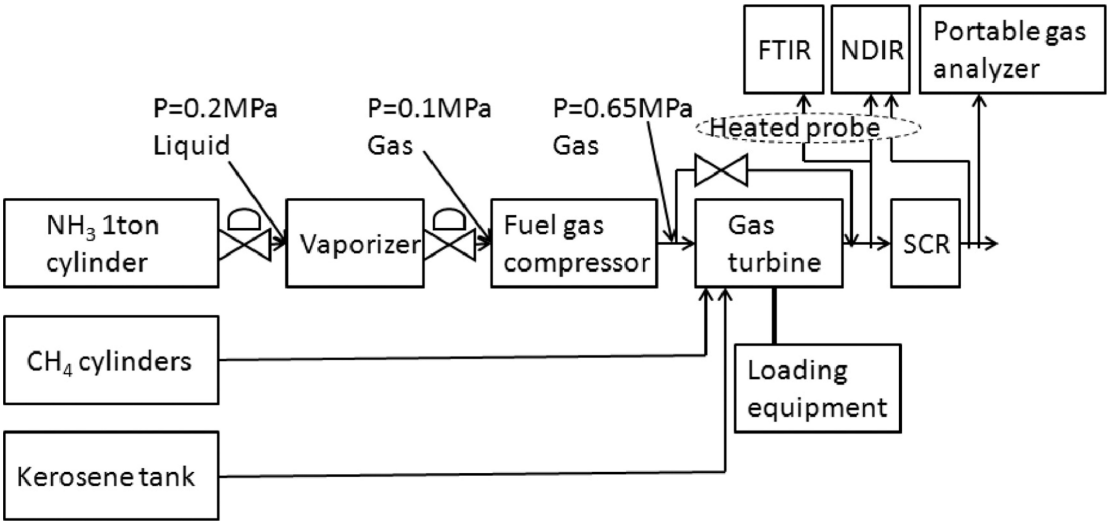


Figure 2.9: Schematic diagram of ammonia powered micro gas turbine [145].

Lately, several big manufacturers are developing ammonia-powered engines for maritime shipping, such as MAN Diesel and Turbo (High Pressure Low Speed Dual Fuel Engine) and Wärtsilä (Low Pressure Dual Fuel Engine) with various fuel injection strategies, i.e., high-pressure in-cylinder direct injection, and low-pressure intake manifold injection respectively, similar to commercial dual fuel engines powered by liquefied natural gas [150]. Deutsche Bahn (German railway company) is attempting to modify existing diesel engines for locomotive and other traction vehicle applications to be able to accommodate a fuel mixture of ammonia

and hydrogen [151]. The decarbonizing locomotive project has been taken a step further by partnering with Fortescue Future Industries, a green energy provider [151].

2.5 Summary

Many researchers have devoted themselves to understanding the ammonia oxidation chemistry and developed more and more accurate chemical kinetic reaction mechanisms for ammonia and ammonia blends. Nevertheless, not any single ammonia (or ammonia blends) mechanism could express ammonia (or ammonia blends) combustion over all range of operational conditions with high fidelity so far. A mechanism screen is necessary to find an appropriate ammonia mechanism under the desired conditions and employ it to examine the ammonia combustion fundamentals. In this thesis, ammonia chemical kinetic reaction mechanism candidates will be firstly selected from the comprehensive literature review. Then, they will be compared against the same sets of published experimental results. The most satisfactory mechanism will be identified for the further parametric study on ammonia/hydrogen combustion fundamentals.

The laminar flame speed of premixed ammonia/hydrogen under practical operation conditions of heat engines has not been extensively discussed. There has been scarce research regarding the ignition delay time and flame structure of ammonia/hydrogen blends, particularly under oxygen-enriched environment.To address another critical problem of ammonia combustion, NO_x emission, the knowledge of NO_x formation pathway (especially NO formation) in ammonia and ammonia blends should be established under various conditions. In this thesis, combustion fundamentals of premixed ammonia/hydrogen combustion will be studied in terms of laminar flame speed, ignition delay and flame structure. The

findings will be discussed under typical operational conditions of a free piston engine with external combustor ($T = 600$K,$P = 15$ bar). The emission performance, exhaust gas temperature and the peak heat production rate of ammonia/hydrogen fuelled gas turbine will be analysed by building a continuous combustion model.

Emissions characteristics in practical combustors are of the deep concern. Premixed and non-premixed type of combustors have been applied for ammonia/air, ammonia/methane/air flames. Modern gas turbine combustors, for example, two-zone rich-lean combustors, combustors with porous medium have also been studied using ammonia/air, ammonia/kerosene/air and ammonia/methane/air. Attempts to inject liquid ammonia into the premixed and two-zone rich-lean types of combustors have also been discussed. Although the addition of hydrogen in ammonia combustion has been analysed in premixed flame type, emission performance of the non-premixed ammonia/hydrogen combustion has not been carried out. Rare experimental data on ammonia slip and unburnt hydrogen has been reported and it is significant for determining a more reasonable fuel blend ratios and equivalence ratios in the development of heat engines. In this PhD work, a swirl-enhanced ammonia and hydrogen combustion test rig will be established. Blowoff limits, emission concentrations including NO_x, unburnt ammonia and unburnt hydrogen at the exhaust will be measured in this combustor test rig. OH^* chemiluminescence imaging will be carried out to explore its relationship with NO emission.

When implementing ammonia and hydrogen as fuel blends to heat engines, it is inevitable that modifications are required in the conventional engines based on ammonia combustion characteristics and emission characteristics. The above-mentioned research area of ammonia/hydrogen combustion needs further study to provide guidance for the development of disruptive heat engines and ultimately the

goal of decarbonization for heavy transport. In this thesis, a comparison analysis will be carried out between the emission results in this PhD project and those published from heat engines (spark-ignition engines, compression-ignition engines, gas turbines and free piston engines) using ammonia. The type of ammonia-powered heat engine with the best emission control will be identified.

Chapter 3. Methodologies

3.1 Introduction

As discussed in Chapter 2, Literature Review, ammonia chemical kinetic reaction mechanisms have been optimised over many decades to understand the ammonia combustion fundamentals. A large number of studies have focused on the fundamental of pure ammonia combustion as well as ammonia/hydrocarbon combustion. Limited work, however, has focused on the fundamental of ammonia/hydrogen combustion, especially under oxygen-enriched environment and operational conditions similar to those of a heat engine. Although in practical terms, the characteristics of premixed ammonia/hydrogen combustion have been efficiently explored, experimental work on non-premixed ammonia/hydrogen combustion has yet to be conducted.

This chapter firstly describes the numerical methodology used for modelling the ammonia and hydrogen combustion fundamentals. It contains zero-dimensional (0D) modelling for premixed laminar flame speed, ignition delay time and flame structure, and one-dimensional (1D) modelling of a continuous combustion model for gas turbine. Secondly, this chapter describes the experimental setup for the combustor test rig establishment, including design, building, commissioning and data collection. The measurements are used to study the blowoff limits, emissions and OH^* chemiluminescence of ammonia/hydrogen combustion in a non-premixed swirl-enhanced combustor.

3.2 Numerical methodology

3.2.1 Premixed Laminar Flame Speed Modelling

One of the most important parameters in the fundamentals of combustion is premixed laminar flame speed. It is defined as the propagation speed of a freely burning premixed laminar flat flame into the unburnt cold flow [64]. In chemical kinetic reaction modelling, laminar flame speed is commonly utilised to validate the chemical kinetic reaction mechanisms, and it plays a decisive role on the turbulent flame speed, which is important when developing practical combustion systems. Since the neat ammonia flame speed was found to be much lower than that of conventional fossil fuels in the previous studies, it is necessary to promote the ammonia combustion by introducing an enhancer, such as hydrogen. Therefore, it is important to understand the effect of various factors on the premixed laminar flame speed of ammonia/hydrogen.

Ansys Chemkin-Pro is a chemistry simulation software for modelling complex chemical reactors, and it has been widely used in automobile, energy and aviation industries , to name just a few [152, 153]. Therefore, in this study, the sub-model of Flame Simulators in Ansys Chemkin-Pro [152], Premixed Laminar Flame-Speed Calculator, has been employed in conjunction with the model of External Source of Inlet Gas and Outlet Flow (Product) of Reactor to calculate the premixed ammonia and ammonia/hydrogen laminar flame speed. The simulation diagram of a $1D$ premixed free-propagating flame is shown in Figure 3.1. Figure 3.2 shows the simulation process in Ansys Chemkin-Pro, which contains model diagram creation, pre-processing for inputting the chemical kinetic reaction mechanism, the reactor model setup for adjusting various parameters, simulation runs and post-processing of the data. The chemical kinetic reaction mechanism is

comprised of the gas-phase kinetics file, thermodynamics data file and gas transport data file. The gas-phase kinetics file is a set of data containing gas phase compositions (elements and species), gas phase chemical reactions (i.e. elementary reaction), their Arrhenius coefficients and other important information. The chemical name, elemental composition, electronic charge, phase and polynomial fitting coefficients for thermodynamics properties (i.e. $C_P(T), S^0(T), H^0(T)$) under a specific temperature range are reported in the thermodynamics data file. The gas transport data file provides data on the geometrical configuration of the molecule (i.e. single, linear, or non-linear), gas phase multi-component viscosity, thermal conductivity, molecular diffusion coefficient, thermal diffusion coefficient, etc. In this thesis, Nakamura's chemical kinetic reaction mechanism [84] was used for all of the numerical study. The mechanism was first chosen as one of three mechanism candidates and then compared against the same sets of experimental results, which can be found in Section 4.2, Chapter 4. In the premixed laminar flame speed simulation, the inlet velocity, equivalence ratio, fuel mixture and oxidant mixture are set in the model of External Source of Inlet Gas. The ambient temperature, pressure, unburnt gas temperature and ending axial position are adjusted in the model of Premixed Laminar Flame-Speed Calculator. The premixed ammonia and ammonia/hydrogen laminar flame speeds were calculated under the estimated temperature profile, which is the default option for simulating cases where the experimental temperature is unknown.

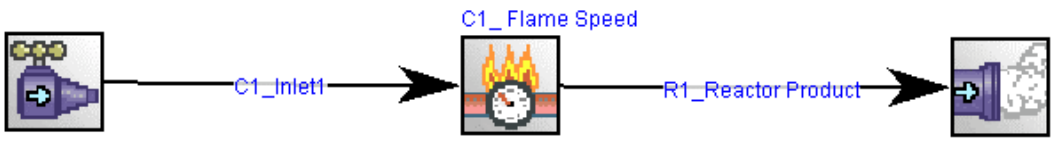


Figure 3.1: Simulation diagram of premixed laminar flame speed.

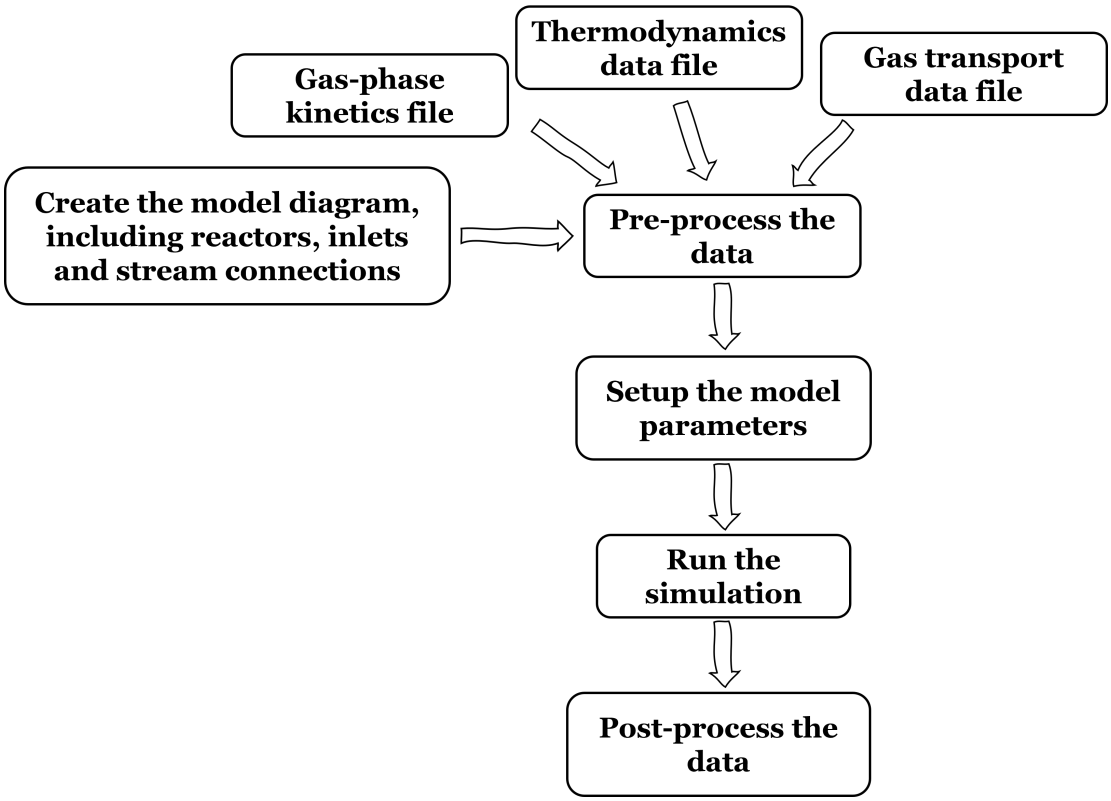


Figure 3.2: Ansys Chemkin-Pro simulation process.

The investigated factors include equivalence ratios ($0.8 - 1.6$), hydrogen blending ratios ($0.0 - 0.6$), oxygen contents in the oxidant ($0.21 - 1.00$), initial gas temperature ($300 - 700$ K) and initial gas pressure ($1 - 20$ bar). The equivalence ratio, ϕ, also known as fuel-air equivalence ratio, is the ratio of the fuel-to-oxidant in the reactor to the fuel-to-oxidant at the stoichiometric condition. The definition is shown in Equation 3.2.1.

$$\phi = \frac{x[fuel]/x[oxidant]}{x[fuel, stoich]/x[oxidant, stoich]} \tag{3.2.1}$$

where $x[fuel]$ and $x[oxidant]$ denote the mole fraction of fuel and oxidant in the mixture, and $x[fuel, stoich]$ and $x[oxidant, stoich]$ refer to the mole fraction of the fuel and oxidant at the stoichiometric condition, respectively. The mixture is

stoichiometric when the equivalence ratio is exactly equal to one. The mixture is in a fuel-lean condition when the equivalence ratio is less than one. When the equivalence ratio exceeds one, the mixture is in a fuel-rich condition. Hydrogen blending ratio, $x\%H_2$, denotes the mole fraction of hydrogen in the fuel blend. It is determined by Equation 3.2.2.

$$x\%H_2 = \frac{x[H_2]}{x[H_2] + x[NH_3]} \tag{3.2.2}$$

As exhibited in Equation 3.2.3, the oxygen contents in the oxidant, Ω, is described as the mole fraction of oxygen in the overall oxidant.

$$\Omega = \frac{x[O_2]}{x[O_2] + x[N_2]} \tag{3.2.3}$$

In the above mentioned equations, $x[H_2]$, $x[NH_3]$, $x[O_2]$, and $x[N_2]$ denote the concentration of hydrogen, ammonia, oxygen and nitrogen, respectively.

The detailed simulation worksheet is provided in Table 3.1. As shown in Case 1-6, the effect of equivalence ratios on the laminar flame speed of ammonia and hydrogen was explored when the hydrogen blending ratio was $0\% - 60\%$. Based on the results shown in Chapter 4, Section 4.3.1, $70\%NH_3/30\%H_2$ blends and the equivalence ratio at 1.1 were chosen for the following studies. Then, the effect of initial temperature on the laminar flame speed of neat ammonia and $70\%NH_3/30\%H_2$ blends was studied when the pressure was at $1 - 20$ bar (Case 7-16). In Case 17-18, the effect of oxygen contents in the oxidant on the laminar flame speed of neat ammonia and $70\%NH_3/30\%H_2$ blends was explored at room temperature and atmospheric pressure.

Table 3.1: Worksheet for premixed laminar flame speed modelling.

Case	$\boldsymbol{T}$ (K)	$\boldsymbol{P}$ (bar)	$\boldsymbol{\phi}$	$\boldsymbol{x\%H_2}$	$\boldsymbol{\Omega}$
1	300	1	0.80, 0.90, 0.95, 1.00, 1.05, 1.10, 1.15, 1.20, 1.25, 1.30, 1.40, 1.50, 1.60	0%	0.21
2				20%	
3				30%	
4				40%	
5				50%	
6				60%	
7	300, 400, 500, 600, 700	1	1.1	0%	0.21
8		5			

(continued at the next page)

Table 3.1 Worksheet for premixed laminar flame speed modelling (continued)

Case	$\boldsymbol{T}$ (K)	$\boldsymbol{P}$ (bar)	$\boldsymbol{\phi}$	$\boldsymbol{x\%H_2}$	$\boldsymbol{\Omega}$
9	300, 400, 500, 600, 700	10	1.1	0%	0.21
10		15			
11		20			
12	300, 400, 500, 600, 700	1	1.1	30%	0.21
13		5			
14		10			
15		15			
16		20			

(continued at the next page)

Table 3.1 Worksheet for premixed laminar flame speed modelling (continued)

Case	$\boldsymbol{T}$ (K)	$\boldsymbol{P}$ (bar)	$\boldsymbol{\phi}$	$\boldsymbol{x\%H_2}$	$\boldsymbol{\Omega}$
17	300	1	1.1	0%	0.21, 0.30, 0.40, 0.50, 0.60, 0.70, 0.80, 0.90, 1.00
18				30%	

(End of Table)

3.2.2 Ignition Delay Time Modelling

Another important parameter in the combustion fundamentals is the ignition delay time. It is defined as the time interval between ignition onset and rapid fuel consumption due to the exponential radical reaction. As the autoignition temperature of ammonia is higher than that of normal fossil fuels, it is beneficial to understand the behaviour of autoignition of ammonia and ammonia/hydrogen blends under different fuel compositions and operating conditions so as to advise the design and development of the next generation heat engines.

In the present study, the ignition delay time of premixed ammonia and ammonia/hydrogen blends is conducted using the sub-model of Closed 0D Reactors in Ansys Chemkin-Pro, Closed-Homogeneous Batch Reactor [152], depicted in Figure 3.3. Since the reactor is a closed environment, no inlet or outlet models are required. The simulation process is the same as shown in Figure 3.2,

with inputting chemistry sets for pre-processing. The calculations were based on constrain pressure and the energy equation was solved. The initial gas temperature and pressure, end time and reactant species were adjusted in the Closed-Homogeneous Batch Reactor. In the experimental tests, the ignition delay time is often obtained in a shock tube that allows the ignition under high-temperature high-pressure conditions. Figure 3.4 illustrates the typical ignition delay time definition to be the time elapsed until the radical of OH^* peaks in the experiment with a shock tube. In the Closed-Homogeneous Batch Reactor, there are two kinds of definition for the computed ignition delay time. One is the time during which the concentration of a certain species achieves its maximum, and the other is defined as the time elapsed when the temperature inflection point occurs [152]. Thus, in this numerical study, the ignition delay time is determined by the time it takes for OH to reach its maximum mole fraction. A wide range of equivalence ratios $(0.5, 1.0, 1.5)$, hydrogen blending ratios $(0.0 - 1.0)$, oxygen contents in the oxidant $(0.21 - 1.00)$, initial temperature $(1400 - 2200$ K) and pressure $(1 - 20$ bar) were discussed in the parametric study. An comprehensive simulation worksheet for ignition delay time modelling is described in Table 3.2. As shown in Case 1-3, the effect of hydrogen blending ratios on the ignition delay time of ammonia and hydrogen was explored when the equivalence ratio was 0.5, 1.0 and 1.5. These three equivalence ratio represents the fuel-lean, stoichiometric and fuel-rich

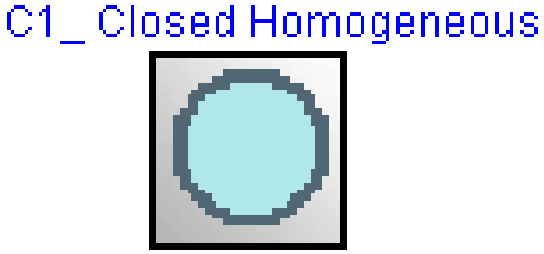


Figure 3.3: Diagram of Closed-Homogeneous Batch Reactor.

conditions, respectively. Based on the results shown in Chapter 4, Section 4.3.1, $70\%NH_3/30\%H_2$ blends and the equivalence ratio at 1.1 were chosen for this study. The effect of initial temperature on the ignition delay time of neat ammonia and $70\%NH_3/30\%H_2$ blends was studied when the pressure is at $1-20$ bar (Case 4-13). In Case 14-17, the effect of oxygen contents in the oxidant on the ignition delay time of neat ammonia and $70\%NH_3/30\%H_2$ blends was explored at the pressure of 1 and 20 bar, respectively.

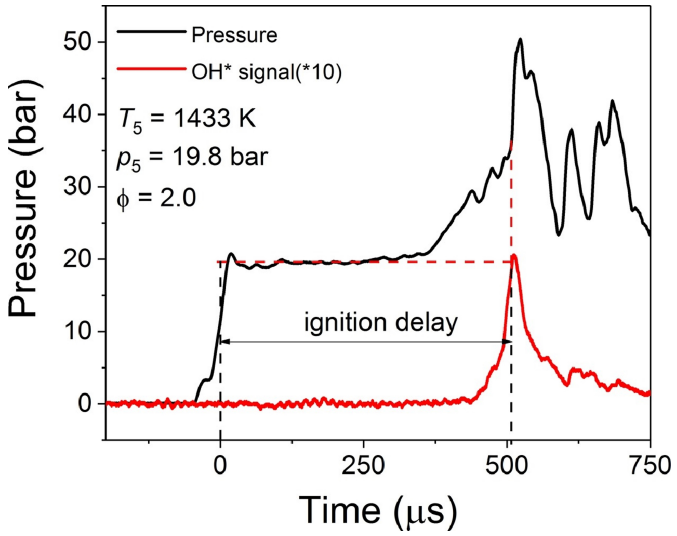


Figure 3.4: Typical definition of ignition delay time in a shock tube [117].

Table 3.2: Simulation worksheet for ignition delay time modelling.

Case	$\boldsymbol{T}$ (K)	$\boldsymbol{P}$ (bar)	$\boldsymbol{\phi}$	$\boldsymbol{x\%H_2}$	$\boldsymbol{\Omega}$
1	1400	1	0.5	0%, 5%, 10%, 15%, 20%, 30%, 40%, 50%, 60%, 80%, 100%	0.21
3			1.0		
3			1.5		
4	1400, 1500, 1600, 1700, 1800, 1900, 2000, 2100, 2200	1	1.1	0%	0.21
5		5			
6		10			
7		15			

(continued at the next page)

Table 3.2 Simulation worksheet for ignition delay time modelling (continued)

Case	$\boldsymbol{T}$ (K)	$\boldsymbol{P}$ (bar)	$\boldsymbol{\phi}$	$\boldsymbol{x\%H_2}$	$\boldsymbol{\Omega}$
8	1400, 1500, 1600, 1700, 1800, 1900, 2000, 2100, 2200	20	1.1	0%	0.21
9	1400, 1500, 1600, 1700, 1800, 1900, 2000, 2100, 2200	1	1.1	30%	0.21
10		5			
11		10			
12		15			
13		20			

(continued at the next page)

Table 3.2 Simulation worksheet for ignition delay time modelling (continued)

Case	$\boldsymbol{T}$ (K)	$\boldsymbol{P}$ (bar)	$\boldsymbol{\phi}$	$\boldsymbol{x\%H_2}$	$\boldsymbol{\Omega}$
14	1400	1	1.1	0%	0.21, 0.30, 0.40, 0.50, 0.60, 0.70, 0.80, 0.90, 1.00
15				30%	
16	1400	20	1.1	0%	0.21, 0.30, 0.40, 0.50, 0.60, 0.70, 0.80, 0.90, 1.00
17				30%	

(End of Table)

3.2.3 Burner-Stabilised Flame Structure Modelling

NO_x emission control is one of the primary obstacles for developing optimal ammonia powered heat engines, because ammonia working as fuel brings the fuel-bound NO generation method as well as thermal NO method which is a usual concern in combustion. In order to minimize NO_x emission from premixed ammonia or ammonia/hydrogen flames, the NO_x generation pathways under different fuel compositions and working environment should be explored. The flame structure

and rate of production and consumption of nitric oxide has been examined with the sub-model of Flame Simulators in Ansys Chemkin-Pro, Premixed Laminar Burner-Stabilised Flame [152]. Figure 3.5 presents the diagram of flame structure simulation, including an external inlet model and products of outlet model. The simulation process is the same as illustrated in Figure 3.2. The chemistry set was first pre-processed, then the parameters such as inlet velocity, species-specific properties, unburnt temperature, initial gas pressure, ambient temperature, ending axial position were set in the external inlet model and reactor model. The simulation was conducted on the basis of gas energy equation under the estimated temperature profile. The effect of a variety of equivalence ratios $(0.9-1.2)$, hydrogen blending ratios $(0.0-0.8)$, oxygen contents in the oxidant $(0.21-1.00)$ and pressure $(1-20$ bar) on the main species profiles of $NH_3, H_2, NO, NO_2, N_2O$ were derived and investigated. Table 3.3 presents the detailed inlet fuel blends and working environment for each case in burner-stabilised flame structure modelling. As shown in Case 1-2, the effect of equivalence ratios on the flame structure of ammonia and hydrogen was explored when the hydrogen blending ratio was 10% and 30%. The value of hydrogen blending ratio at 30% was selected based on the results shown in Chapter 4, Section 4.3.1. The value of hydrogen blending ratio at 10% was also employed to investigate the flame structure at low hydrogen content in the fuel. The initial temperature at 500 K was selected to study the flame structure under a high-temperature environment, which is closer to a practical operational condition in a heat engine. According to the findings shown in Chapter 4, Section 4.3.3, the equivalence ratio at 1.1 were chosen for the following cases. In Case 3, the effect of hydrogen blending ratios on the flame structure was explored. The effect of pressure on the flame structure of $70\%NH_3/30\%H_2$ blends was studied when the initial temperature was 600 K (Case 4). It is because the

simulation was difficult to converge under various pressures when the initial temperature was 500 K. In Case 5, the effect of oxygen contents in the oxidant on the flame structure of $70\%NH_3/30\%H_2$ blends was explored at the initial temperature of 500 K and pressure of 1 bar.

Additionally, the ammonia mole fraction at inlet changes in different cases resulting from different inlet conditions, hence, NO_x concentrations at the post-flame zone were normalised against the imported ammonia mole fraction to prevent any impact on the results interpretation. The normalisation equation is shown in Equation 3.2.4, in which $x[NO_x]'_{end}$, $x[NO_x]_{end}$ and $x[NH_3]_{start}$ indicate the concentrations of normalised NO_x emission, NO_x emission and imported NH_3, respectively. NO_x is an abbreviation for NO, NO_2, N_2O. The normalized emission results show the behaviour of NO_x emissions that generated from burning the same amount of nitrogen atoms in the ammonia fuel during ammonia/hydrogen combustion.



Figure 3.5: Diagram of flame structure simulation.

$$x[NO_x]'_{end} = \frac{x[NO_x]_{end}}{x[NH_3]_{start}} \tag{3.2.4}$$

3.2.4 Continuous combustion model

Ammonia powered gas turbine has attracted a lot of attention recently, especially in power generation field. Although gas turbine powered by neat ammonia has

Table 3.3: worksheet for burner-stabilised flame structure modelling.

Case	$\boldsymbol{T}$ (K)	$\boldsymbol{P}$ (bar)	$\boldsymbol{\phi}$	$\boldsymbol{x\%H_2}$	$\boldsymbol{\Omega}$
1	500	1	0.90, 1.00, 1.05, 1.10, 1.15, 1.20	10%	0.21
2				30%	
3	500	1	1.1	0%, 10% 20%, 50%, 80%	0.21
4	600	1, 5, 10, 15, 20	1.1	30%	0.21
5	500	1	1.1	30%	0.21, 0.40, 0.60, 0.80, 1.00

been succeeded in Japan, NO_x emission is still very high and require to apply SCR technology for aftertreatment [146]. Hence, attempts have been made to analyse the emission performance of gas turbines powered by dual fuels of ammonia and hydrogen. The simulation was conducted with the 1D gas turbine network in Ansys Chemkin-Pro, which is widely utilised to predict premixed flow characteristics in a continuous combustion model similar to gas turbine combustor [152, 154, 155]. The diagram of the continuous combustion model is presented in Figure 3.6. The top diagram is the continuous combustion model without secondary air injection while the bottom one is the system with the secondary air injection. Three Per-

fectly Stirred Reactors (PSRs) and a Plug Flow Reactor (PFR) are the main components in the continuous combustion model. It is illustrated in Figure 3.7 that the PSRs denote the mixing zone at the inlet for fuel and air, recirculation zone and flame zone, respectively. The PFR connected after the flame zone indicates the post-flame zone. In the present study, ammonia/hydrogen blends and oxidant are injected into the first PSR for mixing, passed through the recirculation zone, reacted in the flame zone and the products are eventually delivered to the post-flame zone. The simulation process of the continuous combustion model is shown in Figure 3.2, where the chemistry set was performed before the model setup. In the model setup, the mass flow rate of inlet ammonia stayed identical for all cases at 0.851 g/s, where 20% of the product gas was designated as recirculated, according to previous investigation with the similar combustor configuration [62].

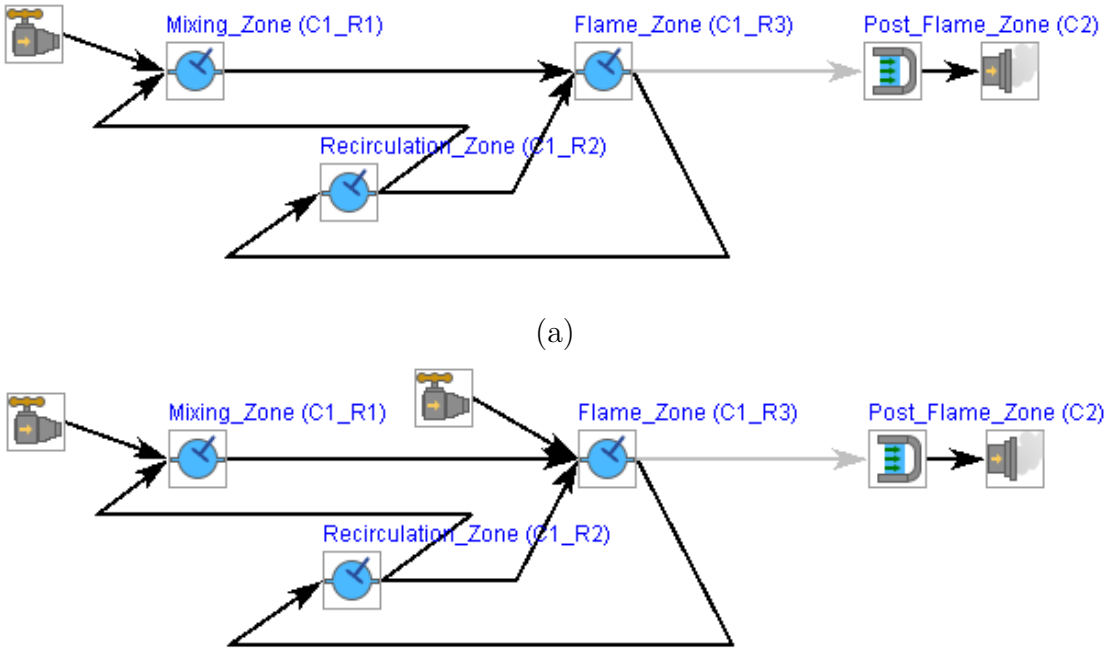


Figure 3.6: Diagram of the continuous combustion model (a) without and (b) with the secondary air injection.

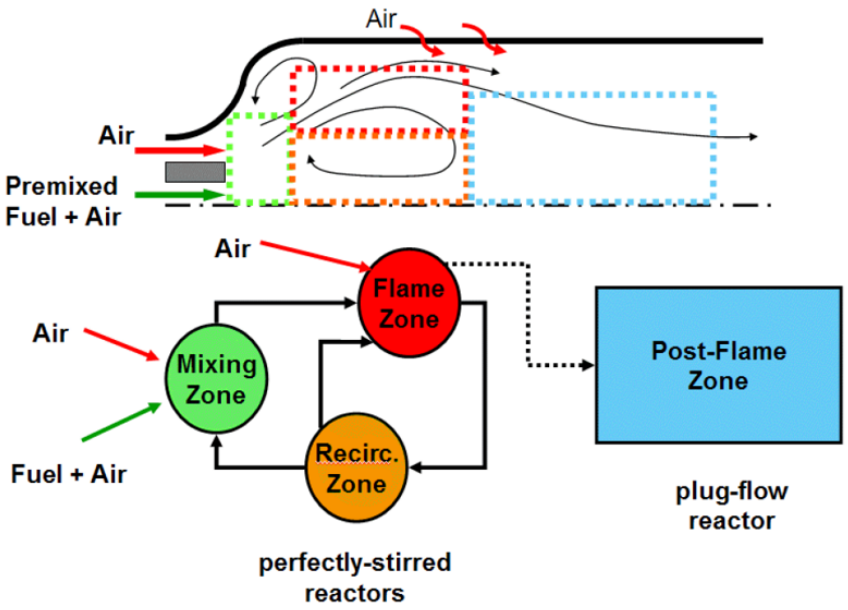


Figure 3.7: Schematic of the continuous combustion model [152].

Since the laboratory-scaled combustor described in Section 3.3 is intended for applications in heat engines, e.g. gas turbines, the parameters of diameter and length of the duct were set to match with the laboratory-scaled combustor, that is, 150 mm and 300 mm, respectively. As illustrated in Figure 3.6, a secondary air injection was introduced in the flame zone which is expected to reduce the incomplete combustion fuel and optimise the combustion efficiency. The effects of initial component ratios, i.e. equivalence ratios $(0.8 - 1.2)$, hydrogen blending ratios $(0.0 - 0.4)$, oxygen contents in the oxidant $(0.21 - 1.00)$ on emission performance (NH_3, H_2, NO_x), exhaust temperature and the peak heat production rates were explored in the first part of this investigation. Then, the effects of initial pressure $(1 - 20$ bar$)$, initial gas temperature $(300 - 500$ K$)$ and overall equivalence ratios in the system with secondary air injection ($\phi_{overall}$: $0.337 - 0.973$) were analysed using the initial component ratios suggested in the first part of study (Section 4.4, Chapter 4). The examined initial component ratios and range for

various parameters for each case are presented in Tables 3.4 - 3.8. The design of the simulation started from analysing the effects of equivalence ratios (Table 3.4), hydrogen blending ratios (Table 3.5) and oxygen contents in the oxidant (Table 3.6). According to the results presented in Chapter 4, Section 4.4, the equivalence ratio of 1.1, hydrogen blending ratio at 40% and oxygen contents in the oxidant at 0.4 were selected to study the effects of initial temperature, pressure and secondary air injection.

Table 3.4: Calculated initial component ratios for studying the impact of equivalence ratios ($T = 300$ K, $P = 1$ bar, $\dot{m}(NH_3) = 0.851$ g/s).

ϕ	$x\%H_2$	Ω	$\dot{m}(H_2)$ (g/s)	$\dot{m}(O_2)$ (g/s)	$\dot{m}(N_2)$ (g/s)
0.8				1.752	5.767
0.9				1.557	5.126
	20%	0.21	0.025		
1				1.402	4.614
1.1				1.274	4.194
1.2				1.168	3.845

Table 3.5: Calculated initial component ratios for studying the impact of hydrogen blending ratio ($T = 300$ K, $P = 1$ bar, $\dot{m}(NH_3) = 0.851$ g/s).

ϕ	$x\%H_2$	Ω	$\dot{m}(H_2)$ (g/s)	$\dot{m}(O_2)$ (g/s)	$\dot{m}(N_2)$ (g/s)
1.1	0%	0.21	0.000	1.092	3.595
	10%		0.011	1.173	3.861
	20%		0.025	1.274	4.194
	30%		0.043	1.404	4.622
	40%		0.067	1.578	5.193

Table 3.6: Calculated initial component ratios for studying the impact of oxygen contents in the oxidant ($T = 300$ K, $P = 1$ bar, $\dot{m}(NH_3) = 0.851$ g/s).

ϕ	$x\%H_2$	Ω	$\dot{m}(H_2)$ (g/s)	$\dot{m}(O_2)$ (g/s)	$\dot{m}(N_2)$ (g/s)
1.1	40%	0.21	0.067	1.578	5.193
		0.4			2.071
		0.6			0.920
		0.8			0.345
		1			0.000

Table 3.7: Operational conditions for the selected initial component ratio ($\phi = 1.1$, $x\%H_2 = 40\%$, $\Omega = 0.4$, $\dot{m}(NH_3) = 0.851$ g/s, $\dot{m}(H_2) = 0.067$ g/s, $\dot{m}(O_2) = 1.578$ g/s, $\dot{m}(N_2) = 2.071$ g/s).

$\boldsymbol{T}$ (K)	$\boldsymbol{P}$ (bar)
300	$1, 5, 10, 15, 20$
$300, 350, 400, 450, 500$	1

Table 3.8: Initial conditions for studying the impact of secondary air injection under $T = 300$ K, $P = 1$ bar (Primary injection: $\phi = 1.1$, $x\%H_2 = 40\%$, $\Omega = 0.4$, $\dot{m}(NH_3) = 0.851$ g/s, $\dot{m}(H_2) = 0.067$ g/s, $\dot{m}(O_2) = 1.578$ g/s, $\dot{m}(N_2) = 2.071$ g/s.

$\boldsymbol{\dot{m}(air, sec)}$ (g/s)	$\boldsymbol{\phi_{overall}}$
0.100	0.973
0.500	0.877
1.000	0.780
3.000	0.542
7.000	0.337

3.3 Experimental setup

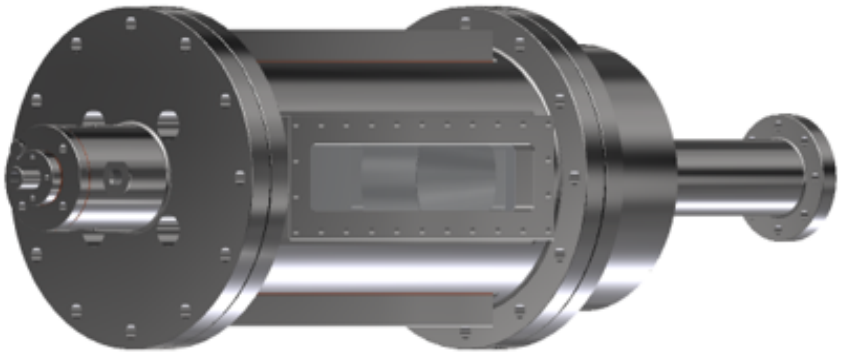
This section introduces all experimental apparatus including the combustor, swirl-enhanced ammonia combustor rig, ignition system, CMOS camera, exhaust emis-

sions measurement instruments and OH^* chemiluminescence measurement instruments. The specification of each equipment is provided in the following subsections. The detailed working sheet for the experimental work has been reported in Chapter 5, Section 5.2.1 and 5.3.1.

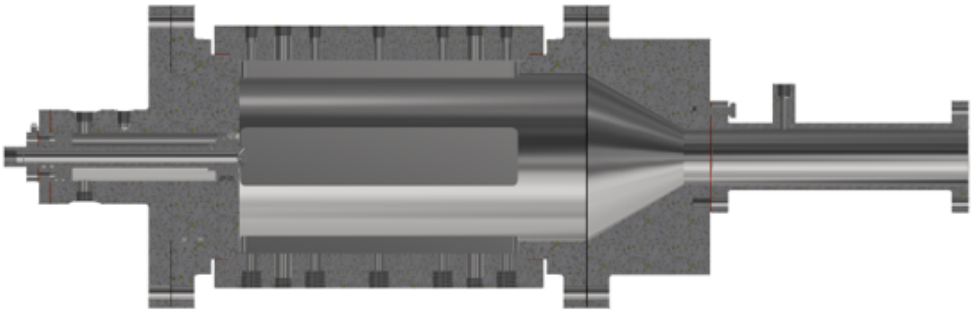
3.3.1 Combustor

The combustor is cylindrical with two detachable facing quartz glass windows. The full and cross-sectional view of combustion geometry are shown in Figure 3.8. The inner chamber is 150 mm in diameter, 310 mm in length with the conical exhaust 110 mm in length. The exhaust gas is discharged to the exhaust port of the test building through an exhaust pipe with a diameter of 25 mm for after-treatment. The two quartz windows are rectangular in shape with a length of 249 mm and a width of 53 mm. Besides this, there are five probe points available on the top of the chamber which allow the inner wall temperature to be measured along the combustion length.

Figure 3.9 illustrates the combustor head including an air swirler and a fuel nozzle. It is designed for testing non-premixed flames. Fuel mixture is directly injected into the combustor through fuel nozzle surrounded by a swirler for oxidant. Figure 3.10 shows the fuel nozzle with 8 holes of 2 mm in diameter. Since the fuel injection angle has a significant impact on flame stability [129], 45 degrees are chosen for each hole in this experiment to improve the mixing of fuel and air and avoid the flame being too close to the chamber liner. Air is utilised as the oxidant and injected into the concentric pipe from four directions (top, bottom, right and left) which then passes through the swirler to the combustor. The purpose of the swirler is to circulate the hot combustion products from downstream to upstream, promoting the mixing rate with the incoming fuel and air and preheating the un-



(a)



(b)

Figure 3.8: (a) Combustor geometry and (b) Half section view of the combustor.

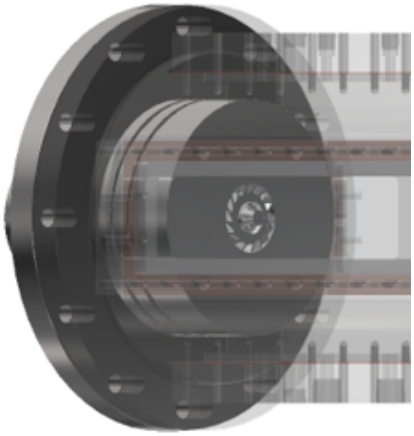


Figure 3.9: 3D CAD model of the combustor head.



Figure 3.10: 3D CAD model of the fuel nozzle.

burned mixture at the upstream [97, 156]. Thus, the swirl-enhanced combustor is very helpful in improving the stabilisation of the ammonia flame. The indicator of the strength of swirling flow is swirl number, S, which is defined as the ratio of the axial flux of angular momentum to the axial flux of the axial momentum [157]. The swirl number for a radial swirler can be calculated as [158]:

$$S = \frac{2}{3} \cdot \frac{1 - \left(\frac{D_i}{D_o}\right)^3}{1 - \left(\frac{D_i}{D_o}\right)^2} \cdot tan\ \alpha, \tag{3.3.1}$$

where D_i, D_o and α denote the inner diameter, outer diameter of the swirler and the vane angle, respectively. Three radial swirlers were developed based on various vane angles. Figure 3.11 depicts the schematic diagram of the swirler. The specification of the three radial swirlers is shown in Table 3.9. In order to achieve a strong swirling flow, the value of swirl number is recognised to be higher than 0.6 [97, 156, 159]. In this study, the swirl number varies from 0.73 to 1.04, which is capable to obtain strong swirling flow.

3.3.2 Swirl-enhanced ammonia combustor rig

The swirl-enhanced ammonia combustor rig is located in the Future Engines & Fuels Laboratory. Figure 3.12 depicts the layout of the swirl-enhanced ammo-

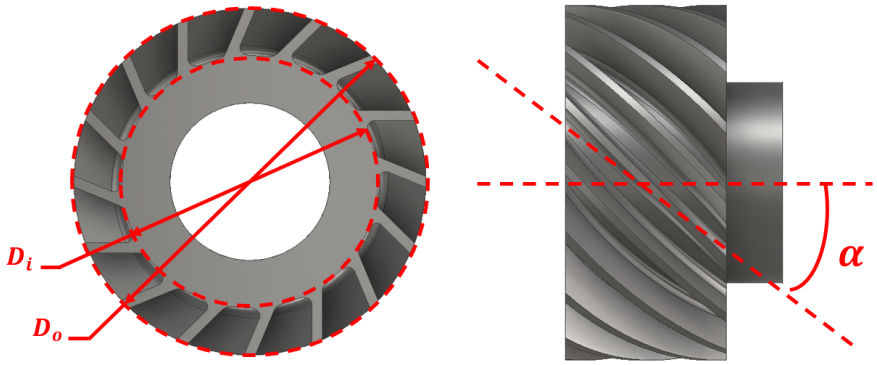


Figure 3.11: 3D CAD model of the swirler.

Table 3.9: Technical data of three radial swirlers.

Swirler	α (°)	D_i (mm)	D_o (mm)	**Number of vanes (-)**	S (-)
(a)	40	32	44	16	0.73
(b)	45	32	44	16	0.87
(c)	50	32	44	16	1.04

nia combustor test rig schematically. The essential components comprise of the gas cylinders, air compressor, mass flowrate controllers (MFCs), flame arrestors, fuel mixer, in-line heating pipes with temperature controllers, combustor, thermocouples, purge system, high speed COMS camera, emission gas analysers, data acquisition device and computer. The experimental equipment spans across the test room, control room, exhaust gas measurement room and gas cylinder storage room. Figure 3.13 and Figure 3.14 show the photos of the test room and the control room. The exhaust gas measurement room is equipped with a Horiba multi-gas analyser, and details are provided in the subsection 3.3.4. A total of 17

cylinders were being used in the tests.

Ammonia (99.98% purity), methane (99.98% purity) and hydrogen (99.99% purity) were supplied in pressurised gas cylinders from BOC Ltd and Air Liquide UK Ltd. Ammonia and hydrogen were then mixed in the bespoke fuel mixer before entering the heating pipe. For the comparison purpose, combustion characteristics of ammonia/methane and pure methane were investigated. The hydrogen blending ratio ($x\%H_2$) and methane blending ratio ($x\%CH_4$) in the fuel are determined by Equation 3.3.2 and 3.3.3, respectively.

$$x\%H_2 = \frac{x(H_2)}{x(H_2) + x(NH_3)} \tag{3.3.2}$$

$$x\%CH_4 = \frac{x(CH_4)}{x(CH_4) + x(NH_3)} \tag{3.3.3}$$

Here, $x(H_2)$, $x(CH_4)$ and $x(NH_3)$ represent the mole fraction of hydrogen, methane and ammonia, respectively. The hydrogen blending ratio varies from 0 to 0.4 because of safety consideration, while the methane blending ratio varies from 0 to 1.0. Air was supplied from the atmosphere via an air compressor.

The flow rate of hydrogen and methane was adjusted by Aalborg^{TM} mass flow rate controller model GFC47S-VDN6 and model GFC37S-VDN6 separately with an accuracy within 1.0% of set point for full scale flow. The full scale for hydrogen is 88 sl/min, while the full scale for methane is 29 sl/min. Aalborg^{TM} mass flow rate controller model GFC67S-VEN2 and model GFC57S-BDN2 are employed to measure the flow rate of air and ammonia, respectively. The accuracy of these two models is 1.5% of set point for $20-100\%$ of full scale flow and 3.0% of set point for $0-20\%$ of full scale range scale. The full scale for air is 323 sl/min and that for ammonia is 67 sl/min. To avoid the reverse gas flow and flashback, flame arrestors were placed after the mass flow meters and before the fuel mixer. WITT

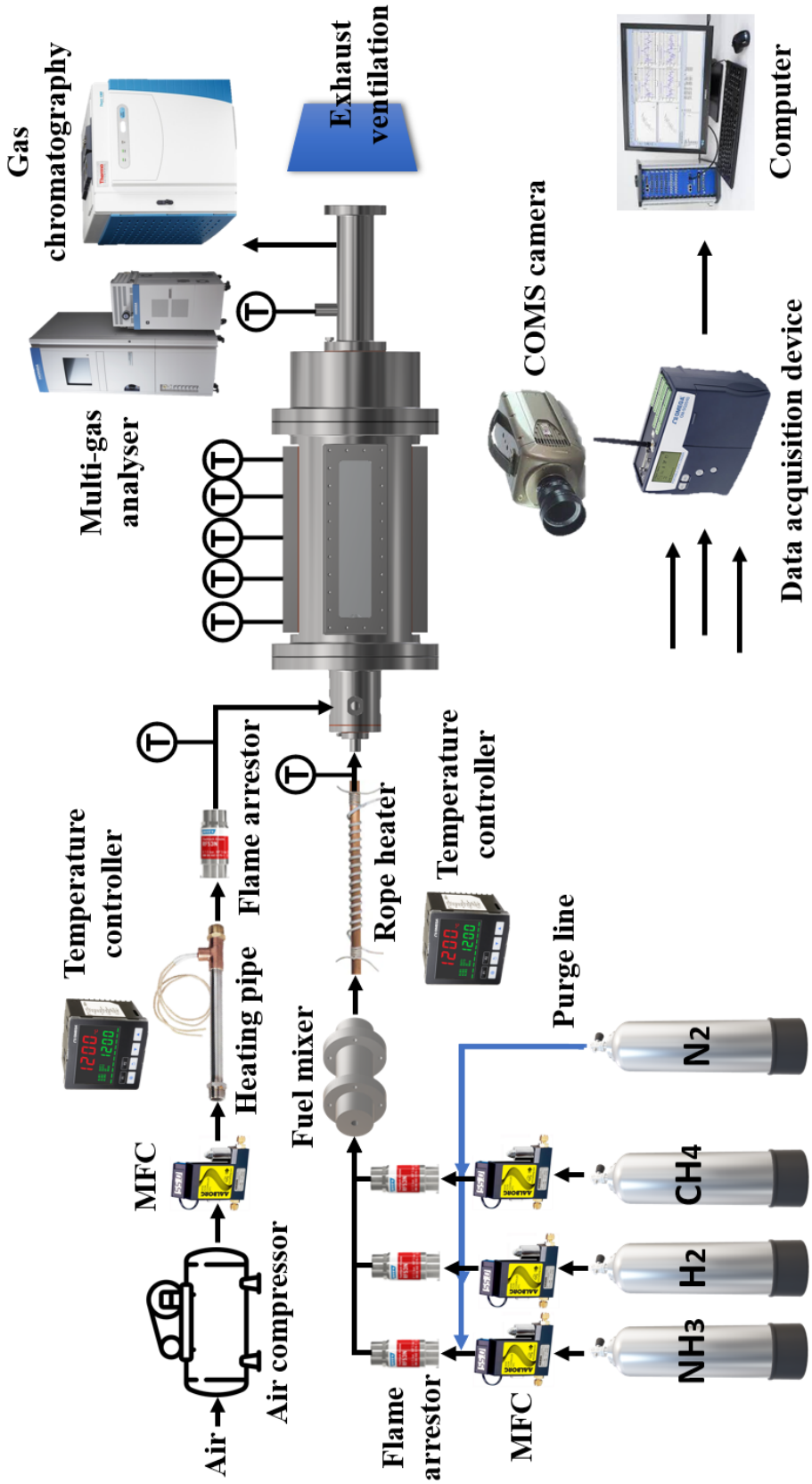


Figure 3.12: Schematic diagram of experiment test rig.

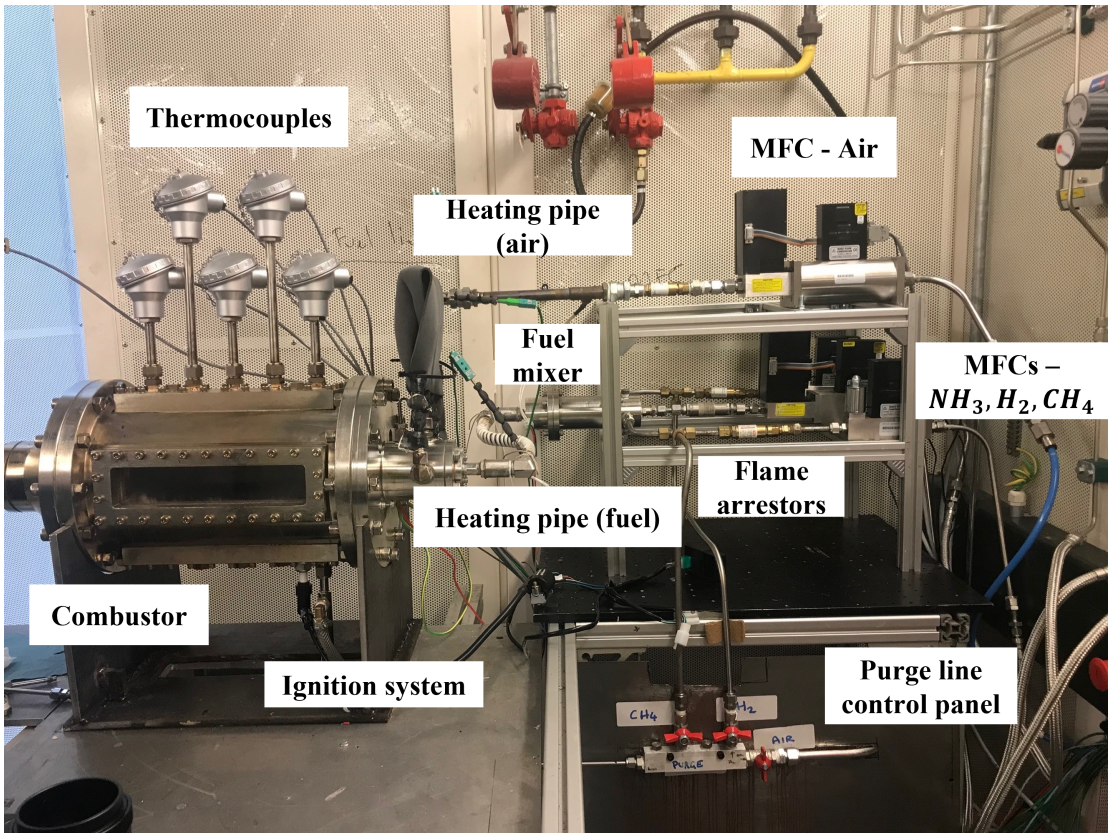


Figure 3.13: Photo of the test room.

RF53N-ES was used as an ammonia flame arrestor, and GCE® Safe-Guard-3 flashback arrestors were applied for hydrogen, methane and air.

The pressure was kept at atmospheric for all of the measurements in the experimental investigation. The initial temperature of air was controlled by an in-line heating pipe OMEGA^{TM} AHP-7562, which can provide hot air up to 540 °C at the exit. It is suitable for the maximum flowrate of 20 CFM (11.564 g/s). A rope heater was employed to preheat the initial temperature of the fuel mixture. The heating temperature was limited by the temperature controller that can reach 500 °C. There were two K-type thermocouples with temperature range of 0−800 °C installed at the inlet of the combustor to measure the initial temperature of air and fuel mixture independently. To measure the temperature profile of the inner

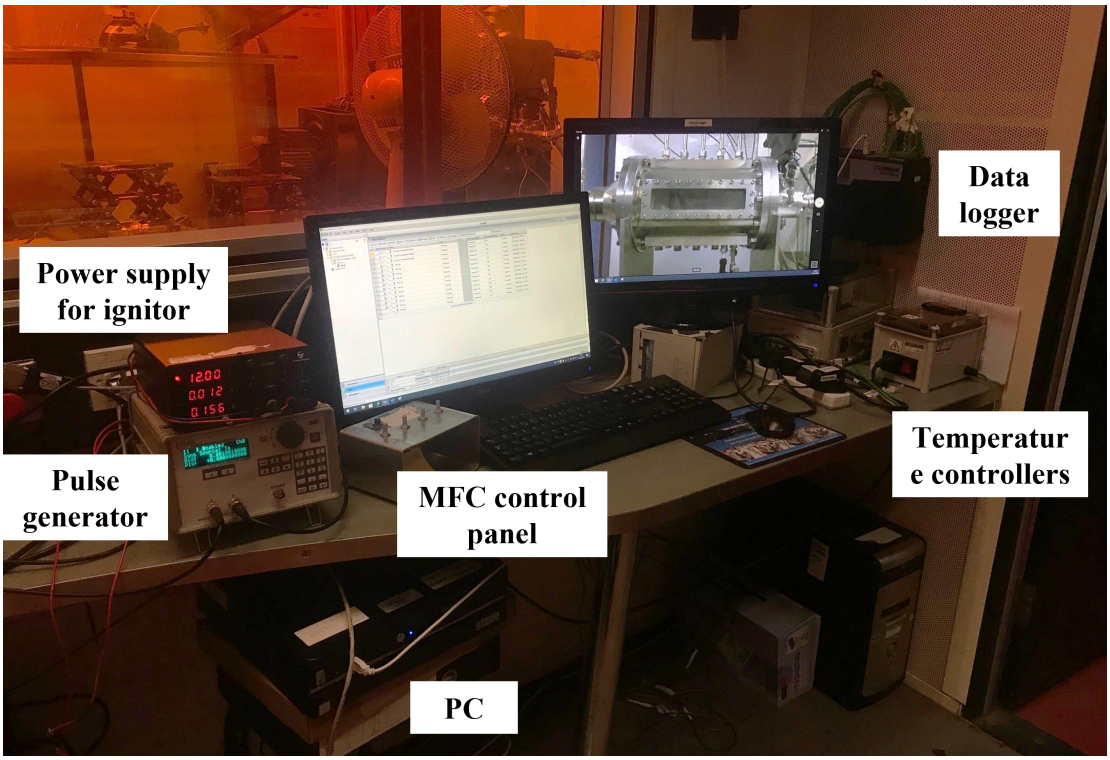


Figure 3.14: Photo of the control room.

combustor wall, five R-type thermocouples with temperature range of $0-1300$ °C were mounted on the top plate at positions of $4, 61, 118, 175$ and 232 mm along the Z-axis of the combustor. In addition, nitrogen was also utilised as a purge gas (blue line in Figure 3.12). Purging was performed before and after each test case to prevent the formation of a combustible environment and cause an explosion.

The ammonia mixture was ignited by spark electrodes. The ignition system is exhaustively described in the subsection 3.3.3. The flame was captured by a CMOS-based digital high speed camera Phantom® v710 (Figure 3.15) with UV-Nikkor 105 mm $f/4.5$ lens (Figure 3.16). The specification of the CMOS camera can be found in Table 3.10. To facilitate flame observation in the control room, Logitech® Webcam C250 with built-in microphone is placed at a distance of 1 m in the front of the quartz window to monitor the combustor.



Figure 3.15: Photo of the Phantom® v710 CMOS camera.



Figure 3.16: Photo of the UV-Nikkor 105mm f/4.5 lens.

The outlet temperature of the exhaust gas was obtained by a K-type thermocouple at approximately 90 mm from the conical exhaust. The exhaust gases containing NO, NO_2, NH_3, H_2,and O_2 were analysed by HORIBA MEXA-7100DEGR multi-gas analyser and Thermo Fisher Trace 1300 gas chromatography. The detailed technical data of the exhaust gas analysers are described in the subsection 3.3.4. All the data were collected and recorded in OMEGA^{TM} OM-SQ2040 data acquisition instrument and monitored with OMEGALOG software.

Table 3.10: Specifications of the Phantom® v710 CMOS camera [160].

Description	Value
Resolution	Up to 1280×800
Frames per second (fps) @ full resolution	> 7500
Maximum frames per second (fps)	723000
Minimum exposure time	1 μs
Sensor	Monochrome CMOS sensor
Pixel bit-depth	8− and 12−bit
Built-in memory size	16 GB

3.3.3 Ignition system

The ignition system, as illustrated in Figure 3.17, is composed of a power supply, capacitor discharge ignition (CDI), a pulse generator, an ignition coil and electrodes. The power supply is set as 12 Vdc to activate the CDI. The CDI consists of a main capacitor, a charging circuit, a trigger circuit and a small type of transformer. Once activated, the current charges the capacitor, storing the power required for ignition. The rectifier in the charging circuit prevents the capacitor from discharging before the ignition signal is received. The pulse generator BNC model 565 is used as the trigger signal source. When the trigger circuit is activated, the capacitor is no longer charged, and the capacitor discharges the primary winding of the ignition coil. The ignition coil's transformer action converts

the ignition coil from the low voltage of the primary winding to the high voltage of the secondary output of the ignition coil, thereby triggering the sparks of the electrodes.

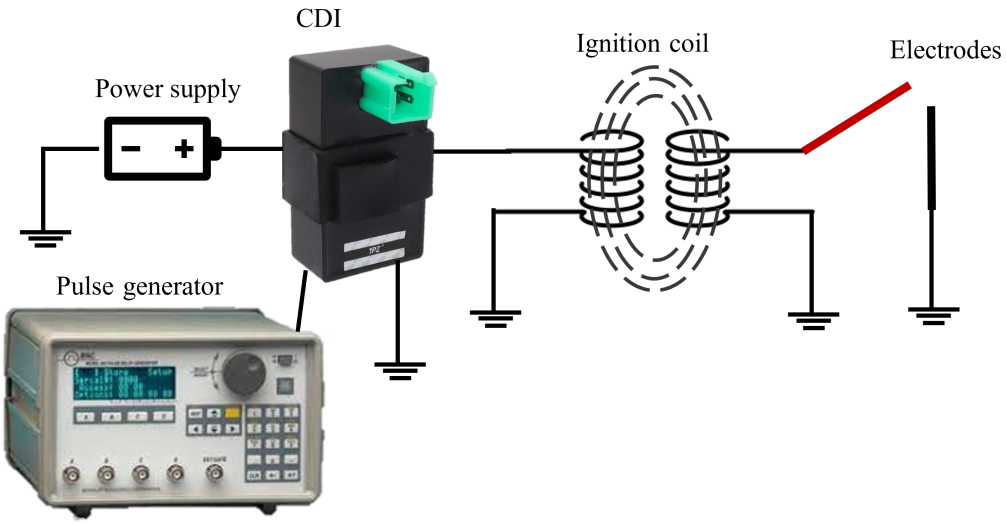
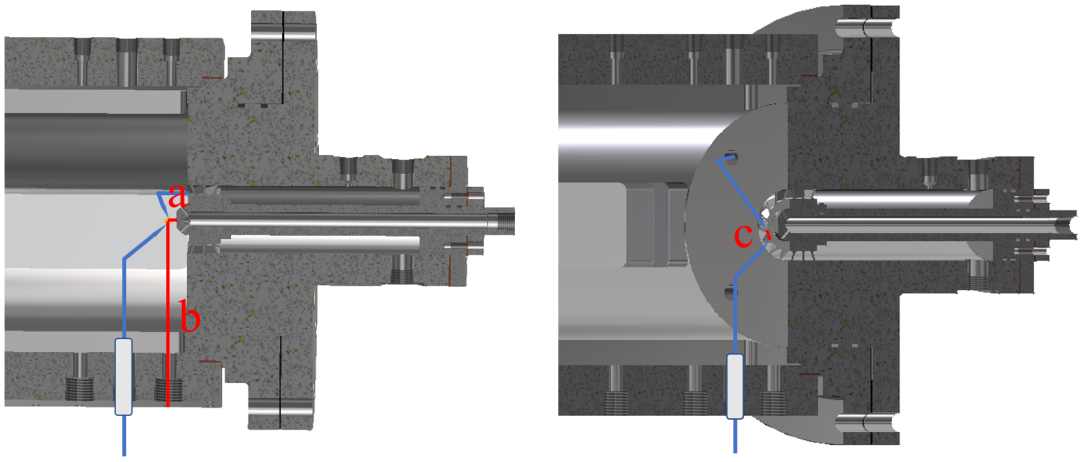


Figure 3.17: Schematic diagram of the ignition system.

The two electrodes are made of stainless steel with a sharpened tip at the front. Figure 3.18 shows a diagram of the location of the electrodes with reference to the combustor. The negative electrode is mounted on the inlet plate of the combustor. The positive electrode is inserted from the bottom plate of the combustor. The distance from the spark to the fuel nozzle (a) is around 5 mm and the distance to the bottom plate (b) is about 75 mm. The electrodes gap, c, is approximately 3 mm.

3.3.4 Exhaust emissions measurement instruments

To detect the concentration of NO, NO_2, O_2 in the exhaust gases, a multi-gas analyser HORIBA MEXA-7100DEGR was used. Its main control unit (MCU)



(a) (b)

Figure 3.18: (a) front angle of the ignitor location (b) 45° angle of the ignitor location.

and oven unit (OVN) are shown in Figure 3.19. The emission gas was sampled from the centreline of the exhaust duct entering from the second probe point. To avoid the water condensation and prevent ammonia gas from dissolving in water, a heating pipe maintaining the temperature at 193 °C was utilised to deliver the gas samples. The sample gas was pumped to heated pre-filter before entering the OVN unit. Ammonia slip was scrubbed from the sample gas in OVN unit using the sample filter and tip filter. The analysers located in OVN unit are heated analysers, such as the NO_x analyser CLA-720MA. The analysers in the analyser rack unit (ANR) under MCU were used to measure the non-heated sample gas (at room temperature) such as O_2 analyser MPA-720. Before each measurement was taken, a calibration procedure was performed to ensure that the measurement is accurate within reasonable limits. A purge procedure was strictly conducted before and after each measurement ensuring a non-combustible environment.

The technical data of each sensor utilised in HORIBA MEXA-7100DEGR is illustrated in Table 3.11. The chemiluminescence method is widely used in



(a) (b)

Figure 3.19: Photo of the HORIBA MEXA-7100DEGR multi-gas analyser (a) Main Control Unit (MCU) (b) Oven Unit (OVN).

detecting NO levels. The reaction of NO with O_3 yields NO_2 in the excited state (NO_2^*) (see Equation 3.3.4). The chemiluminescence phenomenon is generated when NO_2 returns from the excited state to the ground state (see Equation 3.3.5) [161, 162]. The level of NO before the reaction can be detected based on the intensity of the chemiluminescence.

$$NO + O_3 \rightarrow NO_2^* + O_2 \tag{3.3.4}$$

$$NO_2^* \rightarrow NO_2 + hv \tag{3.3.5}$$

Another essential NO_x emission gas, NO_2, can also be detected by converting back to NO using the NO_x converter, as shown in Equations 3.3.6 and 3.3.7. The primary component in the NO_x converter is carbon. The efficiency of NO_x converter was checked on a regular basis to ensure the accuracy of the experimental data. Both NO and NO_2 were obtained based on dry measurement [161, 162]. The NO and NO_x analysers passed the linearization tests conducted by the Horiba on-site engineer. Detailed linearization test report are provided in Appendix 7.2.

$$NO_2 + C \rightarrow NO + CO \tag{3.3.6}$$

$$2NO_2 + C \rightarrow 2NO + CO_2 \tag{3.3.7}$$

The dry oxygen concentration is measured by the magneto-pneumatic (MPA) detector. Oxygen has an incredibly strong paramagnetism compared to other gases. When the sample gas enters the magnetic field, oxygen will be strongly attached to the magnetic pole, resulting in pressure change around the magnetic field. As shown in Equation 3.3.8, the pressure varies in proportion to the oxygen concentration, allowing the oxygen concentration in the sample gas to be calculated [163]. A condenser microphone is utilised to measure the pressure change to an alternating signal when the electric capacity is varied.

$$p = \frac{1}{2} \cdot H^2 \cdot \kappa \cdot x(O_2), \tag{3.3.8}$$

where $H, \kappa, x(O_2)$ denote magnetic field strength, magnetic susceptibility of oxygen, and the concentration of oxygen [163].

In Figure 3.20, Thermo Fisher Trace 1300 gas chromatography was employed to measure the ammonia slip and unburnt hydrogen in the exhaust gas. As a

Table 3.11: Technical data table of HORIBA MEXA-7100DEGR [161, 162, 163].

Emission	**Model**	**Principle**	**Outline**	**Operational gases**	**Calibration gases**	**Response**	**Noise**	**Linearity**	**Repeatability**
NO	CLA-720A	Chemiluminescence (CLD)	Analyser rack (ANR), dry measurement	Ozone generation gas: O_2 99.99%; Dilution gas: N_2 99.99%	Zero gas: N_2 99.99%; Span gas: 2500 ppm NO/N_2	< 1.5 s when NO is 50 ppm or more; < 2.0 s when NO is 50 ppm or less	$< 2.0\%$ of the full scale	Within $\pm 1.0\%$ of the full scale or $\pm 2.0\%$ of the readings	Within $\pm 0.5\%$ of the full scale for zero point or within $\pm 0.5\%$ of the readings for span point
NO_x	CLA-720MA	Chemiluminescence (CLD)	Oven unit (OVN), dry measurement	Ozone generation gas: O_2 99.99%; Dilution gas: N_2 99.99%	Zero gas: N_2 99.99%; Span gas: 2500 ppm NO/N_2	< 2.5 s when NO_2 is 50 ppm or more; < 3.0 s when NO_2 is less than 50 ppm	$< 2.0\%$ of the full scale		
O_2	MPA-720	Magneto-pneumatic (MPA)	Analyser rack (ANR), dry measurement	N_2 99.99%	Zero gas: N_2 99.99%; Span gas: 20.02% O_2/N_2	< 1.5 s when O_2 is 5% or more; < 2.0 s when O_2 is 5% or less	$< 1.0\%$ of the full scale when O_2 is 5% or more; $< 2.0\%$ of the full scale when O_2 is 5% or less		

precaution, a 140 °C heating pipeline was used to deliver the sample gas from the centreline of the exhaust duct. This prevented water from condensing and the ammonia gas from dissolving in water. Ammonia slip was measured using Pulse Discharge helium ionisation Detector (PDD) and hydrogen was measured using Thermal Conductivity Detector (TCD). The configuration can be found in Table 3.12. PDD is a prevalent, non-destructive detector with high sensitivity. The compounds in the sample gas are detected by direct current or glow discharge and then are ionised by photons from the helium. Electrons produced by ionising photons cause changes in the output current [164]. The purity of helium is critical as it considerably affects the performance of detector [165]. The high purity helium (99.999%) with an additional helium purifier was therefore applied in the test to achieve extremely pure helium. TCD is a non-destructive detector and can identify any chemical whose thermal conductivity differs from that of the carrier gas [165]. Due to the different thermal conductivities, there is a shift in the current to maintain the filament temperature. The chemical concentrations are obtained from current changes.

Since the gas chromatography is in the combustion laboratory, the air conditioner in the laboratory was kept at 25 °C in order to prevent from the interference of the signal by the ambient temperature. Before testing each case, a baseline was measured with air to check whether there were any considerable interfering signals which could affect the measurement. The acceptance noise signal of the PDD was $\leq$ 100 μV [165]. The acceptance noise signal of the TCD was $\leq$ 120 μV [165]. The signal-to-noise was then calculated by dividing the peak height of the compound of interest by the noise measured at the baseline to ensure it was within the acceptable range. A description of the emission measurement procedure can be found in the section 5.3.1.



Figure 3.20: Photo of Thermo Fisher Trace 1300 gas chromatography.

All of the data was collected after one hour of measurements and then the combustor was cooled or preheated to the desired initial temperature before starting the next test. The procedure was repeated five times for each case. The average value was calculated. When the equivalence ratio is varied in the emissions test, the level of oxygen concentration at the exhaust also changes. To compare the emission results at different equivalence ratios fairly and comply with the regulation [166, 167], oxygen normalisation was conducted to correct the emission results to a standard oxygen concentration basis (15%). The equation is given by:

$$ppm_{norm} = ppm_{mea}[(20.95 - 15.00)/(20.95 - O_{2_{mea}})], \tag{3.3.9}$$

where ppm_{norm} and ppm_{mea} are the normalised emission concentration and measured emission concentration, respectively, and $O_{2_{mea}}$ denotes the measured oxygen concentration in the exhaust gases [167].

Table 3.12: Technical data table of Thermo Fisher Trace 1300 gas chromatography [165].

Emission gas	$\boldsymbol{NH_3}$	$\boldsymbol{H_2}$
Detector	Pulse Discharge helium ionisation Detector (PDD)	Thermal Conductivity Detector (TCD)
Carrier gas	He 99.999%	N_2 99.999%
Oven operating temperature	Ambient $+3-450$ °C	Ambient $+3-400$ °C
Detector filament temperature	NA	100 °C
Range	100 ppm−4% (with split method)	50 ppm−100%
Typical retention time repeatability:	<0.0008 min	
Typical peak area repeatability:	$<0.5\%$ RSD (Relative Standard Deviation)	

The error bar was calculated using the standard deviation equation (Equation 3.3.10) based on the five measurements. It indicates the uncertainty of the emission measurement at each point.

$$\sigma = \sqrt{\frac{1}{N}\sum_{i=1}^{N}(x_i - \bar{x})^2}, \tag{3.3.10}$$

where N denotes the times of the measurement which is five, x_i and $\bar{x}$ represent the average value for each measurement and average value of the five times

measurements, respectively.

3.3.5 Optical setup for OH^* chemiluminescence imaging

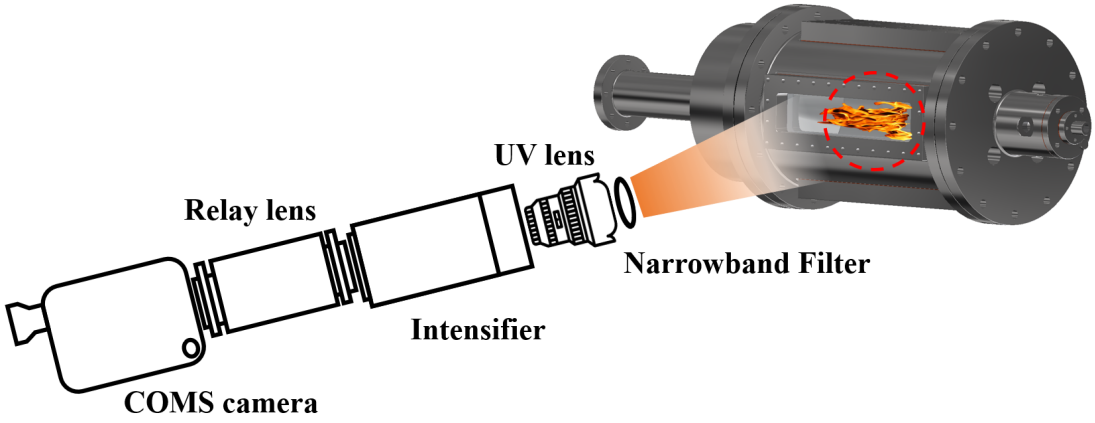


Figure 3.21: Chemiluminescence visualization setup.

The use of chemiluminescence imaging for investigating radicals of interest is non-invasive, cost-effective and has been applied to a variety of combustion applications with small optical access [168, 169, 170, 171]. Figure 3.21 shows the optical system for capturing OH^* chemiluminescence images. A high-speed Phantom® v710 CMOS camera was utilised with resolution of 1280×800, sample rate of 100 pps and exposure time at 9900 μs. Hamamatsu Photonics C10880 image intensifier was connected with the CMOS camera through the relay lens to intensify the chemiluminescence at low-light level and facilitate the image visualisation. The image intensifier gain was constant at 999 in all the measurements. As the OH^* chemiluminescence primarily occurs in the wavelength between $280-350$ nm [172], UV lens (UV-Nikkor 105 mm $f/4.5$ lens) and narrowband filter (centre: 310 nm) are employed. In the present work, OH^* chemiluminescence images have been measured and post-processed in relation to the global equivalence ratios, hydrogen blending ratios, initial temperatures and swirl numbers. For each case, one thousand instantaneous chemiluminescence images and one thousand instan-

taneous background images were collected and post-processed using the bespoke MATLAB code developed by the author. Detailed information about the image processing is provided in the section 5.4.1. The measurements for each case were repeated five times and the error bar for the OH^* intensity were calculated using Equation 3.3.10.

3.4 Summary

In this chapter, a description of numerical methodology for modelling the fundamentals of ammonia and hydrogen combustion and experimental setup for studying non-premixed ammonia and hydrogen flames is provided in detail. In the modelling work, the premixed laminar flame speed, ignition delay time and flame structure have been discussed with a selected ammonia kinetic reaction mechanism. The parametric study has been carried out over a wide range of equivalence ratios, hydrogen blending ratios, oxygen contents in the oxidant, initial temperature and initial pressure. A gas turbine network has been applied to study the emission performance, exhaust gas temperature and peak heat production rate of an ammonia/hydrogen fuelled gas turbine in one dimension. From an experimental point of view, a non-premixed ammonia/hydrogen combustor has been established with the exhaust gas analysers and the optical system setup. The blowoff limits, emission performance and OH^* chemiluminescence have been experimentally investigated. The findings are discussed in Chapter 4, Kinetic study of premixed ammonia/hydrogen combustion characteristics, and Chapter 5, Experimental analysis of non-premixed ammonia flame with hydrogen in a swirl-enhanced combustor.

Chapter 4. Kinetic study of premixed ammonia/hydrogen combustion characteristics

4.1 Introduction

In this chapter, the characteristics of the premixed ammonia/hydrogen laminar flame are appraised numerically with selected chemical kinetic reaction mechanism. First of all, Mechanisms screen was carried out based on the literature review explained in Chapter 2, Section 2.1. Several mechanism candidates were chosen and compared with the same set of combustion fundamentals reported in the experimental literature. Followed by the mechanism screen, a parametric study was conducted to explore the laminar flame speed, ignition delay time and flame structure of premixed ammonia/hydrogen flames by employing the selected ammonia reaction mechanism. The characteristics provides guidance for the development of free piston engine generators and gas turbine. The combustion fundamental of premixed ammonia/hydrogen was also discussed on the basis of the typical operational environment of free piston engine generators. A gas turbine network system was established and applied for examining the emission performance, exhaust gas temperature and the peak heat production rate of ammonia/hydrogen fuelled gas turbine.

The results presented in this chapter have been published in the peer-reviewed journal paper titled Characterising premixed ammonia and hydrogen combustion for a novel Linear Joule Engine Generator [173], and three conference papers titled Characteristics of Ammonia/Hydrogen Premixed Combustion in a Novel Linear Engine Generator [174], Characterising Injection and Combustion of

Ammonia as a Marine Fuel [175], and Combustion and Emission Characteristics of Ammonia Hydrogen dual-fuelled Generic Gas Turbine [176].

4.2 Ammonia chemical kinetic reaction mechanism selection

Three candidates of ammonia chemical kinetic reaction mechanisms were chosen. A cross-comparison with the same sets of measured results from the literature was implemented so as to identify the most appropriate mechanism for further parametric study. Aspects such as laminar flame speed, ignition delay time and flame structure were taken into consideration as important measurements in the literature for comparison. Duynslaegher's mechanism [73] Otomo's mechanism [86] and Nakamura's mechanism [84] were chosen as a short list of candidate ammonia mechanisms considering the convergence performance of the mechanism calculated in Ansys Chemkin-Pro software, accuracy and relevance to the targeted applications; free piston engine generators and gas turbines. The summary of these three ammonia mechanism candidates can be found in Table 2.1 in Chapter 2, Section 2.1.

As depicted in Figure 4.1, the laminar flame speed of premixed ammonia/hydrogen flames was explored with various equivalence ratios and ammonia fractions by energy ($E\%NH_3 = 20\%, 50\%, 80\%$) under standard temperature and pressure (STP) in the experiments by Kumar *et al.* [70]. The data are utilised to compare with the computational results using three candidate ammonia mechanisms. It was found that Duynslaegher's mechanism [73] corresponds better to the measured data in the case of hydrogen as the primary fuel in the blends ($E\%NH_3 = 20\%$). There is more reliability in the predictions of Otomo's mechanism [86] and Nakamura's mechanism [84] in the case of ammonia as the primary fuel in the blends ($E\%NH_3 = 50\%$ and $E\%NH_3 = 80\%$). Due to the fact that

ammonia is used as the primary fuel in the PhD project, Otomo's mechanism and Nakamura's mechanism are deemed to be more appropriate for predicting laminar ammonia and ammonia/hydrogen flame speed.

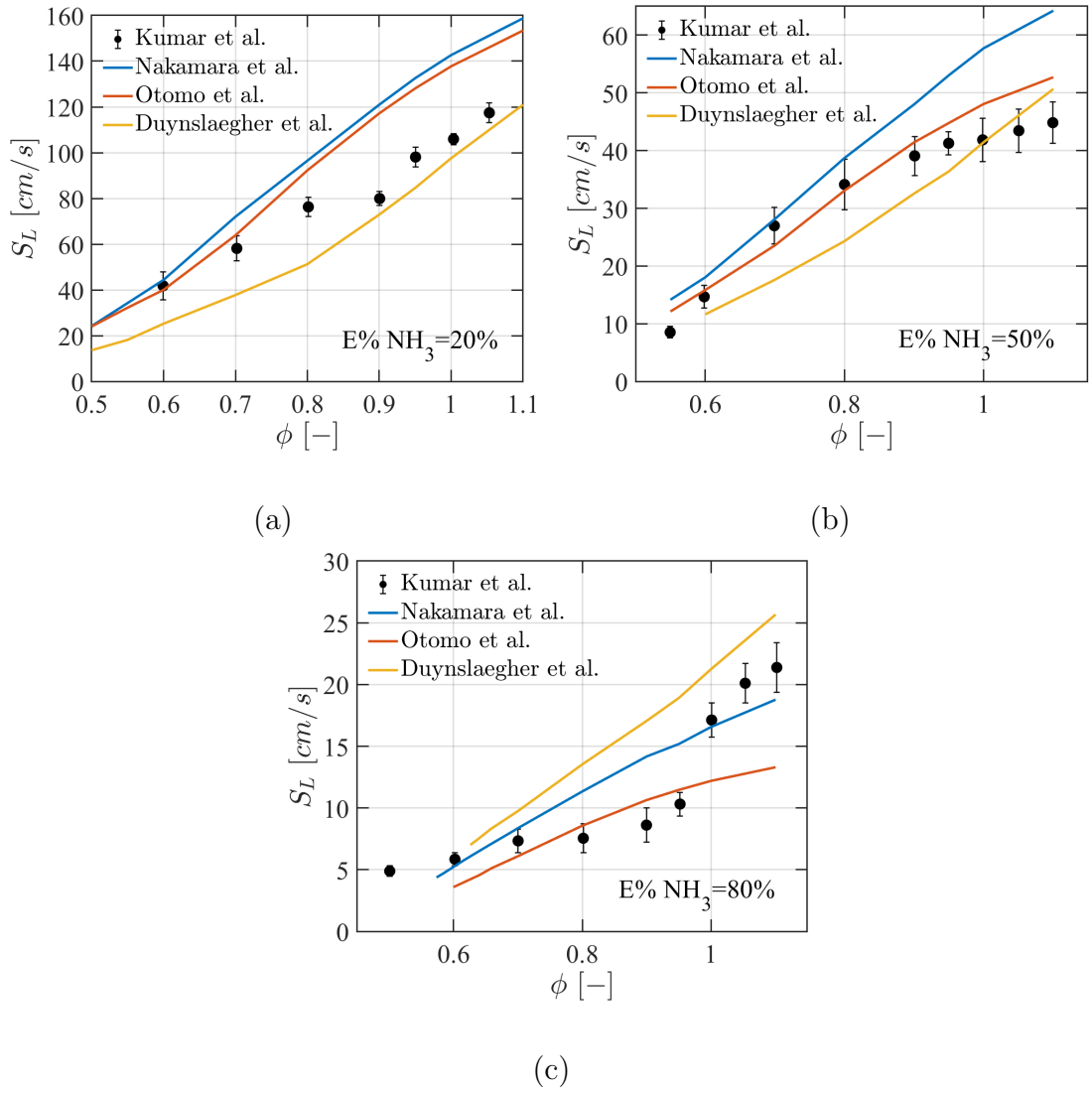


Figure 4.1: Comparison of experimental (symbols) and computational (lines) premixed laminar flame speed of ammonia/hydrogen as a function of equivalence ratios at the ammonia fractions by energy of (a) 20%, (b) 50% and (c) 80%. Experimental data in Kumar's work [70] plotted in conjunction with computational results based on Nakamura's mechanism [84], Otomo's mechanism [86] and Duynslaegher's mechanism [73].

When validating the ignition delay time of ammonia flames, Mathieu's mea-

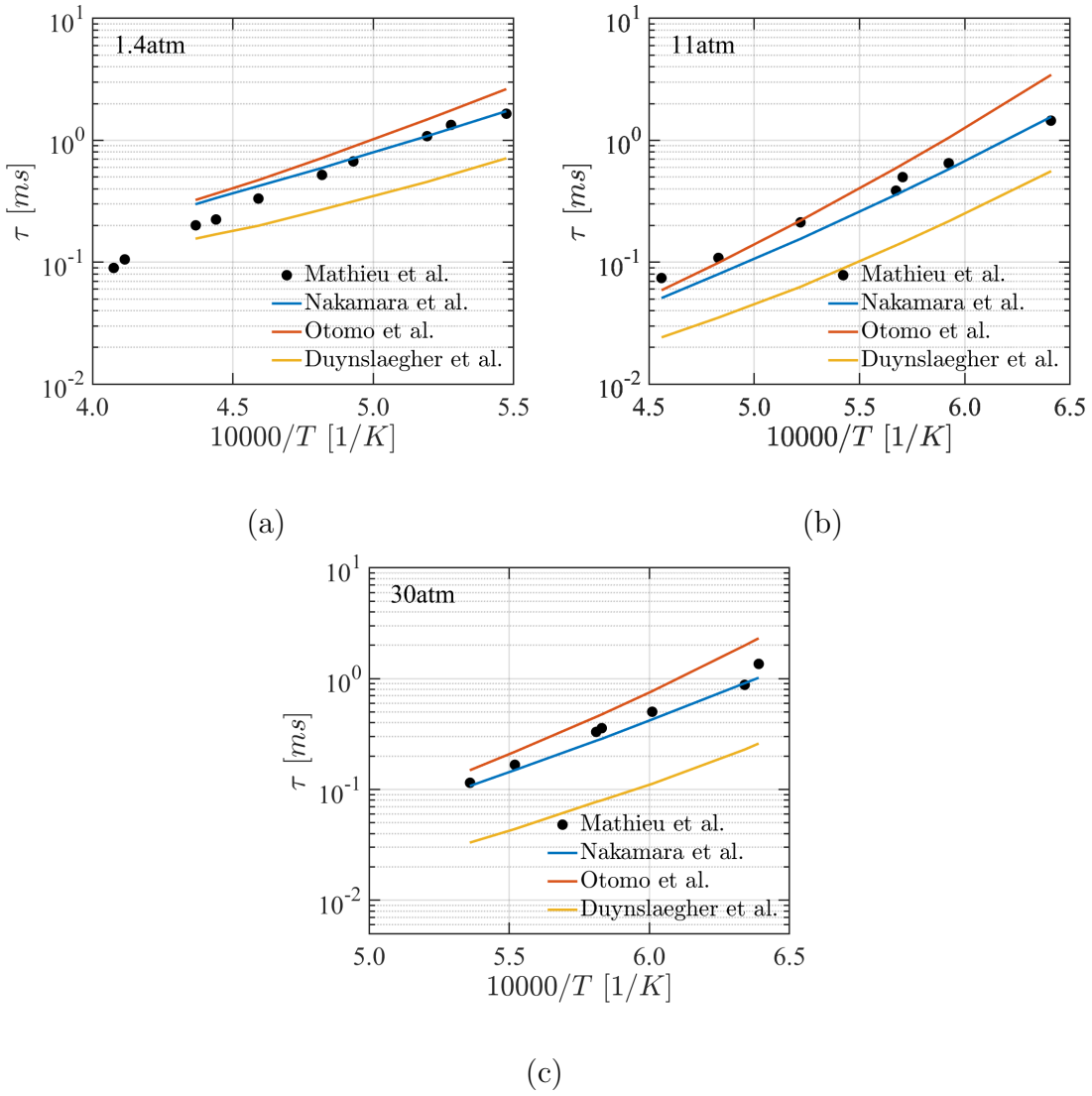


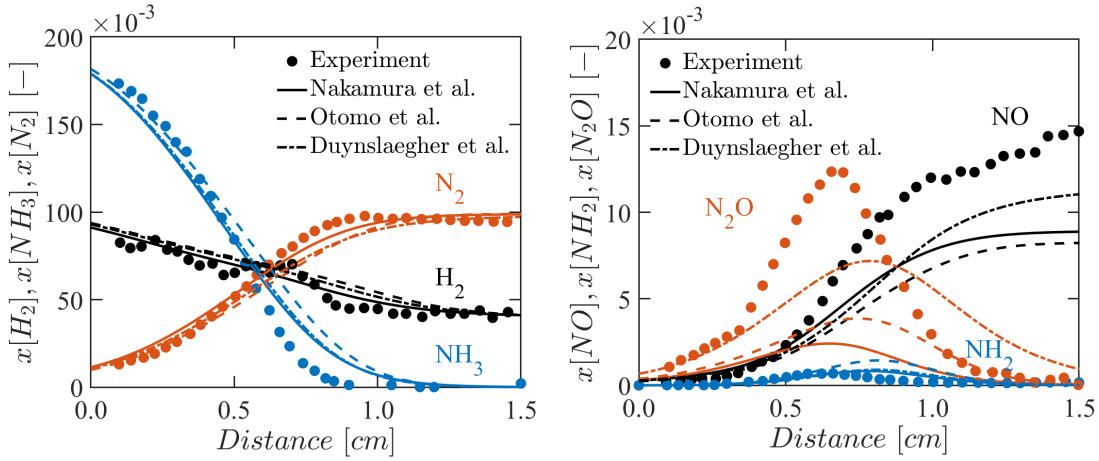
Figure 4.2: Comparison of experimental (symbols) and computational (lines) ignition delay time of $0.01143NH_3/0.00857O_2/0.98Ar$ ($\phi = 1.0$) under the pressure of (a) 1.4 atm, (b) 11 atm and (c) 30 atm. Experimental data in Mathieu's work [81] plotted in conjunction with computational results based on Nakamura's mechanism, Otomo's mechanism and Duynslaegher's mechanism.

surement [81] using shock tube was chosen. In Figure 4.2, the experimental ignition delay time (τ) of $NH_3/O_2/Ar$ blends was presented together with the computational results employing the three candidate mechanisms at $1.4, 11$ and 30 atm. In the experiment, the time period between the passage of the reflected

shock wave and the intersection of the slope of the hydroxyl radical (OH^*) with the zero concentration line was determined as the ignition delay time [81]. Figure 4.2 illustrates Nakamura's mechanism [84] predicts well with the measurements whereas the model based on Otomo's mechanism [86] is moderately overestimated. The computational results employing Duynslaegher's mechanism [73] exhibits a noticeable discrepancy between predictions and measurements. It is primarily due to the fact that the mechanism was initially validated by measurements conducted at low pressures.

Since flame structure have been seldom reported based on ammonia/hydrogen flame experiments, the measurements of premixed $0.21NH_3/0.13H_2/0.21O_2/0.45Ar$ flames at a low pressure (0.05 bar) using molecular beam mass spectrometry (MBMS) conducted by Duynslaegher *et al.* [74] are compared with the calculated computational results. As presented in Figure 4.3, the comparison illustrates the prediction of all three candidate mechanisms agrees well with the experimental data in terms of flame structure of NH_3, H_2 and N_2. By using Duynslaegher's mechanism, the most accurate agreement is achieved with the measured profiles of NO, N_2O and NH_2, although the peak concentrations of NO and N_2O still remain underestimated in the modeling.

Table 4.1 summarises the overall performance of three candidate ammonia mechanisms in the three aspects of ammonia oxidation chemistry. The computational results by employing Nakamura's and Otomo's mechanisms have a more satisfactory agreement with the experimental data in terms of laminar flame speed and ignition delay time in premixed NH_3/H_2 blends. Although there is a large discrepancy between the measured and computational ignition delay times, Duynslaegher's mechanism demonstrates better agreement than the other two candidate mechanisms in respect of flame structure. When compared to Otomo's



(a) (b)

Figure 4.3: Comparison of experimental (symbols) and computational (lines) concentration profiles of (a) NH_3, H_2, N_2 and (b) NO, NH_2, N_2O of $0.21NH_3/0.13H_2/0.21O_2/0.45Ar$ at 0.05 bar. Experimental data in Duynslaegher's work [74] plotted in conjunction with computational results based on Nakamura's mechanism, Otomo's mechanism and Duynslaegher's mechanism.

Table 4.1: Summary of candidate ammonia mechanisms validated with experimental data.

Mechanisms	**Laminar flame speed**	**Ignition delay**	**flame structure**
Duynslaegher's mechanism	↑†	↓	↑↑
Otomo's mechanism	↑	↑	↓
Nakamura's mechanism	↑	↑↑	↑

† The symbols ↑↑,↑,↓ indicate 'good agreement', 'acceptable discrepancy', and 'noticeable discrepancy', respectively.

mechanism, Nakamura's mechanism provides much better prediction in NO profile. Hence, Nakamura's detailed chemical kinetic reaction mechanism is chosen to further analyse premixed NH_3/H_2 flame under the prevalent operating envi-

ronment of free piston engines and gas turbines in the Section 4.3.4 and 4.4.

4.3 Parametric study

4.3.1 Laminar flame speed

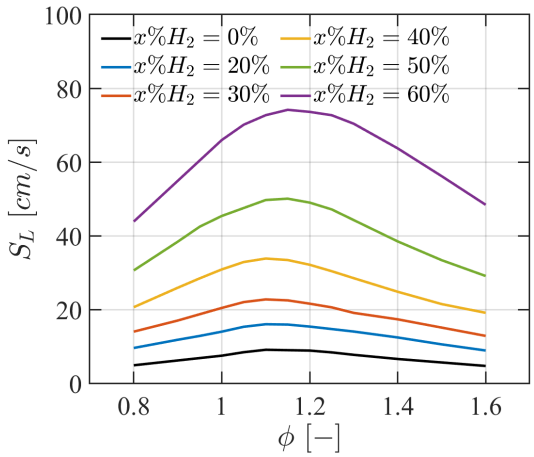


Figure 4.4: The function of laminar flame speed of premixed ammonia/hydrogen flame with equivalence ratios at various hydrogen blending ratios (T = 300 K, P = 1 bar).

The laminar flame speed (S_L) of premixed ammonia and hydrogen flames are plotted over a wide range of equivalence ratios and hydrogen blending ratios in Figure 4.4. Hydrogen has a much higher reactivity compared to ammonia. Additionally, hydrogen laminar flame speed can reach more than 250 cm/s under room temperature and pressure, while ammonia laminar flame speed was reported to be only 7 cm/s under the same conditions [72, 102, 177]. For these reasons, it was noticeable that the laminar flame speed of ammonia was enhanced substantially by introducing hydrogen into the fuel blends and is nonlinearly enhanced with the increase in the hydrogen blending ratio. Nevertheless, extreme high hydrogen blending ratio should be prevented and handled with caution in the practical combustor in the heat engine so that flashback of the boundary layer is avoided, as the high reactivity of hydrogen may lead to back-burning of the flame [62]. It can

be seen in Figure 4.4 that the relationship between premixed laminar flame speed of ammonia and hydrogen and the equivalence ratio is non-monotonic. For all the cases simulated at various hydrogen blending ratios, the laminar flame speed rises gradually under fuel-lean conditions, peaks when the equivalence ratio is about $1.1-1.2$, and then drops gradually under fuel-rich conditions. When 40% hydrogen is blended with ammonia fuel, the premixed laminar flame speed achieves about 34 cm/s with the equivalence ratio at 1.10, and this is comparable to the methane flame ($\sim$ 37 cm/s) under the similar condition [56]. It can be concluded that an equivalence ratio in the range of $1.1-1.2$ is preferable to the improvement of the robustness of premixed combustion of ammonia with hydrogen in the presence of a combustion promoter.

A sensitivity analysis was conducted at the location of the peak heat release rate and three elementary reactions, $NH_3+H \rightarrow NH_2+H_2, NH_3+OH \rightarrow NH_2+H_2O, NH_3+O \rightarrow NH_2+OH$, were found to take the lead in the early stage of ammonia decomposition. The finding aligns with Kumar's work [70] based on Konnov's mechanism [68] and Tian's mechanism [79]. Thus, the radical profiles of O, H, OH for different hydrogen blending ratios are investigated when the equivalence ratio is 1.1, as shown in Figure 4.5. The OH radical dominates in all four cases, indicating the important role of OH in the ammonia decomposition and laminar flame speed. It is also observed that when hydrogen is blended with ammonia, the peaks of all the radicals appear closer to the burner. The peak in Figure 4.5(a) is located at more than 1 cm from the nozzle, while the peaks in Figure 4.5(b)-(d) are located within 1 cm from the nozzle. The radical concentration of H, O and OH all increase with the increase of the hydrogen blending ratio, especially the H and OH radicals. Similar behaviour has been reported in the literature for lean flames and stoichiometric flames [70, 178].

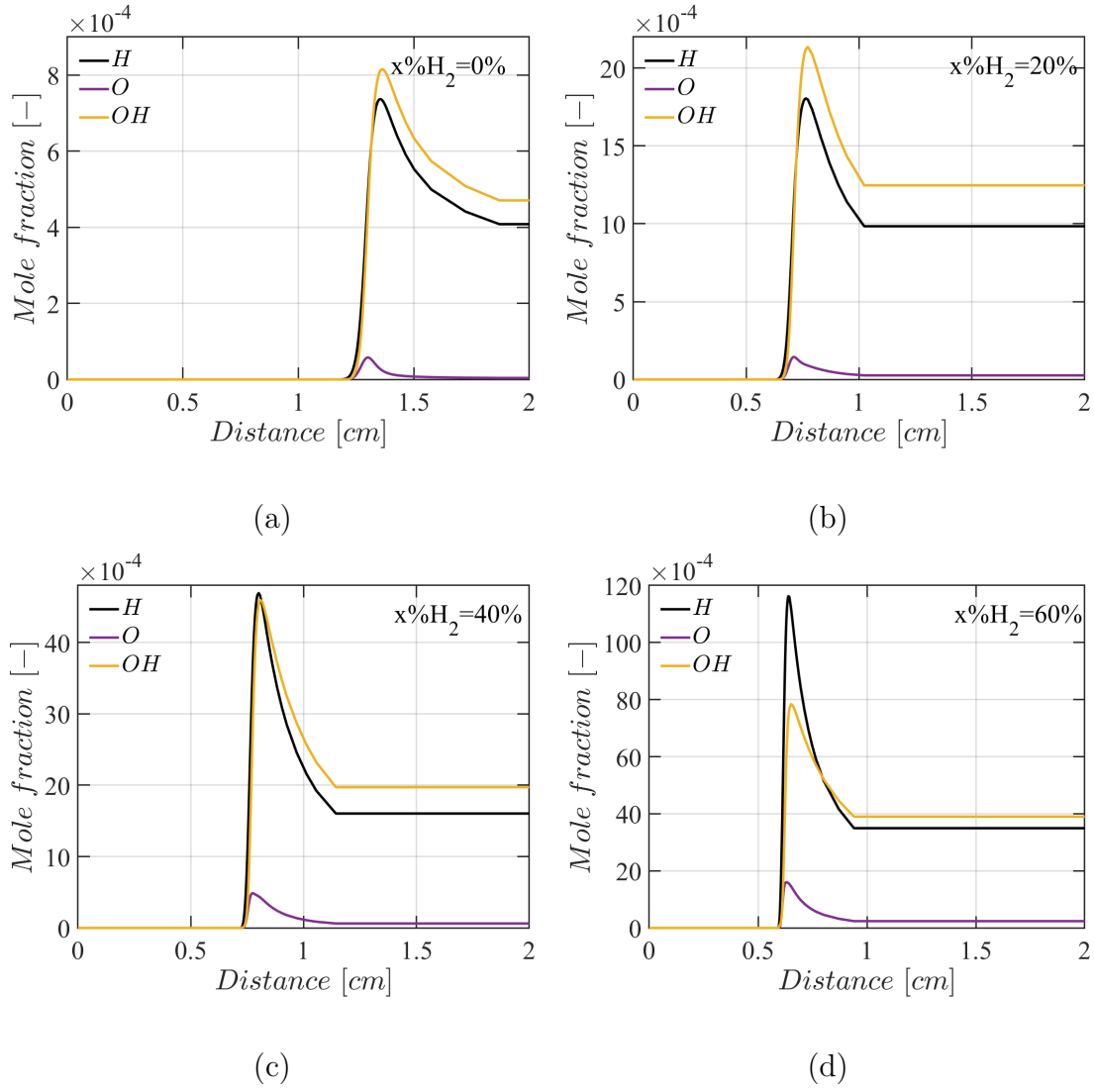


Figure 4.5: Radical profiles of O, H, OH at the equivalence ratio of 1.10 when $x\%H_2$ is (a) 0.0, (b) 0.2, (c) 0.4 and (d) 0.6.

A recent paper [179] demonstrated a clean power generation solution with water as the only reaction product by discussing the prospect of utilizing hydrogen-oxygen combustion in a closed-cycle free piston engine generator. In spite of the fact that ammonia/oxygen combustion cannot eliminate NO_x attributed to the unavoidable formation of fuel-bound NO, the oxygen enrichment imparts a significant benefit to the propagation speed of the ammonia flame. As shown in Figure

4.6, as the oxygen contents in the oxidant rises, the premixed laminar flame speed is increased for both neat ammonia flame and $70\%NH_3/30\%H_2$ flame. Oxygen enrichment is responsible for improving the adiabatic temperature and thus the combustion rate. The same tendency was also observed in the combustion of hydrocarbons [111, 114]. The intersection points in Figure 4.6 denote the value of the laminar flame speed of pure methane under the same working environment. It suggests that the equivalent laminar flame speed can be realised with a premixed neat ammonia flame at 60% oxygen content in the oxidant as well as with a premixed $70\%NH_3/30\%H_2$ flame at 30% oxygen content in the oxidant, indicating that the oxygen environment enables the ammonia and ammonia/hydrogen flames to be as stable as methane flames.

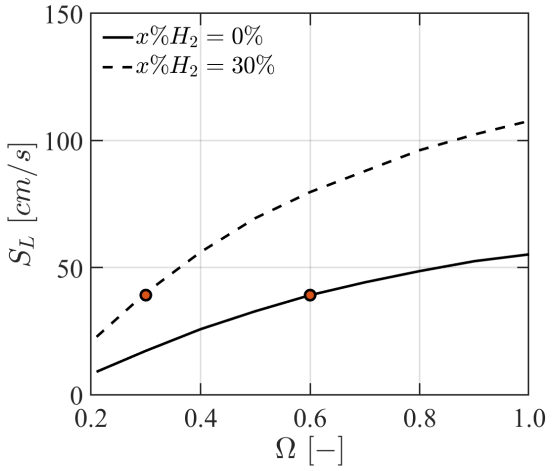


Figure 4.6: The function of laminar flame speed of premixed ammonia/hydrogen flame with oxygen contents in the oxidant (T = 300 K, P = 1 bar, ϕ = 1.10). Symbols represent the value of methane laminar flame speed.

The premixed laminar flame speed in relation to initial temperature for neat ammonia flame and $70\%NH_3/30\%H_2$ flame at various pressures is explored at an equivalence ratio of 1.10 to discover the ideal combustion conditions for the development of ammonia or ammonia/hydrogen fuelled free piston engines. Figure 4.7 reveals that both flame speed of premixed neat ammonia and ammonia/hydrogen

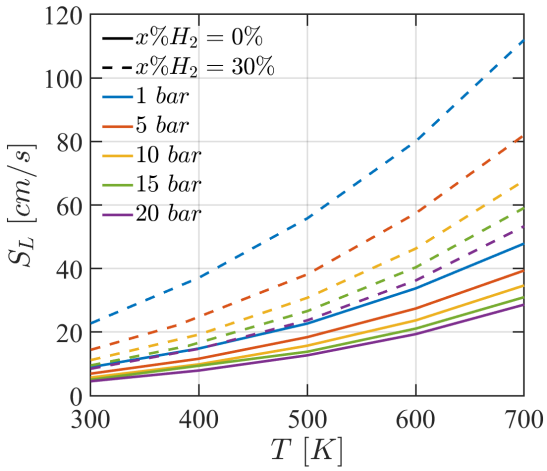


Figure 4.7: The function of laminar flame speed of premixed neat ammonia flame and ammonia/hydrogen flame with initial temperature at various pressure (ϕ = 1.10).

flames were promoted by increasing the initial temperature, which is attributed to the fact that temperature plays an important role in accelerating the rate of chemical reactions. For example, at 1 bar, with an increase in the initial temperature from 300 to 700 K, the premixed laminar flame speed of neat ammonia is improved by approximately 40 cm/s whereas that of $70\%NH_3/30\%H_2$ flame is improved by 90 cm/s. It implies an increase in the initial temperature at the outlet of the compressor in the free piston engines may boost the combustion rate, in particular when hydrogen is introduced as a promoter. In contrast, it is observed that pressure has a negative impact on the premixed laminar flame speed for both neat ammonia and ammonia/hydrogen flames. For instance, at the initial temperature of 700 K, the laminar flame speed of $70\%NH_3/30\%H_2$ flame drops by about 30 cm/s as the pressure is increased from 1 bar to 5 bar. However, it is notable that the negative effect of pressure is attenuated by comparing the reduction in laminar flame speed between $1-5$ bar and $5-10$ bar for both types of flames. The laminar flame speed seems to have less sensitivity to the pressure under high-pressure conditions. For the case of a free piston engine with external

combustor, the typical operating condition is at 15 bar and 600 K at the outlet of the compressor. It is feasible for a premixed $70\%NH_3/30\%H_2$ flame to burn at 40 cm/s. Although higher pressure contributes to the efficiency of the free piston engine, there may be a small penalty to the premixed laminar flame speed of ammonia/hydrogen blends.

4.3.2 Ignition delay time

The effects of hydrogen blending ratios ($0\%-100\%$) and equivalence ratios ($0.5, 1.0, 1.5$) on the ignition delay time (τ) of premixed neat ammonia and ammonia/hydrogen flame are shown in Figure 4.8. For a given equivalence ratio, a small hydrogen blending ratio in the range of $0\%-20\%$ facilitates an effective reduction in ignition delay time. For example, the ignition delay time decreases from $\sim 4 \times 10^{-3}$ s to $\sim 0.6 \times 10^{-3}$ s, when the hydrogen blending ratio increases from 0% to 20% under stoichiometric conditions. Nevertheless, the ignition delay exhibits a relatively small reduction with further hydrogen addition into the fuel blends. A sensitivity analysis of the OH radical at the moment of ignition was performed to evaluate the most relevant reactions to shorten the ignition delay time. Figure 4.9 shows the top five most relevant elementary reactions for reducing the ignition delay and top five most relevant elementary reactions for prolonging the ignition delay in the case of neat ammonia flame and $80\%NH_3/20\%H_2$ flame. The sensitivity coefficients of each elementary reactions are normalised to the value of $O_2+H \rightarrow O+OH$ due to the dominance of this reaction in both neat ammonia and $80\%NH_3/20\%H_2$ blends. It can be seen that the second sensitive reaction for promoting the ignition has changed from $NH_3 + NH_2 \rightarrow N_2H_3 + H_2$ to $H_2 + OH \rightarrow H + H_2O$ as hydrogen is involved. This indicates that hydrogen is rapidly consumed and H radical is generated, promoting the ignition of ammonia. On the other hand, the

elementary reactions of $NH_3 + H \rightarrow NH_2 + H_2$ and $NH_2 + NH_2 \rightarrow N_2H_2 + H_2$ that inhibit ignition become less sensitive in $80\%NH_3/20\%H_2$ blends, leading to the contribution of hydrogen addition to the ignition behaviour. Involving high reactive fuel compositions with ammonia can significantly reduce the ignition delay time, demonstrating the benefits of achieving strong ignition in heat engines.

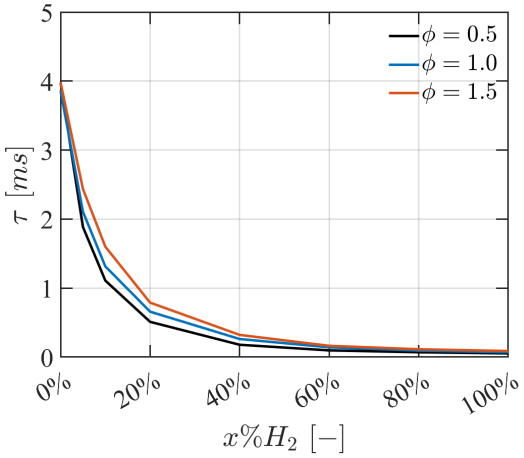
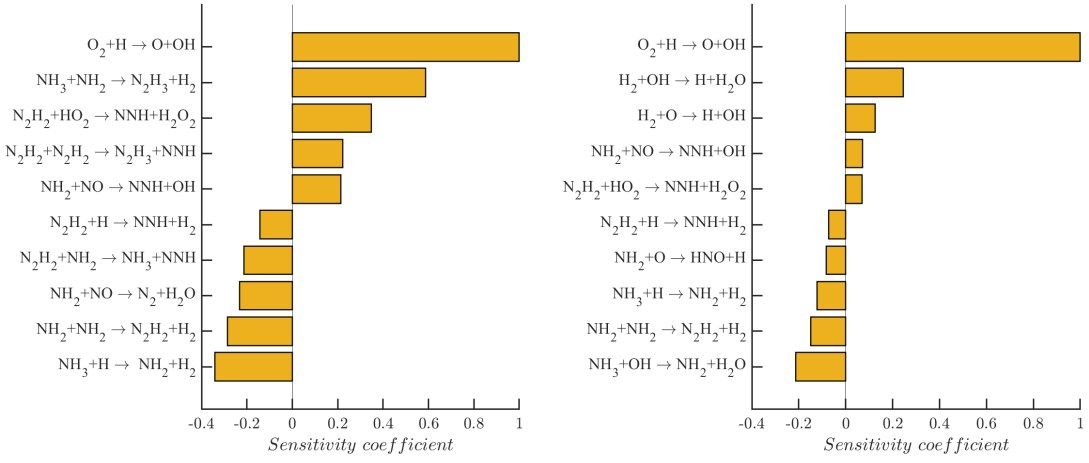


Figure 4.8: Variation of ignition delay time of premixed ammonia/hydrogen with hydrogen blending ratios at different equivalence ratios ($T = 1400$ K, $P = 1$ bar).

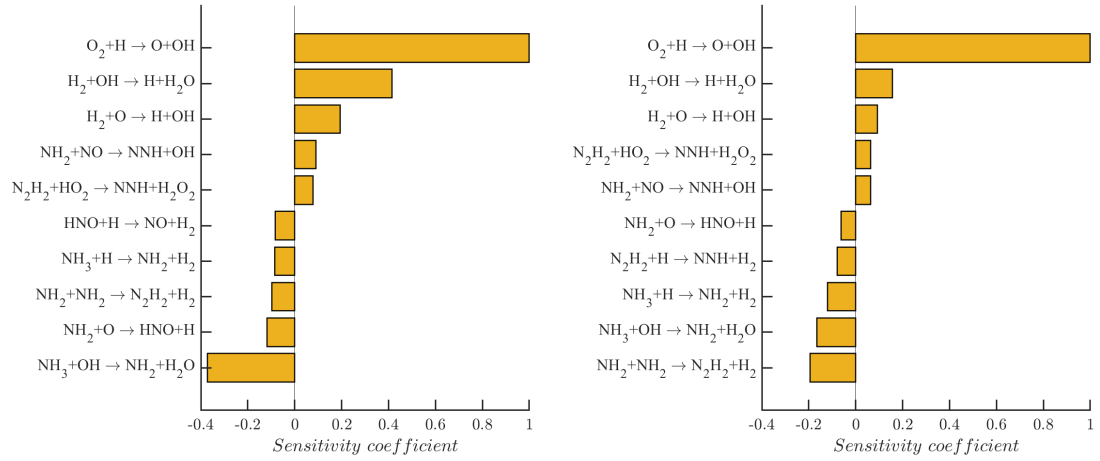


(a) (b)

Figure 4.9: Normalised sensitivity analysis of OH with (a) $x\%H_2 = 0\%$ and (b) $x\%H_2 = 20\%$ ($\Omega = 0.21, \phi = 1, T = 1400$ K, $P = 1$ bar).

Figure 4.8 also illustrates that for a given hydrogen blending ratio, the ignition delay time was more affected by the equivalence ratio when the hydrogen blending ratio is approximately 20%. As hydrogen blending ratio increases further, the effect of the equivalence ratio on ignition delay becomes less important. This result is in agreement with the findings reported by Mathieu *et al.* [81], who measured the ignition delay time for ammonia in highly diluted argon gas. A normalised sensitivity analysis is also conducted to explore the important elementary reactions affected by the equivalence ratios. Figure 4.10 exhibits the normalised sensitivity coefficients of OH at the equivalence ratio of 0.5 and 1.5 which represent a fuel-lean condition and a fuel-rich condition with hydrogen blending ratio at 20%. Under both conditions, the elementary reactions that are sensitive to the ignition delay are similar. The main elementary reactions that promote the ignition are $O_2 + H \rightarrow O + OH$ and $H_2 + OH \rightarrow H + H_2O$, while the main elementary reactions responsible for ignition inhibition are $NH_3 + OH \rightarrow NH_2 + H_2O$ and $NH_2 + NH_2 \rightarrow N_2H_2 + H_2$. In lean flames, the chain branching reaction $O_2 + H \rightarrow O + OH$ is facilitated when more oxygen is engaged, which accounts for the shortening of the ignition delay time at $\phi = 0.5$ as shown in Figure 4.8.

The function of the ignition delay time with oxygen contents in the oxidant is plotted at 1 bar and 20 bar in Figure 4.11. The result shows the ignition delay time for both neat ammonia flame and $70\%NH_3/30\%H_2$ flame is significantly shorter in oxygen-enriched environment and decreased with the increase of oxygen in the oxidant. As presented in Figure 4.12, the elementary reactions of $O_2 + H \rightarrow O + OH$ and $NH_3 + NH_2 \rightarrow N_2H_3 + H_2$ dominate in promoting the ignition of the flame. Similarly to the previous discussion, the elementary reactions of $NH_3 + H \rightarrow NH_2 + H_2$ and $NH_2 + NH_2 \rightarrow N_2H_2 + H_2$ were found to contribute considerably to the retardation of the ignition of ammonia flames in the presence



(a) (b)

Figure 4.10: Normalised sensitivity analysis of OH with (a) $\phi = 0.5$ and (b) $\phi = 1.5$ ($x\%H_2 = 0.2, \Omega = 0.21, T = 1400$ K, $P = 1$ bar).

of air and pure oxygen as oxidants. As the oxygen contents in the oxidant rises, it is noteworthy that the normalised sensitivity coefficients are increased for all the relevant elementary reactions, but the reactions that promote ignition tend to be more sensitive to the oxygen-enriched environment, for example, the sensitivity coefficient for the elementary reaction $NH_3 + NH_2 \rightarrow N_2H_3 + H_2$ increases from ~ 0.5 to ~ 0.8. Consequently, ignition delay time is reduced at oxygen-enriched environment. However, at atmospheric pressure, the reduction in ignition delay time is more attributable to the hydrogen blending ratio than to the oxygen enrichment. The ignition delay time of $70\%NH_3/30\%H_2$ flame at atmospheric pressure is almost comparable to 20 *bar* of neat ammonia. In a high-pressure environment, e.g. 20 bar, more oxygen involvement in the oxidant provides limited benefit for both neat ammonia flames and ammonia/hydrogen flames. Under standard operating conditions of free piston engines, the external combustor pressure stays in the range of $10 - 20$ bar, indicating that the increase in oxygen content in the oxidant have a limited beneficial effect on addressing the ignition delay of neat

ammonia and ammonia/hydrogen flames.

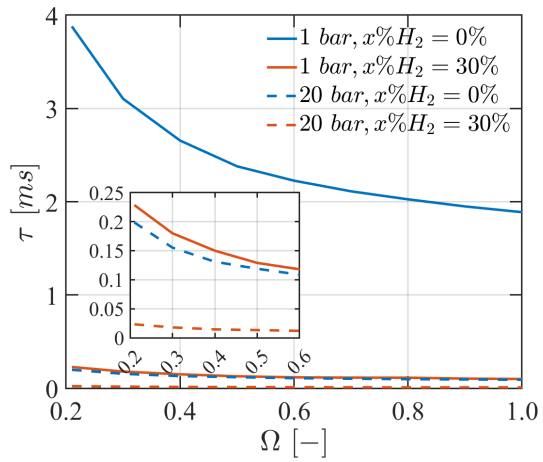
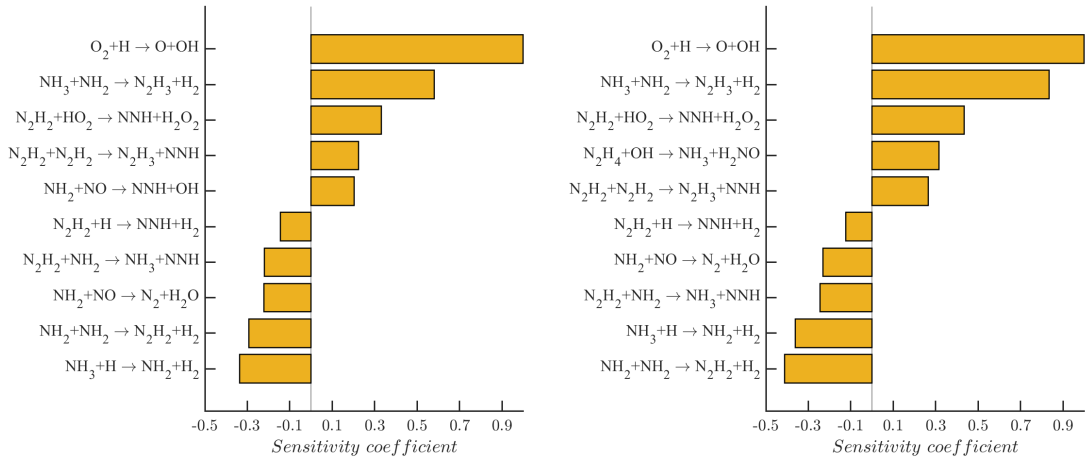


Figure 4.11: Variation of ignition delay time of premixed ammonia/hydrogen with oxygen contents in oxidant ($\phi = 1.10, T = 1400$ K).



(a) (b)

Figure 4.12: Normalised sensitivity analysis of OH with (a) $\Omega = 0.21$ and (b) $\Omega = 1.00$. ($x\%H_2 = 0.0, \phi = 1.1, T = 1400$ K, $P = 1$ bar).

Figure 4.13 illustrates the variation of ignition delay time with initial temperature in the range of $1040 - 1620$ K and pressure in the range of $1 - 20$ bar for neat ammonia flame and $70\%NH_3/30\%H_2$ flame at an equivalence ratio of 1.10. Improving the initial temperature and pressure enables the reduction of the igni-

tion delay time for both types of flame. The impact of pressure on ignition delay, however, decreases as the pressure increases. Taking the case of $70\%NH_3/30\%H_2$ flame as an example, a factor between 1 bar and 5 bar (τ_{1bar}/τ_{5bar}) is about 4.7 at an inlet temperature of 1800 K ($10000/T = 5.56$), over twice as much as the factor between 5 bar and 10 bar ($\tau_{5bar}/\tau_{10bar} \sim 1.9$). It reveals that inlet pressure variations from $1-5$ bar have a significant effect on shortening ignition delay. As the pressure continues to increase, the ignition delay is only marginally reduced.

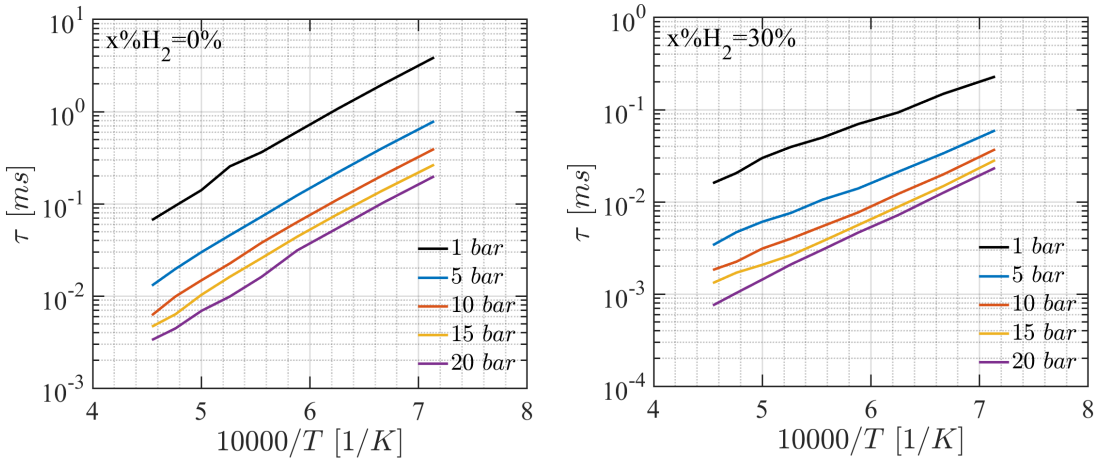


Figure 4.13: Ignition delay time of premixed ammonia/hydrogen with various initial temperature and pressure at (a) $x\%H_2 = 0\%$ and (b) $x\%H_2 = 30\%$. ($\Omega = 0.21, \phi = 1.1$).

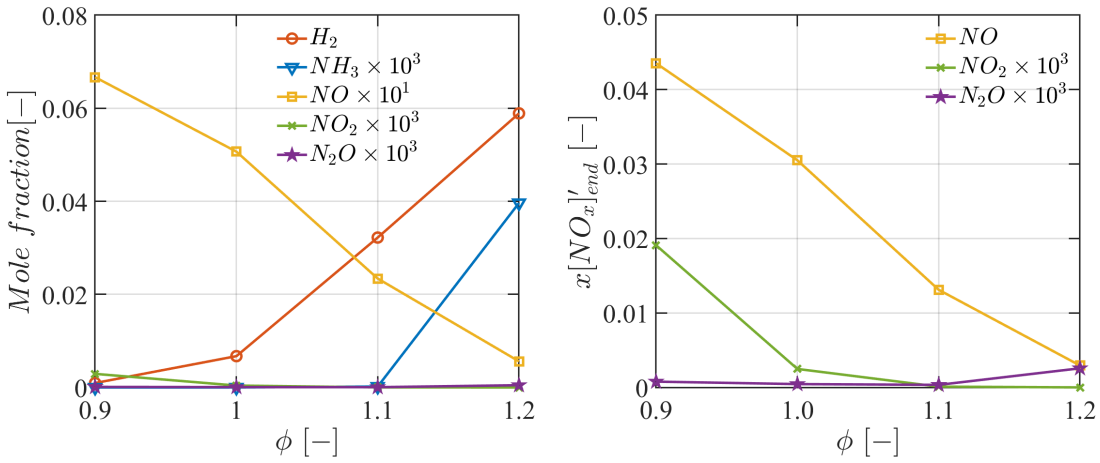
4.3.3 Flame structure

NO_x emissions are a major concern associated with heat engines powered by ammonia fuel. It is interesting to gain the knowledge of how the fuel-bound NO_x pathways brought about by ammonia fuel and the thermal-NO_x pathways induced by high temperature due to hydrogen involvement affect NO_x formation and consumption at various component mixing ratios and operating environment.

This section discusses concentration of key species profiles derived from the model and the rate of production (ROP) analysis to gain insights into species formation and consumption.

As shown in Figure 4.14(a), the emission concentrations of key species, $NH_3, H_2, NO, NO_2, N_2O$, are analysed over a wide range of equivalence ratios $(0.9 - 1.2)$ with 30% hydrogen involvement in the fuel blends. Table 4.2 exhibits the inlet component concentrations in detail. NO_2 and N_2O concentrations at the post-flame zone are found to be almost zero, but NO concentration at the post-flame zone dominates NO_x emission in ammonia/hydrogen flames, which shows the identical tendency as hydrocarbon flames [180]. With an increase in the equivalence ratio from 0.9 to 1.2, NO emission reduces dramatically, especially when the equivalence ratio is slightly greater than unity. Furthermore, Figure 4.14(a) illustrates that hydrogen emission rises substantially at fuel-rich conditions and ammonia slip starts to increase as the equivalence ratio exceeds 1.1, which is attributed to the incomplete combustion. A trade-off needs to be taken into account to avoid excessive unburnt hydrogen and ammonia in a rich flame and high NO_x emission in a lean flame. Thus, it is noted that an equivalence ratio in the range of $1.0 - 1.1$ is preferable for emission minimization. The recognized range of equivalence ratio is also consistent with the aforementioned recommendation of analysis on combustion robustness (Figure 4.4, section 4.3.1). In addition, it can be seen from Table 4.2 that the concentration of ammonia at the inlet varies as hydrogen blending ratio and oxygen content in the oxidant stay unchanged. Normalised NO_x emission is therefore determined by dividing the NO_x concentration at exhaust by the inlet amount of ammonia so that the impact of different inlet ammonia amounts on NO_x emission can be prevented in the analysis. The normalised NO_x emission is shown in Figure 4.14(b), finding normalised NO is

evidently reduced at the rich flames.



(a) (b)

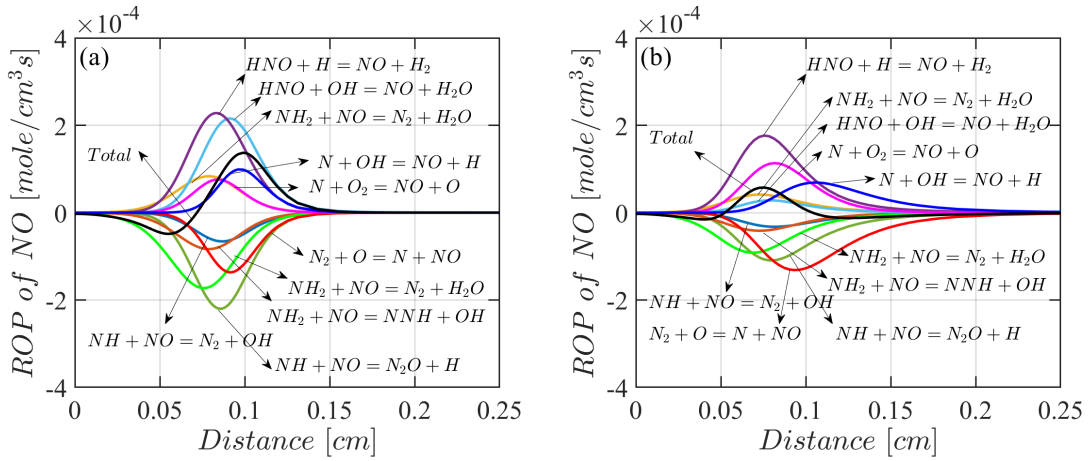
Figure 4.14: (a) $NH_3, H_2, NO, NO_2, N_2O$ emissions and (b) normalised NO_x emission as a function of equivalence ratios for a $70\%NH_3/30\%H_2$ flame ($T = 500$ K, $P = 1$ bar).

Table 4.2: Inlet components with different equivalence ratios for a $70\%NH_3/30\%H_2$ flame.

Case	$\boldsymbol{\phi}$	$\boldsymbol{x\%H_2}$	$\boldsymbol{\Omega}$	$\boldsymbol{x[NH_3]}$	$\boldsymbol{x[H_2]}$	$\boldsymbol{x[O_2]}$	$\boldsymbol{x[N_2]}$
1	0.9			0.15	0.07	0.16	0.62
2	1.0	30%	0.21	0.17	0.07	0.16	0.60
3	1.1			0.18	0.08	0.16	0.59
4	1.2			0.19	0.08	0.15	0.58

A ROP analysis is carried out for NO at the equivalence ratios of 0.9 and 1.2 that denote the fuel-lean conditions and fuel-rich conditions, respectively. Figure

4.15(a) shows that, under the fuel-lean conditions, fuel-bound NO ($HNO + H \rightarrow NO + H_2, HNO + OH \rightarrow NO + H_2O$) is the major method compared to thermal-NO method in NO generation pathways, while the primary NO consumption is via the reactions with NH_i (NH, NH_2) and partly via the reverse reaction of Zeldovich mechanism ($N_2 + O \rightarrow NO + N$). Under the fuel-rich conditions, the decline of fuel-bound NO and the increase in thermal-NO in NO generation is shown in Figure 4.15(b). Meanwhile, NO is primarily consumed by the reverse reaction of Zeldovich mechanism. This result is in agreement with a recent study showing that the contribution of NH_i oxidation to NO production via HNO is suppressed due to the decline of $O/H/OH$ radicals in the rich flame [43]. In addition, the reaction between NH_i and H is facilitated with the growth of H concentration in the rich flame, yielding a large amount of nitrogen atoms (N), which in turn encourages the NO consumption by the reverse reaction of Zeldovich mechanism. Consequently, NO emission falls under the fuel-rich conditions, which assists in explaining the behaviour of NO concentration at the post-flame zone presented in Figure 4.14(a).



(a) (b)

Figure 4.15: ROP analysis for NO at the equivalence ratio of (a) 0.9 and (b) 1.2.

Figure 4.16(a) illustrates the key species concentrations at the post-flame zone of ammonia/hydrogen combustion versus a variety of hydrogen blending ratios. The inlet component concentrations are exhibited in Table 4.3. When hydrogen involvement rises in the fuel blends, NO emission tends to increase moderately, and the amount of hydrogen residuals at the exhaust stays almost identical. NO_x emission is normalised to the same inlet ammonia concentration for further analysis. As can be seen in Figure 4.16(b), there is a pronounced growth in the normalised NO emission owing to the decline in the amount of ammonia at the inlet calculated in Table 4.3. Figure 4.17 and Figure 4.18 illustrate the ROP for NO and H_2. Figure 4.17 shows that the production rates of both fuel-bound NO and thermal-NO are promoted with an increase in hydrogen blending ratio, while NO is strongly consumed by thermal-NO ($N_2 + O \rightarrow N + NO$). The high consumption rate of NO via thermal-NO is dynamically balanced with the production rate via fuel-bound NO and thermal-NO. As a result, only a moderate growth in NO emission is observed. Figure 4.18 depicts that the primary hydrogen formation is through the reactions of $NH_i(NH_3, NH_2, NH, N_2H_2) + H$, NH_i (e.g.$NH_2 + NH_3, NH_2 + NH_2$) as well as $HNO + H$ while the primary hydrogen depletion is through the hydrogen oxidation ($H_2 + O$ and $H_2 + OH$). The rise of hydrogen blending ratio promotes the oxidation of hydrogen, in particular the reaction of $H_2 + OH \rightarrow H + H_2O$. As a result, when the hydrogen blending ratio increases, the unburnt hydrogen at the exhaust remains almost unchanged at the equivalence ratio of 1.1.

The key species concentrations at the post-flame zone of $70\%NH_3/30\%H_2$ flames with various oxygen contents in the oxidant are presented in Figure 4.19(a). Table 4.4 lists the detailed inlet components. There is an increasing trend of NO emission as more nitrogen in the oxidant is substituted by oxygen. According

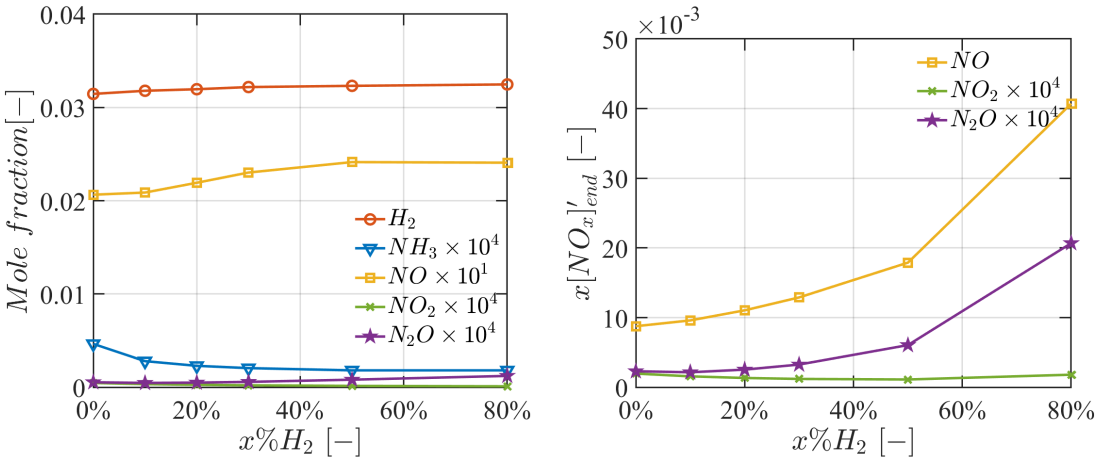


Figure 4.16: (a) $NH_3, H_2, NO, NO_2, N_2O$ emissions and (b) normalised NO_x emission as a function of hydrogen blending ratios ($\phi = 1.1,\ T = 500$ K, $P = 1$ bar).

Table 4.3: Inlet components with hydrogen blending ratios when $\phi = 1.1$.

Case	$\boldsymbol{\phi}$	$\boldsymbol{x\%H_2}$	$\boldsymbol{\Omega}$	$\boldsymbol{x[NH_3]}$	$\boldsymbol{x[H_2]}$	$\boldsymbol{x[O_2]}$	$\boldsymbol{x[N_2]}$
1	1.1	0%	0.21	0.24	0.00	0.16	0.60
2		10%		0.22	0.02	0.16	0.60
3		20%		0.20	0.05	0.16	0.59
4		30%		0.18	0.08	0.16	0.59
5		50%		0.13	0.13	0.15	0.58
6		80%		0.06	0.24	0.15	0.56

to the ROP analysis illustrated in Figure 4.20, the major pathways of production and depletion of nitric oxide are found to be the same when the oxygen

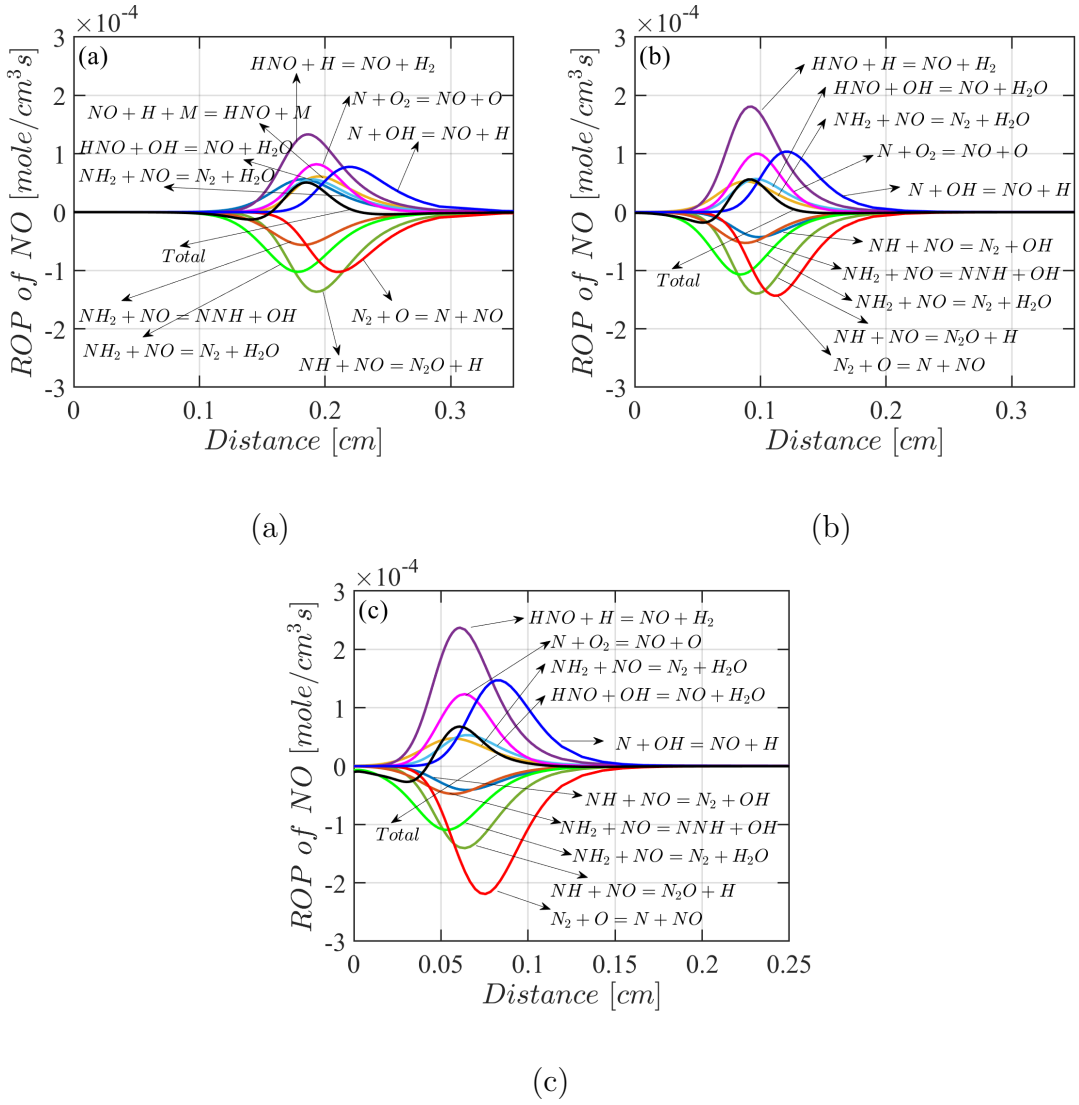


Figure 4.17: ROP analysis of NO at the hydrogen blending ratios of (a) 0.0, (b) 0.2 and (c) 0.5.

contents in the oxidant is at 0.21 (air) and 1.00 (pure oxygen). Fuel-bound NO ($HNO + H \rightarrow NO + H_2$) plays an important role in generation of nitric oxide, while thermal-NO ($N_2 + O \rightarrow N + NO$) dominates in the depletion of nitric oxide. However, it is worth noting that the rates of both generation and depletion are nearly doubled when pure oxygen is employed as the oxidizing agent compared to employing air as the oxidizing agent for the flame. As can be seen from Table

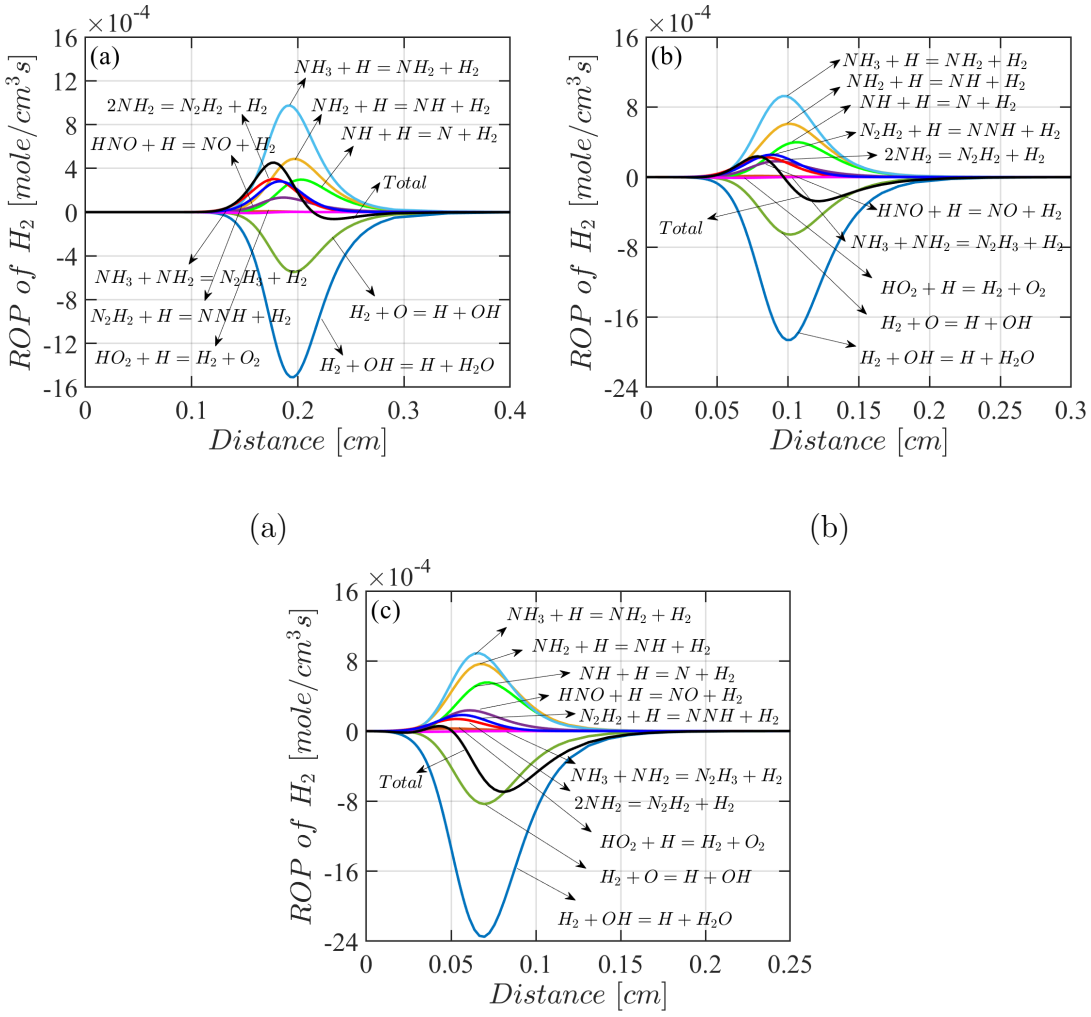
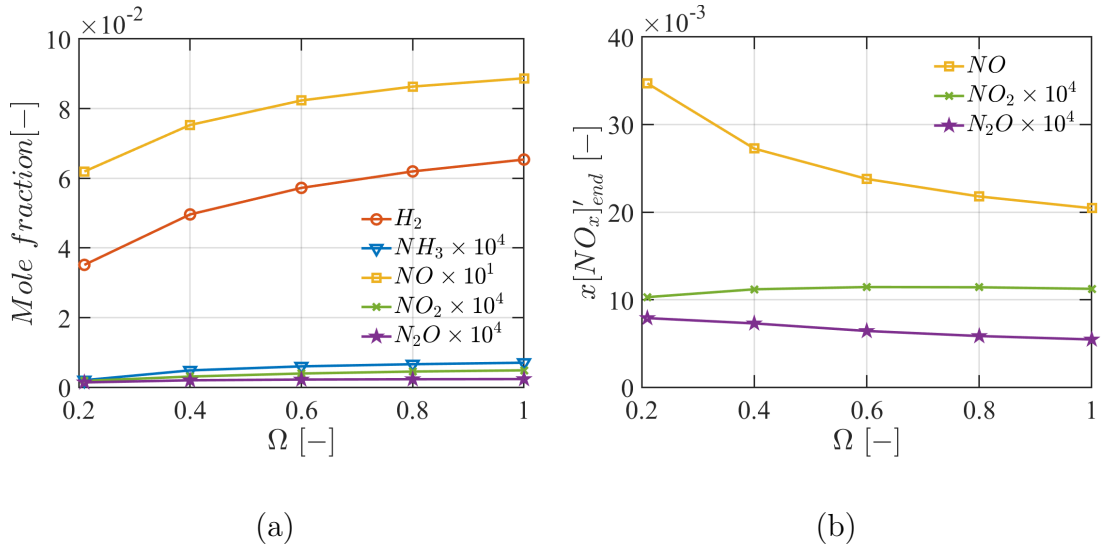


Figure 4.18: ROP analysis of H_2 at the hydrogen blending ratios of (a) 0%, (b) 20% and (c) 50%.

4.4, when keeping the equivalence ratio and hydrogen blending ratio constant, the ammonia concentration at the inlet varies with the rise of oxygen content in the oxidant. It explains the decreasing behaviour of normalised NO emission presented in Figure 4.19(b). It is concluded that the rise in absolute NO emissions is attributed to the offsetting effect of NO formation and depletion, while the decrease in normalised NO emission is the result of an increase in ammonia

concentration in the fuel blends as the denominator corresponding to an increase in oxygen concentration in the oxidant in order to maintain the same equivalence ratio. Besides, Figure 4.19(a) reveals that absolute NO_2 and N_2O emissions are also increased by introducing more oxygen contents in the oxidant. However, the variation of normalised emissions in Figure 4.19(b) indicate the additional oxygen contents in the oxidant provides limited benefit for the normalised NO_2 but it reduces the normalised N_2O emission.



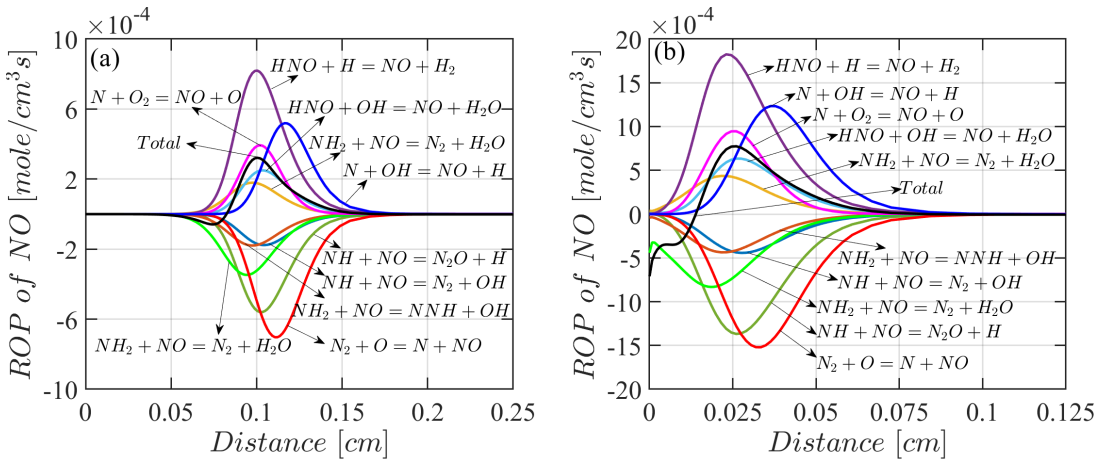
(a) (b)

Figure 4.19: (a) $NH_3, H_2, NO, NO_2, N_2O$ emissions and (b) normalised NO_x emission as a function of oxygen contents in the oxidant for a $70\%NH_3/30\%H_2$ flame ($\phi = 1.1, T = 500$ K, $P = 1$ bar).

The key flame species under various pressures up to 20 bar were compared, taking into account the high-pressure operating conditions of heat engines. Figure 4.21 shows the change in the concentration of key species at the post-flame zone with a variety of pressures when the initial temperature is 600 K and the equivalence ratio is 1.1. A pronounced trend is observed that NO emission reduces with an increase in the pressure. The variation is more evident when the pressure rises from 1 bar to 10 bar than when it rises from 10 bar to 20 bar. There is a similar

Table 4.4: Inlet components at different oxygen contents in the oxidant for a $70\%NH_3/30\%H_2$ flame.

Case	ϕ	$x\%H_2$	Ω	$x[NH_3]$	$x[H_2]$	$x[O_2]$	$x[N_2]$
1			0.21	0.18	0.08	0.16	0.59
2			0.4	0.28	0.12	0.24	0.36
	1.1	30%					
3			0.6	0.35	0.15	0.30	0.20
4			0.8	0.40	0.17	0.35	0.09
5			1	0.43	0.19	0.38	0.00



(a) (b)

Figure 4.20: ROP analysis of NO with oxygen content in the oxidant at (a) 0.21 and (b) 1.00 ($T = 500$ K, $P = 1$ bar).

behaviour discovered in the study on premixed ammonia/methane combustion [57]. Kobayashi *et al.* [43] reported that the reason is that the combination reaction of NH_i radical is promoted at high-pressure conditions (or for rich flames),

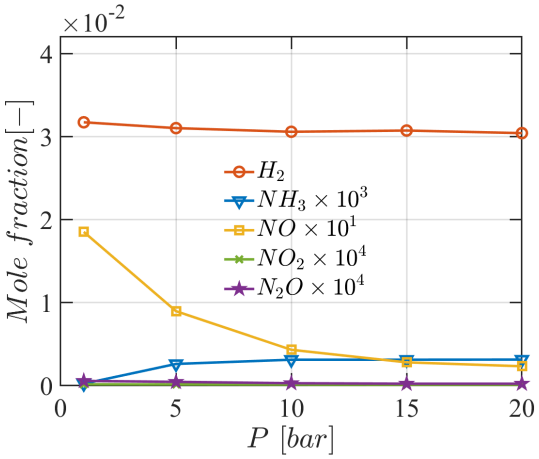


Figure 4.21: $NH_3, H_2, NO, NO_2, N_2O$ emissions as a function of pressures for a $70\%NH_3/30\%H_2$ flame ($\phi = 1.1, \Omega = 0.21, T = 600$ K).

facilitating the yield of nitrogen rather than nitric oxide, which results in the NO concentration decrease at the exhaust. This finding indicates that co-firing with ammonia and hydrogen is also favoured in terms of minimizing emissions under the typical high pressure operating conditions of a heat engine.

4.3.4 Selected parameters for the external combustor of the free piston engine

A comprehensive analysis on how various compositions and operational conditions affect ammonia and ammonia/hydrogen combustion has been carried out. A general recommendation for achieving a reliable, efficient and environmentally friendly operation of ammonia and hydrogen fuelled free-piston engines are proposed with a focus on improving the robustness of ammonia/hydrogen combustion and minimizing NO_x emissions. The laminar flame speed of methane flames (~ 37 cm/s) serve as a benchmark for ammonia flames with the enhancement of promoter and beneficial working conditions. Hydrogen is regarded as an enhancer for ammonia flames and the laminar flame speed of ammonia/hydrogen flame can be readily increased to more than 37 cm/s due to the high laminar flame speed of

hydrogen. Nevertheless, when using high hydrogen blending ratios, it is necessary to adopt high-performance, high-quality catalysts for in-line cracking of ammonia, or a separate hydrogen fuel supply line. Hydrogen involvement should also be taken into account with other parameters, for example, equivalence ratios, initial temperature and pressures in order to facilitate the ammonia/hydrogen flame stability in a cost-effective way. An equivalence ratio in the range of $1.1 - 1.2$ is discovered to be favourable for improving the laminar flame speed of premixed ammonia/hydrogen in majority of cases. Regarding the initial temperature and pressure of ammonia/hydrogen combustor, they are not completely independent parameters and are mainly associated with thermodynamic parameters at the compressor outlet in free piston engines. The laminar flame speed of premixed ammonia and hydrogen is monotonically improved by increasing the initial temperature, but it is suppressed with increasing pressure. It is shown in Figure 4.7 that over 40 cm/s of laminar flame speed can be realized for a $70\%NH_3/30\%H_2$ premixed flame with the equivalence ratio at 1.1 under the typical outlet condition of compressor in the free piston engine (600 K, 15 bar). This meets the requirement of ammonia/hydrogen combustor stability in producing a reliable flame. The oxygen-enriched environment also shows a considerable beneficial impact on the laminar flame speed, which is likely to require a thorough economic analysis to provide a more affordable viable solution. Additional attention of ignition delay and emissions should be given to identify an all-round solution.

With respect to ignition delay, as discussed in Section 4.3.2, hydrogen blending ratio at 20% already greatly shortens the ignition delay time, let alone further increase hydrogen blending ratio to 30%. The standard operational environment of the free piston engine, i.e. 15 bar from the outlet of the compressor (inlet of the external combustor) significantly promotes the ignition process and reduce the

ignition delay time of the premixed ammonia and hydrogen combustion. Jointly, the short ignition delay can also be satisfied under the aforementioned conditions, namely, hydrogen blending ratio at 30%, equivalence ratio at 1.1 and under 15 bar pressure.

From the discussion in Section 4.3.3, there are complex synergistic impacts of various parameters on the flame structure, notably the NO_x emissions are of most concern. In almost all studies on ammonia combustion, equivalence ratios slightly above 1, such as $1.0 - 1.1$, have been broadly recommended. NO_x formation is easily inhibited under fuel-rich conditions, but the rapid growth in the concentration of unburnt hydrogen is undesirable for free piston engines, where multi-zone combustors may be involved, which potentially result in a high NO_x emission in total. Furthermore, ammonia slip is another problem when burning flames at a very high equivalence ratio if the external combustor of the free piston engine is not of optimum design. Accordingly, the moderate equivalence ratio at 1.1, chosen considering the ammonia flame stability, is also preferable in terms of emissions. When it comes to hydrogen blending ratios, 30% is considered as a satisfactory value, because further addition would cause an intensification of thermal-NO formation and ultimately push up NO emission as illustrated in Figure 4.16(a). In addition to the equivalence ratio and hydrogen blending ratio, the most critical parameters governing the emissions are the oxygen contents in the oxidant and the pressure of the combustor. NO_x emission is found to be suppressed in a pressure-elevated environment. In spite of the surge in the absolute NO_x emission with a higher oxygen content in the oxidant, the normalised NO and N_2O emissions are reduced in Figure 4.19(b). After undertaking further research into the economic feasibility of free piston engine, an intermediate oxygen content in the oxidant at 30% is chosen.

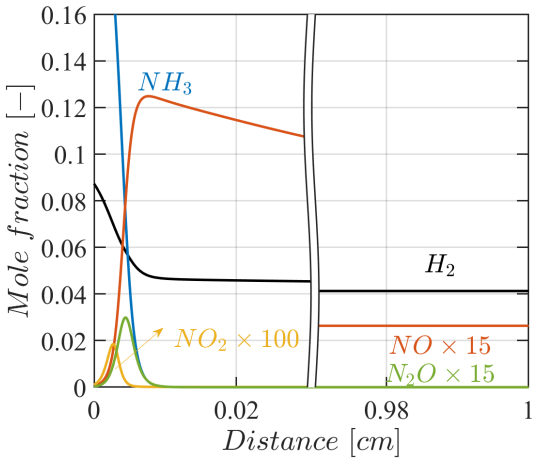


Figure 4.22: Major species concentration under rated operation condition of free piston engines ($30\%H_2/70\%NH_3$, $\Omega = 0.3$, $\phi = 1.1$, $T = 600$ K, $P = 15$ bar).

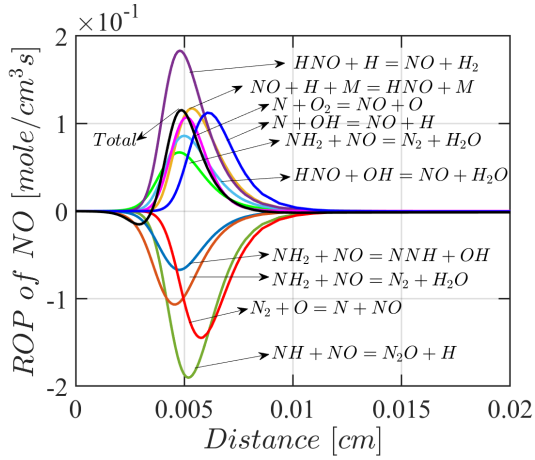


Figure 4.23: ROP analysis of NO under rated operation condition of free piston engines ($30\%H_2/70\%NH_3$, $\Omega = 0.3$, $\phi = 1.1$, $T = 600$ K, $P = 15$ bar).

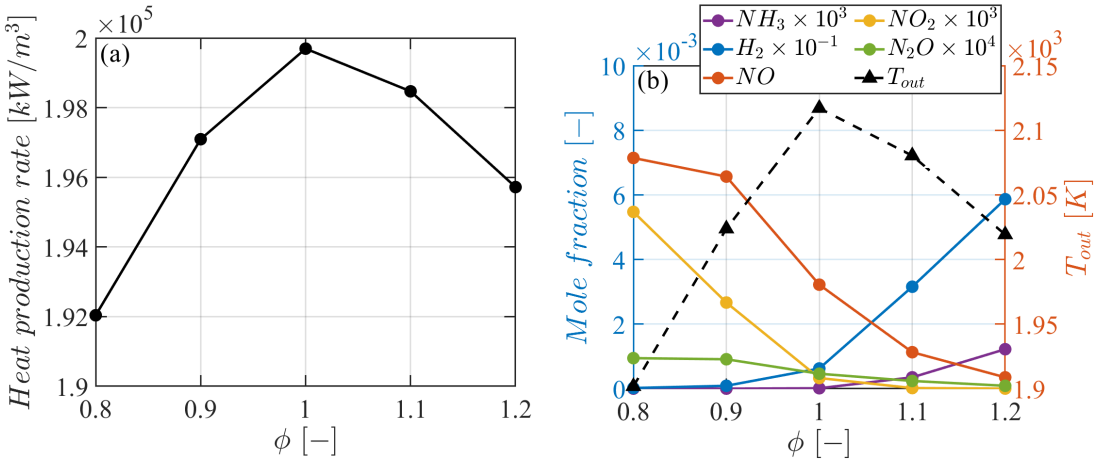
Figure 4.22 shows the species profiles of $NH_3, H_2, NO, NO_2, N_2O$ based on the ideal component ratios selected from the above analysis and typical working conditions of free piston engines ($T = 600$ K, $P = 15$ bar). The emissions are controlled at acceptable levels. The hydrogen concentration at the post-flame zone and NO emission are about 4.1% and 1700 ppmv, respectively. Meanwhile, the concentration of NO_2, N_2O at the exhaust and ammonia slip are very small and negligible. Figure 4.23 shows the ROP of nitric oxide, finding that both the

generation and depletion of NO are driven by fuel-bound NO reactions (reaction with HNO or NH). The component ratios selected are expected to provide important guidance for the development and optimization of ammonia/hydrogen combustors at high pressures in free piston engines. The discovery of the effects of a variety of component ratios and operating conditions on ammonia/hydrogen flames with respect to the laminar flame speed, ignition delay time and flame structure demonstrates a valuable reference for the design of other types of combustors.

4.4 Modelling of premixed ammonia and hydrogen combustion in generic gas turbine

The gas turbine model and detailed case worksheet have been shown in Section 3.2.4, Chapter 3. The model is calculated using the selected ammonia mechanism, Nakamura's mechanism [84], discussed in Section 4.2, Chapter 4. Figure 4.24 shows the effect of equivalence ratios on peak heat production rate, outlet temperature and emissions ($NH_3, H_2, NO, NO_2, N_2O$). The relationship between the peak heat production rate of premixed ammonia and hydrogen combustion in the gas turbine and the equivalence ratios is non-monotonical. The maximum value of peak heat production rate occurs under the stoichiometric condition. The same trend is also found in the analysis for the outlet temperature. The main reason is that the flame speed reached maximum near the stoichiometric condition and it has a decisive influence on the heat production rate and temperature. In Figure 4.24(b), as the equivalence ratio increases, NO_x emissions are reduced, while the ammonia slip and hydrogen residual are increased due to the incomplete combustion in the rich flames. As concluded in Section 4.3.3 that thermal-NO has significant effect on the formation and consumption of nitric oxide in rich

flames, comparing to the fuel-bound NO method. The greater rate of consuming nitric oxide via NH_i and N lead to the drop in NO emission. However, the combustion efficiency is compromised by a considerable amount of ammonia slip and hydrogen residuals at the exhaust, so it is not suggested to apply very high equivalence ratios. In the range of $0.8 - 1.2$, given that NO_x emissions in lean flames are dramatically higher than that in rich flames, an equivalence ratio of 1.1 is considered for further analysis in this section. Jointly, the peak heat production rate and outlet temperature are also relatively high when the equivalence ratio is at 1.1, which can improve the efficiency of the gas turbine.



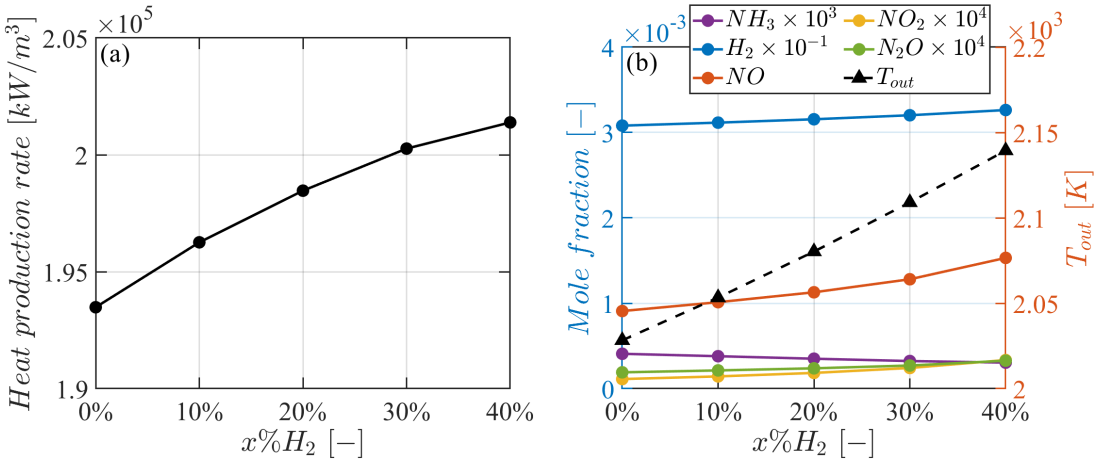
(a) (b)

Figure 4.24: Variations of (a) peak heat production rate and (b) outlet temperature and emissions with different equivalence ratios. ($80\%NH_3/20\%H_2, \Omega = 0.21, T_1 = 300$ K, $P_1 = 1$ bar)

It is known that hydrogen addition and oxygen enrichment are effective ways to improve the flame speed and adiabatic temperature of ammonia flames, which contribute to enhance the robustness of ammonia combustion. The effects of hydrogen blending ratios in the range of $0 - 0.4$ and oxygen contents in the oxidant in the range of $0.21 - 1.00$ on ammonia/hydrogen combustion characteristics in a

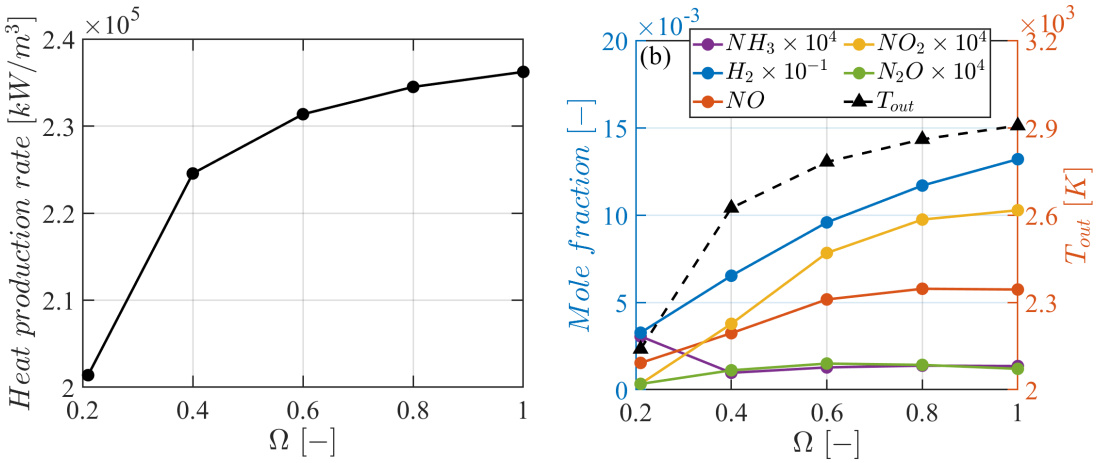
generic gas turbine are shown in Figure 4.25 and Figure 4.26. It is found that either increasing the hydrogen blending ratio or oxygen content in the oxidant promotes the chemical reaction speed, leading to the increase in the peak heat production rate and outlet temperature. Figure 4.25(b) illustrates that there is a slight increase trend in NO_x emission with more hydrogen addition. The temperature is improved significantly owing to the hydrogen involvement. Thermal-NO_x becomes dominant in the production and consumption of NO_x. The increased NO_x emission implies that there is a higher production rate of NO_x than consumption rate of NO_x. Jointly it is recommended to blend 40% hydrogen into the fuel, in consideration of the robustness of the flame, even though the addition of hydrogen will result in more NO_x emissions. Figure 4.26(b) depicts the emission characteristics of a $60\%NH_3/40\%H_2$ flame in a gas turbine under the enriched oxygen environment. It is shown that the highest ammonia slip is emitted when the oxidant is air ($\Omega = 0.21$). When the oxygen content in the oxidant rises up to 0.4, the ammonia slip decreases significantly. Further increase in the oxygen content in the oxidant leads to a slight increase in the ammonia slip. It can be explained that ammonia/hydrogen combustion is incomplete when air is used as oxidant at the equivalence of 1.1 and more oxygen contents in the oxidant promote the ammonia oxidation, resulting in a decrease in the ammonia concentration at the exhaust. Furthermore, the concentration of unburnt hydrogen and NO_x rises at the exhaust when the oxygen content in the oxidant rises from 0.21 to 1.00. Therefore, 40% oxygen in the oxidant is found to be reasonable, considering the goal of minimizing ammonia slip, unburnt hydrogen and NO_x emission, and employed in the subsequent analysis.

The peak heat production rate, outlet temperature and emissions are plotted in Figure 4.27 and Figure 4.28 with various pressures ($1 - 20$ bar) and initial



(a) (b)

Figure 4.25: Variations of (a) peak heat production rate and (b) outlet temperature and emissions with different hydrogen blending ratios. ($\phi = 1.1, \Omega = 0.21, T_1 = 300$ K, $P_1 = 1$ bar)

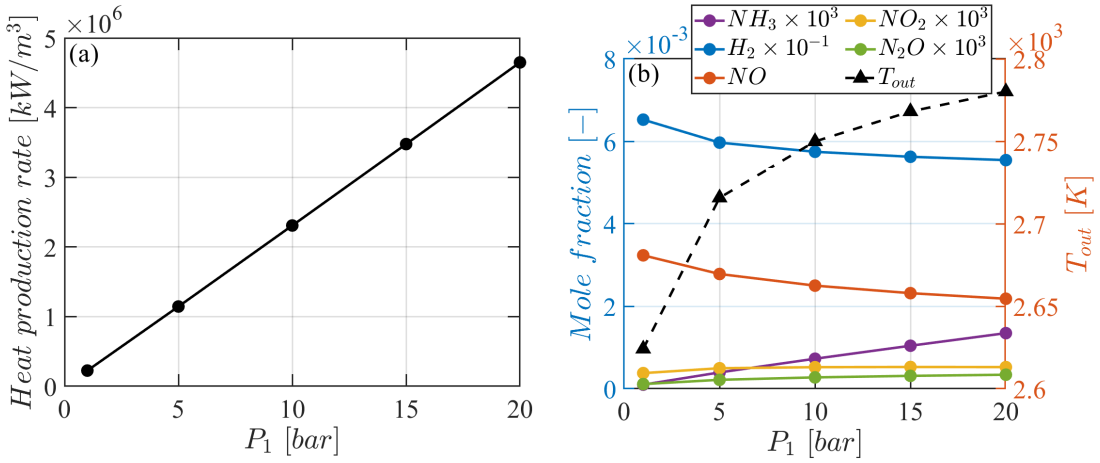


(a) (b)

Figure 4.26: Variations of (a) peak heat production rate and (b) outlet temperature and emissions with different oxygen contents in the oxidant. ($60\%NH_3/40\%H_2, \phi = 1.1, T_1 = 300$ K, $P_1 = 1$ bar)

temperature (300−500 K) at the selected initial component ratios ($\phi = 1.1, x\%H_2 = 40\%, \Omega = 0.4$). Figure 4.27 shows the increase in pressure greatly enhances the peak hear production rate and the outlet temperature rises slightly from 2624 to

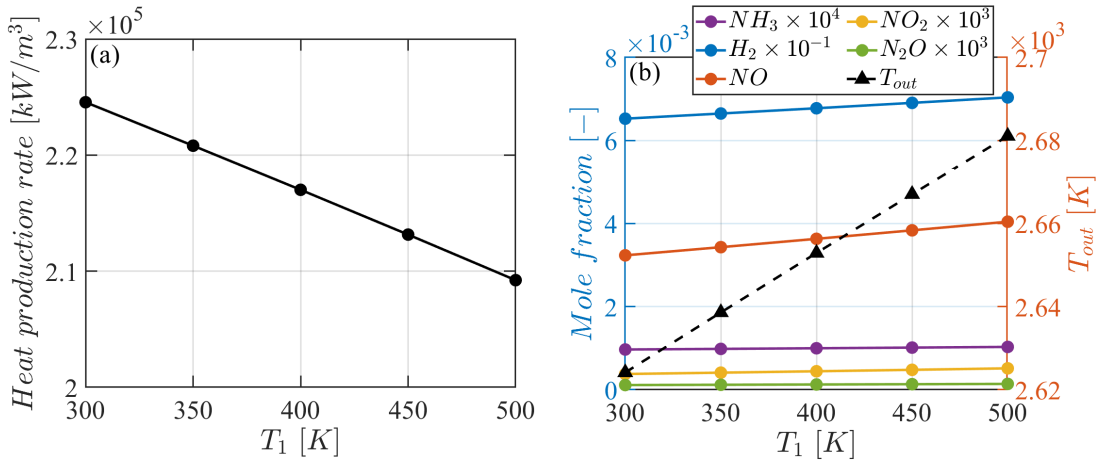
2780 K. In response to increasing pressure, the oxidation of NH_i is substituted by a binding reaction of NH_i, yielding nitrogen rather than nitric oxide [43]. As a result, as shown in Figure 4.27(b), NO_x reduction occurs under a higher pressure. The elevated outlet temperature implies the promoted NO generation by thermal-NO method, but it is observed that the overall NO emission is dropped, indicating thermal-NO is more susceptible to pressure than fuel-bound NO. It also concluded that high-pressure environment is favourable for NO minimization in the industrial operational conditions.



(a) (b)

Figure 4.27: Variations of (a) peak heat production rate and (b) outlet temperature and emissions with different pressures. ($60\%NH_3/40\%H_2, \phi = 1.1, \Omega = 0.4$)

Figure 4.28 shows the changes of the peak heat production rates, outlet temperature and emissions when the initial temperature rises from 300 to 500 K. The pressure is maintained at the atmospheric condition. It can be seen that the outlet temperature rises marginally from 2624 K to 2681 K but the peak heat production rate reduces from 2.25×10^5 to 2.09×10^5 kW/m^3 when the initial temperature is enhanced. The enhancement of the extended Zeldovich mechanism owing to the high temperature environment allows the rapid generation of O/H radical,



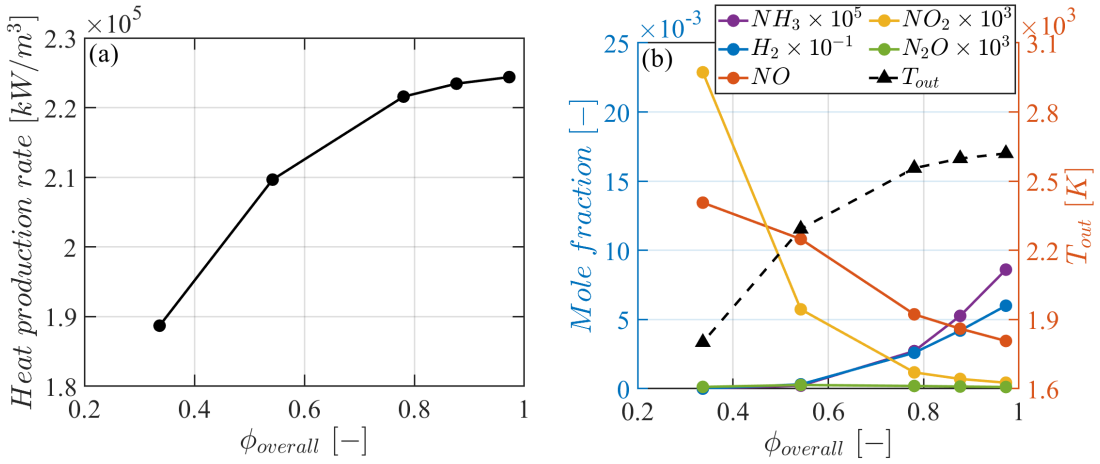
(a) (b)

Figure 4.28: Variations of (a) peak heat production rate and (b) outlet temperature and emissions with different initial temperature ($60\%NH_3/40\%H_2, \phi = 1.1, \Omega = 0.4$)

.

consequently, increased NO emission at the exhaust. It also illustrates that the hydrogen residual increases and NH_3, N_2O, NO_2 emissions stay unchanged with the growth in the initial temperature.

In the modern combustor, secondary air injection is often considered to promote the combustion efficiency as it helps to consume the unburnt fuel. Figure 4.29 shows the combustion characteristics of $60\%NH_3/40\%H_2$ flame with the primary equivalence ratio (ϕ_{prim}) at 1.1. The secondary air injection is introduced into the flame zone and the mass flow rate is controlled in the range of $0.100-7.000$ g/s. Overall equivalence ratio ($\phi_{overall}$) is the equivalence ratio where air includes primary and secondary air injection in this section. As a result, the overall equivalence ratio decreases from 0.973 to 0.337. The result illustrates the peak heat production rate and the outlet temperature increase as the overall equivalence ratio increases, indicating the heat production rate and the outlet temperature are suppressed by the secondary air injection. Regarding the emissions, it is shown



(a) (b)

Figure 4.29: Variations of (a) peak heat production rate and (b) outlet temperature and emissions with secondary air injection. ($60\%NH_3/40\%H_2, \phi_{prim} = 1.1, \Omega = 0.4$)

in Figure 4.29(b) that there is a reduction in the unburnt ammonia and hydrogen but substantial increases in NO and NO_2 emissions as more secondary air is involved. Since the secondary air injection at the flame zone reduces the outlet temperature and causes the flame to slow down, there is not enough time for the NO to be consumed. Instead, NO reacts with the oxygen in the secondary air and yields a large amount of NO_2 at the exhaust. It can be concluded that in the gas turbine, a large amount of secondary air contributes to improving the combustion efficiency, but also cause an increase in NO_x emissions. It is necessary to attain a good balance between high combustion efficiency and low NO_x emission.

4.5 Summary

In this chapter, a detailed ammonia chemical kinetic reaction mechanism, Nakamura's mechanism [84], was first chosen from several ammonia mechanism candidates based on the validation against the same set of literature experimental data.

The parametric study was then conducted to discover the laminar flame speed, ignition delay time and flame structure of premixed ammonia and hydrogen combustion by employing the identified ammonia mechanism. The rate of production (ROP) analysis is investigated in order to obtain a better understanding of the NO_x generation and consumption processes. A wide range of equivalence ratios, hydrogen blending ratios, oxygen contents in the oxidant, initial temperature and pressure have been discussed to support the combustion system development in an external combustion type free-piston engine fuelled by ammonia and hydrogen. A 1D continuous combustion model for gas turbine was then used to reveal the peak heat production rate, outlet temperature and emission performance of premixed ammonia/hydrogen dual fuelled gas turbine. The main conclusions have been summarized as follows.

1) NO emission decreases and ammonia slip and unburnt hydrogen at the exhaust rise significantly when increasing the equivalence ratios. Laminar flame speed peaks at about 1.1 of equivalence ratio. These indicate that an equivalence ratio at 1.1 is advantageous for both combustion stability and emission control.

2) Hydrogen enrichment and oxygen enrichment have profound effects on promoting the laminar flame speed and reducing the ignition delay time of ammonia flames. An ammonia flame with either 40% hydrogen blending ratio or 60% oxygen content in the oxidant can achieve a comparable laminar flame speed to that of methane flames under the same conditions. The hydrogen addition causes a penalty of a slight increase in NO emission. Although a noticeable rise in absolute NO is observed with oxygen enrichment, there are reducing trends of normalised NO and N_2O emissions.

3) The laminar flame speed tends to be inhibited as the pressure increases; however, this effect is attenuated when the pressure is further elevated. Rising pressure contributes to the reduction of ignition delay; however, the effect is also weakened with a further increase in pressure. NO emission drops substantially as pressure rises.

4) In ROP analysis, fuel-bound NO and thermal NO methods both show a strong impact on NO generation and consumption. Depending on the parameters explored, the final level of NOx emissions depends on the relative importance of the two reaction pathways.

5) Taking into account the influence of various parameters, a beneficial combination, i.e., $30\%H_2/70\%NH_3$, $\Omega = 0.3$, $\phi = 1.1$, $T = 600$ K, $P = 15$ bar is chosen for a free piston engine with external combustor to achieve the goal of robust and low NO_x emission combustion. It is found that NO concentration at the exhaust is approximately 1700 ppmv while those of NO_2 and N_2O are negligible, which offers an important guide for designing a low-emission ammonia combustion system in a free piston engine.

6) Based on the 1D simulation results of the gas turbine network, a premixed ammonia flame with a hydrogen blending ratio at 40%, an oxygen content in the oxidant at 40% and an equivalence ratio at 1.1 are primarily chosen and discussed at various initial temperature and pressure as well as with and without secondary air injection for the optimization of combustion efficiency and NO_x emission minimization.

7) As the initial temperature increases, there is a slight increase in the outlet temperature. Owing to the extended Zel'dovich mechanism, the O/H radicals increase, responsible for the increase in NO emissions.

8) The elevation in pressure increases moderately the outlet temperature but inhibits the NO_x production. Thermal NO formation is accelerated with an increased outlet temperature, but overall NO emission is decreased, suggesting that pressure has a more significant effect on fuel-bound NO formation (compared to thermal NO formation) and the high-pressure environment is conducive to the use of ammonia and hydrogen fuelled gas turbines regarding to the NO_x emission control.

9) The combustion efficiency is improved with secondary air injection to the combustor because the excess air enables the unburnt fuel to be consumed, however, it is observed that NO and NO_2 emissions are greatly increased. The secondary air flow suppresses the flame speed, resulting in the incomplete NO consumption and NO oxidation. This indicates the need to select the optimum amount of secondary air to trade-off between combustion efficiency and emission control.

Chapter 5. Experimental analysis of non-premixed ammonia flame with hydrogen in a swirl-enhanced combustor

5.1 Introduction

In this chapter, the combustion and emission performance of non-premixed ammonia/hydrogen flames are investigated experimentally in a swirl-enhanced combustion test rig. Global equivalence ratio is introduced in this chapter, it is the equivalence ratio calculated based on the injection of fuel and air in the case of non-premixed combustion. This term is used to distinguish it from the concept of local equivalence ratio in non-premixed combustion. The blowoff limits were first examined to ensure that a range of stable flames could be achieved. Pilot testing of newly established combustor test rig was conducted with ammonia/methane blends. Some blowoff limit results from the pilot tests for non-premixed ammonia/methane flames were used to compare with the results for non-premixed ammonia/hydrogen flames. Emissions containing nitric oxide (NO), nitrous oxide (NO_2), ammonia slip (NH_3) and unburnt hydrogen (H_2) were then measured with a variety of global equivalence ratios, hydrogen blending ratios, initial gas temperature, swirl numbers and combustion chamber wall conditions. The structure of non-premixed ammonia/hydrogen flames and the relationship between the excited hydroxyl radicals (OH^*) and the NO emission were revealed using OH^* chemiluminescence profiles. The experimental results contribute to the validation and improvement of ammonia combustion mechanism models and provide a guidance

for the development of ammonia/hydrogen fuelled heat engines for decarbonising heavy transport.

The results presented in this chapter are under peer review in the International Journal of Hydrogen Energy, entitled "Experimental Investigation on Combustion and Emission Characteristics of Non-premixed Ammonia/Hydrogen Flame" (Reference number: HE-D-23-09039R1).

5.2 Blowoff limit

5.2.1 Blowoff limit measurement procedure

The blowoff limit is identified by gradually increasing the air flow rate by approximately 2% every 20 seconds while keeping the fuel flow rate unchanged until blowoff occurs [181]. The error therefore is the 2% of the full range of the mass flow rate of air. The procedure was repeated five times for each case. The blowoff limit of ammonia and hydrogen was investigated at different hydrogen blending ratios, initial temperatures and swirl numbers so as to first gain the knowledge of the conditions of non-premixed ammonia/hydrogen flame stability. This would aid in the subsequent analysis on emission characteristics and OH^* chemiluminescence. The experimental conditions for examining the blowoff limits is shown in Table 5.1. The effect of hydrogen blending ratios on the blowoff limits have been studied first. The stable range for $60\%NH_3/40\%H2$ flames is the widest. Therefore, 40% of hydrogen blending ratio was selected for the following studies on analysing the effect of initial temperature. However, 30% hydrogen blending ratio was used for analysing the effect of different swirlers due to the limited experimental time and funding. The initial temperature of air and fuel were controlled independently. Due to the efficiencies of different preheaters for air and fuel lines and the laboratory working conditions, initial air temperatures of up to 435 K and initial fuel

temperature of up to 475 K were reached. Thus, the effect of initial temperature on blowoff limits were conducted at the following conditions: $T_{air} = 300$ K, $T_{fuel} = 300$ K; $T_{air} = 400$ K, $T_{fuel} = 400$ K; $T_{air} = 435$ K, $T_{fuel} = 475$ K. Moreover, the findings are compared with the blowoff limit results of ammonia and methane achieved on the same test rig.

Table 5.1: The experimental conditions for blowoff limit test.

Factor	**Range**
Air flow rate	$1.37 - 6.87$ g/s
Hydrogen blending ratio	$0.2, 0.3, 0.4$
Fuel initial temperature	$300, 400, 475$ K
Air initial temperature	$300, 400, 435$ K
Swirl number	$0.73, 0.87, 1.04$

5.2.2 Results and Discussion

It has been reported that ammonia flames have narrow flammability and low flame velocity, so it is important to determine the flame stability conditions when ammonia is used as the primary fuel and blended with a high flame velocity substance, such as hydrogen. Blowoff limits were examined with various hydrogen blending ratios and different swirlers at different gas initial temperature to ensure the flame stability condition and range (from lean blowoff limit to rich blowoff limit). The rich blowoff limit is defined as the minimum mass flow rate of air that

can ignite and burn the fuel blends stably while the lean blowoff limit is defined as the maximum mass flow rate of air that keeps the flame stable before blowing off at a constant mass flow rate of fuel blends [182].

The effect of hydrogen blending ratios varying from 10% to 40% on the blowoff limits of non-premixed ammonia flames was conducted with swirler $S(b)$ (swirl number: 0.87) at the initial gas temperature of 300 K. It was observed that the flame was not stable when only 10% hydrogen is blended with ammonia. When the hydrogen blending ratio was above 20%, the flame was stabilised. The rich and lean blowoff limits of non-premixed ammonia flames with $20\%, 30\%, 40\%$ hydrogen addition is plotted in Figure 5.1. It can be seen that the hydrogen involvement expands the stable range of ammonia flames, and it has a more pronounced effect on the lean blowoff limits than that on rich blowoff limits. For example, the stable range (global equivalence ratio) for the $80\%NH_3/20\%H_2$ flame is $0.576 - 1.084$ while that for the $70\%NH_3/30\%H_2$ is $0.388 - 1.141$. Due to the limitation of the maximum air flow rate, the $60\%NH_3/40\%H_2$ flame burns steadily at 6.870 g/s and its lean blowoff limit can be extended further. This finding is comparable with the conclusions drawn from the lean blowoff limits of premixed ammonia/hydrogen flames [183]. The trend of lean blowoff limit in the non-premixed ammonia/hydrogen flames is consistent with that of the premixed ammonia/hydrogen flames, i.e., the lean blowoff limit is gradually decreased as hydrogen blending ratio increases.

Methane involvement also contributes to improving the ammonia flame stabilisation. In Figure 5.1, the rich and lean blowoff limits of non-premixed ammonia/methane flame and non-premixed methane flame are presented for comparison with that of the non-premixed ammonia/hydrogen flame. The non-premixed ammonia flames with methane addition at 40% and below were unstable or non-

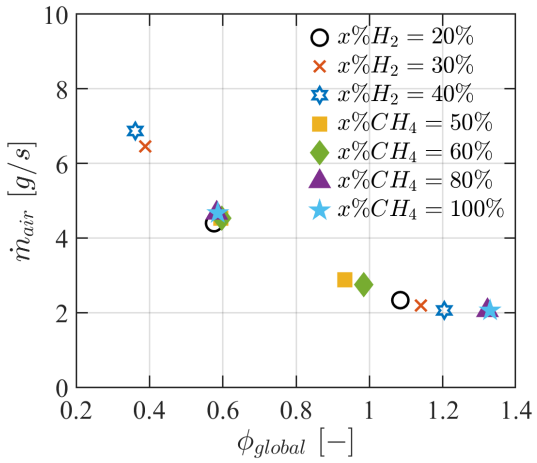


Figure 5.1: Blowoff limits of non-premixed ammonia/hydrogen flames (empty symbols) and ammonia/methane flames (filled symbols).

ignitable. The stable non-premixed ammonia/methane flames were achieved when the methane blending ratio was at 50%, 60%, 80%. A clear extension on the rich blowoff limits as the methane addition increased was found. Low-flame-speed ammonia requires a high-flame speed substance to initialize the flame and raise the temperature to aid in ignition. As a result, a flame was ignited and reached the steady state at a lower air flow rate and the rich blowoff limits were extended as more hydrogen or methane is added into the fuel. Owing to a higher reactivity and flame speed of hydrogen than that of methane, the rich blowoff limits of ammonia flames with hydrogen blending ratio at $20\% - 40\%$ is lower than that of ammonia flames with methane blending ratio at $80\% - 100\%$. When the flame is stabilised, continuing to increase the air mass flow rate leads to the flame being blown away. However, the primary fuel was methane rather than ammonia in non-premixed ammonia/methane flames tested in this experiment. The flame was kept at a relatively high speed, consequently, no noticeable effect is found on the lean blowoff behaviour.

The effect of initial temperature on the blowoff limits of non-premixed

$60\%NH_3/40\%H_2$ flame is shown in Figure 5.2 with non-premixed $40\%NH_3/\ 60\%CH_4$ flame as well as methane flame for comparison. It is noticed that the lean blowoff limits of non-premixed $60\%NH_3/40\%H_2$ can be further extended because the flames under room temperature and elevated temperature are still robust with the maximum air mass flow rate available in the laboratory. Therefore, only the effect of initial temperature on the rich blowoff limit can be observed. The ranges to achieve the stable flames are widened for all three fuel blends when rising the initial temperature. For instance of non-premixed $60\%NH_3/40\%H_2$ flames, the rich blowoff limit is extended from 1.204 to 1.290 when the initial temperature rises from 300 K to 400 K and it extends further to 1.505 when the initial air temperature rises to 425 K and the initial fuel temperature rises to 475 K. This is due to the increase in flame speed caused by the increase in initial temperature, which balances the inlet flow rate and promotes flame stability. It is observed that the lean blowoff limits of non-premixed $40\%NH_3/60\%CH_4$ and methane flames are not significantly affected by increasing the initial temperature, and the same trend is found for premixed ammonia/hydrogen flames in the literature [183]. Furthermore, non-premixed $60\%NH_3/40\%H_2$ flame is shown to have the widest stable range among the three types of flames, although its lean blowoff limits under all conditions are still extendable.

The shear layer region is a thin region with intensive vorticity where the tangential velocity component varies greatly. Swirlers are generally considered as an effective way to increase the mixing ratio of fuel and oxidant in the shear layer region, and therefore improve the flame stability. Three swirlers, $S(a)$, $S(b)$, and $S(c)$, are employed to investigate the effect of swirl numbers on the blowoff limits of non-premixed ammonia/hydrogen flames. Due to the limited experimental time and funding, $70\%NH_3/30\%H_2$ flame was selected for analysing the effect of

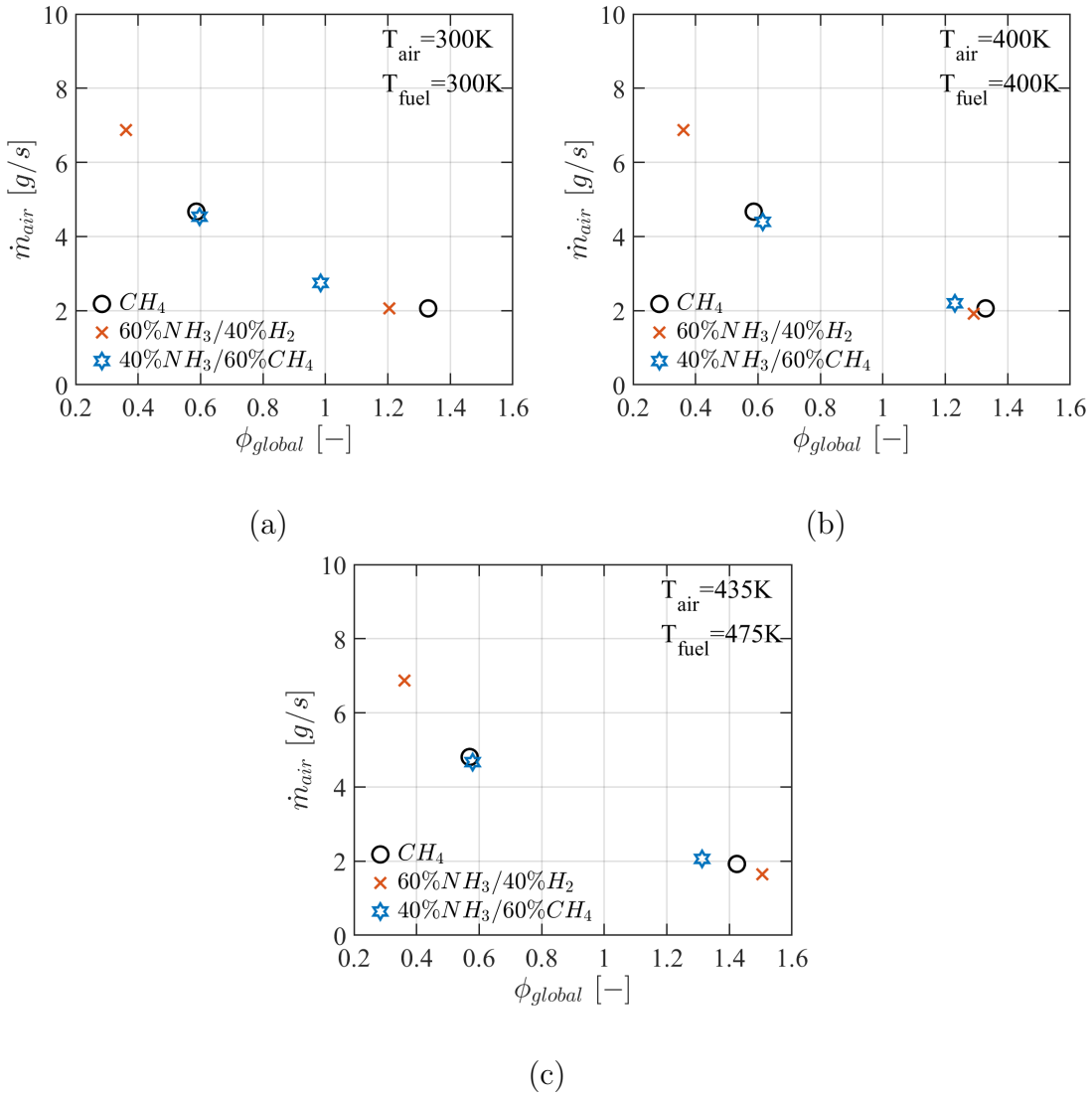


Figure 5.2: Blowoff limits of non-premixed $CH_4, 60\%NH_3/40\%H_2$ and $40\%NH_3/60\%CH_4$ flames when (a) $T_{air} = 300$ K, $T_{fuel} = 300$ K , (b) $T_{air} = 400$ K, $T_{fuel} = 400$ K and (c) $T_{air} = 435$ K, $T_{fuel} = 475$ K.

different swirlers (including blowoff limit tests, the emission tests and OH^* chemiluminescence imaging). Figure 5.3 shows the increase in the swirl number shortens the flame stability range considerably for non-premixed $70\%NH_3/30\%H_2$ flames. It is noticeable that the effect on the rich blowoff limits is more pronounced than the effect on the lean blowoff limits. The effect of swirl numbers on the blowoff limits of premixed ammonia/methane was also reported by Zhang *et al.* [98], who

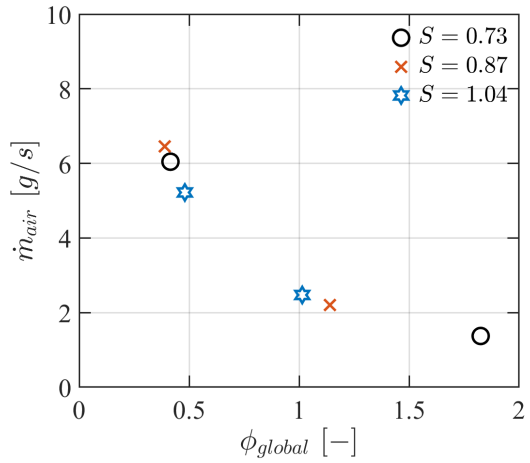


Figure 5.3: Blowoff limits of non-premixed $70\%NH_3/30\%H_2$ flames with different swirl numbers.

reported that when the swirl number changes to values equal to 0.42, 0.73, and 1.27, the lean and rich blowoff limits almost stay unchanged in premixed ammonia flames; however, an apparent extension on the lean blowoff limits was observed in the premixed $50\%NH_3/50\%CH_4$ flames.

5.3 Exhaust emissions analysis

5.3.1 Exhaust emissions measurement procedure

Emissions are a major concern in ammonia/hydrogen combustion. The Horiba multi-gas analyser (MEXA-7100DEGR) was employed to measure NO and NO_2 emissions and oxygen levels at the exhaust. The repeatability is within 0.5% of the full scale for zero point or within 0.5% of the readings for span point. Thermo Fisher Trace 1300 gas chromatography was installed with Pulse Discharge helium ionisation Detector (PDD) and Thermal Conductivity Detector (TCD) to measure unburnt ammonia and hydrogen at the exhaust. For both types of detectors, the repeatability of typical retention time is less than 4.8×10^{-2} s and the repeatability of the typical peak area is less than 0.5% of the relative standard deviation. Before

the tests, the gas analyser, gas chromatography and two heating pipes were pre-heated to their operational conditions. Span gases for each emission were used to calibrate the gas analyser and ensure the measurement accuracy. Then, purge gas was injected to clear the concentration. For gas chromatography, additional injections were performed after each case to ensure that the previous exhaust gas was evacuated before the start of the new case. The NO_x emissions from non-premixed ammonia/methane flame using the current test rig were validated with the single-zone combustion results of premixed ammonia/methane flames available in the literature [89]. The trends of NO and NO_2 showed satisfactory agreements with the literature results. The effects of global equivalence ratios, hydrogen blending

Table 5.2: The experimental conditions for emission measurements and OH^* chemiluminescence imaging.

Factor	**Range**
Global equivalence ratio	$0.6 - 1.2$
Hydrogen blending ratio	$20\%, 30\%, 40\%$
Fuel initial temperature	$300, 325, 350, 400\ K$
Air initial temperature	$300, 325, 350\ K$
Swirl number	$0.73, 0.87, 1.04$
combustion chamber wall condition†	with and without silicate ceramic fibre blanket insulation

† OH^* chemiluminescence imaging was performed without silicate ceramic fibre blanket insulation.

ratios, initial temperature, swirl numbers and combustion chamber wall conditions on emissions of non-premixed ammonia/hydrogen combustion were studied using the swirl-enhanced combustor. The experimental conditions are summarised in Table 5.2. The effect of global equivalence ratios on emissions has been studied first at various hydrogen blending ratios. According to the results in Section 5.2.2, 40% of hydrogen blending ratio was selected for the following studies on analysing the effect of initial temperature. However, 30% hydrogen blending ratio was used for analysing the effect of different swirlers and combustion chamber wall conditions due to the limited experimental time and funding. The initial temperature of air and fuel were controlled independently. Due to the efficiencies of different preheaters for air and fuel lines and the laboratory working conditions, initial air temperatures of up to 350 K and initial fuel temperature of up to 400 K were reached. Thus, the effect of initial temperature on blowoff limits were conducted at the following conditions: $T_{air} = 300$ K, $T_{fuel} = 300$ K;$T_{air} = 325$ K, $T_{fuel} = 325$ K; $T_{air} = 350$ K, $T_{fuel} = 350$ K; $T_{air} = 350$ K, $T_{fuel} = 400$ K. In order to film OH^* chemiluminescence images, combustion chamber insulation material has to be removed. The working conditions are the same for emission measurement and OH^* chemiluminescence imaging. All data were collected while the emission levels remained stable. As ammonia and hydrogen were burnt under different global equivalence ratios, oxygen normalisation was applied to compare the emissions. According to the Equation 3.3.9, all the emission results were normalised to the standard oxygen concentration basis at 15%.

5.3.2 Results and Discussion

5.3.2.1 Emission performance of different hydrogen blending ratios at different equivalence ratios

Although no carbon-related emissions will be emitted from non-premixed ammonia/hydrogen combustion, nitric oxides, ammonia slip and unburnt hydrogen can be produced, all of which are harmful to the atmosphere. A clear knowledge of emission characteristics of non-premixed ammonia/hydrogen combustion is beneficial for emission control when designing the industrial applications powered by ammonia and hydrogen. Therefore, emissions of NO, NO_2, NH_3, and H_2 are emphasised in this section and all the results have been normalised to the standard oxygen level of 15%(vol).

Figure 5.4 depicts the effects of global equivalence ratios and hydrogen blending ratios on the emissions of non-premixed ammonia/hydrogen flames. When the hydrogen blending ratio is 20% and 30%, it can be seen that the NO, NO_2 emissions increase when the global equivalence ratio rises from 0.6 to 0.8, reach the peak at the global equivalence ratio of 0.8 measuring about 100 ppmvd@15%O_2 for NO emission and about 35 ppmvd@15%O_2 for NO_2 emission and decrease with further increase in the global equivalence ratio. A similar trend is also observed when the hydrogen blending ratio is 40%, but both NO and NO_2 emissions are much higher at a low global equivalence ratio compared to the results with hydrogen blending ratio at 20% and 30%. The maximum NO and NO_2 emissions reach approximately 350 ppmvd@15%O_2 and 60 ppmvd@15%O_2, respectively. There are dramatic reductions for NO and NO_2 emission when the global equivalence ratio is close to the unity and becomes almost the same low value under fuel-rich conditions as the emissions with hydrogen blending ratio at 20% and 30%.

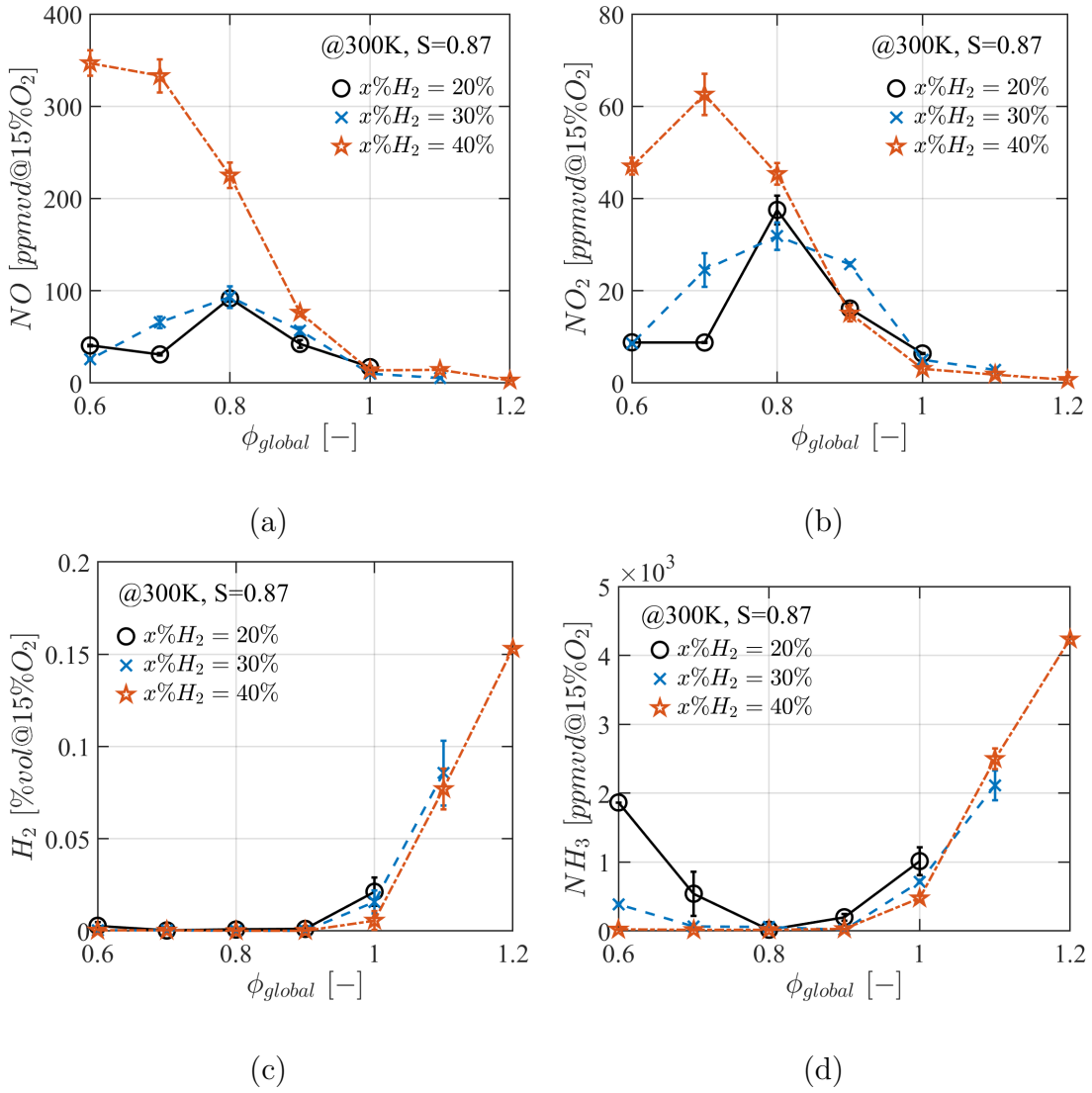


Figure 5.4: (a) NO, (b) NO_2, (c) H_2 and (d) NH_3 emissions of non-premixed ammonia/hydrogen flames versus various global equivalence ratios at different hydrogen blending ratios ($S = 0.87$).

In ammonia combustion, NO and NO_2 formations and consumptions are mainly associated with the flame temperature (thermal NO_x route) and concentrations of $O/H/OH$ radicals in the flame (fuel-bound NO_x route). When the global equivalence ratio is far-lean, the flame temperature is very low which suppressed NO and NO_2 production. As the global equivalence ratio increases but below the unity, fuel-bound NO_x ($HNO+H \rightarrow NO+H_2$, $HNO+OH \rightarrow NO+H_2O$)

is the main pathway for NO_x formation. Meanwhile, the flame temperature is relatively higher which induced further NO_x emission caused by the thermal NO_x formation. This explains the reason of low emissions of NO, NO_2 found at a very low equivalence ratio and the increase of emissions with the global equivalence ratio increasing to one. Conversely, under fuel-rich conditions, the fuel-bound route for NO_x formation is inhibited as the concentrations of $O/H/OH$ radicals are decreased. Instead, the thermal NO_x route for NO_x consumption is promoted and dominates to consume NO_x, resulting in the reduction of NO and NO_2 emissions when the global equivalence ratio is greater than one.

Although NO and NO_2 emissions keep decreasing under fuel-rich conditions, the unburnt fuel concentration, including that of hydrogen and ammonia rises significantly. At the global equivalence ratio of 1.2, ammonia slip surpassed the concentration level of 4000 ppmvd@15%O_2 while unburnt hydrogen was over 0.15%vol@15%O_2 at the exhaust. Taking the combustion efficiency into account, the optimal emission control occurs at stoichiometric condition. Relatively low emissions, including NO_x and unburnt fuel, were also found at far-lean global equivalence ratio with hydrogen blending ratio at 20% and 30%, but the flame robustness of ammonia and hydrogen at far-lean global equivalence ratio should be considered and investigated further.

Surprisingly, changes in hydrogen blending ratios have no significant impact on the unburnt hydrogen over the wide range of the global equivalence ratios. However, due to the flame temperature elevated by more hydrogen involvement, thermal NO_x formation is greatly affected. The elevated flame temperature also improves the ammonia fuel consumption. Consequently, increased NO and NO_2 as well as reduced ammonia slip at the exhaust were observed as more hydrogen was blended with ammonia. However, the effect is weakened considerably when

the global equivalence ratio is above the unity. It indicates that more hydrogen blending ratios provide less penalty on emissions under fuel-rich conditions.

5.3.2.2 Emission performance at different initial temperatures

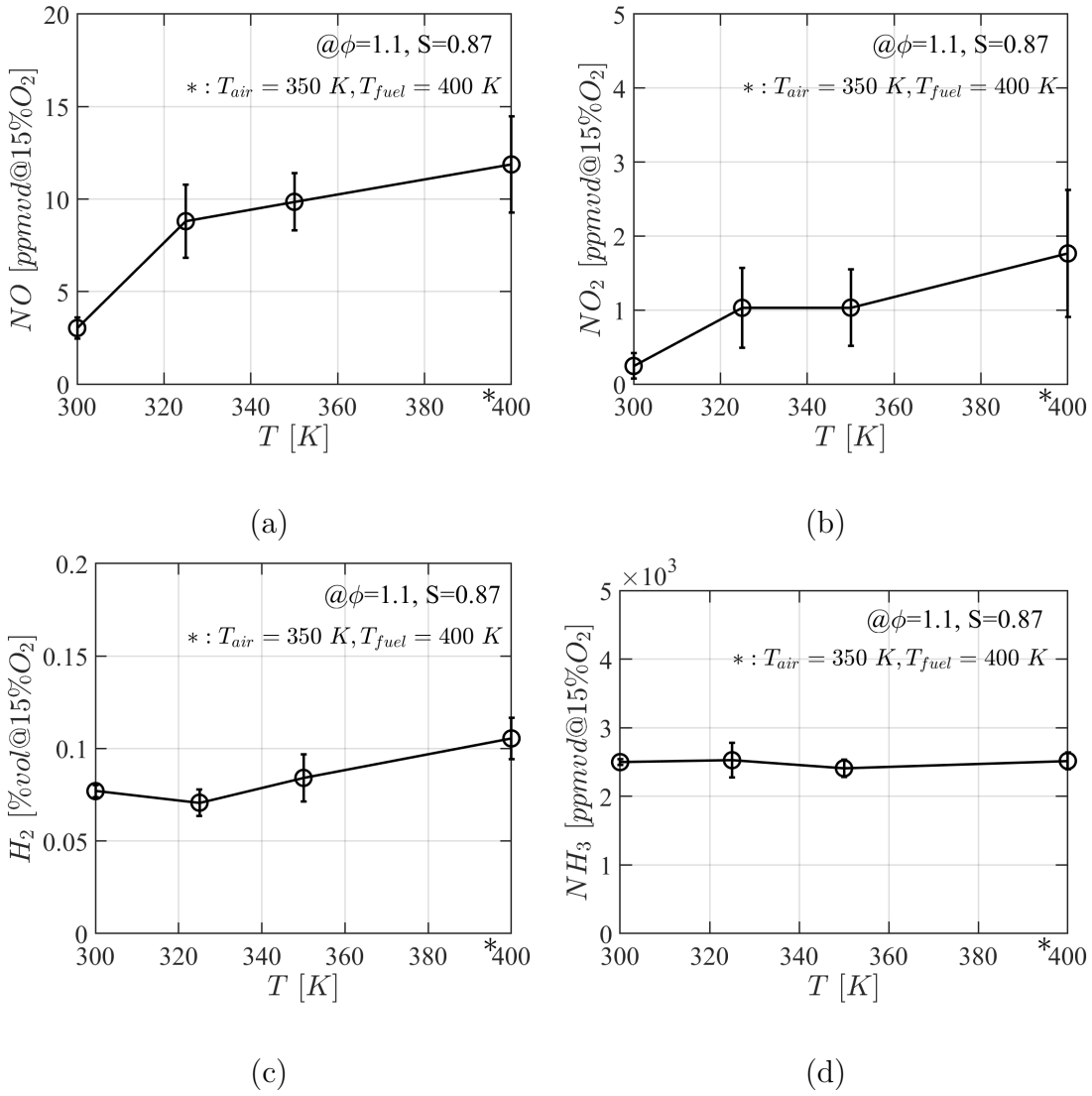


Figure 5.5: (a) NO, (b) NO_2, (c) H_2 and (d) NH_3 emissions of non-premixed ammonia/hydrogen flames versus different initial temperature ($S = 0.87$).

In Figure 5.5, the variations of emissions for non-premixed $60\%NH_3/40\%H_2$ flames are presented with the constant global equivalence ratio at 1.1 at different

initial temperatures. The measurement was conducted first when the initial temperature of air and fuel were both 300 K. The second measurement was conducted when initial temperature of air and fuel were both preheated to 325 K. Then, the initial temperature of air and fuel were both preheated to 350 K for the third measurement. Due to the efficiency of air preheater and test room environment, the maximum initial temperature for air was 350 K. Thus, in the last case, the initial air temperature was still 350 K while the initial fuel temperature was preheated to 400 K. It was well known that increasing the initial temperature improves the flame temperature and chemical reaction rate. According to the Zel'dovich mechanism, when the temperature is above 1800 K, NO_x formation through thermal NO_x route is promoted. Valera-Medina *et al.* [62] investigated premixed ammonia/hydrogen flames using 0D Gaseq analysis, finding NO_x concentration of flue gas was increased as the initial temperature increase from 300 to 900 K at 10 bar. However, the experimental results in the present work show the lifted initial temperature has no obvious impact on the emission at the global equivalence ratio of 1.1. The measured inner wall temperature was increased by approximately 46 K for every 25 K increase in the initial temperature. The moderate effect of increasing the initial gas temperature on the inner wall temperature could be owing to the heat loss from the sizeable optical window and the insufficient increase in the inlet temperature. This suggests that the increase in the flame temperature not be significant in showing the profound difference in emissions. As verified in the OH^* chemiluminescence images in Section 5.4.2, the flame temperature was not affected much with the increase in the initial temperature.

5.3.2.3 Emission comparison under the wall insulated and non-insulated conditions

As temperature plays a key role in the flame and affects emissions considerably, the effect of wall condition on emissions of non-premixed ammonia/hydrogen combustion has been investigated. The combustion chamber was insulated with silicate ceramic fibre blankets to compare the emission results between insulated wall conditions and non-insulated wall conditions. Figure 5.6 illustrates the emissions for non-premixed $70\%NH_3/30\%H_2$ flames with the initial gas temperature of 300 K under insulated wall condition and non-insulated wall condition. The results show that a substantial growth in NO and NO_2 and a significant reduction in unburnt ammonia slip at the exhaust when the combustion chamber is converted from non-insulated to insulated. Meanwhile, unburnt hydrogen kept almost the same. It suggests a great heat loss from the optical window and combustion chamber. The great heat loss, especially in the region close to the wall, considerably suppresses the generation of O/H radicals which are mainly yielded by the chain branching reaction, $H + O_2 \rightarrow OH + O$ [88]. Thus, thermal NO_x generation is suppressed. The substantial ammonia concentration at the exhaust suggests a further low NO_x generation from ammonia. The emission trends are consistent with the study on non-premixed ammonia/air flames that have been examined experimentally with non-insulated quartz glass liner, non-insulated steel liner and insulated steel liner [184].

5.3.2.4 Emission performance at different swirl numbers

Three swirlers with different vane angles were tested. Figure 5.7 shows the emissions of non-premixed $70\%NH_3/30\%H_2$ flames with various swirl numbers. Due to the flame stability difference using different swirl numbers, flames measured

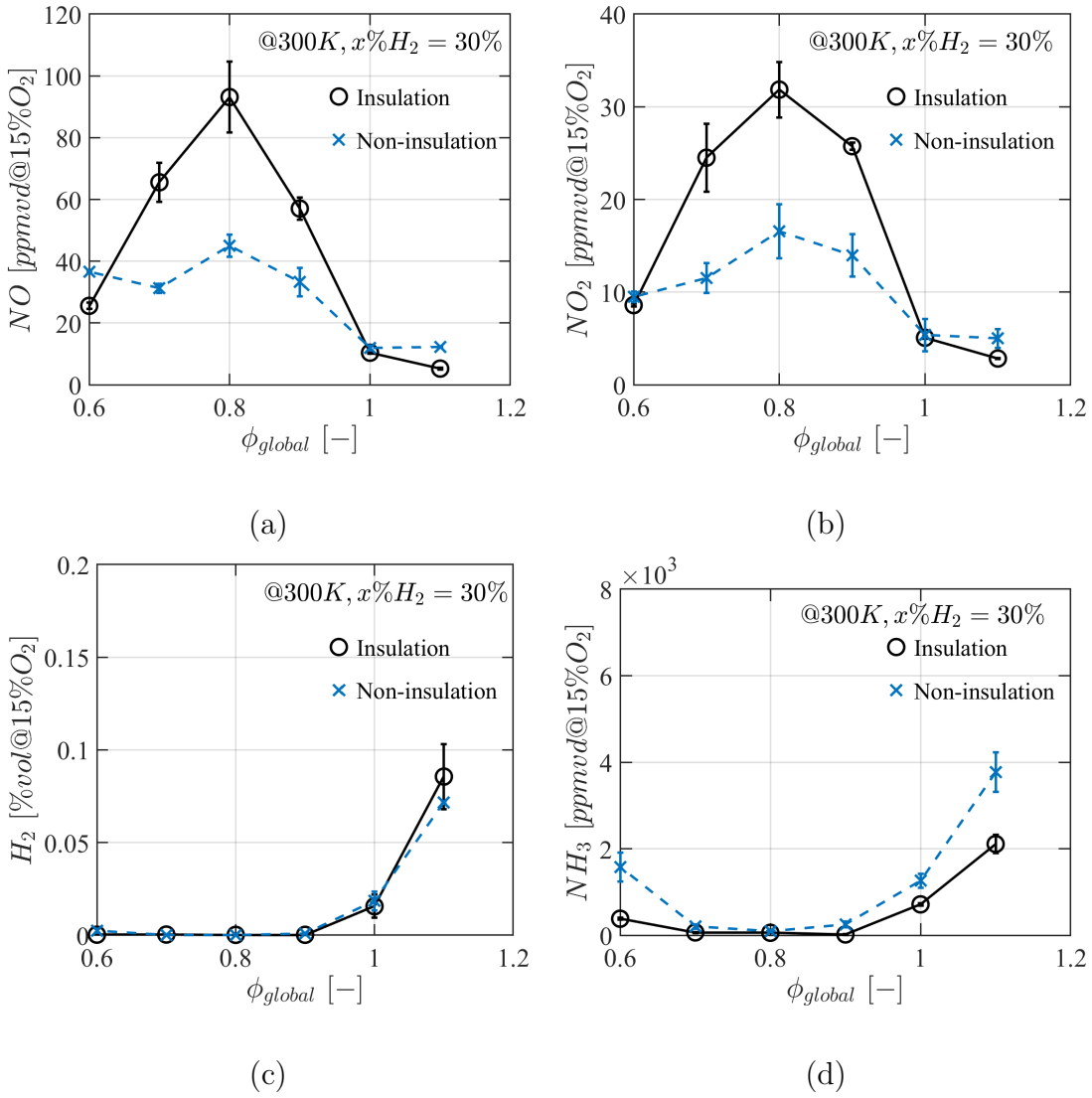


Figure 5.6: (a) NO, (b) NO_2, (c) H_2 and (d) NH_3 emissions of non-premixed ammonia/hydrogen flames versus various global equivalence ratios under insulated and non-insulated wall conditions ($S = 0.87$).

with small swirl number provide a wider range of emission results. It is found that the change in the swirl number has a moderate effect on the NO_x emission, although a slight reduction of NO and NO_2 concentration with swirler number at 0.87 and 1.04 was observed when the global equivalence ratio was greater than 0.8. Under far-lean conditions, unburnt hydrogen concentration at the exhaust is almost unaffected by swirl numbers while unburnt ammonia concentration at

the exhaust is reduced considerably. For instance, at the global equivalence ratio of 0.6, the unburnt ammonia was 1880 ppmvd@15%O_2 with swirl number at 0.73, 1580 ppmvd@15%O_2 with swirl number at 0.87 and 887 ppmvd@15%O_2 with swirl number at 1.04. In the premixed 30%NH_3/70%CH_4 flames, it was reported in the literature by conducting a large eddy simulation that a decreased NO emission

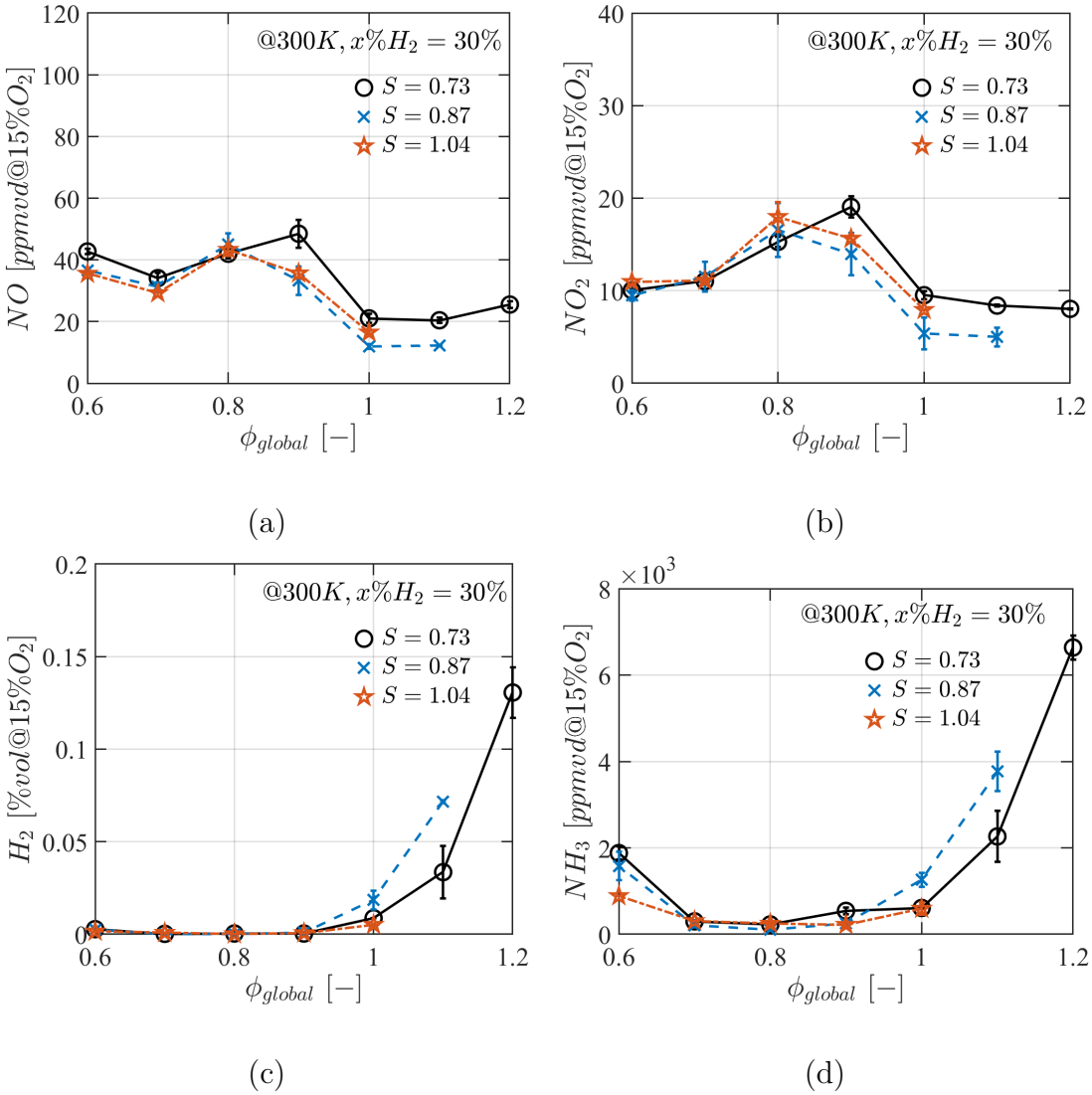


Figure 5.7: (a) NO, (b) NO_2, (c) H_2 and (d) NH_3 emissions of non-premixed ammonia/hydrogen flames versus various global equivalence ratios with different swirl numbers (non-insulation condition).

was achieved by increasing the swirl number from 0.58 to 0.99, and when the swirl number was greater than 0.76, less effect was observed on NO reduction [185]. It suggests there is potentially an optimal swirl number for NO emission control in non-premixed ammonia/hydrogen flames. Under the fuel-rich conditions, both the concentrations of unburnt hydrogen and ammonia were increased dramatically with a higher swirl number. As the angle of fuel nozzle is 45°, the vane angle of swirler at 40° ($S = 0.73$) enables the fuel and air to be mixed near the nozzle. The vane angle of swirler at 50° ($S = 1.04$) provides a stronger swirling flow but the mixing flow is being pushed closer to the cold wall. The mixing flow is burnt near the nozzle but the mixing flow close to the cold wall is likely to be pushed to the exhaust without reacting. The behaviour became stronger with more fuel dominate in the chamber, which led to the unburnt fuel (hydrogen and ammonia) is less with a low swirl number under fuel-rich condition. The effect of swirl numbers on unburnt fuel emission became greater when the global equivalence ratio was further increased.

5.4 OH* chemiluminescence

5.4.1 Image processing technique

Chemiluminescence of a flame is the spontaneous emission of light that occurs when a chemical species descends from the excited to the ground state. Excited hydroxyl (OH^*) chemiluminescence is recognised as an important parameter to understand physical properties without interfering with the actual flame, e.g. flame structure, relationship with NO concentration. OH^* chemiluminescence images were taken under the experimental conditions shown in Table 5.2. Then, they were processed using a bespoke MATLAB code (provided in Appendix). The workflow of the image processing technique is shown in Figure 5.8. One thousand

instantaneous OH^* chemiluminescence images and one thousand background images were collected using Phantom PCC1.2 software and averaged respectively. After the background correction and minimum value correction, image was filtered with 2D 3×3 median filter to remove salt and pepper noise. An example of image processing is presented in Figure 5.9.

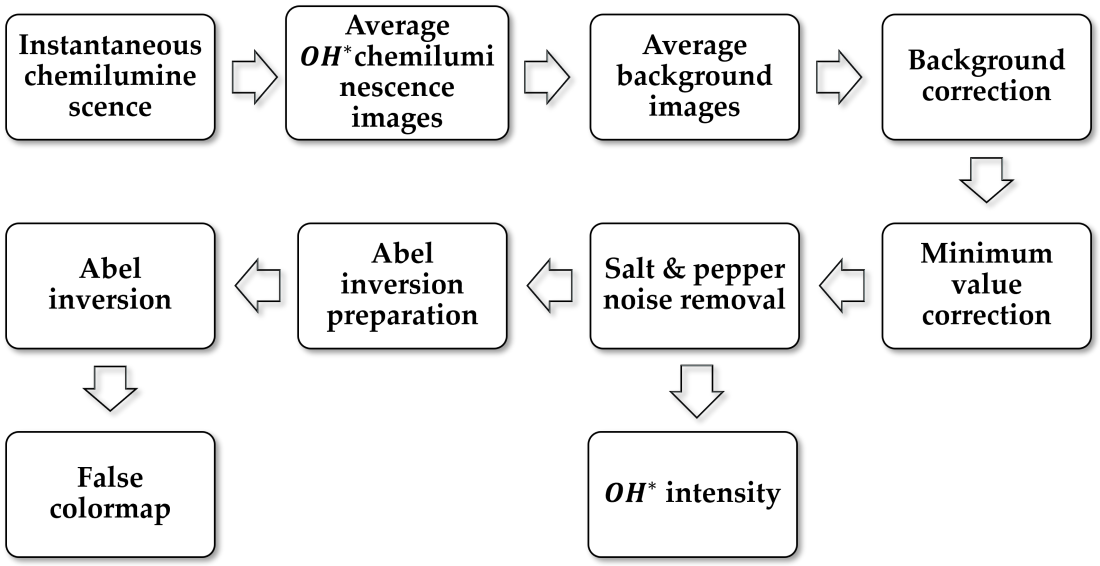


Figure 5.8: The workflow of image processing.

It is generally challenging to measure the spatially resolved distribution of physical properties $f(r)$ itself, e.g., OH^* chemiluminescence. The OH^* chemiluminescence images collected are line-of-sight images. However, $f(r)$ has a mathematical relationship to a function $h(y)$, as shown in Equation 5.4.1. The Abel inversion formula, illustrated in Equation 5.4.2, can be used to reconstruct a spatially resolved distribution $f(r)$ from $h(y)$ for axisymmetric objects [186]. Hence, the Abel inversion algorithm [186, 187] was applied to obtain a representative spatially resolved image of the OH^* chemiluminescence distribution. The Abel inversion algorithm utilised in this project is built on the Fourier-analysis principle, in which each row of image is deconvoluted into a set of integrals on the

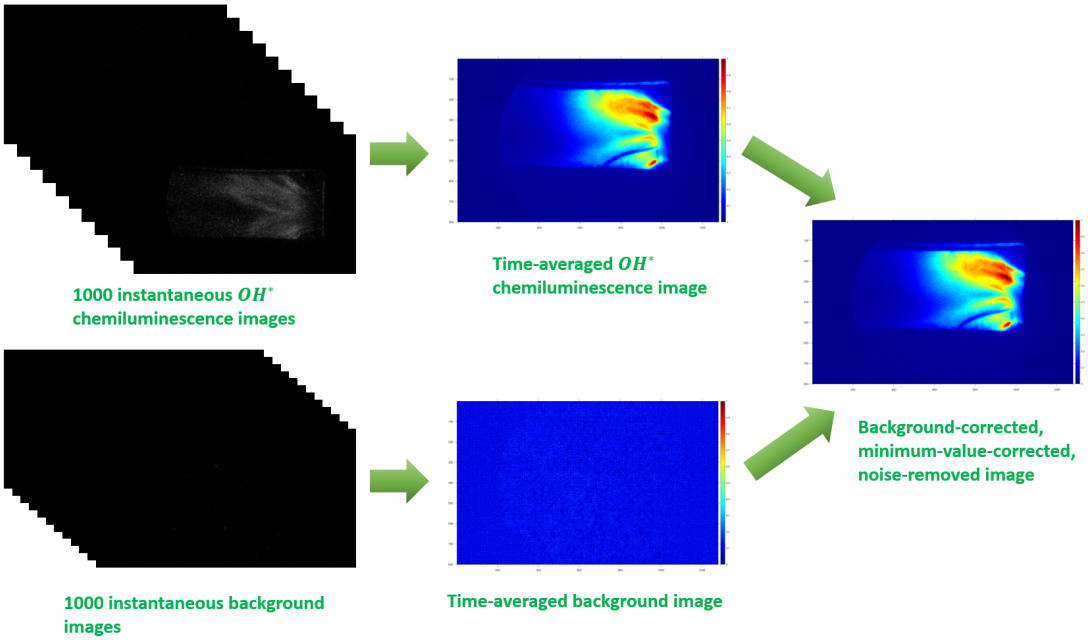


Figure 5.9: An example of image processing before using Abel inversion algorithm.

basis of the expansion of cosine functions [186, 187]. The expansion value of cosine functions plays an important role as a noise-filter and it was set as 5 in this project due to the computational time.

$$h(y) = 2\int_{y}^{R} f(r)\frac{r}{\sqrt{r^2 - y^2}}dr \tag{5.4.1}$$

$$f(r) = -\frac{1}{\pi}\int_{r}^{R} \frac{dh(y)}{dy}\frac{1}{\sqrt{y^2 - r^2}}dy \tag{5.4.2}$$

The bottom half of the image processed in Figure 5.9 is where the ignitor creates a scratch-like notch in the image. In Figure 5.10, the image without the false colormap provides clear evidence of this. The boundary of the combustor, fuel nozzle and swirler are axisymmetric. The OH^* chemiluminescence of flame is assumed as axisymmetric, which is applicable to use Abel inversion algorithm. Preparations for using the Abel inversion formula involves rotating and cropping

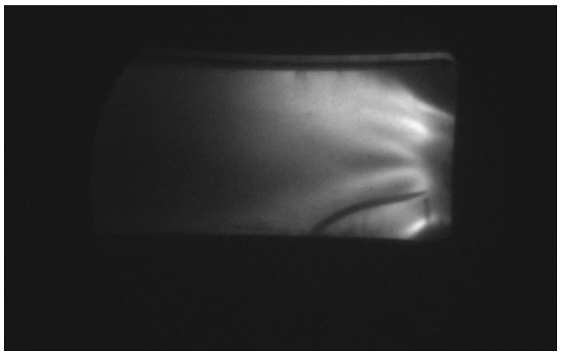


Figure 5.10: Background-corrected, minimum-value-corrected, noise-removed image without false colormap.

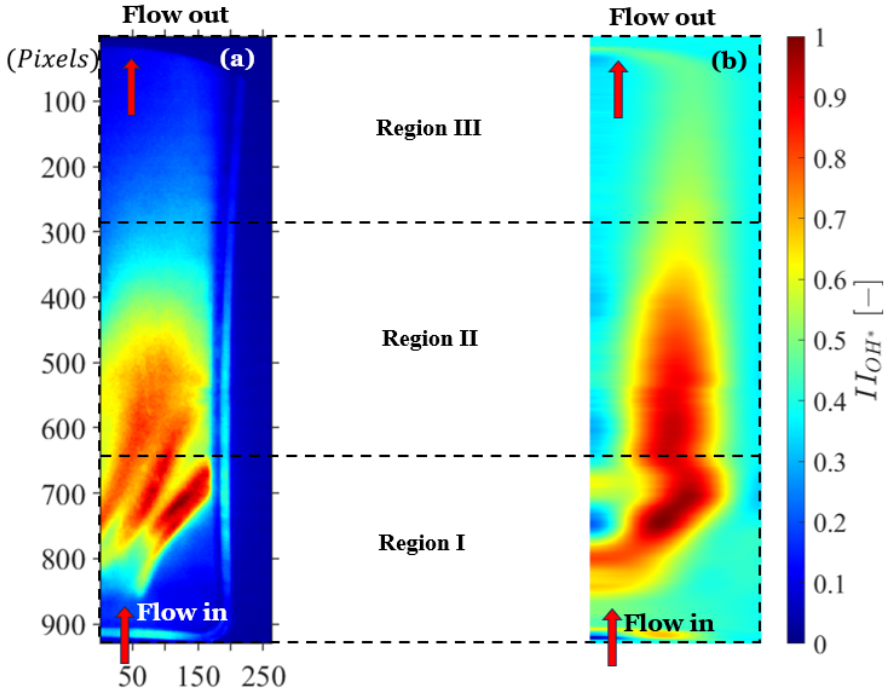


Figure 5.11: Time-averaged OH^* chemiluminescence distributions (a) before and (b) after Abel inversion algorithm in different regions. [*: near the nozzle (I), the transition region (II) and downstream of the flame (III)]

the image in half. The observation target is thus moved to monitoring the right half of the OH^* chemiluminescence. Figure 5.11 shows the time-averaged line-of-sight OH^* chemiluminescence image ((a) before Abel inversion algorithm) and time-averaged spatially resolved OH^* chemiluminescence image ((b) after Abel

inversion algorithm) with false colour mapping. The fuel nozzle and air swirler are located at the bottom and the ignitor is not shown in this half of the image. The flame direction is from bottom to top. To gain a quantitatively comparison, OH^* intensity (II'_{OH^*}) was calculated based on the pixels in the image before applying the Abel inversion algorithm. The formula for calculating the OH^* intensity is [188]:

$$\mathrm{II}'_{\mathrm{OH}^*} = \sum_{i=1}^{800} \sum_{j=1}^{1280} \overline{I_{OH^*_{ij}}} \tag{5.4.3}$$

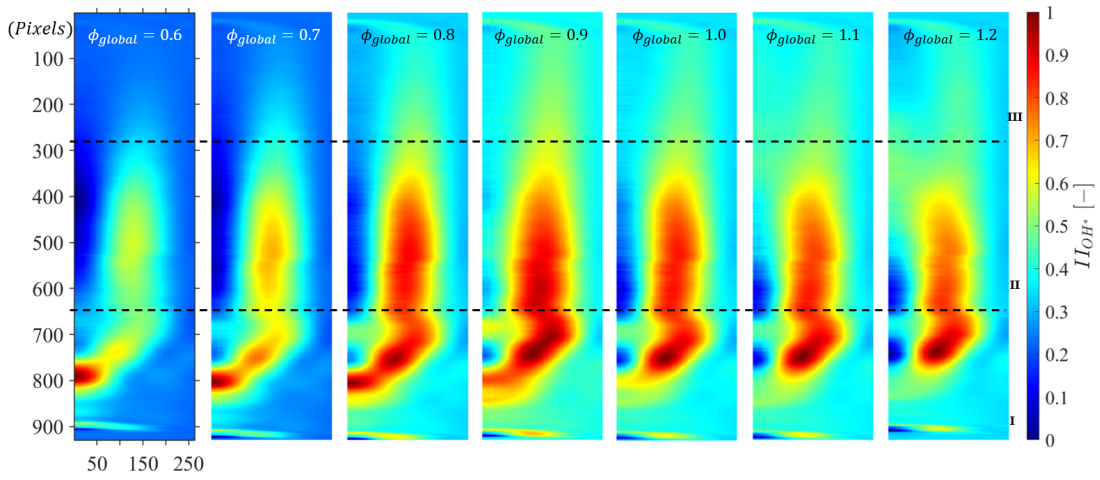
5.4.2 Results and Discussion

In this section, a thousand of images of OH^* chemiluminescence were taken for each case. For the distribution of OH^* chemiluminescence, normalisation was conducted to the image data by dividing by the maximum intensity of each case and rescaling to the same range shown in the colour bar. Therefore, it is noted that the value does not represent the absolute value.

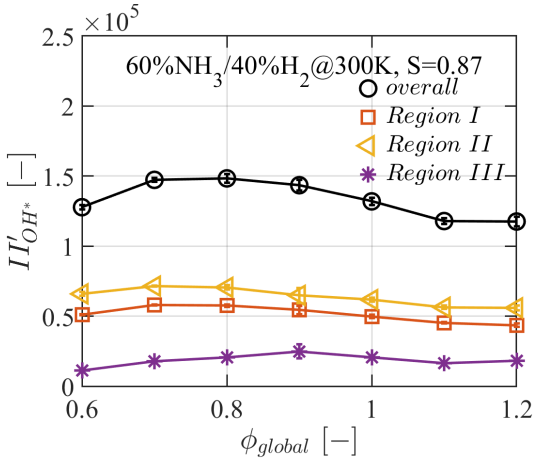
Figure 5.12 (a) shows the OH^* chemiluminescence profiles of the non-premixed $60\%NH_3/40\%H_2$ flame with various global equivalence ratio in the range of $0.6-1.2$ measured at the room temperature with the swirl number of 0.87. Owing to the axis symmetry of the image, only the top half of each image is rotated for analysis. From the perspective of topology in each case, it is found that the OH^* concentration was generally located at the upstream close to the nozzle in all cases and it was moved further away from the nozzle when the global equivalence ratio rises. Furthermore, OH^* chemiluminescence distribution was expanded as the flame became richer. The phenomenon is consistent with the observation of flame shape. At the far-lean conditions, the flame height of ammonia/hydrogen was short and orangish. As less oxidant participated in the reaction, the flame height became longer and turned to yellow-ish. It shows that the feature of OH^*

chemiluminescence distribution that can be used to identify flame shape can also be extended to non-premixed ammonia and hydrogen flames. Figure 5.12 (b) reveals the OH^* intensity results with the respect to the global equivalence ratios. It can be seen that the overall OH^* intensity trend is compatible with the trend in NO emission in Figure 5.4 (a). Hydroxyl radical plays a critical role in fuel-bound NO formation ($HNO + OH \rightarrow NO + H_2O$) and fuel-bound NO formation dominates in the NO emission under fuel-lean conditions. Under fuel-rich conditions, fuel-bound NO formation route is inhibited due to the insufficient $O/H/OH$ radicals. Therefore, hydroxyl radical and excited hydroxyl radical measurement reflects nitric oxide concentrations in the post-flame zone. The findings agree with the results observed with premixed ammonia/air flames and partially premixed ammonia/hydrogen flames in the literature [136]. OH^* intensities in three regions were illustrated individually in Figure 5.12 (b). Since the transition region is the largest of the three regions, the OH^* intensity is greatest in region II, followed by that of region I, with the weakest OH^* intensity downstream.

In Figure 5.13 (a), it is depicted that OH^* chemiluminescence images of the non-premixed ammonia/hydrogen flames with hydrogen blending ratio at 20%, 30% and 40% at stoichiometric condition. It is worth noting that non-premixed $80\%NH_3/20\%H_2$ flame failed to stabilize by itself, thus a high flow rate of air was injected first to achieve a stable flame, and then decreased to the actual amount for image measurement. The result shows that OH^* chemiluminescence near the nozzle region was evidently enlarged as more hydrogen was involved in the fuel blends. For the case of non-premixed $80\%NH_3/20\%H_2$ flame, OH^* is intense at the region near the nozzle and downstream, showing a weak flame behaviour. As illustrated in Figure 5.13 (b), the overall OH^* intensity is about 37% higher at a hydrogen blending ratio of 20% than at a hydrogen blending ratio of



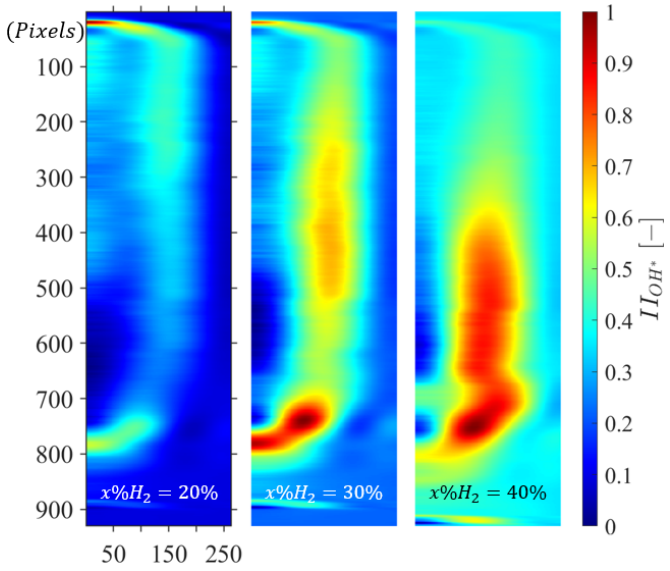
(a)



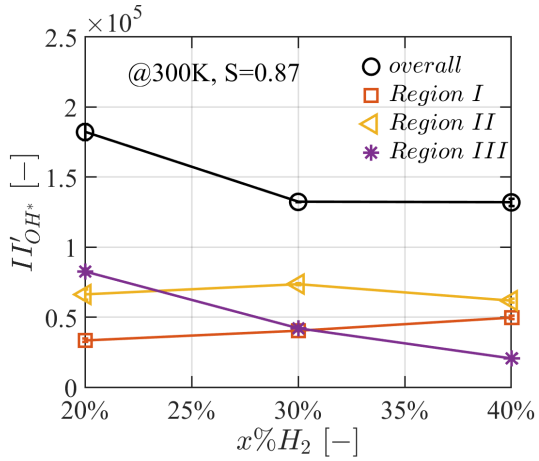
(b)

Figure 5.12: (a) OH^* chemiluminescence profiles (normalised colormap applied) (b) OH^* intensity for non-premixed $60\%NH_3/40\%H_2$ flames with various global equivalence ratios (T_{in} = 300 K, $S = 0.87$).

30% that is almost the same as at the hydrogen blending ratio of 40%. Hydrogen involvement lifted the flame temperature, an increase in NO emission via thermal NO production is expected. However, much higher OH^* concentration was found in $80\%NH_3/20\%H_2$, indicating that the fuel-bound NO route still substantially contributes to NO production and is slightly greater than the effect of increasing



(a)



(b)

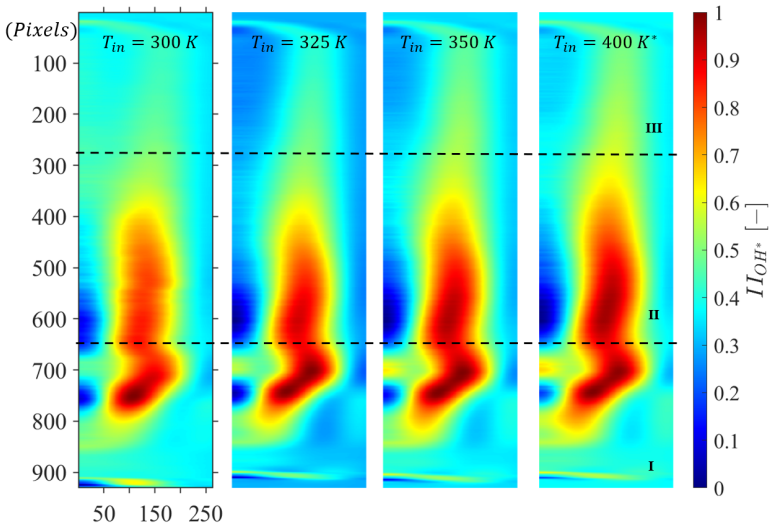
Figure 5.13: (a) OH^* chemiluminescence profiles (normalised colormap applied) (b) OH^* intensity for non-premixed ammonia/hydrogen flames with various hydrogen blending ratios ($\phi_{global} = 1,\ T_{in} = 300$ K, $S = 0.87$).

the hydrogen blending ratio up to 40% when the global equivalence ratio was at 1.0. Figure 5.13 (b) depicts the OH^* intensities in three regions respectively. The OH^* intensity in region III shows a pronounced reducing trend while the OH^* intensity in region I shows an increasing trend. It emphasizes that as the hydrogen

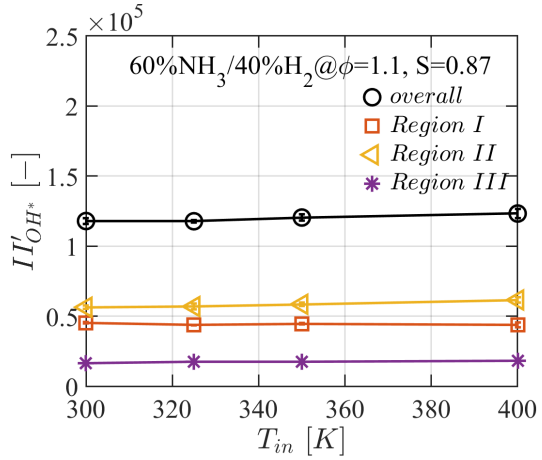
blending ratio rose, the OH^* became more concentrated near the nozzle and the flame became more robust when the hydrogen blending ratio was 40%.

In Figure 5.14 (a), the distributions of OH^* chemiluminescence of non-premixed $60\%NH_3/40\%H_2$ flames are presented with different initial temperature at the global equivalence ratio of 1.1. The details of initial air and fuel temperature has been explained in Section 5.3.2.2. The flame shape remained almost unchanged, but the regions of the peak OH^* concentration (deep red) was expanded. Figure 5.14 (b) also reflects rising the initial temperature has no significant effect on the overall OH^* intensity, with a slight increase observed. It indicates that there was no considerable change in the flame temperature in the current experiment as the initial air temperature rising from room temperature to 350 K and initial fuel temperature rising to 400 K. Therefore, it can explain the result of NO emission in Figure 5.5 which was found almost constant. The OH^* intensity was divided into three regions. Figure 5.14 (b) shows all OH^* intensities in three regions stayed almost unchanged under the different initial temperature.

Three different swirlers were changed to create various flow recirculations in the combustor. The profiles of OH^* chemiluminescence of non-premixed $70\%NH_3/30\%H_2$ flames with different swirlers are presented in Figure 5.15 (a) at the stoichiometric condition under the room temperature. As the vane angle of the swirler varied from 40° to 50°, it can be seen that the angle of the OH^* concentration upstream was deflected, which helped the circulation and mixing ratio of the fuel and air near the nozzle. Additionally, with a higher swirl number, OH^* concentration in the region near the nozzle and transition region expanded, showing a strengthened flame. For instance, when the swirl number reached 1.04, the red marked OH^* chemiluminescence was all the way downstream from the nozzle. Figure 5.15 (b) shows the overall OH^* intensity and OH^* intensities in three regions. It is



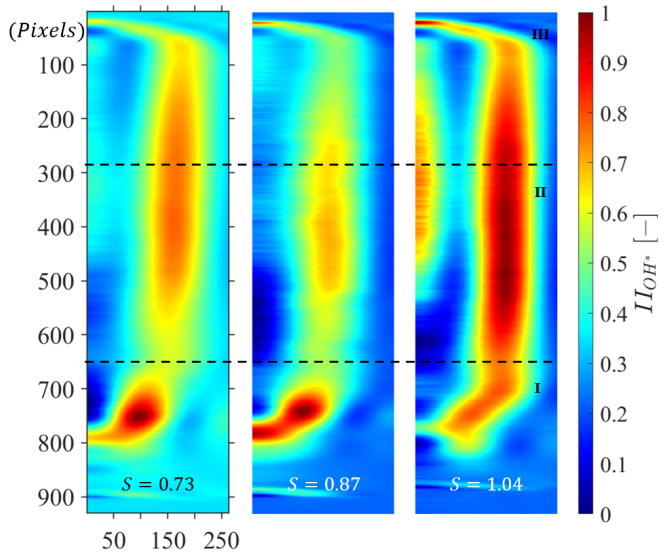
(a)



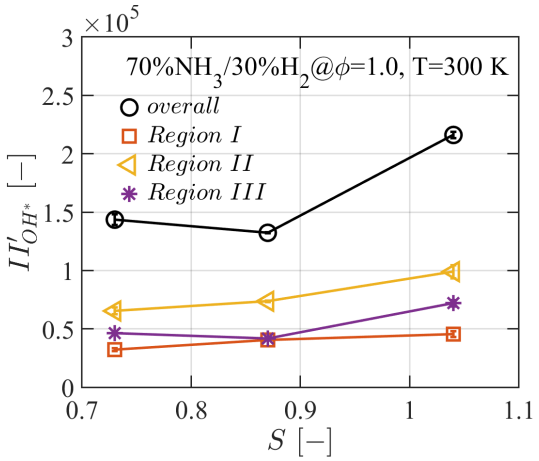
(b)

Figure 5.14: (a) OH^* chemiluminescence profiles (normalised colormap applied) (b) OH^* intensity for non-premixed $60\%NH_3/40\%H_2$ flames at various initial temperature ($\phi_{global} = 1.1, S = 0.87$) (*: initial air temperature: 350 K, initial fuel temperature: 400 K).

notable that the overall OH^* intensity decreased and then increased significantly as the swirl number rose from 0.73 to 1.04, mainly attributed to the OH^* intensity increase in the transition region and downstream. However, the emission results in Figure 5.7 (a) show a higher NO emission was found at the swirl number of



(a)



(b)

Figure 5.15: (a) OH^* chemiluminescence profiles (normalised colormap applied) (b) OH^* intensity for non-premixed $70\%NH_3/30\%H_2$ flames with various swirl numbers ($\phi_{global} = 1.0, T_{in} = 300$ K).

0.73, which does not match the results of OH^* intensity under the same condition. It is necessary to investigate the spatial and temporal information of NO formation pathway (thermal NO and fuel-bound NO) near the nozzle by building a computational fluid dynamics model to understand the reasons behind it.

5.5 Summary

In this chapter, combustion and emission characteristics of non-premixed ammonia/hydrogen flames were studied experimentally with a swirl-enhanced combustor test rig. The blowoff limits were measured firstly to identify the range of stable non-premixed ammonia/hydrogen flame. The effects of global equivalence ratios $(0.6 - 1.2)$, hydrogen blending ratios $(0.2 - 0.4)$, initial gas temperature $(300 - 400$ K), swirl numbers $(0.73, 0.87, 1.04)$ and combustion chamber wall conditions on emissions (NO, NO_2, NH_3, H_2) were analysed. Excited hydroxyl radical (OH^*) chemiluminescence imaging technology was utilised to unveil the flame structure of non-premixed ammonia/hydrogen and its association with NO emission. The main findings are summarized below.

1) Taking the combustion efficiency into account, the optimal emission control occurs at stoichiometric condition. At far-lean equivalence ratios, NO_x and unburned fuel also showed relatively low emissions with hydrogen blending ratio at 20% and 30%; however, flame stability of ammonia and hydrogen should be examined.

2) Increasing hydrogen blending ratios, initial gas temperature and decreasing the swirl numbers are effective ways to broaden the flame stability range of non-premixed ammonia/hydrogen. Robust flames were obtained at hydrogen blending ratio over 20%. More hydrogen involvement resulted in the increase of NO and NO_2 emissions and the decreased ammonia slip. However, the effect was weakened under fuel-rich conditions.

3) With the global equivalence ratio of 1.1, the rising initial temperature has a marginal effect on emissions due to the heat loss from the combustor wall and optical windows. After the non-insulation rig was converted to the wall

insulated condition, NO and NO_2 emissions increased significantly although the ammonia slip decreased considerably.

4) In the current combustor test rig setup, at the global equivalence ratio above 0.8, NO and NO_2 emissions were lower with the swirl number of 0.87 and 1.04 than that with the swirl number of 0.73. It is suggested there is an optimal swirl number for NO_x control and its value changes depending on the geometry and size of combustor.

5) OH^* chemiluminescence distribution can effectively identify the shape of non-premixed ammonia and hydrogen flames. The trend of OH^* intensity was consistent with the results of NO emissions at the same swirl number.

Chapter 6. Comparison of emission characteristics of different ammonia fuelled heat engines

6.1 Introduction

In this chapter, NO_x and ammonia emissions from different types of ammonia-fuelled heat engines in the literature were investigated including Spark-Ignition (SI) engines, Compression-Ignition (CI) engines, Gas Turbines (GTs) and Free Piston Engines (FPEs). A comparison was made between the literature emission data and the modelling results of premixed ammonia/hydrogen combustion in gas turbines in Chapter 4 as well as experimental results of non-premixed ammonia/hydrogen combustion for external combustion engines in Chapter 5. Due to the different units used in emission measurement and oxygen standards for each country, all the emission concentrations in the comparison were converted to dry emission at 15% oxygen level (ppmvd@15%O_2). Indicated specific emissions are in the unit of g/kWh. The findings reflect the current level of key emission species from different ammonia fuelled heat engines. In addition, the most appropriate heat engine using ammonia as fuel in terms of emission control was identified.

6.2 Development of ammonia fuelled heat engines

6.2.1 Spark-ignition engines

Studies on using ammonia for internal combustion engines usually focus on spark-ignition (SI) engines and compression-ignition (CI) engines. Since ammonia has a high octane number (~ 130), it is possible to apply high compression ratios on SI

engines using ammonia without knocking [16]. However, it was found that using neat ammonia as fuel for SI engines is hard to achieve decent engine efficiency and performance due to the slow flame speed and high ignition temperature of ammonia [15]. Thus, a fuel promoter is always introduced to the cylinder in SI engines, such as gasoline [15, 189, 190], hydrogen [16, 191, 192], natural gas [193, 194]. Ryu *et al.* [189] carried out tests in a gasoline and ammonia dual fuelled four-stroke Cooperative Fuel Research (CFR) SI engines with the compression ratio at $10:1$ and constant speed at 1800 rpm. The engine model is Waukesha CFR-48 with a bore and stroke at 82.5 and 114.3 mm, respectively [189]. Gaseous ammonia was the first time to be directly injected into a SI engine with a bespoke injection system. The injection pressure was carefully designed to be sufficient to deliver ammonia gas into the cylinder without ammonia liquification. The engine performance proves that the direct injection of ammonia gaseous was viable. With advanced ammonia injection timing and prolonged injection duration, the power output was improved [189]. In terms of emissions, the brake specific NO_x emission (normalised by engine power output) from ammonia/gasoline dual fuelled engines were observed considerably higher than that from neat gasoline fuelled engines. The increase in ammonia addition resulted in the augment in unburnt ammonia concentration and NO_x emissions. Furthermore, it is also revealed that increasing the engine loads reduced the brake specific NO_x and ammonia emissions. The Korea Institute of Energy Research (KIER) converted a LPG-gasoline bi-fuel 3-cylinder engine into an ammonia/gasoline dual fuelled SI engine [190]. The cylinder bore and stroke were 71 and 84 mm. The tests were measured under the compression ratio at $10.5:1$. Reduction of carbon emissions was expected with the enhancement in ammonia involvement (energy basis). However, unburnt ammonia and NO_x emissions were high and an improved construction of catalytic

converter was required [190]. The engine using $70\%NH_3/30\%$ gasoline (energy basis) was later tested with a customised ECU and released in a vehicle prototype "AmVeh" [190]. The engine performance and emissions of ammonia/hydrogen fuelled SI engine were analysed by Lhuillier *et al.* [16] over various hydrogen blending ratios $(0-60\%)$ and equivalence ratios $(0.6-1.2)$. The four-cylinder SI engine (model: PSA EP6DT) was employed but only one cylinder was fuelled by ammonia and hydrogen. The cylinder bore and stroke were 77 and 85.8 mm. The compression ratio was $10.5:1$ and the speed was stabilised at 1500 rpm. Fuel and air were premixed in a mixer and preheated to 323 K before delivering to the cylinder. Wet emissions (NO, NO_2, N_2O, NH_3) were measured with Gasmet Fourier-Transform InfraRed (FTIR) gas analyser. It concluded that the utilisation of ammonia in SI engine is promising and requires zero or little engine retrofits. Hydrogen addition was helpful in enhancing the engine performance and stability, particularly at the early stage of combustion. It also shows a higher hydrogen blending ratio led to the reduction of the unburnt ammonia at the exhaust but increase in NO_x emission. The levels of NO_x emission from hydrogen/ammonia fuelled SI engines are comparable or even less to that from gasoline fuelled SI engines, even though the formations of NO_x in these two mixtures are different [191, 192]. Thermal NO_x and prompt NO_x are the main routes in gasoline fuelled engines while fuel-bound NO_x and thermal NO_x are the main routes in ammonia/hydrogen dual fuelled engines. Additionally, when using high levels of hydrogen, the wall heat loss problem should be addressed to improve the thermal efficiency. In order to develop an ammonia-powered marine engine, both Oh *et al.* [193] and Wei *et al.* [194] proposed to premix natural gas (mainly methane) with ammonia in the intake manifold before the gas mixture entering the engine cylinder. Oh *et al.* [193] conducted the experiment in a 6-cylinder turbocharged

SI engine with compression ratio at 10.5 : 1. The cylinder bore and stroke were 123 and 155 mm. The experiment was performed at the low speed (840 rpm) and low load which is close to the working condition of practical marine engines [193]. The air-fuel equivalence ratio of 1.5 was identified as the upper limit for ammonia/natural gas dual fuelled SI engines. Owing to the slow flame speed of the mixture, it was observed that at the air-fuel equivalence ratio of 1.5, the combustion efficiency was decreased rapidly (ammonia slip increased dramatically) when increasing ammonia concentration in the fuel blend [193]. Wei *et al.* [194] tested the performance and emissions of an ammonia/natural gas dual fuelled SI engine in a 6-cylinder turbocharged engine with a compression ratio at 11.5 : 1. The cylinders of this four-stroke engine have a bore and stroke of 123 and 145 mm respectively. The combustion duration especially the initial combustion duration was increased with the increase in ammonia concentration in the fuel blends [194]. The best thermal efficiency was 33.6% which was 1% higher than that of pure natural gas fuelled SI engine. Moreover, it was found in both Oh's [193] and Wei's [194] works that as ammonia substitution was increased to 50%vol (or 60%vol in Wei's work), carbon dioxide and carbon monoxide emissions decreased significantly, but NO_x emission and ammonia slip increased as shown in Figure 6.1 [193, 194]. Meanwhile, the peak pressure was either reduced or maintained at the same level with a higher ammonia blending ratio. It implies thermal NO_x formation was supposed to decrease in the total NO_x formation, however, the overall NO_x emission deteriorated. Therefore, fuel-bound NO_x was concluded to dominate the overall NO_x emission.

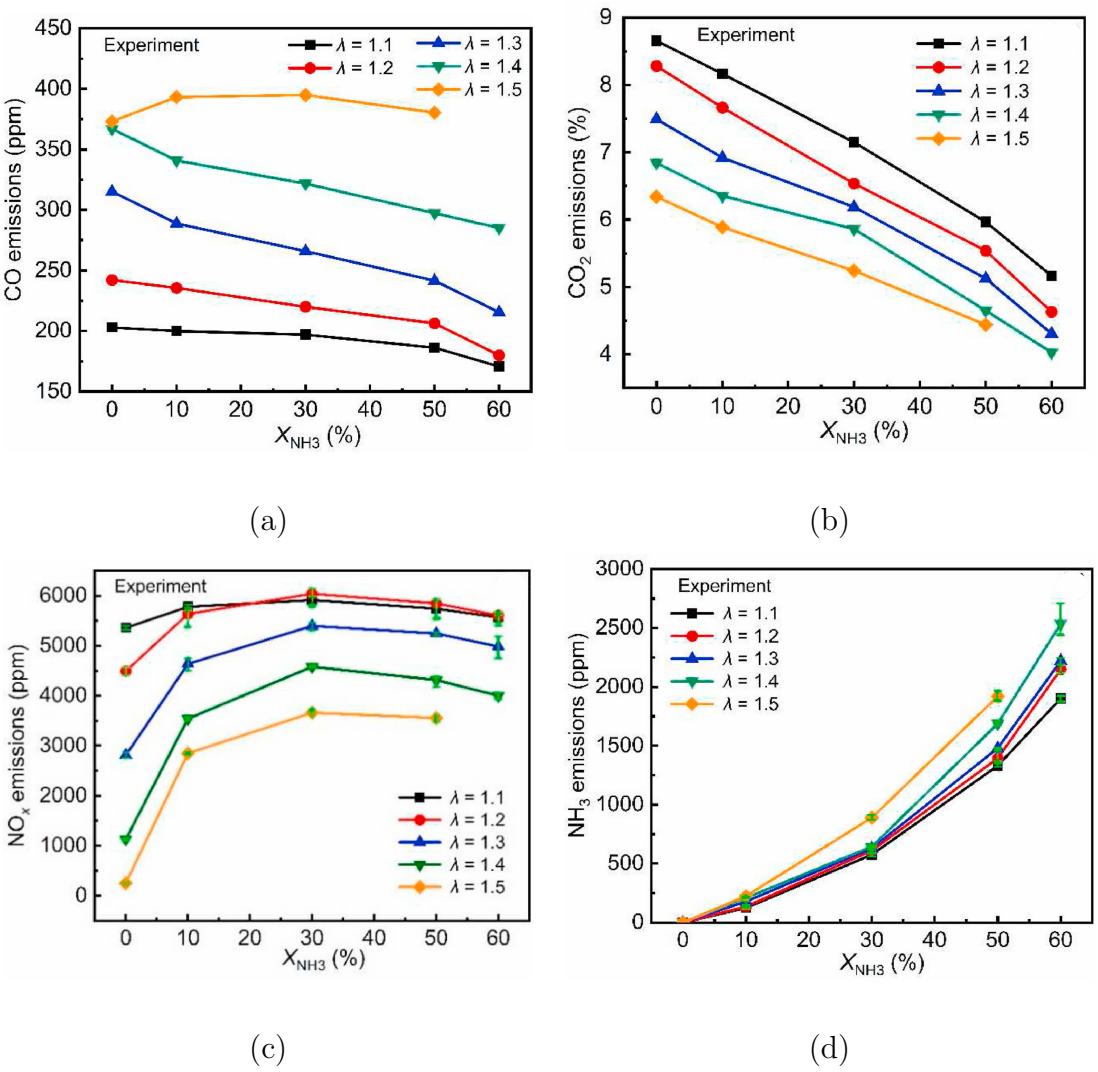


Figure 6.1: (a) CO, (b) CO_2, (c) NO_x and (d) NH_3 emission from Ammonia/natural gas SI engine [194].

6.2.2 Compression-ignition engines

CI engines are capable of maintaining high thermal efficiency and long-term operability under high loads, therefore they have been widely used in heavy transport, power plants, and marine applications [195]. The use of ammonia in CI engines has been discussed in many studies in order to decarbonise heavy transport. Ryu *et al.* [143] studied the CI engine performance using ammonia and dimethyl ether

(DME). DME has a high cetane number and its vapor pressure is similar to that of ammonia. The test engine was a four-stroke single-cylinder with a bore and stroke of 78 and 67 mm [143]. The compression ratio was 20 : 1. The injection system and cylinder head were modified to allow controlled ammonia injection. Pure DME was first injected to warmup the engine, then ammonia was introduced and the desired fuel blend ratio was achieved. Due to the high autoignition of ammonia, advanced injection timing was necessary. The results showed with a higher ammonia concentration in the fuel blends, the injection timing range had to be advanced even further. For instance, the optimal injection timing range for 20%NH_3/80%DME, 40%NH_3/60%DME and 60%NH_3/40%DME was $5-35$ BTDC °CA, $20-50$ BTDC °CA and $90-340$ BTDC °CA, respectively [143]. As a highly advanced injection timing was applied for 60%NH_3/40%DME blend, fuel and air were completely premixed which causes the homogeneous charge compression ignition (HCCI) combustion [143]. Yousefi *et al.* [195] analysed the effect of ammonia energy fraction and start diesel injection timing (SODI) on the emissions of an ammonia/diesel dual-fuel CI engine. The engine model was Caterpillar 3401 and the bore and stroke of the single cylinder were 137.2 and 165.1 mm [195]. The premixed ammonia and air blend was drawn into the engine cylinder and compressed during the intake and compression strokes. A separate diesel injection to the engine cylinder triggered the ignition process. The compression ratio was 16.25 : 1, which is much lower than the required compression ratio of neat ammonia fuelled CI engines (35 : 1) [14]. As ammonia energy fraction rose to 40%, thermal DeNO_x process was promoted, in which NO was consumed by the radical NH_2 generated from the combination of ammonia and hydroxyl and oxygen atoms. It led to a 58.8% reduction of NO_x emission. However, with a higher ammonia energy fraction, the increase in N_2O was observed which led to a higher GHG (Greenhouse

gas) emissions. The GHG emissions produced by N_2O exceed the GHG emissions saved by the reduction in carbon emissions. Consequently, as illustrated in Figure 6.2, comparing to sole diesel fuelled CI engines, ammonia/diesel dual-fuelled CI engines produced a higher GHG emissions overall [195]. In addition, N_2O can

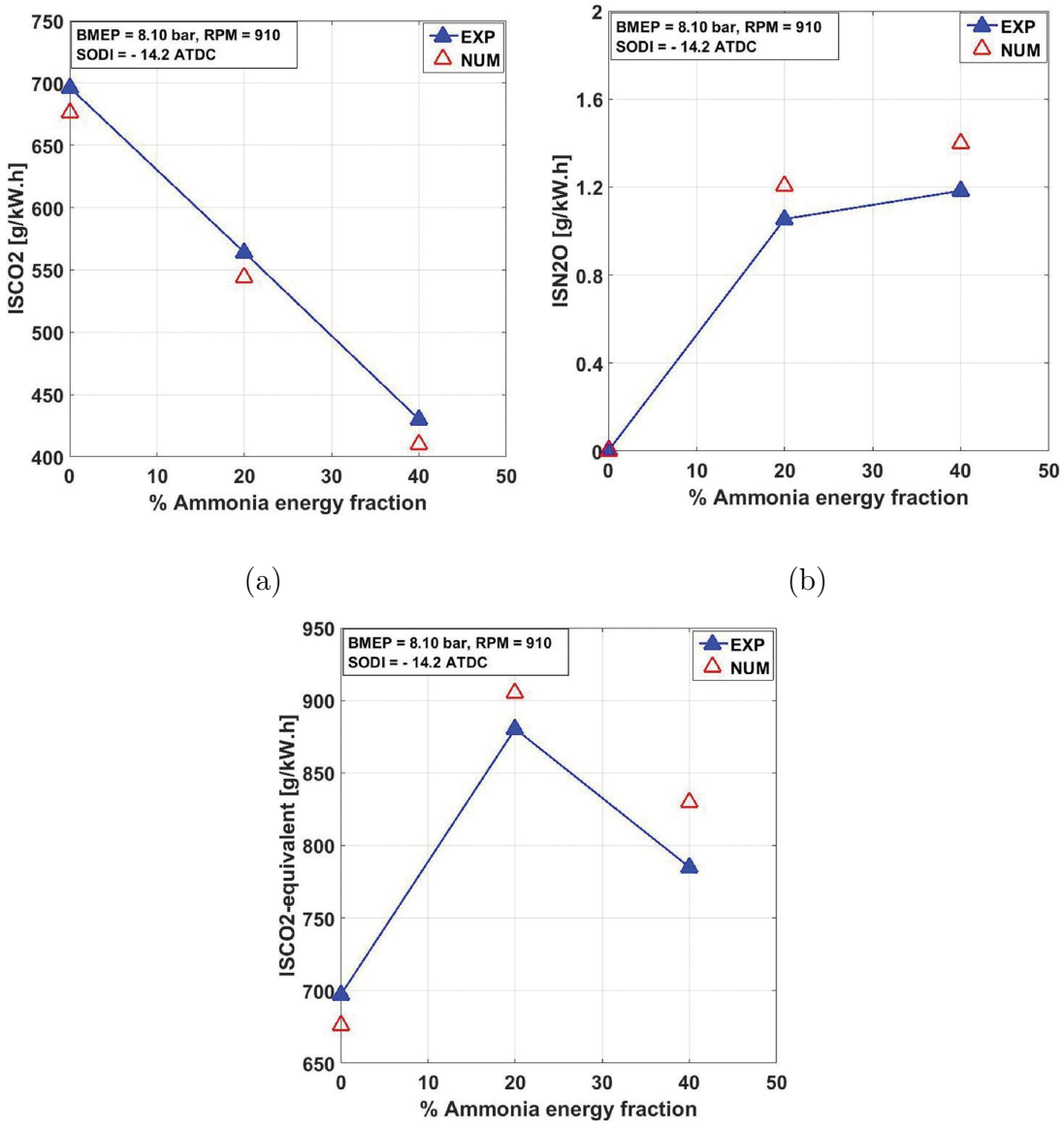


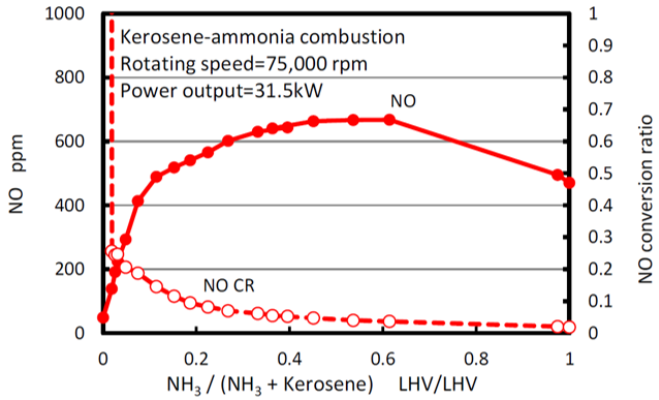
Figure 6.2: (a) Indicated specific CO_2, (b) indicated specific N_2O and (c) GHG emissions from ammonia/diesel dual fuelled CI engines [195].

be reduced with advanced SODI. The minimum N_2O emission of 0.6 g/kWh was achieved when the advance SODI was at $-24°$ ATDC (after top dead centre) [195]. In another work, Yousefi *et al.* [196] investigated different types of diesel injection strategies in an ammonia/diesel duel fuelled CI engine by changing to two-pulse diesel injection, diesel split ratios, start and end of pre and main diesel injection. The indicated thermal efficiency reached highest at approximately 40% with the split diesel injection strategy (40% pilot diesel injection and 60% main diesel injection, start of pre diesel injection at $-46°$ ATDC and start of main diesel injection at $-16°$ ATDC) [196]. The maximum ammonia energy share (energy fraction) which can substitute diesel was measured by Nadimi *et al.* [197] with a single cylinder CI engine at full load and constant engine speed at 1200 rpm. The compression ratio was $16.5:1$. It concluded that the maximum ammonia energy fraction that could keep the ammonia/diesel dual-fuelled CI engine operating was 84.2%. The NO emission was reduced with the growth of ammonia energy fraction up to 27.9%, which is consistent with the finding in Yousefi's work [195]. It was mainly because less NO was produced from the thermal NO route as ammonia flame temperature is much lower than that of diesel. With a further increase of ammonia energy fraction, NO emission substantially increased owing to the fuel-bound NO formation. Both NO_2 and N_2O emissions were higher when ammonia was added to the fuel than those of neat diesel fuelled CI engine. A monotonically increasing trend of ammonia emission was observed with more ammonia injected to the cylinder. In Sivasubramanian's work [198], rather than using diesel, biodiesel (mustard methyl ester) was chosen as a fuel promoter for ammonia fuelled CI engine. NO_x emission was tested in a single-cylinder CI engine at various loads. The compression ratio was $18:1$. It was found the increase in load led to an augment of NO_x emission. Diesel fuelled CI engine produced the least NO_x emission among the four blends

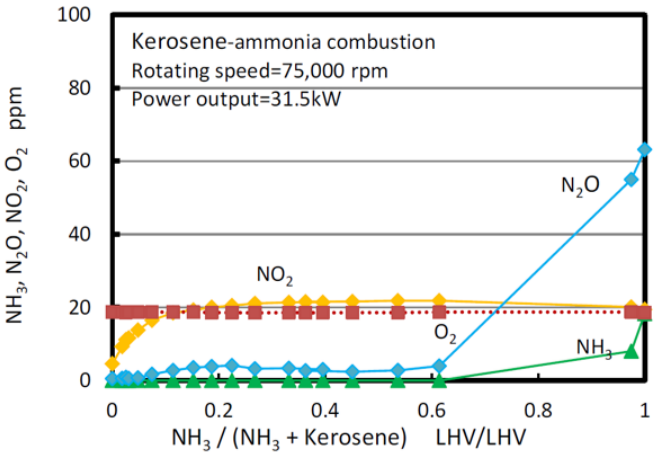
(pure biodiesel, pure diesel, 90% biodiesel/10% ammonia and 80% biodiesel/20% ammonia). Conversely, NO_x emission from pure biodiesel fuelled CI engine was the highest. Ammonia addition to biodiesel helped to reduce the NO_x emission, which was claimed to attribute to the high octane number of ammonia [198].

6.2.3 Gas turbines

The last decades have seen a growing interest in gas turbines (GT) fuelled by ammonia and various ammonia blends. Micro GT powered by ammonia/kerosene [60, 146, 147], ammonia/methane [145, 147] and neat ammonia [145, 146, 147] in non-premixed mode were successfully implemented by the National Institute of Advanced Industrial Science and Technology (AIST) in Japan with Tohoku University during 2014-2020. According to the measured results from an output power of 21 kW micro GT, higher ammonia concentration of the ammonia/kerosene fuel blends deteriorates NO_x emissions [60]. The maximum NO emission in the measurements reached approximately 550 ppmv ($\sim$ 1500 ppmv@15%O_2). Figure 6.3 presents the emissions performance of ammonia/kerosene fuelled 31.5 kW micro GT. As ammonia energy fraction rose, NO emission was increased and reached peak when ammonia energy fraction was around 60%, and then started to decrease [147]. For comparison, emission performance of ammonia/methane fuelled micro GT with output power of 31.4 kW was tested. The emission trends were similar to that fuelled by ammonia and kerosene, and NO emission was over 600 ppm when ammonia energy fraction was $30\% - 90\%$. In the pure ammonia fuelled micro GT, it was expected that NO emission increased monotonously and rapidly as the inlet temperature rose because of the promoted thermal NO formation and ammonia emission was reduced to almost null when the inlet temperature reached 850 K [145]. Although SCR (Selective catalytic reduction) units assisted



(a)



(b)

Figure 6.3: (a) NO, NO conversion ratio and (b) NH_3, N_2O, NO_2, O_2 emission from ammonia/kerosene GT [147].

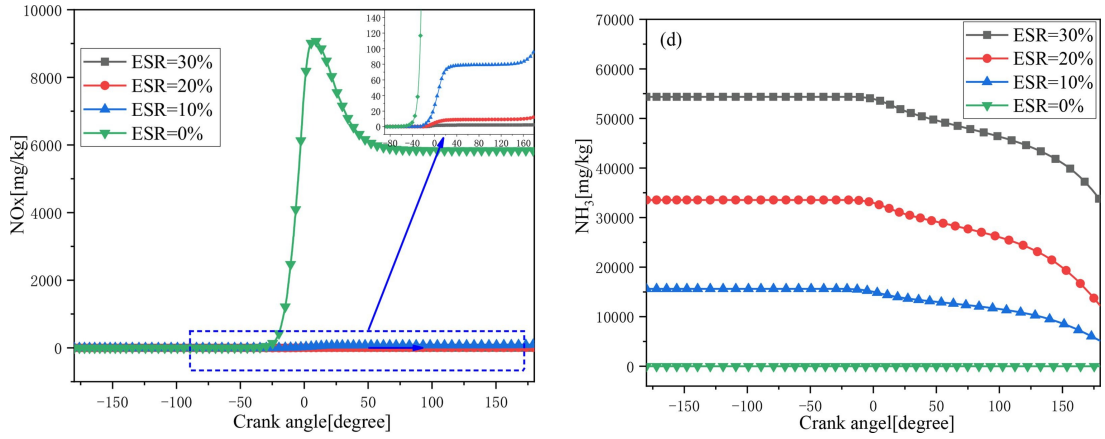
NO_x minimization to an acceptable level in the previous micro gas turbine studies, the cost of larger scale SCR system, such as building cost and maintenance cost, remains a challenge for medium and large scale gas turbines [148]. Therefore, a neat ammonia combustor with two-zone rich-lean burn configuration was developed to minimize the emissions [148]. It concluded that the increase in fuel nozzle angle (0°, 30°, 45°) lessened NO emission. The lowest NO emission was found in two cases where the fuel nozzle angle was 45° [148]. Besides, it was found that

no additional regenerative heat exchanger was required for ammonia reduction because ammonia slip was inhibited at the inlet combustion temperature below 800 K [148].

6.2.4 Free piston engines

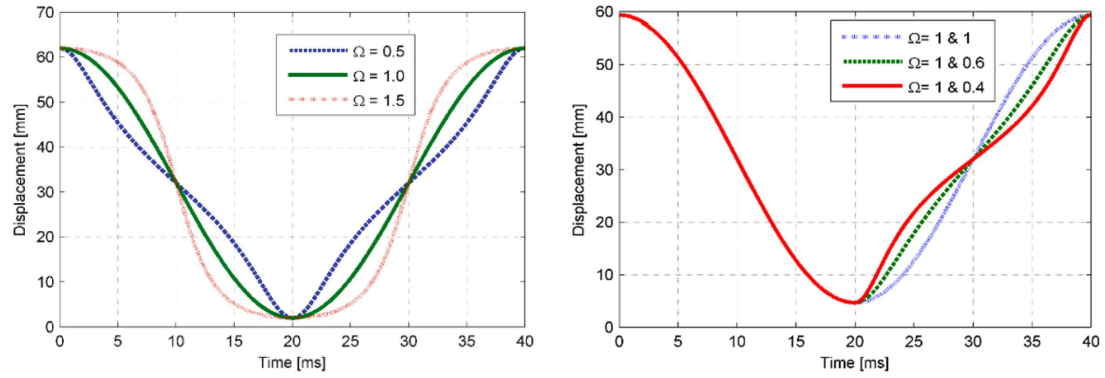
Free piston engine (FPE) is a novel engine that can be operated as an internal or an external combustion engine. Recently, the use of ammonia for FPE has also attracted the attention of some researchers. A stable operation of ammonia/methane dual-fuelled FPE generator was achieved by Huang *et al.* [199]. Ammonia, methane and air were premixed before entering the cylinder. The operation stability and engine performance were experimentally studied, which found that the growth of the ammonia energy fraction led to a deterioration in the stability of the operation. Combustion performance was analysed numerically. More ammonia addition lowers the flame temperature, promotes NH_2 generation and reduces combustion efficiency, which inhibits thermal NO_x production and promotes NO consumption through NH_2 to generate nitrogen. Consequently, NO_x emission was lessened as more ammonia was involved as shown in Figure 6.4 (a). Unburnt ammonia at the end of cycle was moderately increased as ammonia energy fraction rose [199]. Zhang *et al.* [200] studied numerically the effect of compression ratio and piston trajectory shape (symmetric and asymmetric) of a neat ammonia fuelled FPE on engine and combustion performance such as thermal efficiency, peak pressure location, exhaust temperature. The initial temperature and pressure were set as 473 K and 1 bar [200]. Ω_{comp} and Ω_{exp} represent the piston motion pattern during the compression and expansion process respectively. Figure 6.5 depicts the examples of various piston motion patterns. The findings show increasing compression ratio, Ω_{comp} and Ω_{exp} generally led to the increase

in NO_x. However, when the compression ratio is too high (27 : 1), increasing Ω_{comp} resulted in NO_x reduction due to heat loss [200]. It was concluded that the thermal efficiency reached the highest when the compression ratio was 25 : 1 and the trajectory shape was symmetric with Ω_{comp} and Ω_{exp} at 0.5 [200].



(a) (b)

Figure 6.4: (a) NO_x emission and (b) NH_3 emission from ammonia/methane dual-fuelled FPE [199]. (ESR refers to ammonia energy fraction.)



(a) (b)

Figure 6.5: Examples of (a) symmetric and (b) asymmetric piston motion patterns [200].

6.3 Calculation methodology for emission comparison

The experimental emissions from SI engines, CI engines, GTs involving ammonia as fuel are summarized in Table 6.1, 6.3, 6.4. Due to the lack of experimental emission results for ammonia-fuelled FPEs, the simulated emissions are presented in Table 6.5. As the utilisation of ammonia reduces the carbon emissions, only NO_x, unburnt ammonia and hydrogen are focused. However, it is rare to find unburnt hydrogen emissions in the literature. When developing disruptive heat engines, thermal efficiencies, indicated thermal efficiencies power output and emissions are the most critical parameters. The emissions were chosen when the engine performance achieved their highest thermal efficiency (HTE), highest indicated thermal efficiency (HITE), highest power output (HP), lowest NO_x emissions (LNE), lowest ammonia emission (LAE) and lowest GHG emissions (LGHG).

The emissions were post-processed for comparison. First of all, all the data were collected either from literature or estimated using a plot digitizer tool. The ammonia energy fraction ratio and ammonia mass fraction ratio were converted to ammonia mole fraction ratio. In the field of heat engines, the air-fuel equivalence ratio (λ) is commonly used, which has been converted to the fuel-air equivalence ratio using Equation 6.3.1, where x denotes the molar fraction, and *stoich* denote value under the stoichiometric condition.

$$\phi = \frac{1}{\lambda} = \frac{1}{\frac{x[oxidant]/x[fuel]}{x[oxidant,stoich]/x[fuel,stoich]}} \tag{6.3.1}$$

The emission is usually considered in concentration in the tailpipes, such as ppm,%. The emissions can be measured on a wet or dry basis depending on the measurement equipment. A moisture correction factor (F_m) is therefore required to multiply with the wet concentrations using Equation 6.3.2 and 6.3.3

[166]. Water represents the water percentage in the tailpipe. It is rare to obtain measured water value in the literature. Since it was reported that $6-8\%$ water in the coal combustion exhaust, 8% is assumed in the present work for water content [201]. Furthermore, oxygen normalisation is also applied to the emissions so as to maintain the oxygen level in the exhaust gas at 15% using Equation 3.3.9 in Chapter 3. Therefore, emissions units were converted to ppmvd@15%O_2. However, when the application has a power output, weight of emissions normalised by power output is considered as the unit for indicated specific emissions, for example, g/kWh, lb/btu.

$$F_m = \frac{100}{100 - water} \tag{6.3.2}$$

$$ppm_{dry} = ppm_{wet} \times F_m \tag{6.3.3}$$

The conversion of emission results from mass basis to concentration basis requires some important information (e.g. molar mass of the exhaust for individual cases) which is usually missing in the literature. Therefore, the emissions data listed in this section is based on either concentration basis (ppmvd@15%O_2) or mass basis (g/kWh). An example is shown below using the NO emission data in the reference [195]:

$$ppmv(NO) = \frac{m(NO)/M(NO)}{m(exh)/M(exh)} \tag{6.3.4}$$

The conversion formula is shown in Equation 6.3.4, where $ppmv(NO)$ is emission based on concentration basis; m and M refers to mass and molar mass of the species; subscript exh denote the exhaust gas. Given the mass flow rates of ammonia (3.01 kg/h) and diesel (1.96 kg/h) as well as the lower heating values of

ammonia (18.5 MJ/kg) and diesel (43.45 MJ/kg), one hour of the input thermal power is calculated as $(18.5 \times 3.01 + 43.45 \times 1.96) \times 1 = 140.847$ MJ/h= 39.13 kWh. The thermal efficiency was provided as approximately 37.8%. The output power is therefore $39.13 \times 37.8\% = 14.8$ kWh. NO emission is known as 9 g/kWh. Hence, $m(NO) = 9 \times 14.8 = 133.2$ g. Based on the principle of conservation of mass, the mass of exhaust gas is equal to the total mass of inlet ammonia, diesel and air, which is 82750 g. Since fuel in CI engines is generally burnt at fuel-lean conditions where air is the main component, the exhaust gas of ammonia blends in CI engines is assumed to be mainly air. In this case, the molar mass of the exhaust gas is assumed to be that of air, which is 29 g/mol. Therefore, using Equation 6.3.4, the concentration of NO emission can be calculated as 1556 ppmv. The discrepancy with the measurements in the literature [195] (1461 ppmv) is due to the lack of the exact molar mass of the exhaust gas.

6.4 Comparison results

In Table 6.1, it can be seen that premixed type of ammonia flames with fuel promoter was widely investigated in SI engines. When the equivalence ratio was 0.8, both 82.7% ammonia/ 17.3% hydrogen and 30% ammonia/ 70% natural gas fuelled SI engines reached their highest thermal efficiencies at 28.3% and 33.5%, respectively [191, 194]. Due to the significant fuel-bound NO_x and thermal NO_x formation at fuel-lean conditions, NO_x emission was observed at around 1900 ppmvd@15%O_2. It reveals that the high thermal efficiency in SI engine is accompanied by significant NO_x emissions. In the case of using 80%NH_3/20%H_2 blends, the highest indicated thermal efficiency ($\sim$ 39%) occurred at stoichiometric condition [16], which is in the range of the ideal equivalence ratio for emission control as reported in the findings in Section 4.3.3, Chapter 4. NO_x emission was rela-

tively low at 926.1 ppmvd@15%O_2 [16]. The highest power output was recognised with 90%NH_3/10%H_2 blends, but there was still 568 ppmvd@15%O_2 NO_x at the exhaust gas [192]. As expected, the cases with lowest NO_x emission occurred at the fuel-rich conditions. It was found in the range of $1 - 1.2$, NO_x emission can be less than 100 ppmvd@15%O_2. However, ammonia emission is relatively high due to the incomplete combustion, which was 1489.6 ppmvd@15%O_2 in some case [16]. As aforementioned in Chapter 4, there is a trade-off between NO_x emission and unburnt ammonia emission, NO_x emission was very high in the cases with lowest ammonia emissions. For instance, 40%NH_3/60%H_2 duel fuelled SI engine emitted 2745.8 ppmvd@15%O_2 NO_x and 474.3 ppmvd@15%O_2 unburnt ammonia [16]. In the ammonia/natural gas fuelled SI engine, an optimal point was suggested in consideration of turbulent flame propagation and piston movement with a high NO_x emission at 32.4 g/kWh [193]. NO_x emission is much more than the proposed EURO 7 regulation standards shown in Table 6.2.

Fuel is ignited in a diesel engine by the elevated temperature in the cylinder due to a high geometrical compression ratio. The fuel-air mixing ratio highly depends on the injection timing and strategy. If the fuel injection time and air intake time are early enough, the fuel and air are fully premixed. If the fuel injection time is late and closer to the ignition time, fuel and air are most likely to be non-premixed. In ammonia/diesel dual fuelled CI engines, the ammonia blends and the air are delivered to the chamber during the intake stroke, compressed during the compression stroke, and then ignited with diesel direct injection. It is considered to be partially premixed combustion. Emissions from CI engines fuelled by ammonia/diesel blends using single diesel injection mode and diesel split injection mode, as well as ammonia/biodiesel and ammonia/DME blends were included in Table 6.3. The fuel-air equivalence ratio (or air-fuel equivalence

Table 6.1: Summary of experimental emissions from ammonia fuelled SI engines.

Ammonia amount (%vol.)	**Flame type**	**Fuel promoter**	ϕ	**Emissions**				**ref**
				NO	NO_2	NH_3	**Conditions**	
80%	premixed	H_2	1.0	926.1 ppmvd@15%O_2		1852.2 ppmvd@15%O_2	HITE(39%)	[16]
40%	premixed	H_2	1.2	97.7 ppmvd@15%O_2		1489.6 ppmvd@15%O_2	LNE	[16]
40%	premixed	H_2	0.6	2745.8 ppmvd@15%O_2		474.3 ppmvd@15%O_2	LAE	[16]
NA	premixed	Gasoline	NA	56.3 g/kWh		2.9 g/kWh	LNE	[189]
82.7%	premixed	H_2	0.8	1862.9 ppmvd@15%O_2		NA	HTE (28.3%)	[191]
76.1%	premixed	H_2	1.0	1064.8 ppmvd@15%O_2		NA	LNE	[191]
90%	premixed	H_2	1.0	568 ppmvd@15%O_2		NA	HP	[192]
80%	premixed	H_2	1.1	142 ppmvd@15%O_2		NA	LNE	[192]

Table 6.1 Summary of experimental emissions from ammonia fuelled SI engines.(Continued)

Ammonia amount (%vol.)	**Flame type**	**Fuel promoter**	ϕ	**Emissions**				**ref**
				NO	NO_2	NH_3	**Conditions**	
41%	premixed	Natural gas	0.7	32.4 g/kWh		2.6 g/kWh	Suggested optimal point	[193]
30%	premixed	Natural gas	0.8	1991.0 ppmvd	@15%O_2	226.0 ppmvd@15%O_2	HTE(33.5%)	[194]
80%	premixed	H_2	1.0	150 ppmvd @15%O_2	1 ppmvd @15%O_2	676.2 ppmvd @15%O_2	LNE	[202]
80%	premixed	H_2	0.9	1283.9 ppmvd @15%O_2	13.1 ppmvd @15%O_2	219.5 ppmvd @15%O_2	LAE	[202]

Table 6.2: Proposed EURO 7 regulation standards of NO_x and ammonia emissions for buses and commercial trucks with internal combustion engines [203].

	NO_x (g/kWh)	NH_3 (g/kWh)
$WHTC_{cold}$	0.35	0.065
$WHTC_{hot}$	0.09	0.065

*WHTC: World Harmonized Transient Cycle

ratio) was not always provided in the literature, an assumption has been made for the fuel-air equivalence ratio to be 0.6 in that case. It was concluded that dual fuel diesel split injection mode had the best indicated thermal efficiency (39.7%) compared to duel fuel single injection mode and diesel only single injection mode [196]. It produced 8 g/kWh ammonia emissions which is lower than all the cases conducted with single diesel injection mode. NO_x emission was 10 g/kWh which is more than that from CI engines with the single diesel injection mode. The diesel split injection mode effectively reduced the unburnt ammonia. Up to 83.5% of ammonia emission was reduced when switching from dual fuel single injection mode to dual fuel diesel split injection mode [196]. GHG emissions, namely, total equivalent CO_2 emissions were obtained by calculating the sum of the indicated specific CO_2 and three hundred times of indicated specific N_2O [195]. The lowest GHG emission was recognised in different diesel injection strategies. Two sets of lowest GHG emissions (525.51 g/kWh and 478.1 g/kWh) from dual fuelled diesel split injection mode were achieved with 40% pilot diesel injection and 60% main diesel injection, start of pre diesel injection at $-57°$ ATDC and start of main diesel injection at $-16°$ ATDC and $-20°$ ATDC, respectively [196]. Meanwhile, NO_x emission was 11.09 and 15.24 g/kWh while ammonia emission was 3.2 and 2.56 g/kWh. In single diesel injection mode, the lowest GHG emission (606.2 g/kWh) was found when start of main diesel injection at $-24°$ ATDC [195]. At that point, NO_x emission was less at 9 g/kWh (528.882 ppmvd@15%O_2) but ammonia emission reached 15.53 g/kWh (1609.1 ppmvd@15%O_2) [195]. When diesel, biodiesel and DME were considered as a fuel promoter for CI engines, the lowest NO_x could achieve 208.2 ppmvd@15%O_2, 108.6 ppmvd@15%O_2 and 3.5 g/kWh, respectively. The lowest ammonia slip could achieve 6.3 g/kWh with DME as the fuel promoter. However, the lowest emissions are still greater than

the proposed EURO 7 regulation standards where NO_x emission is less than 0.35 g/kWh and ammonia emission is less than 0.065 g/kWh in Table 6.2.

Table 6.4 presents emissions produced from ammonia fuelled single-zone and two-zone rich-lean gas turbines. The ammonia amount was based on energy fraction in these literature and the detailed flow rates of fuel and air in each case were not included. Neat ammonia fuelled two-zone micro gas turbine managed to achieve approximately 22% of thermal efficiency with NO emission at 709.7 ppmvd@15%O_2 and ammonia emission at 0.6 ppmvd@15%O_2 [148]. Both emissions were lower than those from ammonia/methane fuelled single-zone gas turbine at their highest thermal efficiencies. The lowest NO_x emission cases were identified, showing the NO_x emission from ammonia fuelled gas turbine can be minimized to 506.04 ppmvd@15%O_2 in single-zone gas turbine [145] and 404.4 ppmvd@15%O_2 in two-zone gas turbine [148]. Meanwhile, unburnt ammonia was reduced to 1.2 ppmvd@15%O_2 in two-zone gas turbine [148], which is even lower than the lowest ammonia emission (15.8 ppmvd@15%O_2) achieved in single-zone gas turbine [145]. The reason is that the secondary air promoted the consumption of the large amount of unburnt ammonia produced in the first-zone combustion. Gas Turbine Research Centre (GTRC) in Cardiff University has also conducted ammonia combustion experiments for gas turbine applications [62, 101, 204]. The best emissions from their combustor were reduced to 23.4 ppmvd@15%O_2 NO_x and 9.4 ppmvd@15%O_2 NH_3. More details were discussed in Section 2.3, Chapter 2. Additionally, simulated results in Section 4.4, Chapter 4, and experimental results in Section 5.3.2, Chapter 5 were listed together in the Table 6.4 for comparison. Ammonia emission from gas turbine modelling of premixed ammonia/hydrogen combustion was only 0.4 ppmvd@15%O_2. This is much less than other single-zone gas turbine cases as premixed flame effectively improves the combustion efficiency

Table 6.3: Summary of experimental emissions from ammonia fuelled CI engines.

Ammonia amount (%vol.)	**Flame type**	**Fuel promoter**	ϕ	**Emissions**				**ref**
				NO	NO_2	NH_3	**Conditions**	
94.8%	Partially premixed	Diesel	0.6	5.9 g/kWh	NA	15.8 g/kWh	HITE (38.4%)	[195]
94.8%	Partially premixed	Diesel	NA	9 g/kWh	NA	15.53 g/kWh	LGHG	[195]
94.8%	Partially premixed	Diesel	0.6	528.9 ppmvd @15%O_2	NA	1609.1 ppmvd @15%O_2	LGHG	[195]
40%	Partially premixed	DME	NA	3.5 g/kWh		8.5 g/kWh	LNE	[143]
60%	Partially premixed	DME	NA	6.4 g/kWh		6.3 g/kWh	LAE	[143]
94.7%	Partially premixed (diesel split injection)	Diesel	NA	10 g/kWh		8 g/kWh	HITE (39.7%)	[196]

Table 6.3 Summary of experimental emissions from ammonia fuelled CI engines.(Continued)

Ammonia amount (%vol.)	**Flame type**	**Fuel promoter**	ϕ	**Emissions**				**ref**
				NO	NO_2	NH_3	**Conditions**	
94.7%	Partially premixed (diesel split injection)	Diesel	NA	11.09 g/kWh		3.2 g/kWh	LGHG	[196]
94.7%	Partially premixed (diesel split injection)	Diesel	NA	15.24 g/kWh		2.56 g/kWh	LGHG	[196]
99.3%	Partially premixed	Diesel	0.7	883 ppmvd @15%O_2	59.4 ppmvd @15%O_2	6027.2 ppmvd @15%O_2	HITE (37.6%)	[197]
82.4%	Partially premixed	Diesel	0.7	186.5 ppmvd @15%O_2	21.7 ppmvd @15%O_2	1544 ppmvd @15%O_2	LNE	[197]
20%	NA	Biodiesel	NA	108.6 ppmvd@15%O_2		NA	LNE	[198]

Table 6.4: Summary of emissions from ammonia fuelled GTs.

Ammonia amount (%vol.)	**Flame type**	**Fuel promoter**	ϕ	**Emissions**				**ref**
				NO	NO_2	NH_3	**Conditions**	
NA	Non-premixed	CH_4	NA	1219 ppmvd @15%O_2	43.9 ppmvd @15%O_2	3.3 ppmvd @15%O_2	HTE (22.2%)	[145]
100%	Non-premixed	NA	NA	506 ppmvd @15%O_2	NA	2018.7 ppmvd @15%O_2	LNE	[145]
100%	Non-premixed	NA	NA	1496.9 ppmvd @15%O_2	NA	15.8 ppmvd @15%O_2	LAE	[145]
100%	Non-premixed	NA	Primary: 1.1 (two-zone combustion)	709.7 ppmvd @15%O_2	NA	0.6 ppmvd @15%O_2	HTE (21.2%)	[148]
100%	Non-premixed	NA	Primary: 0.9 (two-zone combustion)	404.4 ppmvd @15%O_2	NA	1.2 ppmvd @15%O_2	LNE	[148]
61%	Premixed	CH_4	1.23	23.4 ppmvd@15%O_2		9.4 ppmvd @15%O_2	LNE&LAE	[101]
60%	Premixed	H_2	1.1	616.3 ppmvd @15%O_2	0.1 ppmvd @15%O_2	0.4 ppmvd @15%O_2	LNE	Chapter 4
60%	Non-premixed	H_2	1.0	14.5 ppmvd @15%O_2	3.1 ppmvd @15%O_2	476.5 ppmvd @15%O_2	Suggested point	Chapter 5

Table 6.5: Summary of simulated emissions from ammonia fuelled FPEs.

Ammonia amount (%vol.)	**Flame type**	**Fuel promoter**	ϕ	**Emissions**				**ref**
				NO	NO_2	NH_3	**Conditions**	
51.6%	Premixed	CH_4	1.0	1.5 ppmvd@15%O_2		10095.6 ppmvd @15%O_2	LNE	[199]
21.8%	Premixed	CH_4	1.0	20.7 ppmvd@15%O_2		1484.7 ppmvd @15%O_2	LAE	[199]
100%	Premixed	NA	0.3	4769.6 ppmvd@15%O_2		NA	HTE (58.1%)	[200]

and reduce the unburnt fuel at the exhaust. In the non-premixed ammonia/hydrogen combustor, the best emission control was found with NO emission at 14.5 ppmvd@15%O_2 and ammonia emission at 476.5 ppmvd@15%O_2.

Considering that ammonia fuelled FPEs are still a very new concept, very few investigations have yet been conducted. Only simulated emission results were found in the literature and listed in Table 6.5. It was found that neat ammonia fuelled FPE could achieve up to 58.1% of thermal efficiency, but NO_x emission was very high (4769.6 ppmvd@15%O_2) [200]. Based on the simulation results, NO_x emission from ammonia/methane fuelled FPE could be minimized to 1.5 ppmvd@15%O_2 but a very high level of unburnt ammonia was noticed. The lowest ammonia emission was still at 1484.7 ppmvd@15%O_2.

6.5 Summary

In this chapter, the state-of-the-art of emissions from ammonia fuelled heat engines were analysed and compared. The emissions were normalised to the same concentration units (ppmvd@15%O_2) or mass-based units (g/kWh). The main findings are shown below:

1) The use of ammonia as fuel for SI engines were widely investigated with fuel promoters such as natural gas, hydrogen and gasoline. Fuel and air are premixed in a mixer before entering the engine cylinder. In CI engines, ammonia is considered to blend with diesel, biodiesel and DME in the cylinder.

2) Optimizing the thermal efficiency of SI and CI engines using ammonia always comes with the penalty of high NO_x emissions (SI: $\sim$ 1990 ppmvd@15%O_2 with thermal efficiency at 33.5%; CI: $\sim$ 900 ppmvd@15%O_2 with indicated thermal efficiency at 37.6%). The relationship between ammonia emission

and NO_x emission is negatively correlated.

3) In ammonia/diesel dual fuelled CI engines, split diesel injection is an effective method to control the ammonia emission. The lowest ammonia emission was 2.56 g/kWh, which was 83.5% lower than that from dual fuel single injection mode. Meanwhile, NO_x emission was 15.24 g/kWh and it was also the lowest GHG emission point.

4) Based on the simulation results, ammonia fuelled FPEs (internal combustion type, premixed combustion) could achieve high thermal efficiency (58.1%), but high NO_x (4769.6 ppmvd@15%O_2) and ammonia emissions (1484.7 ppmvd@15%O_2) are of concern.

5) Most of the emission results from SI engines, CI engines and FPEs using ammonia were higher than the recently proposed EURO 7 regulation standard. The two-zone rich-lean neat ammonia fuelled micro gas turbine shows the best control of emission (NO: 709.7 ppmvd@15%O_2, NH_3 : 0.6 ppmvd@15%O_2) with thermal efficiency of $\sim$ 22%, although the aftertreatment is still required for NO_x emission. It indicates that further research into emission control strategies is needed so as to develop ammonia-fuelled heat engines that meet emission standards.

Chapter 7. Conclusions and future work

The aim of this PhD project is to investigate the ammonia and hydrogen combustion and its utilisation in disruptive heat engines. As discussed in the previous chapters, it has been studied numerically and experimentally from the perspective of combustion fundamentals, flame characteristics in a lab-scaled swirl-enhanced combustor, as well as comparison analysis of emissions from different types of heat engines. This chapter highlights the main conclusions drawn from the present research and discusses possible future research directions.

7.1 Conclusions

In the present work, Nakamura's chemical kinetic reaction mechanism [84] has been identified for numerical simulations based on the comparison between three candidate mechanisms against the same sets of experimental data in the literature. Nakamura's mechanism has the best agreement with the ignition delay and provides good prediction in laminar flame speed and flame structure. Following this, the premixed laminar flame speed, ignition delay time and flame structure of ammonia and hydrogen combustion were analysed exhaustively over a wide range of parameters in Chapter 4. With its main conclusions summarised as follows:

- An equivalence ratio of 1.1 is advantageous for both combustion stability and emission control in premixed ammonia and hydrogen combustion. Hydrogen enrichment and oxygen enrichment effectively promote the laminar flame speed and reduce the ignition delay time. However, they comes at the cost of higher NO emission. Elevated pressure tends to inhibit the laminar flame

speed and shorten the ignition delay time, but the effect is attenuated with a further increase in pressure. As pressure rises, the NO emission drops substantially.

- Taking into account the influence of various parameters, a beneficial combination, i.e. $30\%H_2/70\%NH_3$, $\Omega = 0.3$, $\phi = 1.1$, $T_1 = 600$ K, $P_1 = 15$ bar is chosen for a free piston engine (external combustion type) to achieve the goal of robust and reduced NO_x emission combustion.

- Based on the 1D simulation results of the continuous combustion model, a premixed $60\%NH_3/40\%H_2$ flame at $\Omega = 0.4$, $\phi = 1.1$ are primarily chosen and discussed at various initial temperature, pressure as well as with and without secondary air injection for optimising the combustion efficiency and reducing NO_x emissions. A rise in the initial temperature results in the increase of NO emissions due to the extended Zel'dovich mechanism. The increase in pressure has a more significant effect on the fuel-bound NO_x formation compared to thermal NO_x formation. The reduced NO_x emission indicates a high-pressure environment is favourable for the use of ammonia and hydrogen fuelled gas turbines regarding the NO_x emission control. The secondary air injection enhances the combustion efficiency because the excess air enables the unburnt fuel to be further consumed. However, NO and NO_2 emissions are considerably increased.

Subsequently, a swirl-enhanced ammonia/hydrogen combustor rig has been established. The non-premixed ammonia and hydrogen flames was investigated in terms of blowoff limits, emission performance and excited hydroxyl radical in Chapter 5. The main conclusions drawn from the experiments are:

- Increasing hydrogen blending ratios, initial gas temperature and decreasing

the swirl numbers are effective ways to broaden the flame stability range of non-premixed ammonia/hydrogen. The effect of swirl numbers on the rich blowoff limits is more pronounced than the effect on the lean blowoff limits. Robust flames were obtained at hydrogen blending ratio over 20%. More hydrogen involvement resulted in the increase of NO and NO_2 emissions and the decrease in ammonia slip. However, the effect was weakened under fuel-rich conditions.

- The optimal emission control occurs at stoichiometric condition. Although NO_x and unburned fuel also showed relatively low emissions at far-lean equivalence ratios with $x\%H_2$ at 20% and 30%, flame stability should be further examined. Increasing the initial temperature has a marginal effect on emissions at $\phi_{global} = 1.1$ due to the heat loss from the combustor wall and optical windows. After the non-insulation rig was converted to the wall insulated condition, NO and NO_2 emissions increased significantly although the ammonia slip decreased considerably. In the current combustor test rig setup, NO and NO_2 emissions were lower with the swirl number of 0.87 and 1.04 than that at swirl numbers of 0.73 when ϕ_{global} was above 0.8. This suggested there is an optimal swirl number for NO_x control and its value changes depending on the geometry and size of combustor.

- OH^* chemiluminescence distribution can effectively identify the shape of non-premixed ammonia and hydrogen flames. As the flame became richer, the OH^* concentration was moved further away from the nozzle and the OH^* distribution was expanded. With an increase in the hydrogen blending ratio, the OH^* distribution near the nozzle was evidently enlarged. When the initial temperature increased, the flame shape remained unchanged but

the region of the peak OH^* concentration was expanded. As the vane angle of the swirler varied from 40° to 50°, the angle of the OH^* concentration upstream was deflected. Furthermore, the trend of OH^* intensity was consistent with the results of NO emissions at the same swirl number.

Finally, emissions from Spark-ignition (SI) engines, Compression-ignition (CI) engines, Gas Turbines (GTs) and Free Piston Engines (FPEs) using ammonia as fuel were compared on the basis of the same concentration units (ppmvd@15%O_2) or mass-based units (g/kWh) in Chapter 6. The main findings are summarised as below:

- Optimising the thermal efficiency of SI and CI engines using ammonia always comes with the penalty of high NO_x emissions (SI: $\sim$ 1990 ppmvd@15%O_2 with thermal efficiency at 33.5%; CI: $\sim$ 900 ppmvd@15%O_2 with indicated thermal efficiency at 37.6%). The relationship between ammonia emission and NO_x emission is negatively correlated. In ammonia/diesel dual fuelled CI engines, split diesel injection is an effective method to control the ammonia emission. The lowest ammonia emission was 2.56 g/kWh, which was 83.5% lower than that of the dual fuel single injection mode.

- Based on the simulation results, the ammonia fuelled FPEs (internal combustion type, premixed combustion) could achieve high thermal efficiency (58.1%), but high NO_x (4769.6 ppmvd@15%O_2) and ammonia emissions (1484.7 ppmvd@15%O_2) are of concern.

- Most of the emission results from SI engines, CI engines and FPEs using ammonia were higher than the recently proposed EURO 7 regulation standard. The two-zone rich-lean neat ammonia fuelled micro gas turbine shows the best control of emission (NO : 709.7 ppmvd@15%O_2, NH_3 : 0.6

ppmvd@15%O_2) with thermal efficiency of $\sim$ 22%, although the aftertreatment is still required for the NO_x emission. It indicates that further research into emission control strategies is needed so as to develop ammonia-fuelled heat engines that meet stringent emission standards.

7.2 Future work

Based on the present work, some future work recommendations are made as follows:

- Now that the most appropriate ammonia/hydrogen detailed chemical kinetic reaction mechanism has been identified, it is worthwhile to develop a reduced mechanism based on it. The reduced mechanism can be employed in a CFD (Computational Fluid Dynamics) simulation to understand the spatial and temporal information on the structure of non-premixed ammonia/hydrogen flame in the combustor used in Chapter 5 and extend the experimental findings.

- The N_2O emission was calculated and analysed in the numerical work presented in Section 4.3.3, 4.3.4 and 4.4. In experimental work, N_2O emission was not reported due to the limited budget for N_2O measurement purchase. Although N_2O accounts for a small percentage in NO_x emission, it cannot be ignored. It is a long-lived greenhouse gas emission which is about three hundred times harmful than CO_2 and it accelerates the depletion of the ozone layer. It is necessary to investigate the climate impact, such as the CO_2-equivalent emission, by considering N_2O and CO_2 emissions.

- The present experimental work has been conducted under atmospheric pressure so far. To obtain the operational conditions similar to the practical

heat engines, an elevated pressure environment is needed. According to the author's findings, NO_x generation decreases as pressure increases, while NO_x generation increases with a higher temperature. The behaviour of NO_x emission under a high-temperature high-pressure environment is still unknown.

- In this work, ammonia is blended with a certain ratio of hydrogen in advance before entering the combustor in the modelling and experiments. Instead of an additional fuel cylinder, the coupling of hydrogen production from ammonia decomposition to a non-premixed ammonia/hydrogen combustor has not been studied. Coupling parameters analysis, for example size and system efficiency, can be studied.

- Some advanced laser diagnostics technologies such as PIV (Particle Image Velocimetry) and PLIF (Planar Laser Induced Fluorescence), can be used in the freshly built combustor to understand the velocity distribution, flame visualization, instable and stable region of non-premixed ammonia and hydrogen flame. For example, understand the relationship between flame velocity and blowout limit for non-premixed ammonia/hydrogen flames.

APPENDIX

A. Calibration reports for NO_x analysers

The HORIBA MEXA-7100DEGR was calibrated by the Horiba on-site engineers on August 17-18, 2021. Figure 1 and 2 show the calibration report of NO analyser and NO_x analyser. The reports showed both analysers passed all of the linearization tests.

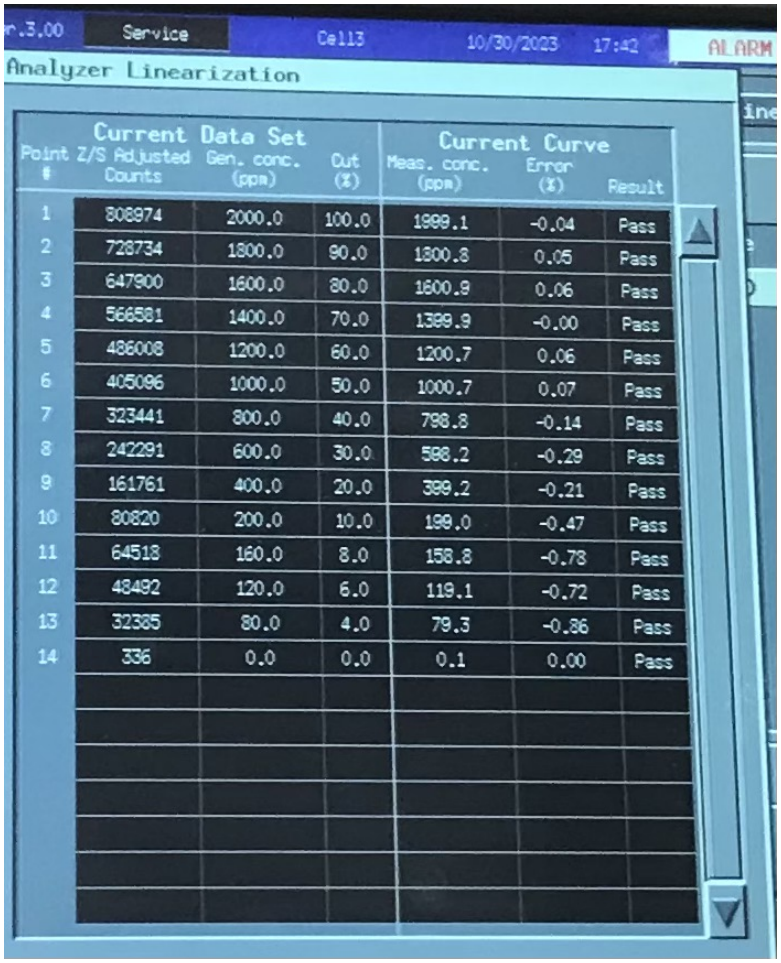


Figure 1: NO analyser linearization report.

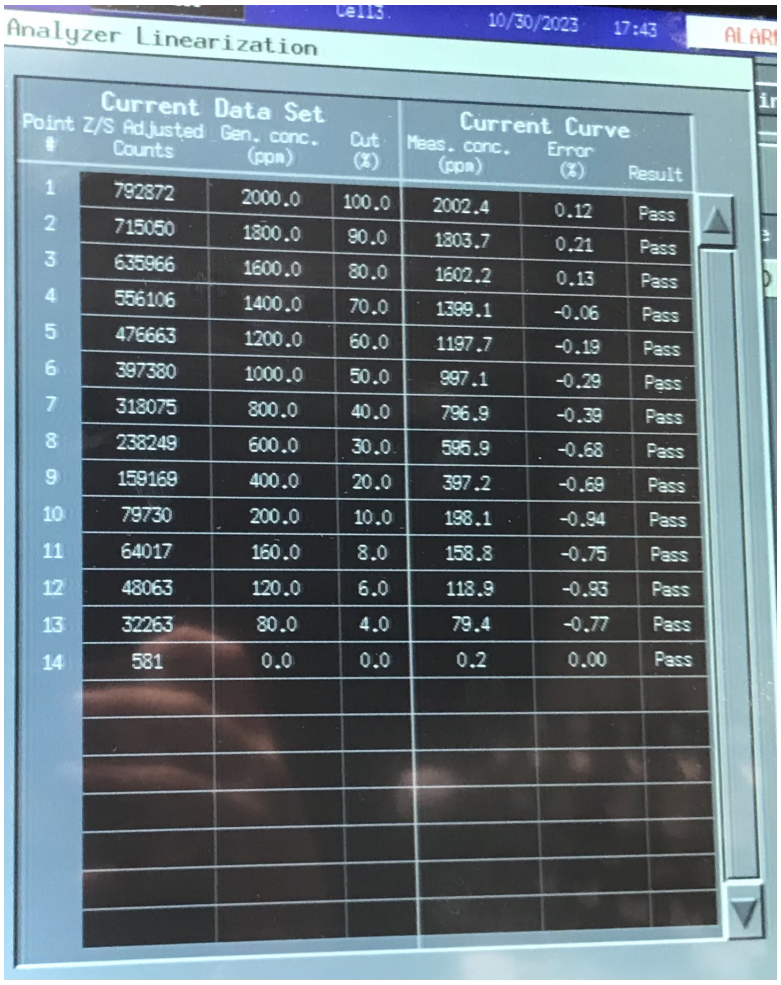


Figure 2: NO_x analyser linearization report.

B. MATLAB code for OH^* chemiluminescence image post-processing

This code was developed by the author to post-process OH^* chemiluminescence images and calculate the OH^* intensity.

```
%Average the OH* chemiluminescence images
ds=imageDatastore("H17")
dataFilenames=ds.Files;
nFiles=numel(dataFilenames);
Sum1=double(readimage(ds,1));
```

```
6           for j = 2:nFiles
7           I1=double(readimage(ds,j));
8           Sum1=Sum1+I1;
9           end
10          average1=Sum1/nFiles;
11
12          %Average the background images
13          ds2=imageDatastore("background")
14          dataFilenames2=ds2.Files;
15          nFiles2=numel(dataFilenames2);
16          Sum2=double(readimage(ds2,1));
17          for j = 2:nFiles2
18          I2=double(readimage(ds2,j));
19          Sum2=Sum2+I2;
20          end
21          average2=Sum2/nFiles2;
22
23          % Background correction
24          test_BGR=average1-average2;
25          % apply 2D median filter to remove salt and pepper
                noise
26          test_BGR_median = medfilt2(test_BGR);
27          % minimum value correction
28          test_BGR_min=test_BGR_median-min(test_BGR_median
                (:));
29          %rescale the averaged image to [0,1]
```

```
30          test_BGR_rescale=rescale(test_BGR_min);
31
32          %Calculate the OH* intensity
33          intensity = sum(test_BGR_rescale, 'all')
34
35          %Apply Abel inversion algorithm
36          test_BGR_rot=imrotate(test_BGR_rescale,-90);
37          test_BGR_right = imcrop(test_BGR_rot,[401 0 400
                1280]);
38          R=400;
39          upf=5;
40          plot_results=1;
41          lsq_solve=0;
42          h=test_BGR_right(1,:);
43          f_rec_right= abel_inversion(h,R,upf,plot_results,
                lsq_solve);
44          for i = 2:1280
45          h=test_BGR_right(i,:);
46          f_rec= abel_inversion(h,R,upf,plot_results,
                lsq_solve);
47          f_rec_right=[f_rec f_rec_right];
48          end
49          f_rec_right=imrotate(rescale(f_rec_right),90);
```

Bibliography

[1] J. Murray, "Which countries have legally-binding net-zero emissions targets?," 2020. (see pages 1)

[2] GOV.UK, "Transport and environment statistics: Autumn 2021," 2022. (see pages 1)

[3] GOV.UK, "Uk territorial greenhouse gas emissions national statistics," 2022. (see pages 1, 2)

[4] IMO, "Initial imo ghg strategy," 2018. (see pages 1)

[5] WhatCar?, "Uk petrol and diesel car ban delayed to 2035," 2023. (see pages 2)

[6] S. Gross, "The challenge of decarbonizing heavy transport," report, 2020. (see pages 3)

[7] S. J. Davis, N. S. Lewis, M. Shaner, S. Aggarwal, D. Arent, I. L. Azevedo, S. M. Benson, T. Bradley, J. Brouwer, Y. M. Chiang, C. T. M. Clack, A. Cohen, S. Doig, J. Edmonds, P. Fennell, C. B. Field, B. Hannegan, B. M. Hodge, M. I. Hoffert, E. Ingersoll, P. Jaramillo, K. S. Lackner, K. J. Mach, M. Mastrandrea, J. Ogden, P. F. Peterson, D. L. Sanchez, D. Sperling, J. Stagner, J. E. Trancik, C. J. Yang, and K. Caldeira, "Net-zero emissions energy systems," *Science*, vol. 360, no. 6396, 2018. Davis, Steven J Lewis, Nathan S Shaner, Matthew Aggarwal, Sonia Arent, Doug Azevedo, Ines L Benson, Sally M Bradley, Thomas Brouwer, Jack Chiang, Yet-Ming

Clack, Christopher T M Cohen, Armond Doig, Stephen Edmonds, Jae Fennell, Paul Field, Christopher B Hannegan, Bryan Hodge, Bri-Mathias Hoffert, Martin I Ingersoll, Eric Jaramillo, Paulina Lackner, Klaus S Mach, Katharine J Mastrandrea, Michael Ogden, Joan Peterson, Per F Sanchez, Daniel L Sperling, Daniel Stagner, Joseph Trancik, Jessika E Yang, Chi-Jen Caldeira, Ken eng Review Research Support, U.S. Gov't, Non-P.H.S. 2018/06/30 Science. 2018 Jun 29;360(6396). pii: 360/6396/eaas9793. doi: 10.1126/science.aas9793. (see pages 3)

[8] TWI, "What are the pros and cons of hydrogen fuel cells?," 2022. (see pages 4)

[9] D. A. Cullen, K. C. Neyerlin, R. K. Ahluwalia, R. Mukundan, K. L. More, R. L. Borup, A. Z. Weber, D. J. Myers, and A. Kusoglu, "New roads and challenges for fuel cells in heavy-duty transportation," *Nature Energy*, vol. 6, no. 5, pp. 462–474, 2021. (see pages 4)

[10] G. Jeerh, M. Zhang, and S. Tao, "Recent progress in ammonia fuel cells and their potential applications," *Journal of Materials Chemistry A*, vol. 9, no. 2, pp. 727–752, 2021. (see pages 4)

[11] E. Lindstad, B. Lagemann, A. Rialland, G. M. Gamlem, and A. Valland, "Reduction of maritime ghg emissions and the potential role of e-fuels," *Transportation Research Part D: Transport and Environment*, vol. 101, 2021. (see pages 4)

[12] V. S. Sikarwar, M. Zhao, P. S. Fennell, N. Shah, and E. J. Anthony, "Progress in biofuel production from gasification," *Progress in Energy and Combustion Science*, vol. 61, pp. 189–248, 2017. (see pages 4)

[13] R. v. Basshuysen and F. Schäfer, *Internal Combustion Engine Handbook - Basics, Components, System, and Perspectives (2nd Edition)*. 2.2.2 Fuel, SAE International, 2016. (see pages 5)

[14] P. Dimitriou and R. Javaid, "A review of ammonia as a compression ignition engine fuel," *International Journal of Hydrogen Energy*, vol. 45, no. 11, pp. 7098–7118, 2020. (see pages 5, 43, 169)

[15] S. M. Grannell, D. N. Assanis, S. V. Bohac, and D. E. Gillespie, "The fuel mix limits and efficiency of a stoichiometric, ammonia, and gasoline dual fueled spark ignition engine," *Journal of Engineering for Gas Turbines and Power*, vol. 130, no. 4, 2008. (see pages 5, 13, 45, 165)

[16] C. Lhuillier, P. Brequigny, F. Contino, and C. Mounaïm-Rousselle, "Experimental study on ammonia/hydrogen/air combustion in spark ignition engine conditions," *Fuel*, vol. 269, 2020. (see pages 5, 165, 166, 178, 179, 180)

[17] H. Meng, C. Ji, J. Yang, K. Chang, G. Xin, and S. Wang, "A knock study of hydrogen-fueled wankel rotary engine," *Fuel*, vol. 321, 2022. (see pages 5)

[18] S. Verhelst, "Recent progress in the use of hydrogen as a fuel for internal combustion engines," *International Journal of Hydrogen Energy*, vol. 39, no. 2, pp. 1071–1085, 2014. (see pages 5)

[19] P. P. Walsh and P. Fletcher, *Gas Turbine Performance (2nd Edition)*. 13.1 The Combustion Process and Gas Turbine Fuel Types, John Wiley & Sons, 2004. (see pages 6)

[20] P. Breeze, *Chapter 4 - Gas Turbines*, pp. 31–42. Academic Press, 2016. (see pages 6)

[21] Libertine.co.uk, "What is a free piston engine?," 2017. (see pages 6)

[22] Y. Zhou, A. Sofianopoulos, B. Lawler, and S. Mamalis, "Advanced combustion free-piston engines: A comprehensive review," *International Journal of Engine Research*, vol. 21, no. 7, pp. 1205–1230, 2018. (see pages 6)

[23] U. Ngwaka, F. Chen, S. Qiu, M. Li, C. Zhang, and D. Wu, "Recent progress on performance and control of linear engine generator," *International Journal of Engine Research*, 2022. (see pages 7)

[24] N. C. f. B. Information, "Pubchem compound summary for cid 222, ammonia," 2022. (see pages 9, 10)

[25] N. C. f. B. Information, "Pubchem compound summary for cid 783, hydrogen," 2022. (see pages 9, 10)

[26] N. C. f. B. Information, "Pubchem compound summary for cid 297, methane," 2022. (see pages 9, 10)

[27] N. C. f. B. Information, "Pubchem compound summary for cid 6334, propane," 2022. (see pages 9, 10)

[28] N. I. o. S. WebBook and T. Chemistry, "Ammonia," 2022. (see pages 9, 10)

[29] N. I. o. S. WebBook and T. Chemistry, "Hydrogen," 2022. (see pages 9, 10)

[30] N. I. o. S. WebBook and T. Chemistry, "Methane," 2022. (see pages 9, 10)

[31] N. I. o. S. WebBook and T. Chemistry, "Propane," 2022. (see pages 9, 10)

[32] D. Erdemir and I. Dincer, "A perspective on the use of ammonia as a clean fuel: Challenges and solutions," *International Journal of Energy Research*, vol. 45, no. 4, pp. 4827–4834, 2021. (see pages 9, 10)

[33] M. Aziz, A. T. Wijayanta, and A. B. D. Nandiyanto, "Ammonia as effective hydrogen storage: A review on production, storage and utilization," *Energies*, vol. 13, no. 12, p. 3062, 2020. (see pages 9, 10)

[34] E. ToolBox, "Adiabatic flame temperatures," 2005. (see pages 9, 10)

[35] C. T. Chong and S. Hochgreb, "Measurements of laminar flame speeds of liquid fuels: Jet-a1, diesel, palm methyl esters and blends using particle imaging velocimetry (piv)," *Proceedings of the Combustion Institute*, vol. 33, no. 1, pp. 979–986, 2011. (see pages 9, 10)

[36] S. C. Gad, *Diesel Fuel*, pp. 115–118. Oxford: Academic Press, 2014. (see pages 9, 10)

[37] Z. S. Steven, Z. A. Susan, and D. J. Donald, *Chemistry*. Cengage, 2017. (see pages 9, 10)

[38] T. E. ToolBox, "Gases - explosion and flammability concentration limits," 2003. (see pages 9, 10)

[39] T. E. ToolBox, "Fuels - higher and lower calorific values," 2003. (see pages 9, 10)

[40] DNV, "Energy transition outlook — maritime forecast to 2050," 2020. (see pages 8)

[41] B. Trevor, "Maritime fuel mix could be 25(see pages 8, 11)

[42] D. GL, "Energy transition outlook 2019: Maritime forecast to 2050," report, 2019. (see pages 8, 11)

[43] H. Kobayashi, A. Hayakawa, K. D. . Somarathne, and E. Okafor, "Science and technology of ammonia combustion," *Proceedings of the Combustion Institute*, vol. 37, no. 1, pp. 109–133, 2019. (see pages 8, 112, 118, 127)

[44] A. Valera-Medina, H. Xiao, M. Owen-Jones, W. I. F. David, and P. J. Bowen, "Ammonia for power," *Progress in Energy and Combustion Science*, vol. 69, pp. 63–102, 2018. (see pages 8, 11, 12, 45)

[45] J. Li, H. Huang, L. Deng, Z. He, Y. Osaka, and N. Kobayashi, "Effect of hydrogen addition on combustion and heat release characteristics of ammonia flame," *Energy*, vol. 175, pp. 604–617, 2019. (see pages 8)

[46] E. Morgan, J. Manwell, and J. McGowan, "Wind-powered ammonia fuel production for remote islands: A case study," *Renewable Energy*, vol. 72, pp. 51–61, 2014. (see pages 8)

[47] Y. Bicer, I. Dincer, C. Zamfirescu, G. Vezina, and F. Raso, "Comparative life cycle assessment of various ammonia production methods," *Journal of Cleaner Production*, vol. 135, pp. 1379–1395, 2016. (see pages 8)

[48] D. R. MacFarlane, P. V. Cherepanov, J. Choi, B. H. R. Suryanto, R. Y. Hodgetts, J. M. Bakker, F. M. Ferrero Vallana, and A. N. Simonov, "A roadmap to the ammonia economy," *Joule*, vol. 4, no. 6, pp. 1186–1205, 2020. (see pages 8, 12)

[49] R. Banares-Alcantara, G. Dericks, M. Fiaschetti, P. Grunewald, J. M. Lopez, E. Tsang, A. Yang, L. Ye, and S. Zhao, "Analysis of islanded nh3-based energy storage system," 2015. (see pages 8)

[50] b. p. office, "bp study confirms feasibility of large-scale production of green hydrogen and green ammonia using renewable energy in australia," 2021. (see pages 11)

[51] b. p. office, "bp to lead and operate one of the world's largest renewables and green hydrogen energy hubs based in western australia," 2022. (see pages 11)

[52] Y. Kojima, "High purity hydrogen generation from ammonia," in *ABSTRACTS OF PAPERS OF THE AMERICAN CHEMICAL SOCIETY*, vol. 254, AMER CHEMICAL SOC 1155 16TH ST, NW, WASHINGTON, DC 20036 USA. (see pages 11, 12)

[53] E. A. Brohi, *Ammonia as fuel for internal combustion engines? An evaluation of the feasibility of using nitrogen-based fuels in ICE*. Thesis, 2014. (see pages 11)

[54] H. Lesmana, Z. Zhang, X. Li, M. Zhu, W. Xu, and D. Zhang, "Nh 3 as a transport fuel in internal combustion engines: A technical review," *Journal of Energy Resources Technology, Transactions of the ASME*, vol. 141, no. 7, 2019. Export Date: 30 April 2019. (see pages 11)

[55] C. W. Gross and S.-C. Kong, "Performance characteristics of a compression-ignition engine using direct-injection ammonia–dme mixtures," *Fuel*, vol. 103, pp. 1069–1079, 2013. (see pages 11, 45, 46)

[56] E. C. Okafor, Y. Naito, S. Colson, A. Ichikawa, T. Kudo, A. Hayakawa, and H. Kobayashi, "Experimental and numerical study of the laminar burning velocity of ch4–nh3–air premixed flames," *Combustion and Flame*, vol. 187, pp. 185–198, 2018. (see pages 13, 21, 22, 24, 26, 28, 100)

[57] H. Xiao, A. Valera-Medina, and P. J. Bowen, "Study on premixed combustion characteristics of co-firing ammonia/methane fuels," *Energy*, vol. 140, pp. 125–135, 2017. (see pages 13, 32, 33, 118)

[58] A. Ichikawa, Y. Naito, A. Hayakawa, T. Kudo, and H. Kobayashi, "Burning velocity and flame structure of ch4/nh3/air turbulent premixed flames at high pressure," *International Journal of Hydrogen Energy*, vol. 44, no. 13, pp. 6991–6999, 2019. (see pages 13, 26, 27)

[59] K. H. Ryu, G. Zacharakis-Jutz, and S.-C. Kong, "Effects of fuel compositions on diesel engine performance using ammonia-dme mixtures," 2013. (see pages 13)

[60] N. Iki, O. Kurata, T. Matsunuma, T. Inoue, M. Suzuki, T. Tsujimura, and H. Furutani, "Micro gas turbine firing kerosene and ammonia," in *Proceedings of the ASME Turbo Expo*, vol. 8. Cited By :17 Export Date: 12 November 2020. (see pages 13, 46, 47, 172)

[61] J. H. Lee, J. H. Kim, J. H. Park, and O. C. Kwon, "Studies on properties of laminar premixed hydrogen-added ammonia/air flames for hydrogen production," *International Journal of Hydrogen Energy*, vol. 35, no. 3, pp. 1054–1064, 2010. (see pages 13)

[62] A. Valera-Medina, D. G. Pugh, P. Marsh, G. Bulat, and P. Bowen, "Preliminary study on lean premixed combustion of ammonia-hydrogen for swirling gas turbine combustors," *International Journal of Hydrogen Energy*, vol. 42, no. 38, pp. 24495–24503, 2017. (see pages 13, 39, 68, 99, 147, 183)

[63] J. M. Joo, S. Lee, and O. C. Kwon, "Effects of ammonia substitution on combustion stability limits and nox emissions of premixed hydrogen–air flames,"

International Journal of Hydrogen Energy, vol. 37, no. 8, pp. 6933–6941, 2012. (see pages 13, 26, 39)

[64] J. Warnatz, "Combustion : physical and chemical fundamentals, modeling and simulation, experiments, pollutant formation / j. warnatz, u. maas, r.w. dibble," 2001. (Ulrich) Includes bibliographical references and index. (see pages 25, 31, 53)

[65] P. Glarborg, J. A. Miller, and R. J. Kee, "Kinetic modeling and sensitivity analysis of nitrogen oxide formation in well-stirred reactors," *Combustion and Flame*, vol. 65, no. 2, pp. 177–202, 1986. (see pages)

[66] J. A. Miller, M. D. Smooke, R. M. Green, and R. J. Kee, "Kinetic modeling of the oxidation of ammonia in flames," *Combustion Science and Technology*, vol. 34, no. 1-6, pp. 149–176, 1983. (see pages 18, 23)

[67] R. Lindstedt, F. Lockwood, and M. Selim, "Detailed kinetic modelling of chemistry and temperature effects on ammonia oxidation," *Combustion Science and Technology*, vol. 99, pp. 253–276, 1994. (see pages 18, 19, 23)

[68] A. A. Konnov, "Implementation of the ncn pathway of prompt-no formation in the detailed reaction mechanism," *Combustion and Flame*, vol. 156, no. 11, pp. 2093–2105, 2009. (see pages 19, 21, 23, 100)

[69] A. Hayakawa, T. Goto, R. Mimoto, Y. Arakawa, T. Kudo, and H. Kobayashi, "Laminar burning velocity and markstein length of ammonia/air premixed flames at various pressures," *Fuel*, vol. 159, pp. 98–106, 2015. (see pages 19, 26)

[70] P. Kumar and T. R. Meyer, "Experimental and modeling study of chemical-

kinetics mechanisms for h2–nh3–air mixtures in laminar premixed jet flames," *Fuel*, vol. 108, pp. 166–176, 2013. (see pages 19, 94, 95, 100)

[71] H. Xiao, A. Valera-Medina, P. Bowen, and S. Dooley, "3d simulation of ammonia combustion in a lean premixed swirl burner," 2017/12/01/ 2017. (see pages 19)

[72] A. Ichikawa, A. Hayakawa, Y. Kitagawa, K. D. Kunkuma Amila Somarathne, T. Kudo, and H. Kobayashi, "Laminar burning velocity and markstein length of ammonia/hydrogen/air premixed flames at elevated pressures," *International Journal of Hydrogen Energy*, vol. 40, no. 30, pp. 9570–9578, 2015. (see pages 19, 26, 29, 99)

[73] C. Duynslaegher, F. Contino, J. Vandooren, and H. Jeanmart, "Modeling of ammonia combustion at low pressure," *Combustion and Flame*, vol. 159, no. 9, pp. 2799–2805, 2012. (see pages 19, 23, 94, 95, 97)

[74] C. Duynslaegher, H. Jeanmart, and J. Vandooren, "Flame structure studies of premixed ammonia/hydrogen/oxygen/argon flames: Experimental and numerical investigation," *Proceedings of the Combustion Institute*, vol. 32, no. 1, pp. 1277–1284, 2009. (see pages 19, 33, 97, 98)

[75] P. S. Gregory, M. G. David, F. Michael, W. M. Nigel, E. Boris, G. Mikhail, T. B. C., K. H. Ronald, S. Soonho, C. G. William, Jr., V. L. Vitali, and Q. Zhiwei, "Gri-mech 3.0," 1999. (see pages 19, 21)

[76] Mechanical and U. o. C. a. S. D. Aerospace Engineering (Combustion Research), "Chemical-kinetic mechanisms for combustion applications," 2005. (see pages 19, 21)

[77] B. Jiang, *Mécanisme de formation et de disparition des oxydes d'azote dans les flammes : étude expérimentale et modélisation*. Thesis, 1990. (see pages 19)

[78] T. Meyer, P. Kumar, M. Li, K. Redfern, and D. Diaz, "Ammonia combustion with near-zero pollutant emissions," in *NH3 Congress*. (see pages 19)

[79] Z. Tian, Y. Li, L. Zhang, P. Glarborg, and F. Qi, "An experimental and kinetic modeling study of premixed nh3/ch4/o2/ar flames at low pressure," *Combustion and Flame*, vol. 156, no. 7, pp. 1413–1426, 2009. (see pages 19, 20, 21, 23, 33, 100)

[80] T. Mendiara and P. Glarborg, "Ammonia chemistry in oxy-fuel combustion of methane," *Combustion and Flame*, vol. 156, no. 10, pp. 1937–1949, 2009. (see pages 20, 21, 23, 30)

[81] O. Mathieu and E. L. Petersen, "Experimental and modeling study on the high-temperature oxidation of ammonia and related nox chemistry," *Combustion and Flame*, vol. 162, no. 3, pp. 554–570, 2015. (see pages 20, 21, 23, 31, 96, 97, 106)

[82] Y. Song, H. Hashemi, J. M. Christensen, C. Zou, P. Marshall, and P. Glarborg, "Ammonia oxidation at high pressure and intermediate temperatures," *Fuel*, vol. 181, pp. 358–365, 2016. (see pages 20, 21, 23)

[83] J. A. Miller and C. T. Bowman, "Mechanism and modeling of nitrogen chemistry in combustion," *Progress in Energy and Combustion Science*, vol. 15, no. 4, pp. 287–338, 1989. (see pages 21)

[84] H. Nakamura, S. Hasegawa, and T. Tezuka, "Kinetic modeling of ammonia/air weak flames in a micro flow reactor with a controlled temperature

profile," *Combustion and Flame*, vol. 185, pp. 16–27, 2017. (see pages 21, 24, 54, 94, 95, 97, 123, 129, 190)

[85] J. Bugler, K. P. Somers, J. M. Simmie, F. Güthe, and H. J. Curran, "Modeling nitrogen species as pollutants: Thermochemical influences," *The Journal of Physical Chemistry A*, vol. 120, no. 36, pp. 7192–7197, 2016. (see pages 21)

[86] J. Otomo, M. Koshi, T. Mitsumori, H. Iwasaki, and K. Yamada, "Chemical kinetic modeling of ammonia oxidation with improved reaction mechanism for ammonia/air and ammonia/hydrogen/air combustion," *International Journal of Hydrogen Energy*, vol. 43, no. 5, pp. 3004–3014, 2018. (see pages 21, 24, 32, 33, 94, 95, 97)

[87] E. C. Okafor, Y. Naito, S. Colson, A. Ichikawa, T. Kudo, A. Hayakawa, and H. Kobayashi, "Measurement and modelling of the laminar burning velocity of methane-ammonia-air flames at high pressures using a reduced reaction mechanism," *Combustion and Flame*, vol. 204, pp. 162–175, 2019. (see pages 22, 24, 26, 27)

[88] K. D. K. A. Somarathne, E. C. Okafor, A. Hayakawa, T. Kudo, O. Kurata, N. Iki, and H. Kobayashi, "Emission characteristics of turbulent non-premixed ammonia/air and methane/air swirl flames through a rich-lean combustor under various wall thermal boundary conditions at high pressure," *Combustion and Flame*, vol. 210, pp. 247–261, 2019. (see pages 22, 148)

[89] E. C. Okafor, K. D. . A. Somarathne, R. Ratthanan, A. Hayakawa, T. Kudo, O. Kurata, N. Iki, T. Tsujimura, H. Furutani, and H. Kobayashi, "Con-

trol of nox and other emissions in micro gas turbine combustors fuelled with mixtures of methane and ammonia," *Combustion and Flame*, vol. 211, pp. 406–416, 2020. (see pages 22, 36, 37, 141)

[90] J. Zhang, C. Sui, L. Zhang, J. Jiang, and B. Zhang, "Effects of differential diffusion on flame structure of non-premixed ammonia/methane combustion," 2021. (see pages 22)

[91] H. Mikulčić, J. Baleta, X. Wang, J. Wang, F. Qi, and F. Wang, "Numerical simulation of ammonia/methane/air combustion using reduced chemical kinetics models," *International Journal of Hydrogen Energy*, vol. 46, no. 45, pp. 23548–23563, 2021. (see pages 22)

[92] J. Zhang, C. Sui, L. Zhang, J. Jiang, and B. Zhang, "Effects of ammonia addition on combustion characteristics in partially-premixed swirling ammonia/methane/air flame," *Thermal Science*, vol. 26, no. 6 Part A, pp. 4547–4559, 2022. (see pages 22)

[93] R. Li, A. A. Konnov, G. He, F. Qin, and D. Zhang, "Chemical mechanism development and reduction for combustion of nh3/h2/ch4 mixtures," *Fuel*, vol. 257, 2019. (see pages 22, 24)

[94] C. Duynslaegher, *Experimental and numerical study of ammonia combustion*. Thesis, 2011. (see pages 23)

[95] M. K. Hossaini, *Review of the New Combustion Technologies in Modern Gas Turbines*, p. Ch. 6. Rijeka: IntechOpen, 2013. (see pages 25)

[96] I. Puri and S. Aggarwal, *Partially-Premixed Flames: Applications and Issues*. Aerospace Sciences Meetings, American Institute of Aeronautics and Astronautics, 2007. doi:10.2514/6.2007-597. (see pages 25)

[97] A. Hayakawa, Y. Arakawa, R. Mimoto, K. D. K. A. Somarathne, T. Kudo, and H. Kobayashi, "Experimental investigation of stabilization and emission characteristics of ammonia/air premixed flames in a swirl combustor," *International Journal of Hydrogen Energy*, vol. 42, no. 19, pp. 14010–14018, 2017. (see pages 26, 27, 75)

[98] M. Zhang, X. Wei, J. Wang, Z. Huang, and H. Tan, "The blow-off and transient characteristics of co-firing ammonia/methane fuels in a swirl combustor," *Proceedings of the Combustion Institute*, vol. 38, no. 4, pp. 5181–5190, 2021. (see pages 26, 139)

[99] E. C. Okafor, H. Yamashita, A. Hayakawa, K. D. K. A. Somarathne, T. Kudo, T. Tsujimura, M. Uchida, S. Ito, and H. Kobayashi, "Flame stability and emissions characteristics of liquid ammonia spray co-fired with methane in a single stage swirl combustor," *Fuel*, vol. 287, 2021. (see pages 26, 38)

[100] H. Xiao, A. Valera-Medina, R. Marsh, and P. J. Bowen, "Numerical study assessing various ammonia/methane reaction models for use under gas turbine conditions," *Fuel*, vol. 196, pp. 344–351, 2017. (see pages 26)

[101] A. Valera-Medina, R. Marsh, J. Runyon, D. Pugh, P. Beasley, T. Hughes, and P. Bowen, "Ammonia–methane combustion in tangential swirl burners for gas turbine power generation," *Applied Energy*, vol. 185, pp. 1362–1371, 2017. (see pages 26, 37, 183, 186)

[102] J. H. Lee, S. I. Lee, and O. C. Kwon, "Effects of ammonia substitution on hydrogen/air flame propagation and emissions," *International Journal of*

Hydrogen Energy, vol. 35, no. 20, pp. 11332–11341, 2010. (see pages 26, 28, 29, 99)

[103] C. Lhuillier, P. Brequigny, N. Lamoureux, F. Contino, and C. Mounaïm-Rousselle, "Experimental investigation on laminar burning velocities of ammonia/hydrogen/air mixtures at elevated temperatures," *Fuel*, vol. 263, 2020. (see pages 26, 29)

[104] A. A. Khateeb, T. F. Guiberti, G. Wang, W. R. Boyette, M. Younes, A. Jamal, and W. L. Roberts, "Stability limits and no emissions of premixed swirl ammonia-air flames enriched with hydrogen or methane at elevated pressures," *International Journal of Hydrogen Energy*, vol. 46, no. 21, pp. 11969–11981, 2021. (see pages 26, 29, 38, 39, 40)

[105] X. Han, Z. Wang, M. Costa, Z. Sun, Y. He, and K. Cen, "Experimental and kinetic modeling study of laminar burning velocities of nh3/air, nh3/h2/air, nh3/co/air and nh3/ch4/air premixed flames," *Combustion and Flame*, vol. 206, pp. 214–226, 2019. (see pages 26, 29)

[106] J. Li, H. Huang, N. Kobayashi, Z. He, Y. Osaka, and T. Zeng, "Numerical study on effect of oxygen content in combustion air on ammonia combustion," *Energy*, vol. 93, pp. 2053–2068, 2015. (see pages 29, 30)

[107] H. Takeishi, J. Hayashi, S. Kono, W. Arita, K. Iino, and F. Akamatsu, "Characteristics of ammonia/n2/o2 laminar flame in oxygen-enriched air condition," *Transactions of the JSME (in Japanese)*, vol. 81, no. 824, pp. 14–00423–14–00423, 2015. (see pages 29)

[108] B. Mei, X. Zhang, S. Ma, M. Cui, H. Guo, Z. Cao, and Y. Li, "Experimental and kinetic modeling investigation on the laminar flame propagation

of ammonia under oxygen enrichment and elevated pressure conditions," *Combustion and Flame*, vol. 210, pp. 236–246, 2019. (see pages 29, 30)

[109] Q. Liu, X. Chen, J. Huang, Y. Shen, Y. Zhang, and Z. Liu, "The characteristics of flame propagation in ammonia/oxygen mixtures," *J Hazard Mater*, vol. 363, pp. 187–196, 2019. Liu, Qingming Chen, Xu Huang, Jinxiang Shen, Yang Zhang, Yunming Liu, Ziwei eng Netherlands 2018/10/12 06:00 J Hazard Mater. 2019 Feb 5;363:187-196. doi: 10.1016/j.jhazmat.2018.09.073. Epub 2018 Sep 29. (see pages 29, 30)

[110] F.-H. Wu and G.-B. Chen, "Numerical study of hydrogen peroxide enhancement of ammonia premixed flames," *Energy*, p. 118118, 2020. (see pages 29, 30)

[111] K.-K. Wu, Y.-C. Chang, C.-H. Chen, and Y.-D. Chen, "High-efficiency combustion of natural gas with 21–30no. 9, pp. 2455–2462, 2010. (see pages 29, 30, 102)

[112] X. Huang, J. Guo, Z. Liu, and C. Zheng, *Opportunities and Challenges of Oxy-fuel Combustion*, pp. 1–12. 2018. (see pages 29)

[113] M. Barbas, M. Costa, S. Vranckx, and R. X. Fernandes, "Experimental and chemical kinetic study of co and no formation in oxy-methane premixed laminar flames doped with nh3," *Combustion and Flame*, vol. 162, no. 4, pp. 1294–1303, 2015. (see pages 30)

[114] W. Zhang, Z. Chen, Y. Shen, G. Shu, G. Chen, B. Xu, and W. Zhao, "Influence of water emulsified diesel & oxygen-enriched air on diesel engine no-smoke emissions and combustion characteristics," *Energy*, vol. 55, pp. 369–377, 2013. (see pages 30, 102)

[115] X. Cai, J. Wang, W. Zhang, Y. Xie, M. Zhang, and Z. Huang, "Effects of oxygen enrichment on laminar burning velocities and markstein lengths of ch4/o2/n2 flames at elevated pressures," *Fuel*, vol. 184, pp. 466–473, 2016. (see pages 30)

[116] H. Xiao, Z. Wang, A. Valera-Medina, and P. J. Bowen, "Study on characteristics of co-firing ammonia/methane fuels under oxygen enriched combustion conditions," *Journal of Thermal Science*, vol. 27, no. 3, pp. 270–276, 2018. (see pages 30)

[117] B. Shu, S. K. Vallabhuni, X. He, G. Issayev, K. Moshammer, A. Farooq, and R. X. Fernandes, "A shock tube and modeling study on the autoignition properties of ammonia at intermediate temperatures," *Proceedings of the Combustion Institute*, vol. 37, no. 1, pp. 205–211, 2019. (see pages 31, 61)

[118] L. Dai, H. Hashemi, P. Glarborg, S. Gersen, P. Marshall, A. Mokhov, and H. Levinsky, "Ignition delay times of nh3 /dme blends at high pressure and low dme fraction: Rcm experiments and simulations," *Combustion and Flame*, vol. 227, pp. 120–134, 2021. (see pages 31)

[119] H. Xiao, S. Lai, A. Valera-Medina, J. Li, J. Liu, and H. Fu, "Experimental and modeling study on ignition delay of ammonia/methane fuels," *International Journal of Energy Research*, vol. 44, no. 8, pp. 6939–6949, 2020. (see pages 32)

[120] J. Li, H. Huang, N. Kobayashi, C. Wang, and H. Yuan, "Numerical study on laminar burning velocity and ignition delay time of ammonia flame with hydrogen addition," *Energy*, vol. 126, pp. 796–809, 2017. (see pages 32)

[121] L. Dai, S. Gersen, P. Glarborg, H. Levinsky, and A. Mokhov, "Experimental and numerical analysis of the autoignition behavior of nh3 and nh3/h2 mixtures at high pressure," *Combustion and Flame*, vol. 215, pp. 134–144, 2020. (see pages 32)

[122] M. Hori, N. Matsunaga, N. Marinov, P. William, and W. Charles, "An experimental and kinetic calculation of the promotion effect of hydrocarbons on the no-no2 conversion in a flow reactor," *Symposium (International) on Combustion*, vol. 27, no. 1, pp. 389–396, 1998. (see pages 33)

[123] Z. Li and S. Li, "Kinetics modeling of nox emissions characteristics of a nh3/h2 fueled gas turbine combustor," *International Journal of Hydrogen Energy*, vol. 46, no. 5, pp. 4526–4537, 2021. (see pages 34)

[124] N. statistics, "Emissions of air pollutants in the uk – nitrogen oxides (nox)," 2022. (see pages 35)

[125] U. o. E. Anglia, "Nitrous oxide emissions pose an increasing climate threat, study finds," 2020. (see pages 35)

[126] A. Valera-Medina, F. Amer-Hatem, A. K. Azad, I. C. Dedoussi, M. de Joannon, R. X. Fernandes, P. Glarborg, H. Hashemi, X. He, S. Mashruk, J. McGowan, C. Mounaim-Rouselle, A. Ortiz-Prado, A. Ortiz-Valera, I. Rossetti, B. Shu, M. Yehia, H. Xiao, and M. Costa, "Review on ammonia as a potential fuel: From synthesis to economics," *Energy & Fuels*, vol. 35, no. 9, pp. 6964–7029, 2021. (see pages 35)

[127] N. statistics, "Emissions of air pollutants in the uk – ammonia (nh3)," 2022. (see pages 35)

[128] A. Hayakawa, T. Goto, R. Mimoto, T. Kudo, and H. Kobayashi, "No formation/reduction mechanisms of ammonia/air premixed flames at various equivalence ratios and pressures," *Mechanical Engineering Journal*, vol. 2, no. 1, pp. 14–00402–14–00402, 2015. (see pages 35)

[129] E. C. Okafor, K. D. . A. Somarathne, A. Hayakawa, T. Kudo, O. Kurata, N. Iki, and H. Kobayashi, "Towards the development of an efficient low-nox ammonia combustor for a micro gas turbine," *Proceedings of the Combustion Institute*, vol. 37, no. 4, pp. 4597–4606, 2019. (see pages 35, 36, 37, 73)

[130] M. Woo, B. C. Choi, and A. F. Ghoniem, "Experimental and numerical studies on nox emission characteristics in laminar non-premixed jet flames of ammonia-containing methane fuel with oxygen/nitrogen oxidizer," *Energy*, vol. 114, pp. 961–972, 2016. (see pages 37)

[131] X. Zhu, A. A. Khateeb, W. L. Roberts, and T. F. Guiberti, "Chemiluminescence signature of premixed ammonia-methane-air flames," *Combustion and Flame*, vol. 231, 2021. (see pages 39)

[132] A. Valera-Medina, M. Gutesa, H. Xiao, D. Pugh, A. Giles, B. Goktepe, R. Marsh, and P. Bowen, "Premixed ammonia/hydrogen swirl combustion under rich fuel conditions for gas turbines operation," *International Journal of Hydrogen Energy*, vol. 44, no. 16, pp. 8615–8626, 2019. (see pages 40)

[133] H. Nozari, G. Karaca, O. Tuncer, and A. Karabeyoglu, "Porous medium based burner for efficient and clean combustion of ammonia–hydrogen–air systems," *International Journal of Hydrogen Energy*, vol. 42, no. 21, pp. 14775–14785, 2017. (see pages 41)

[134] N. A. Hussein, A. Valera-Medina, and A. S. Alsaegh, "Ammonia- hydrogen

combustion in a swirl burner with reduction of nox emissions," in *Energy Procedia*, vol. 158, pp. 2305–2310. Cited By :5 Export Date: 12 November 2020. (see pages 41)

[135] X. Zhu, A. A. Khateeb, T. F. Guiberti, and W. L. Roberts, "No and oh* emission characteristics of very-lean to stoichiometric ammonia–hydrogen–air swirl flames," *Proceedings of the Combustion Institute*, vol. 38, no. 4, pp. 5155–5162, 2021. (see pages 41, 42)

[136] D. Pugh, J. Runyon, P. Bowen, A. Giles, A. Valera-Medina, R. Marsh, B. Goktepe, and S. Hewlett, "An investigation of ammonia primary flame combustor concepts for emissions reduction with oh*, nh2* and nh* chemiluminescence at elevated conditions," *Proceedings of the Combustion Institute*, vol. 38, no. 4, pp. 6451–6459, 2021. (see pages 41, 156)

[137] A. J. Reiter and S.-C. Kong, "Combustion and emissions characteristics of compression-ignition engine using dual ammonia-diesel fuel," *Fuel*, vol. 90, no. 1, pp. 87–97, 2011. (see pages 43)

[138] E. Koch, "Ammonia–a fuel for motor buses," *J. Inst. Pet*, vol. 31, p. 213, 1945. (see pages 44, 45)

[139] W. Cornelius, L. W. Huellmantel, and H. R. Mitchell, "Ammonia as an engine fuel," *SAE Transactions*, vol. 74, pp. 300–326, 1966. (see pages 44)

[140] NASA, "Nasa dryden fact sheets - x-15 hypersonic research program," 2014. (see pages 44)

[141] D. Pratt, *Performance of Ammonia-Fired GasTurbine Combustors*. Thesis, 1967. (see pages 44)

[142] J. T. Gray, E. Dimitroff, N. T. Meckel, and R. D. Quillian, "Ammonia fuel - engine compatibility and combustion," 1966. (see pages 44)

[143] K. Ryu, G. E. Zacharakis-Jutz, and S.-C. Kong, "Performance characteristics of compression-ignition engine using high concentration of ammonia mixed with dimethyl ether," *Applied Energy*, vol. 113, pp. 488–499, 2014. (see pages 46, 168, 169, 184)

[144] S. Frigo and R. Gentili, "Analysis of the behaviour of a 4-stroke si engine fuelled with ammonia and hydrogen," *International Journal of Hydrogen Energy*, vol. 38, no. 3, pp. 1607–1615, 2013. (see pages 46, 47)

[145] O. Kurata, N. Iki, T. Matsunuma, T. Inoue, T. Tsujimura, H. Furutani, H. Kobayashi, and A. Hayakawa, "Performances and emission characteristics of nh3–air and nh3ch4–air combustion gas-turbine power generations," *Proceedings of the Combustion Institute*, vol. 36, no. 3, pp. 3351–3359, 2017. (see pages 46, 47, 48, 172, 183, 186)

[146] O. Kurata, N. Iki, T. Matsunuma, T. Inoue, T. Tsujimura, H. Furutani, A. Hayakawa, and H. Kobayashi, "Success of ammonia-fired, regenerator-heated, diffusion combustion gas turbine power generation and prospect of low nox combustion with high combustion efficiency," in *American Society of Mechanical Engineers, Power Division (Publication) POWER*, vol. 1. Cited By :1 Export Date: 12 November 2020. (see pages 46, 67, 172)

[147] N. Iki, O. Kurata, T. Matsunuma, T. Inoue, T. Tsujimura, H. Furutani, H. Kobayashi, and A. Hayakawa, "Operation and flame observation of micro gas turbine firing ammonia," in *Proceedings of the ASME Turbo Expo*, vol. 8. Cited By :4 Export Date: 12 November 2020. (see pages 46, 172, 173)

[148] O. Kurata, N. Iki, T. Inoue, T. Matsunuma, T. Tsujimura, H. Furutani, M. Kawano, K. Arai, E. C. Okafor, A. Hayakawa, and H. Kobayashi, "Development of a wide range-operable, rich-lean low-nox combustor for nh3 fuel gas-turbine power generation," *Proceedings of the Combustion Institute*, vol. 37, no. 4, pp. 4587–4595, 2019. (see pages 48, 173, 174, 183, 186)

[149] R. Harding, "Japan bets on ammonia as the fuel of the future," 2020. (see pages 48)

[150] S. Ushakov, D. Stenersen, and P. M. Einang, "Methane slip from gas fuelled ships: a comprehensive summary based on measurement data," *Journal of Marine Science and Technology*, vol. 24, no. 4, pp. 1308–1325, 2019. (see pages 48)

[151] J. Atchison, "Fortescue & deutsche bahn to develop ammonia-powered trains in germany," 2022. (see pages 49)

[152] Ansys, "Ansys chemkin pro version 17.0," 2019. (see pages 53, 59, 60, 65, 67, 69)

[153] ANSYS, "Ansys chemkin-pro," 2023. (see pages 53)

[154] T. Rutar and P. C. Malte, "Nox formation in high-pressure jet-stirred reactors with significance to lean-premixed combustion turbines," *Journal of Engineering for Gas Turbines and Power*, vol. 124, no. 4, pp. 776–783, 2002. (see pages 67)

[155] A. Bhargava, M. Colket, W. Sowa, K. Casleton, and D. Maloney, "An experimental and modeling study of humid air premixed flames," *Journal of*

Engineering for Gas Turbines and Power, vol. 122, no. 3, pp. 405–411, 2000. (see pages 67)

[156] A. H. Lefebvre, *Gas turbine combustion / Arthur H. Lefebvre*. Washington: Washington : Hemisphere Pub. Corp. : McGraw-Hill, 1983. (Arthur Henry). (see pages 75)

[157] A. K. Gupta, *Swirl flows / A.K. Gupta, D.G. Lilley, N. Syred*. Tunbridge Wells: Tunbridge Wells : Abacus, 1984. (Ashwani K.) (Nick). (see pages 75)

[158] J. M. C. N. A. Beer, *Combustion aerodynamics*. London: Applied Science Publishers, 1972. (see pages 75)

[159] N. Syred and J. M. Beér, "Combustion in swirling flows: A review," *Combustion and Flame*, vol. 23, no. 2, pp. 143–201, 1974. (see pages 75)

[160] V. r. company, "Phantom v710 data sheet," 2009. (see pages 82)

[161] L. HORIBA, "Cla-720ma no/nox analyzer," report, July 2004 2004. (see pages 85, 86, 87)

[162] L. HORIBA, "Cla-720a no/nox analyzer," report, July 2004 2004. (see pages 85, 86, 87)

[163] L. HORIBA, "Mpa-720 o2 analyzer," report, July 2004 2004. (see pages 86, 87)

[164] C. Today, "What is pulsed discharge detector (pdd) for gas chromatography?," Apr 04 2022. (see pages 88)

[165] T. Scientific, "Trace 1300 and trace 1310 gas chromatographs user guide," report, 2016. (see pages 88, 90)

[166] GOV.UK, "Monitoring stack emissions: guidance for selecting a monitoring approach," 2019. (see pages 89, 177)

[167] C. E. Baukal and P. B. Eleazer, "Quantifying nox for industrial combustion processes," *J Air Waste Manag Assoc*, vol. 48, no. 1, pp. 52–8, 1998. (see pages 89)

[168] S. K. Gupta, P. Prabhudeva, M. Kumar, P. K. Ojha, and S. Karmakar, "Investigation on spray combustion characteristics of boron-loaded slurry fuel in a swirl-stabilized combustor," *Fuel*, vol. 323, 2022. (see pages 91)

[169] X. Ma, Z. Wang, C. Jiang, Y. Jiang, H. Xu, and J. Wang, "An optical study of in-cylinder ch2o and oh chemiluminescence in flame-induced reaction front propagation using high speed imaging," *Fuel*, vol. 134, pp. 603–610, 2014. (see pages 91)

[170] M. Zhao, D. Buttsworth, and R. Choudhury, "Experimental and numerical study of oh* chemiluminescence in hydrogen diffusion flames," *Combustion and Flame*, vol. 197, pp. 369–377, 2018. (see pages 91)

[171] S. Zhou, X. Zhu, B. Yan, Q. Gao, G. Chen, and B. Li, "Role of a hot coflow on establishment of mild combustion of biomass gasified gas," *Fuel*, vol. 314, 2022. (see pages 91)

[172] Y. Liu, J. Tan, M. Wan, L. Zhang, and X. Yao, "Quantitative measurement of oh* and ch* chemiluminescence in jet diffusion flames," *ACS Omega*, vol. 5, no. 26, pp. 15922–15930, 2020. Liu, Yao Tan, Jianguo Wan, Minggang Zhang, Lang Yao, Xiao eng 2020/07/14 ACS Omega. 2020 Jun 25;5(26):15922-15930. doi: 10.1021/acsomega.0c01093. eCollection 2020 Jul 7. (see pages 91)

[173] F. Zhang, G. Chen, D. Wu, T. Li, Z. Zhang, and N. Wang, "Characterising premixed ammonia and hydrogen combustion for a novel linear joule engine generator," *International Journal of Hydrogen Energy*, vol. 46, no. 44, pp. 23075–23090, 2021. (see pages 93)

[174] F. Zhang, G. Chen, D. Wu, T. Li, Z. Zhang, and N. Wang, "Characteristics of ammonia/hydrogen premixed combustion in a novel linear engine generator," in *The First World Energies Forum*, vol. 58. (see pages 93)

[175] F. Zhang, Z. Zhang, N. Wang, T. Li, and D. Wu, "Characterising injection and combustion of ammonia as a marine fuel," in *The 3rd International Conference on Smart & Green Technology for shipping and Maritime Industries*. (see pages 94)

[176] F. Zhang, G. Chen, and D. Wu, "Combustion and emission characteristics of ammonia hydrogen dual-fuelled generic gas turbine," 2021. (see pages 94)

[177] O. C. Kwon and G. M. Faeth, "Flame/stretch interactions of premixed hydrogen-fueled flames: measurements and predictions," *Combustion and Flame*, vol. 124, no. 4, pp. 590–610, 2001. (see pages 99)

[178] H. Nozari and A. Karabeyoğlu, "Numerical study of combustion characteristics of ammonia as a renewable fuel and establishment of reduced reaction mechanisms," *Fuel*, vol. 159, pp. 223–233, 2015. (see pages 100)

[179] U. Ngwaka, D. Wu, J. Happian-Smith, B. Jia, A. Smallbone, C. Diyoke, and A. P. Roskilly, "Parametric analysis of a semi-closed-loop linear joule engine generator using argon and oxy-hydrogen combustion," *Energy*, 2020. (see pages 101)

[180] S. M. Correa, "A review of nox formation under gas-turbine combustion conditions," *Combustion Science and Technology*, vol. 87, pp. 329–362, 1993. (see pages 110)

[181] D. E. Cavaliere, J. Kariuki, and E. Mastorakos, "A comparison of the blow-off behaviour of swirl-stabilized premixed, non-premixed and spray flames," *Flow, Turbulence and Combustion*, vol. 91, no. 2, pp. 347–372, 2013. (see pages 134)

[182] E. Okafor, K. Sakai, A. Hayakawa, T. Kudo, O. Kurata, N. Iki, and H. Kobayashi, "Stabilization and emission characteristics of ammonia flames in a micro gas turbine combustor," 2017. (see pages 136)

[183] G. Tang, P. Jin, Y. Bao, W. S. Chai, and L. Zhou, "Experimental investigation of premixed combustion limits of hydrogen and methane additives in ammonia," *International Journal of Hydrogen Energy*, vol. 46, no. 39, pp. 20765–20776, 2021. (see pages 136, 138)

[184] E. C. Okafor, M. Tsukamoto, A. Hayakawa, K. D. . A. Somarathne, T. Kudo, T. Tsujimura, and H. Kobayashi, "Influence of wall heat loss on the emission characteristics of premixed ammonia-air swirling flames interacting with the combustor wall," *Proceedings of the Combustion Institute*, vol. 38, no. 4, pp. 5139–5146, 2021. (see pages 148)

[185] J. Zhang, C. Sui, B. Zhang, and J. Li, "Effects of swirl intensity on flame stability and no emission in swirl-stabilized ammonia/methane combustion," *Applications in Energy and Combustion Science*, vol. 14, 2023. (see pages 151)

[186] G. Pretzler, "A new method for numerical abel-inversion," *Zeitschrift für Naturforschung A*, 1991. (see pages 152, 153)

[187] C. Killer, "Abel inversion algorithm," 2016. (see pages 152, 153)

[188] J. Runyon, R. Marsh, P. Bowen, D. Pugh, A. Giles, and S. Morris, "Lean methane flame stability in a premixed generic swirl burner: Isothermal flow and atmospheric combustion characterization," *Experimental Thermal and Fluid Science*, vol. 92, pp. 125–140, 2018. (see pages 155)

[189] K. Ryu, G. E. Zacharakis-Jutz, and S.-C. Kong, "Effects of gaseous ammonia direct injection on performance characteristics of a spark-ignition engine," *Applied Energy*, vol. 116, pp. 206–215, 2014. (see pages 165, 180)

[190] Y. Woo, J. Y. Jang, Y. J. Lee, and J.-N. Kim, "Recent progress on the ammonia-gasoline and the ammonia-diesel dual fueled internal combustion engines in korea," in *11th Annual NH3 Fuel Conference*. (see pages 165, 166)

[191] M. Comotti and S. Frigo, "Hydrogen generation system for ammonia–hydrogen fuelled internal combustion engines," *International Journal of Hydrogen Energy*, vol. 40, no. 33, pp. 10673–10686, 2015. (see pages 165, 166, 178, 180)

[192] C. S. Mørch, A. Bjerre, M. P. Gøttrup, S. C. Sorenson, and J. Schramm, "Ammonia/hydrogen mixtures in an si-engine: Engine performance and analysis of a proposed fuel system," *Fuel*, vol. 90, no. 2, pp. 854–864, 2011. (see pages 165, 166, 179, 180)

[193] S. Oh, C. Park, S. Kim, Y. Kim, Y. Choi, and C. Kim, "Natural gas–ammonia dual-fuel combustion in spark-ignited engine with various

air–fuel ratios and split ratios of ammonia under part load condition," *Fuel*, vol. 290, 2021. (see pages 165, 166, 167, 179, 181)

[194] W. Wei, G. Li, Z. Zhang, Y. Long, H. Zhang, Y. Huang, M. Zhou, and Y. Wei, "Effects of ammonia addition on the performance and emissions for a spark-ignition marine natural gas engine," *Energy*, vol. 272, 2023. (see pages 165, 166, 167, 168, 178, 181)

[195] A. Yousefi, H. Guo, S. Dev, B. Liko, and S. Lafrance, "Effects of ammonia energy fraction and diesel injection timing on combustion and emissions of an ammonia/diesel dual-fuel engine," *Fuel*, vol. 314, 2022. (see pages 168, 169, 170, 171, 177, 178, 182, 184)

[196] A. Yousefi, H. Guo, S. Dev, S. Lafrance, and B. Liko, "A study on split diesel injection on thermal efficiency and emissions of an ammonia/diesel dual-fuel engine," *Fuel*, vol. 316, 2022. (see pages 171, 182, 184, 185)

[197] E. Nadimi, G. Przybyła, M. T. Lewandowski, and W. Adamczyk, "Effects of ammonia on combustion, emissions, and performance of the ammonia/diesel dual-fuel compression ignition engine," *Journal of the Energy Institute*, vol. 107, 2023. (see pages 171, 185)

[198] R. Sivasubramanian, J. B. Sajin, and G. Omanakuttan Pillai, "Effect of ammonia to reduce emission from biodiesel fuelled diesel engine," *International Journal of Ambient Energy*, vol. 43, no. 1, pp. 661–665, 2019. (see pages 171, 172, 185)

[199] F. Huang, S. Guo, L. Wang, Z. Yang, and W. Kong, "Experimental and numerical study on the performances of a free-piston engine generator using

ammonia and methane fuel mixtures," *Fuel*, vol. 341, 2023. (see pages 174, 175, 187)

[200] C. Zhang, B. Lu, J. Wang, L. Zhu, J. Xiao, Z. Sun, and Z. Huang, "Numerical analysis of ammonia hcci combustion in a free piston engine through trajectory-based combustion control," *Fuel*, vol. 341, 2023. (see pages 174, 175, 187, 188)

[201] L. I. I. Office, "Combustion calculations, normalisations and conversions," report, 2004. (see pages 177)

[202] F. R. Westlye, A. Ivarsson, and J. Schramm, "Experimental investigation of nitrogen based emissions from an ammonia fueled si-engine," *Fuel*, vol. 111, pp. 239–247, 2013. (see pages 181)

[203] E. Commission, "Commission proposes new euro 7 standards to reduce pollutant emissions from vehicles and improve air quality," report, 2022. (see pages xxviii, 181)

[204] A. Valera-Medina, S. Morris, J. Runyon, D. G. Pugh, R. Marsh, P. Beasley, and T. Hughes, "Ammonia, methane and hydrogen for gas turbines," *Energy Procedia*, vol. 75, pp. 118–123, 2015. (see pages 183)